

**INFLUENCE OF MICROSTRUCTURE ON MECHANICAL  
PROPERTIES AND DAMAGE CHARACTERISTICS OF AL-SI  
ALLOYS**

**DISSERTATION**

zur Erlangung des Grades

des Doktors der Ingenieurwissenschaften

der Naturwissenschaftlich-Technischen Fakultät

der Universität des Saarlandes

von

**ANASTASIA KRUGLOVA**

Saarbrücken

2017

**Tag des Kolloquiums:** 26.03.2018

**Dekan:** Prof. Dr. rer. nat. G. Kickelbick

**Berichterstatter:** Prof. Dr.-Ing. F. Mücklich  
Prof. Dr.-Ing. S. Diebels

**Vorsitz:** Prof. Dr. mont. C. Motz

**Akad. Mitarbeiter:** Dr. rer. nat. M. Roland

## **ABSTRACT**

Nowadays Al-Si alloys have an increasing share in automobile parts and are seen as a promising material for new structural applications that require an improved strength and fracture resistance. In this respect, the functionality of the alloys is mostly defined by their mechanical performance. The latter, in turn, strongly depends on the microstructure. With respect to the most relevant mechanical properties, tailoring the microstructure more closely to each specific application needs requires a deep understanding of the relations between morphological and mechanical properties of a structure.

In this study, an extensive analysis of morphological properties, mechanical behavior and damage characteristics of Al-Si alloys under different loading conditions is conducted and corresponding structure-properties relations are investigated. The limits of 2D characterization of Si morphology and damage in the eutectic structure are discussed. Furthermore, a model for the simulation of a system of dimples on the fracture surface of the eutectic phase is proposed and its application to studying the relation between Si morphology and eutectic fracture toughness is described. The work thus contributes to better understanding of structure-properties relations and developing quantitative methods enabling a microstructure-based prediction of properties without their direct measurements.

## ZUSAMMENFASSUNG

Heutzutage werden Al-Si-Legierungen zunehmend in der Automobilindustrie eingesetzt und gelten als vielsprechender Strukturwerkstoff für Anwendungen, die erhöhte Festigkeit und Bruchfestigkeit erfordern. Somit wird die Funktionalität der Legierungen meist über ihre mechanischen Eigenschaften definiert, welche wiederum vom Gefüge abhängen. In Bezug auf die wichtigsten mechanischen Eigenschaften erfordert die Einstellung des Gefüges für spezifische Anwendungen ein tiefes Verständnis des Zusammenhangs zwischen den morphologischen und den mechanischen Eigenschaften einer Struktur.

In dieser Arbeit wurde eine grundlegende Analyse der morphologischen Eigenschaften, des mechanischen Verhaltens und des Schädigungsverhaltens von Al-Si-Legierungen in verschiedenen Lastsituationen durchgeführt und die entsprechenden Struktur-Eigenschafts-Beziehungen untersucht. Die Grenzen der 2D-Charakterisierung der Silizium-Morphologie und der Schädigung im eutektischen Gefüge werden diskutiert. Darüber hinaus wird ein Modell für die Simulation der Bruchoberfläche der eutektischen Phase vorgeschlagen und seine Anwendung auf die Untersuchung des Zusammenhangs zwischen der Siliziummorphologie und der Bruchzähigkeit des Eutektikums beschrieben. Damit trägt diese Arbeit zu einem besseren Verständnis der Struktur-Eigenschafts-Beziehung bei und zur Entwicklung gefügebasierter Methoden zur quantitativen Vorhersage von Eigenschaften ohne diese direkt messen zu müssen.

ABSTRACT .....	III
ZUSAMMENFASSUNG .....	IV
PREFACE .....	IX
SYMBOLS AND ABBREVIATIONS .....	XI
<b>1 Introduction .....</b>	<b>1</b>
1.1 Motivation.....	1
1.2 Outline .....	4
<b>2 State of the art .....</b>	<b>5</b>
2.1 Al-Si alloys .....	5
2.1.1 Al-Si system.....	5
2.1.2 Thermal treatment.....	6
2.1.3 Eutectic modification .....	8
2.2 Mechanical properties of Al-Si alloys .....	12
2.3 Effect of connectivity .....	13
2.4 Damage behavior of Al-Si alloys .....	15
2.4.1 Fundamentals .....	15
2.4.2 Damage mechanism in Al-Si alloys.....	16
2.4.3 Impact of second phase particles .....	20
2.4.4 Damage modes of Si particles.....	22
2.4.5 Orientation of cracks.....	23
2.4.6 3D damage characterization.....	24
2.4.7 Fracture toughness of Al-Si alloys.....	27
2.4.8 Fracture toughness estimation methods .....	30
<b>3 Experimental methods .....</b>	<b>33</b>
3.1 Elaboration of Al-Si castings.....	33
3.2 Metallographic examination .....	35
3.3 Focused Ion Beam/Scanning Electron Microscope (FIB/SEM) tomography .....	35
3.3.1 Principles of FIB/SEM tomography .....	35
3.3.2 3D reconstruction.....	37
3.4 Quantitative microstructure characterization.....	39

3.4.1	2D microstructure characterization.....	39
3.4.2	3D microstructure characterization.....	41
3.4.3	Evaluation of connectivity.....	43
3.4.4	Orientation distribution of cracks.....	44
3.4.5	Evaluation of inter-particle spacing.....	44
3.5	Characterization of mechanical behavior.....	45
3.5.1	FEM simulations.....	45
3.5.2	Compression tests.....	46
3.5.3	Tensile tests.....	47
3.6	Fracture surface characterization.....	48
3.6.1	Fractography.....	48
3.6.2	Image processing of fractographic images.....	49
3.6.3	Estimation of dimple depth-to-width ratio.....	50
3.6.4	Estimation of fracture surface area.....	51
3.6.5	Fracture toughness measurements.....	53
3.6.6	Analytical estimation of fracture toughness.....	54
3.7	Stochastic modeling.....	55
3.7.1	Principles of competitive stochastic growth model.....	55
3.7.2	Parameters of competitive stochastic growth model.....	57
3.7.3	Experimental data for simulation study.....	58
3.7.4	Fundamentals of tessellation models.....	60
3.7.5	Tessellation model of fracture surface.....	62

## **4 Results and Discussion.....65**

4.1	Simulation study: Influence of Si morphology on compression strength.....	66
4.1.1	Influence of connectivity and degree of branching of particles.....	68
4.1.2	Influence of number of particles in simply connected structures.....	73
4.1.3	Evaluation of Si connectivity in Al-Si alloys.....	75
4.1.4	Stress-strain state in simulation volume.....	77
4.2	Micrographic analysis of eutectic phase in Al-Si alloys.....	78
4.2.1	As-cast Al-Si alloys.....	78
4.2.2	Solution treated Al-Si alloys.....	80

4.2.3	Referencing of samples .....	82
4.3	Mechanical behavior of Al-Si alloys .....	83
4.4	Influence of Si morphology on mechanical properties .....	89
4.5	Damage behavior of Al-Si alloys .....	92
4.5.1	Metallographic examination of damage.....	93
4.5.2	3D damage investigation.....	95
4.5.3	Limits and potentials of 2D damage characterization.....	104
4.6	Fractography of Al-Si eutectic.....	110
4.6.1	SEM fractography .....	110
4.6.2	Correlation between dimples and Si particles geometry.....	116
4.7	Fracture surface modeling .....	122
4.7.1	Pre-conditions and motivation .....	122
4.7.2	Model fitting and verification .....	123
4.7.3	Simulation of fracture surfaces .....	127
4.7.4	Estimation of topographic features .....	129
4.7.5	Example of fracture toughness estimation.....	132
<b>5</b>	<b>Conclusions and Outlook.....</b>	<b>139</b>
5.1	Conclusions.....	139
5.2	Outlook .....	142
<b>6</b>	<b>Appendix .....</b>	<b>143</b>
6.1	Calculations of the volumetric change .....	143
<b>7</b>	<b>Bibliography.....</b>	<b>145</b>



## PREFACE

### Dissemination of the work

The results of the present work have been summarized in several publications which contain different parts of the work:

- A. Kruglova, M. Roland, S. Diebels, F. Mücklich, “Combination of experimental and numerical methods for mechanical characterization of Al-Si alloys”, *IOP Conference Series: Materials Science and Engineering*, 258 (2017) 012004.
- A. Kruglova, M. Roland, S. Diebels, T. Dahmen, P. Slusallek, F. Mücklich, “Modelling and characterization of ductile fracture surface in Al-Si alloys by means of Voronoi tessellation”, *Materials Characterization*, 131 (2017) 1-11.
- A. Kruglova, M. Engstler, G. Gaiselmann, O. Stenzel, V. Schmidt, M. Roland, S. Diebels, F. Mücklich, “3D connectivity of eutectic Si as a key property defining strength of Al-Si alloys”, *Computational Materials Science*, 120 (2016) 99-107.
- M. Roland, A. Kruglova, G. Gaiselmann, T. Brereton, V. Schmidt, F. Mücklich, S. Diebels, “Numerical simulation and comparison of a real Al-Si alloy with virtually generated alloys”, *Archive of Applied Mechanics*, 85 (2015) 1161-1171.
- M. Roland, A. Kruglova, N. Harste, F. Mücklich, S. Diebels, “Numerical simulation of Al-Si alloys with and without a directional solidification”, *Image Analysis and Stereology*, 33 (2014) 29-37.
- G. Gaiselmann, O. Stenzel, A. Kruglova, F. Mücklich, V. Schmidt, “Competitive stochastic growth model for the 3D morphology of eutectic Si in Al-Si alloys”, *Computational Materials Science*, 69 (2013) 289-298.

### Acknowledgments

First of all I express my special gratitude to my supervisor Prof. Dr. Frank Mücklich for giving me the opportunity to pursue my doctoral studies, his trust and support by establishing new research collaborations. His guidance, expert knowledge and highly valuable advices made this dissertation possible.

I am very grateful to Prof. Dr. Stefan Diebels for accepting the request to review this thesis and his scientific support on the subject of the mechanical characterization during our collaborative work.

I sincerely thank Michael Engstler for the tomographic experiments and his assistance in the image data characterization. He was always ready to give me a helping hand, and I could always count on his support and insightful advices. I also thank him for his comments on this manuscript.

I would like to thank all researchers with whom we collaborated on different parts of this work. Without their outstanding expertise this interdisciplinary study could not be performed. I am very thankful to Dr. Michael Roland for his assistance in mechanical characterization of Al-Si alloys and extensive discussions of various aspects of this work. I also deeply appreciate his help with proofreading this thesis and our publications. I would like to express my sincerest gratitude to Prof. Dr. Volker Schmidt, Dr. Gerd Gaiselmann and Dr. Ole Stenzel for the pleasant and successful collaboration on the topic of the stochastic microstructure modeling. I owe special thank to Priv.-Doz. Dr. Michael Marx and Matthias Thielen for investigations and helpful discussions of the fracture behavior of Al-Si alloys. I am also grateful to Prof. Dr. Philipp Slusallek and Dr. Tim Dahmen for their contribution to the fracture surface modeling approach.

I am very thankful to Dr. Sebastian Suarez, Timothy MacLucas, and Dr. Alexey Ershov for reviewing this manuscript and their excellent suggestions, and Christoph Pauly for translating the abstract to German.

I acknowledge with gratitude the pleasant and friendly working environment, which would not be possible without my colleagues at the Chair of Functional Materials at Saarland University. Special thanks go to my colleagues, who contributed to this work with their expertise and helpful advices or just sharing this time with me for their help, support and inspiration.

Finally, I extend my deepest thank to my family for their support and sharing with me all the cheerful and stressful periods of my PhD.

## SYMBOLS AND ABBREVIATIONS

### Symbols

$2X$	AlSi12 (unmodified)
$3X$	AlSi12 with 212 ppm of Sr (modified)
$7X$	AlSi12 with 208 ppm of Sr and 0.31 wt.% of Mg (inhomogeneously modified)
$A'$	Projected surface area
$C$	Connectivity
$d$	Equivalent particle diameter
$e$	Elongation
$E$	Young's modulus
$h_s$	Average dimple depth
$J_C$	J-integral fracture toughness
$K_{Ic}$	Plain-strain fracture toughness
$K_C$	Fracture toughness
$K_Q$	Conditional fracture toughness
$K_V$	Specific integral of total curvature
$L'$	Projected profile length
$L_t$	True profile length
$MaxFerret$	Maximum diameter of an object
$MinFerret$	Minimum diameter of an object
$N$	Number of particles
$N'_A$	Particle density on projection plane
$N_A$	Particle density on plane of polish
$N_V$	Number density
$r_{cox}$	Hardcore radius
$\mathbb{R}^n$	n-dimensional real space
$R_L$	Profile roughness parameter
$R_S$	Surface roughness parameter
$S_t$	True surface area
$S_{total}$	Fracture surface area
$t_{external}$	External competition parameter
$t_{internal}$	Internal competition parameter
$T4$	Heat treatment cycle: solution heat treatment and quenching
$T6$	Heat treatment cycle: solution heat treatment, quenching and artificial aging

$V_{MaxCluster}$	Volume of the largest individual particle (cluster) of Si
$V_{TotalSi}$	Total volume of Si particles
$V_V$	Volume fraction
$wd$	Weighted distance between two points
$\lambda$	Inter-particle spacing
$\nu$	Poisson's ratio
$\sigma_{UTS}$	Ultimate tensile strength
$\sigma_y$	Yield strength
$\chi$	Euler number
$\chi_v$	Specific Euler number

## Abbreviations

2D	Two dimensional
3D	Three dimensional
AC	As-cast
CSGM	Competitive stochastic growth model
DAS	Secondary dendrite arm spacing
DC	Direct chill
EDX	Energy dispersive X-ray analysis
ETD	Everhard-Thornley detector
FEM	Finite element method
FIB	Focused ion beam
GP	Guinier-Preston
IIT	Impurity-induced twinning
LM	Light microscopy
LOT	Light optical tomography
MAVI	Modular algorithms for volume images
PM	Permanent mold
sXCT	Synchrotron tomography
SEM	Scanning electron microscope (microscopy)
ST	Solution treatment (treated)
TEM	Transmission electron microscope (microscopy)
TLD	Through lens detector
TPRE	Twin plane re-entrant edge
UTS	Ultimate tensile strength
wt. %	Weight percent
XCT	X-ray tomography
YS	Yield strength



# 1 Introduction

---

## 1.1 Motivation

The global tendency towards miniaturization and eco-conception requires the development of new high-performance, lighter-weight and fuel saving vehicles [1,2]. In this concern, light aluminium alloys have been used to substitute conventional heavier materials like steel, cast iron and copper in automobile parts, in particular, for producing cylinder heads [3], engine blocks [4] and heat exchangers. Owing to their large variety of physical and mechanical properties, different aluminium alloys are used in the automotive industry. Aluminium-silicon (Al-Si) castings are the most used castings in the automobile branch due to their good castability and corrosion resistance [5]. Besides, Al-Si-Mg casting alloys are widely used in aircraft applications [6].

In general, Al-Si alloys are the material of choice for many engineering applications due to their attractive strength characteristics combined with the low weight of casting components. In this respect, the functionality of the alloys is mostly defined by their mechanical performance. Steady improvements in casting processes allow to produce casting microstructures with reduced amount of casting defects and improved properties [4]. The properties, in turn, strongly depend on the microstructure, i.e. they are defined by the morphology and arrangement of the microconstituents, such as primary aluminium dendrites, silicon particles, intermetallic inclusions and casting defects. Thus, a thorough characterization of the microstructure and mechanical performance of the alloys is necessary to better understand the relations between morphological and mechanical features of a structure. It will allow to tailor the microstructure more closely to the specific application needs and develop quantitative methods enabling a microstructure-based prediction of properties without their direct measurements. To do so, the use of methods of the so-called 3D materials science is of great importance nowadays.

Advanced methods in the field of the 3D materials science imply a multidisciplinary approach which combines 3D reconstruction of materials structures, virtual simulations and analysis of the data in 3D. Although 3D characterization methods are often complex and time-consuming, they can provide unique information for understanding structure-properties relationships. The traditional characterization methods in 2D are often limited by the amount and quality of information that can be obtained. Moreover, estimation of 3D properties from

2D data usually requires application of simplifying assumptions and stereological methods, whereby some features cannot be determined based on 2D data at all. Therefore, the information derived from 2D investigations is likely to be incomplete or inaccurate, especially, for complex anisotropic structures [7].

Advances in experimental techniques and computational power have enabled a more effective use of state-of-the-art methods from different disciplines. For instance, experimentally obtained structures are often replaced by virtual models that capture relevant morphological features of the real structures and are more appropriate for finite-element simulations than the large and complex experimental data.

Until recently, the conventional approach to the investigation of the influence of Si particle morphology on the mechanical behavior of Al-Si alloys has been based on 2D unit cell and multi-particle models. These models enable the generation and numerical analysis of simplified synthetic structures with different distribution of geometric features of the second phase particles [8–10]. Such idealized structures allow to independently study the impact of different morphological parameters of Si particles on the mechanical behavior of the material, which cannot be realized by investigating real microstructures due to the difficulties in controlling every single parameter during the manufacturing process. However, the multi-particle models have shown to be less accurate in the prediction of the macroscopic mechanical behavior compared to the microstructure based models since they do not take into account the shape irregularities and microstructure anisotropy inherent to the real structures [11,12]. At the same time, stress distributions obtained by the numerical analysis of 2D multi-particle models of metal matrix composites have shown to disagree with the results predicted by the 3D models [13]. Thus, the 3D microstructural data is necessary for the accurate prediction of the mechanical behavior of the material.

The use of 3D structural data obtained by means of tomographic methods solely would not be very effective since these techniques are very costly and time-consuming. Thus, the development of a 3D microstructure based model that enables a generation of a large variety of virtual structures more efficiently is important for a deeper understanding of structure-properties relationships. In this respect, a Competitive Stochastic Growth Model (CSGM) introduced in [14] is capable of reproducing morphological features of Si particles in Al-Si alloys which are relevant for the mechanical performance of the structure. This model can thus be used to study the relations between the 3D morphology of the eutectic Si and the mechanical response of the eutectic structure in a more detailed way.

The characterization of damage and fracture resistance of Al-Si alloys is also getting an increasing importance in light of using the alloys for new structural applications, for example, in commercial aircraft structures [6]. Although there are many studies dealing with damage behavior of Al-Si alloys, the topic of 3D damage characteristics in relation to the microstructural morphology has been barely addressed therein. Most of the time, damage in Al-Si alloys has been studied using 2D characterization techniques that cannot provide thorough and ambiguity-free information. Therefore, 3D analysis could provide a clue to the phenomena observed in 2D and define the limits and potentials of conventional characterization techniques.

Besides, the development of a simple and reliable methodology allowing for the effective study of the relation between Si morphology and fracture resistance is essential for the material's design. Due to the lack of available information on the fracture toughness of Al-Si alloys and the fact that it is not always possible to measure it via experimental methods, having such a method at hand could help to evaluate the impact of microstructure on the fracture resistance of the material in a relatively simple way.

The following work addresses the presented issues by using virtual simulations and laboratory experiments. Thereby, a thorough analysis of morphological properties, mechanical behavior and damage characteristics of Al-Si alloys under different loading conditions has been conducted and the underlined structure-properties relations have been investigated. Furthermore, a model for the simulation of a system of dimples on the fracture surface of Al-Si alloys has been proposed and its application to studying the relation between Si morphology and eutectic fracture toughness has been described.

## 1.2 Outline

The present work is structured in the following way:

Chapter 1 describes the motivation for this work and how the work addresses the presented issues.

Chapter 2 presents the state of the art in the field of investigation including the relevant knowledge on Al-Si alloys, their mechanical properties and damage behavior as well as fundamentals of stochastic methods used in materials science.

Chapter 3 describes experimental methods used for the imaging, characterization and stochastic modeling of microstructures as well as characterization of the damage and mechanical behavior of the material. The fundamentals of the model for the fracture surface simulation are presented.

Chapter 4 is dedicated to the results and discussion. It can be divided into four major parts:

- The first part presents a simulation study that elaborates on the influence of Si morphology on the mechanical behavior of the material by applying mechanical simulations to virtual samples of the eutectic phase.
- The second part is devoted to the laboratory investigations of the mechanical behavior of Al-Si alloys under different loading conditions and its correlation with the microstructure of the alloys.
- The third part is dedicated to the damage characterization in Al-Si alloys after mechanical tests using 2D and 3D image analysis methods and fractographic characterization of the specimens after tensile loading.
- And finally, the fourth part presents the model developed for the simulation of the system of dimples on the fracture surface of the eutectic phase in Al-Si alloys. The examples of the application of the modelling results are described.

Chapter 5 summarizes the relevant results of the present work and provides an outlook on further investigations.

## 2 State of the art

---

### 2.1 Al-Si alloys

#### 2.1.1 Al-Si system

According to the phase diagram of the Al-Si binary system [15], that describes phase transformations as a function of temperature for every given chemical composition of the alloy in the equilibrium state, the eutectic reaction takes place at the temperature of around 577 °C and the resulting eutectic phase contains 12.6 wt.% of Si in the Al matrix. The alloys with Si content lower than the eutectic composition are called hypoeutectic and consist of primary  $\alpha$ -Al dendrites and the Al-Si eutectic. The hypereutectic alloys with Si content higher than the eutectic composition contain primary Si crystals and the eutectic phase.

In the non-equilibrium state, which is mostly the case of a large-scale production and high cooling rates, the eutectic composition can be moved to higher concentrations of Si. Shifting of the eutectic point toward a higher Si level is also observed by the presence of different alloying elements [16]: for example, modification of the alloy with Na moves the eutectic point to approximately 14 wt.% of Si [17]; the Sr modification exerts a similar effect [18]. Figure 2.1 shows an example of an Al-Si alloy which has the eutectic composition (according to the phase diagram), yet exhibits a hypoeutectic microstructure.

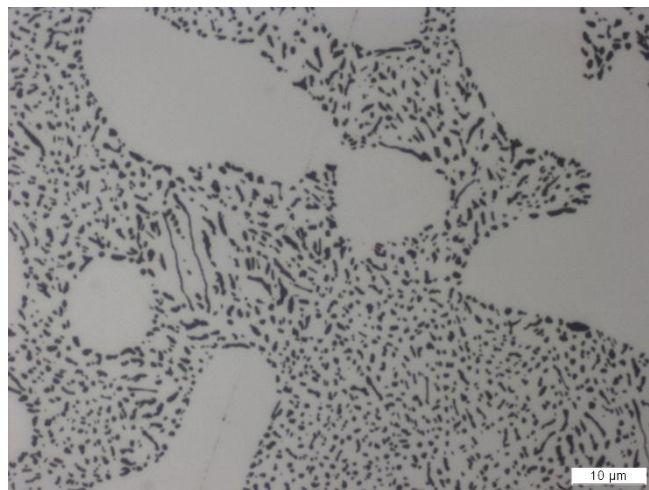


Figure 2.1: Optical micrograph of the as-cast AlSi12 alloy modified with 212 ppm of Sr. Though the content of Si corresponds to the eutectic composition, the alloy contains many dendrites of primary  $\alpha$ -Al which are characteristic for the hypoeutectic composition.

According to designations of the Aluminum Association, Al-Si alloys are represented by two alloy families: 4xx.x stands for the binary alloys and 3xx.x specifies the Al-Si alloys containing also Mg and/or Cu. In these alloys, the major alloying element Si improves casting properties of the melt, in particular, fluidity, hot tear resistance, etc. The optimal Si content in the alloy depends on the casting process. In general, Si content in the alloy increases with the cooling rate of the casting, from sand casting to permanent mold and die casting, respectively [19]. Mg is often added to the alloy in the amount of 0.40 to 0.70 % in order to improve its strength and hardness. Here, the strengthening effect is achieved by the formation of  $Mg_2Si$  phase precipitates. The strength in Al-Si-Mg alloys increases with Mg content, however at the expense of ductility [20]. Apart from the major alloying elements, chemical modification of hypoeutectic alloys by adding small amount of modifiers like Na or Sr is often used to alter the morphology of Si and improve mechanical characteristics of the alloy [19].

### **2.1.2 Thermal treatment**

Al-Si castings are used either in the as-cast state (AC) or after a heat treatment. There is a wide range of heat treatment cycles standardized by the Aluminum Association which are used to improve mechanical properties of the alloys through the changes of phase compositions, morphology of microconstituents as well as by reducing microsegregations and residual stresses. The T4 heat treatment cycle, for example, implies a solution heat treatment and quenching of the casting. It is applied to binary Al-Si alloys particularly to alter the morphology of Si and thus improve the ductility of the material [19]. For Al-Si-Mg alloys, the T6 heat treatment cycle is commonly used. It is composed of the solution heat treatment, quenching and artificial aging [21]. The first stage results in the homogenization and dissolution of  $Mg_2Si$  as well as the fragmentation and spheroidization of Si particles improving the ductility and fracture toughness of the alloy whereas the latter stage leads to the precipitation of the strengthening  $Mg_2Si$  phase in the Al matrix [22,23].

Both thermal cycles described above begin with the solution heat treatment (ST). The solution heat treatment implies an exposure of the alloy to elevated temperatures. The temperature is the crucial parameter in the process: it has to be high enough to reach the maximum possible degree of solution; however it still has to prevent the blistering of the eutectic. The time of the solution treatment depends on the casting procedure and geometry of the parts to be treated, i.e. the finer the microstructure and thinner the product thickness, the shorter can be the thermal exposure time. Obviously, for industrial purposes, the thermal cycle has to be as short

as possible. For the Al-Si permanent mold castings, the ST is usually carried out at the temperature between 505 and 540 °C for 4 to 12 hours [19].

In [22], the influence of ST parameters such as temperature and duration of the heat treatment cycle T6 on mechanical properties of the unmodified and Sr-modified Al-Si-Mg alloy A356.2 has been investigated. It has been shown that the presence of Sr in the alloy influences the kinetics of Si spheroidization and coarsening during the solution heat treatment, so that in the Sr-modified alloys, the spheroidization rate is higher while the coarsening rate is lower than in the unmodified alloys. It implies therefore the shorter time needed for the ST of Sr-modified alloys. Both spheroidization and coarsening rates of Si particles increase with the ST temperature. The increment of the ST temperature up to 550 °C is beneficial to the mechanical strength whereas the further increase of the temperature above 560 °C is, in contrary, disadvantageous for the mechanical properties because it causes the liquid formation at the eutectic grain boundaries. According to the maximum strength properties, the optimum solution treatment time of 1 to 2 hours at 540 °C has been proposed for the permanent mold castings. Zhang et al. [23] have shown that a short solution treatment time of 30 min at 540 °C within the T6 heat treatment is sufficient to achieve more than 90 % of the maximum tensile properties of the modified Al-Si-Mg alloys.

The solution heat treatment of aluminium alloys is then followed by the quenching in hot or boiling water. The temperature of water is chosen depending on the purpose of the quenching: maximum strength and corrosion characteristics are related to the lower temperature of the quench medium, i.e. more rapid quenching, whereas minimum residual stresses are associated with the higher quench medium temperature, i.e. less drastic temperature changes [19]. The quenching of Al-Si-Mg alloys within the T6 heat treatment cycle aims at suppressing the precipitation to retain a maximum of solute in solid solution [21].

And finally, a precipitation hardening (age hardening) is often used to improve mechanical stability of the casting and reduce residual stresses induced by the foregoing quenching. Precipitation of solute atoms in form of the independent phase exerts strengthening and hardening effects on the material, and that is, however, in disadvantage of the ductility [19]. The artificial aging of Al-Si-Mg alloys is carried out in the temperature range of 150 – 210 °C [21], whereby the precipitation occurs in the following sequence: coherent spherical Guinier-Preston (GP) zones enriched in Mg and Si atoms → coherent needle-shaped GP zones → semicoherent rod-like precipitates → non-coherent equilibrium platelets of Mg<sub>2</sub>Si [24,25]. Matsuda et al. [26] have proposed a shape of the GP zone to be a fine plate with a periodic

arrangement of columns of Mg and Si atoms (i.e. Mg:Si = 1.0) which grows by aggregation of several GP zones. Apart from the artificial aging procedure applied to the alloy on purpose, the natural age hardening takes place to a certain degree in many alloys at room temperature. Depending on the alloy, the age hardening can run over a period ranging from a few days to several years [19].

### 2.1.3 Eutectic modification

The primary purpose of the eutectic modification is the improvement of mechanical properties of Al-Si alloys. The effect of the modification is achieved by the morphological transformation of the eutectic phase. In particular, Si in the unmodified alloys solidifies in form of coarse plate-like particles occurring in form of needles on a polished surface while in the modified alloys it has more fine fibrous shape with globular cross sections as can be observed on optical micrographs (see Figure 2.2) [5].

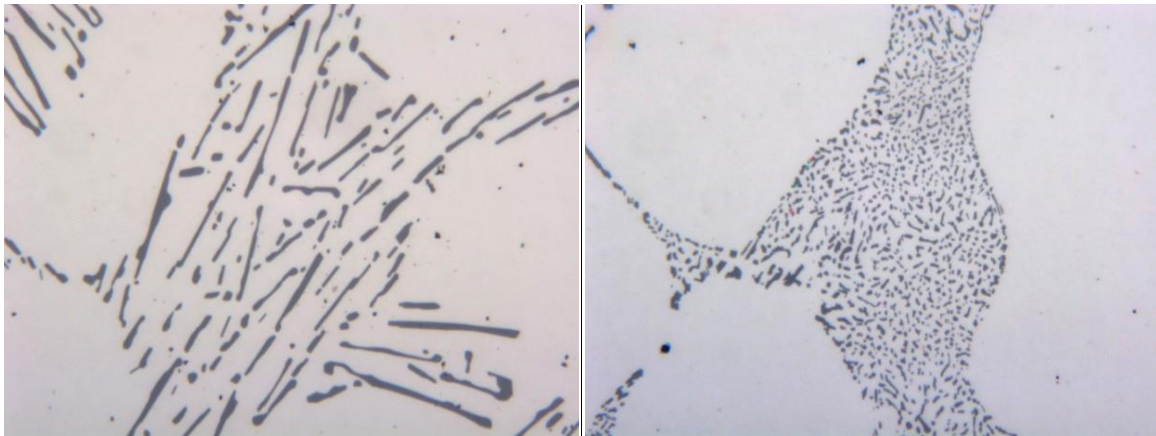


Figure 2.2: Optical micrographs (magnification 1600 $\times$ ) of (a) unmodified Al-Si alloy with needle-like particles of Si and (b) Sr-modified Al-Si alloy with globular cross-sections of Si. The modified structure is much finer than the unmodified one.

Many chemical elements can exert a modifying effect on Al-Si alloys, such as Na, Sr, and Sb. The latter, however, results in rather needle-shaped eutectic in contrary to the effect of the other elements [5]. Na has a high effectiveness with respect to the homogeneity of the modified structure and in promoting Si twinning [27] but it suffers from the rapid fading [5,28]. Nowadays, the preference for the modification is given to Sr [18,19]. The optimum level of Sr added to Al-Si castings is about 0.005 – 0.015 % [29]. The modified structure can also be obtained by quenching the alloys. It is important to note, however, that in the case of the quench modification the structure of Si remains similar to that in the unmodified alloys with respect to the twin density, the only difference is that it is much finer [30]. The quench

modification along is of little use in industrial conditions because of the limited cooling rates that can be achieved via regular casting procedures [5].

There are different theories explaining the effect of the modification in Al-Si alloys: some of them consider the changes on the nucleation level while the others look at the growth level [28]. The most generally accepted theories explaining the eutectic modification on the growth level are the impurity-induced twinning (IIT) [30] and the twin plane re-entrant edge (TPRE) poisoning mechanisms [31].

It is generally accepted that Si crystals grow preferentially in the  $\langle 112 \rangle$  direction across the  $\{111\}$  planes which results in such a flat plate-like structure of Si particles in unmodified alloys. The growth of Si crystal occurs by the addition of Si atoms onto the steps formed across the  $\{111\}$  planes at the solid-liquid interface. According to the IIT mechanism [30], atoms of a modifier are adsorbed on these steps, distorting the normal crystal growth and causing the multiple twinning of Si crystals. It results in a multitude of microfacets covering the surface of Si crystals and thus producing such a rough fibrous shape of Si particles. The high twin density in Si crystals prompts their branching.

Lu and Hellawell [30] have proposed an optimal ratio between the atomic radii of a modifying agent and silicon to be 1.65 in order to enable the IIT mechanism. However, it has been shown that fulfilling the requirement does not always indicate a modifying efficiency of an element. For example, such commonly used modifiers as Sr and Na, though exhibit a ratio different from the optimal one (1.84 and 1.58, respectively), exert a pronounced modifying effect on the eutectic Si. On the other hand, a rare earth element Yb, while having the optimal ratio, does not lead to the modification of the eutectic structure but contributes to its refinement solely [27].

Kobayashi and Hogan [31] have explained the modification mechanism relying on the TPRE mechanism of the Si crystal growth which implies that Si crystal grows readily in the  $\langle 112 \rangle$  direction by the attachment of Si atoms at the twin plane re-entrant edges. The proposed modification mechanism, the TPRE poisoning, suggests that the modifier atoms are preferentially adsorbed at the twin plane re-entrant edges and therefore, hinder the further crystal growth in the favorable direction which causes the crystal twinning and branching of Si flakes. Shamsuzzoha and Hogan [32] have shown that the growth of fibrous Si particles also conforms with the TPRE mechanism. They have proposed a zigzag growth mechanism where segments of Si fibers grow in a wide range of directions by means of large-angle

internal branching while the local growth direction of Si crystals always remains the  $\langle 112 \rangle$  direction, in accordance with the TPRE mechanism.

To summarize, the modification effect expressed on the growth level of the eutectic Si is related to the restriction of the Si growth in the habit plane by the adsorption of modifier atoms and thereby increasing the twin density. Although the modification effect cannot always be explained by the existing models, they still remain the most discussed ones [27].

Recently, important advancements in understanding the modification mechanism have been made. In particular, high resolution techniques such as atom probe tomography (APT) and transmission electron microscopy (TEM) have enabled the identification of different types of Sr co-segregations with Al and Si in the eutectic Si and reconsidering the existing modification models [33,34]. Timpel et al. [33] have identified two types of those co-segregations: type I Sr-Al-Si co-segregations induce the crystal twinning by distorting the normal stacking sequence in accordance with the IIT mechanism while type II Sr-Al-Si co-segregations restrict the crystal growth and promote branching according to the TPRE poisoning mechanisms (see Figure 2.3). Barrirero et al. [34] have distinguished three types of segregations having different shape and impact on the Si growth: rod-like segregations (often V-shaped) contribute to the smoothening of Al-Si interface and influence the Si growth front so that irregular twin boundaries are formed, particle-like segregations restrict the Si growth and planar segregations promote the formation of grain and twin boundaries.

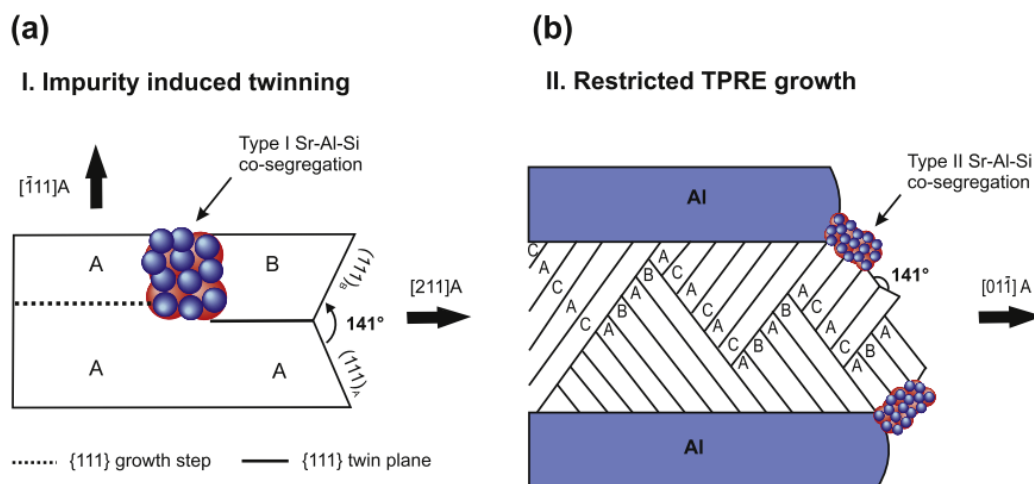


Figure 2.3: Schematic illustration of the location of (a) type I and (b) type II Sr-Al-Si co-segregations in the eutectic Si in accordance with IIT and TPRE poisoning mechanisms, respectively [33].

On the nucleation level, Sr modification hampers the nucleation of eutectic grains so that it occurs at the lower temperatures whereby fewer grains are formed as compared to the unmodified alloys. Thus, the eutectic grains in Sr-modified alloys are much larger than the grains in the unmodified alloys. It has been suggested that while the eutectic grains in the unmodified alloys nucleate at AIP particles, a modifier can neutralize these nuclei by forming modifier-containing intermetallics prior to the eutectic solidification, i.e. the amount of nucleation sites for the eutectic Si is reduced due to their poisoning through the addition of the modifier [35–37]. However, Shankar et al. [38] have shown that Si nucleates at  $\beta$ -(Al, Si, Fe) particles since trace amounts of Fe are always present in Al-Si alloys. Though phosphorus is also present in most commercial castings [35], no AIP particles have been identified in the investigated unmodified hypoeutectic Al-Si alloys. According to the proposed theory, the solidification of the iron-containing intermetallic phase takes place above the eutectic temperature. Then, the eutectic Si nucleates at the  $\beta$ -(Al, Si, Fe) particles ahead of the growing dendrite tips which is followed by the nucleation of the eutectic Al on the eutectic Si from the surrounding liquid enriched with Al [38].

In the unmodified alloys, the grains grow from the dendrite tips while in the modified alloys, the nucleation of the grains occurs independently in the interdendritic liquid. However, it has been shown that when the amount of Sr increases up to 500 ppm, the eutectic nucleation occurs again on the dendrites, although Si particles may still have a well modified morphology. Thus, it can be assumed that the effects of the modification on the eutectic Si particles and eutectic grains are not related to each other [36].

And finally, on the microstructural level, the effect of the modification is primary concerned with the change of the morphology of Si particles. Hafiz and Kobayashi [39] suggest a beneficial effect of the Sr modification on the properties of Al-Si alloys being a result of a more regular shape and smaller size of Si particles and reduced inter-particle spacing which in turn results in improved tensile characteristics and fracture toughness. Fat-Halla [16] has shown that the Sr modification of the eutectic Al-Si alloy contributes primarily to the significant improvement of the ductility while the improvement of the strength is rather moderate. Closset and Gruzleski [29] have reported an increase of nearly 50 % in the elongation due to the Sr modification without significant changes in strength characteristics. The beneficial effect of the Sr modification on the tensile strength and ductility of Al-Si alloys have been thoroughly reported in the literature [18,22,40,41]. A side effect often associated

with the modification is a casting porosity [4,22,42]. Still, modified alloys exhibit superior tensile properties as compared to unmodified alloys [22].

## **2.2 Mechanical properties of Al-Si alloys**

In general, the mechanical behavior of Al-Si alloys has a morphological genesis, i.e. it is defined by the morphology and arrangement of the microconstituents [39], such as Al dendrites, Si particles, intermetallic compounds as well as casting defects (e.g. pores). The modern casting procedures allow to decrease/control the porosity to mitigate its effects on properties of the alloys [4,43] as well as to control a chemical composition and casting parameters to produce a structure with the desired performance. As the brittle Si is not able to accommodate a plastic deformation of the ductile Al matrix, it reduces the ductility of the alloy as compared to the pure Al [44]. Chemical modification of the alloys with the addition of Sr or Na is one of the most used methods to improve the strength and ductility of the material [18,45]. The obtained properties can be further tailored by applying different heat treatment cycles. Both procedures alter the morphology and spatial arrangement of the eutectic Si which in its turn influences the properties [46].

For many engineering applications the strength and ductility of the material are adequate criteria for the design. But as far as the susceptibility to fracture is considered, the only high strength characteristics are not enough, and then it is important to know how the material withstands the fracturing. The property of the material to resist fracturing by absorbing energy and deforming plastically is called toughness. Thus, materials with high toughness are able to tolerate large plastic deformations without fracturing. These materials and fracture types they exhibit are called ductile. Al-Si alloys are typical ductile materials. On the contrary, brittle materials can tolerate only little plastic deformation and are characterized by cleavage fracture [44,47].

For a material to be tough, a balance of both strength and ductility is required. Indeed, when the yield strength of the material is too high, even a small plastic strain can already induce the stress in a structure sufficient to cause the particles fracture. Therefore, materials with higher strength characteristics usually have lower ductility and toughness [44,48]. Different microstructural features are considered to control the ductility of Al-Si alloys. Kobayashi et al. [49] have shown that increasing the porosity level and the size of the largest pore have an adverse effect on mechanical properties of Al-Si-Mg alloys. In particular, an occurrence of regions with a high local volume fraction of micropores results in a strong reduction of the

fracture strain. In the earlier studies, the volume fraction of second phase particles has been regarded as the major factor affecting the ductility; an influence of the particles morphology and nature has been of secondary importance [50].

Some researchers [43,51–54] relate the ductility with the features of both primary Al phase and eutectic Si particles, in particular, with the dendrite cell size and the size and aspect ratio of Si particles, while others emphasize that the size and morphology of Si particles have a dominant influence on mechanical properties [39,55]. Moreover, according to Dighe and Gokhale [56], the microstructural extrema such as the largest Si particles exert a much stronger influence on mechanical properties of the alloys than the average microstructure properties and, therefore, control the fracture properties and ductility of the material. Also, the presence of large intermetallic Fe-rich phases has been shown to play a critical role in mechanical properties of Al-Si alloys leading to large cracks that can be a few hundred micrometers long [57].

On the contrary, Doglione [58] has suggested that the ductility of the alloys depends mostly on the size of dendrite arms whereas the size-shape parameters of Si particles and their inter-particle spacing are less significant for the ductility. Although Liao et al. [45] have agreed that both the primary Al phase and the eutectic phase exert a combined effect on mechanical properties of Al-Si alloys, they have shown that the ultimate tensile strength and fracture elongation of fully modified Al-11.6%Si alloys linearly increase with the amount of primary aluminium dendrites where the latter increases with the amount of Sr modifier. In general, the ductility of the alloys decreases with increasing secondary dendrite arm spacing (DAS) [20], with the exception of Al-Si alloys with large DAS values [52–54].

Until recently, the study of the relation between the silicon morphology and mechanical properties of Al-Si alloys has been limited to 2D investigations in most cases [8–10,59]. However, some specific properties such as the connectivity and particle density, which can only be determined in 3D [60], also exert a significant impact on mechanical properties of Al-Si alloys [61] and therefore, will be considered in more detail in the following section.

### **2.3 Effect of connectivity**

The connectivity of the eutectic Si strongly influences the mechanical properties of Al-Si alloys. In particular, a network of stiff Si particles in a ductile Al matrix increases the strength of the material but at the same time it reduces the ductility [61,62]. The coarse flakes of a brittle phase such as the eutectic Si also facilitate the crack propagation [16].

Requena et al. [61] have reviewed the effect of the connectivity of a rigid phase on the strength of different Al-Si-based alloys. In particular, an unmodified AlSi12 alloy has been investigated in the as-cast state and after the solution treatment. The alloy in the as-cast state with interconnected Si lamellae has shown an increase in strength and work hardening as compared to the same alloy after the solution treatment at 540 °C for 4h resulted in a disintegration of the lamellae and loss of interconnections between the particles [62]. In this context, Al-Si alloys can be regarded as metal matrix composites with the eutectic Si as a strengthening phase [63]. The strengthening effect of Si in Al-Si alloys is due to the load transfer from the matrix to Si particles and the difference in thermal expansion coefficients between the components which results in formation of strain-hardened regions around Si particles during the cooling process. The stiff Si network interpenetrating the ductile Al matrix increases the load transfer from the matrix to the reinforcement and thus enhances the strength. The disintegration of the network due to the heat treatment has, on the contrary, an adverse effect on the strength, though it is beneficial to the ductility [61].

Some elements are added to Al-Si alloys for the purpose of retaining the connectivity of the second phase. For example, Ni is added to Al-Si alloys to improve their high temperature strength. Indeed, Ni in Al-Si alloys forms Ni-containing aluminides which together with eutectic Si build a complex network structure. While Si particles undergo disintegration during the solution treatment of binary alloys, the connectivity and contiguity of Si particles and aluminides in the solution treated Al-Si-Ni alloys remain preserved, which ensures their increased high temperature strength [64].

From a quantitative point of view, the connectivity of a phase reflects the number of connections between the phase constituents in a structure. It is a topological property as it does not depend on the size-shape characteristics of components. The connectivity can only be determined in a volume [65]. For complex structures, it can be characterized in different ways. Tolnai et al. [46] have used the volume fraction of the largest single particle within the analyzed component as a measure of the interconnectivity. The connectivity of the component can also be evaluated by means of the Euler number [66] that represents the difference between the number of particles in a structure and their connectivity [65]. The Euler number can be computed via 3D image analysis software like, for example, MAVI [67].

Although the influence of the connectivity of Si on the strength of different Al-Si alloys has been investigated over the past years, the relation between the damage components and 3D

architecture of the eutectic Si is still not fully explored, especially in what concerns the effect of the connectivity and 3D morphological features of Si on damage characteristics.

### 2.4 Damage behavior of Al-Si alloys

#### 2.4.1 Fundamentals

The ability of a material to resist fracturing is characterized by the fracture toughness which is conventionally described by the critical value of the stress intensity factor,  $K_{Ic}$ . The subscript I indicates the opening mode of the fracture loading, i.e. the fracture occurs under uniaxial tensile loading where the loading axis is normal to the crack plane [47]. The critical value of the stress intensity factor implies that after reaching it, the material cannot accommodate more stress by the plastic deformation which leads either to brittle fracture of the material or instable crack propagation with subsequent material's failure. The fracture susceptibility of the material depends on its chemical composition and microstructure including phase constitution, presence of impurities and defects. Most of the industrial castings contain more than one phase and are not free of casting defects and impurities (though the last two are usually intended to be minimized) [68].

Consider now an alloy which contains isolated elastic particles in the plastic matrix. Upon the loading of the metallic alloy, it deforms elastically until the yield strength is reached [68]. Then, the plastic deformation proceeds by the dislocation pile-ups at the second-phase particles. These pile-ups exert an increasing amount of stress on the particles and hinder the plastic flow in the material. When critical stress concentration is reached, the particles are susceptible to failure [69,70].

Yeh and Liu [71] have reviewed studies dealing with the calculation of the critical stress or strain necessary for a particle to crack: in most cases, the critical stress and strain are related to the particle size. Joseph and Kumar [72] have shown that the particle shape also makes an influence, so that large and elongated particles are more susceptible to fracture. Depending on the particle morphology, the critical stress level for Si particles has been found in the range of 500 – 1000 MPa [12]. However, Yeh and Liu [71] have shown that the particle size and shape are not the only and most important factors influencing the particles breaking probability. According to their observations, both round and elongated particles have been found to fracture under the loading while large particles have often remained intact in the vicinity of smaller particles. Therefore, the cracking of particles is a localized event which can be explained by the presence of dislocation pileups at the particles [71].

It is important to distinguish between the cracking of individual microconstituents such as the second-phase particles and a global failure of the material which can take place in a brittle or ductile manner. Przystupa and Courtney [73] have reported a monotonous increase of the amount of fractured particles with the tensile loading, whereby the final fracture takes place when “a critical distribution of internal cracks is attained”. A different approach has been described by Caceres and Griffiths [51], who have suggested that fracture of a material occurs when a certain critical amount of damage is reached. For example, a fracture criterion of 0.2 has been adopted for the investigated alloy Al-7%Si-0.4%Mg, which means that 20 % of Si particles have been cracked at fracture. Thus, for every structure there is a certain critical amount and distribution of cracks which can entail an immediate failure of the material.

#### **2.4.2 Damage mechanism in Al-Si alloys**

Consider now the eutectic Al-Si alloy composed of two major constituents: eutectic Si particles and the Al matrix. In materials like Al-Si alloys which consist of isolated elastic particles in a plastic matrix fracture initiates in two ways: cracking of particles or debonding of particles from the matrix [73]. The damage in Al-Si alloys is revealed by the formation of voids or cracks. An example of the damage in the Al-Si alloy fractured under tension loading is shown in Figure 2.4(a).

The fracture surface appearance is related to the amount of plastic deformation accommodated by the material prior to the failure. In ductile materials such as aluminium alloys, the fracture surface is composed of dimples which result from the void coalescence upon the material failure. Depending on the loading condition, the shape of dimples can be different. Under uniaxial tensile loading, the dimples are nearly equiaxed and have defined borders (see Figure 2.4(b)). Under tear or shear loading, the dimples exhibit elongated parabolic shapes with one end that is opened. However, the real fracture usually occurs under mixed loading modes and propagates along multiple planes which results in the asymmetry in dimple shapes within a particular fracture surface and mismatch between the mating fracture surfaces in general [47].

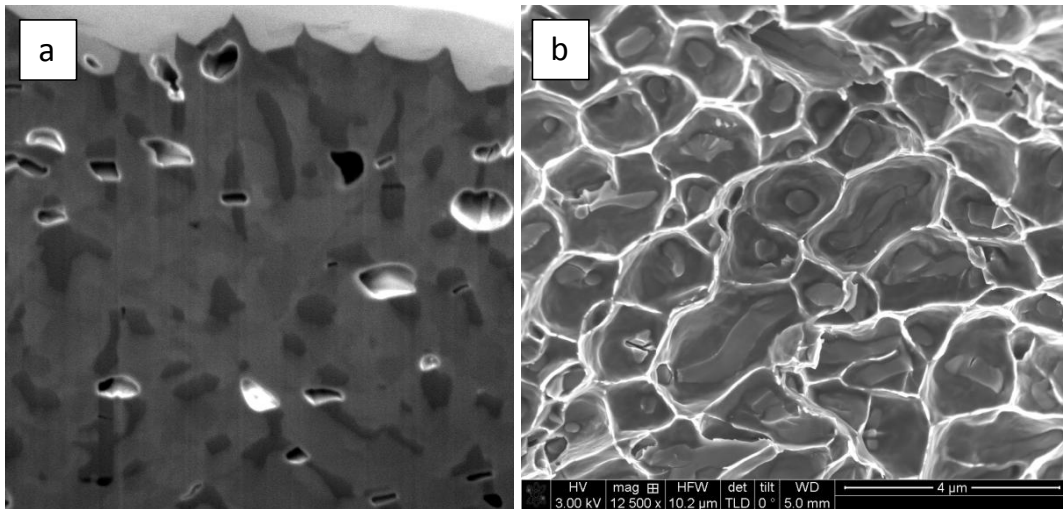


Figure 2.4: (a) FIB/SEM cross-section of a tensile test specimen of Sr-modified AlSi12 alloy which illustrates the fracture surface profile and damage in the material's volume; (b) SEM fractograph of the alloy which shows a typical ductile fracture surface consisting of dimples.

It is important to note that there is always inhomogeneous stress distribution in the alloy: even in the unstrained state there are local stress concentrations around the second phase particles and residual thermal stresses. Therefore, these particles represent a milieu for the damage initiation. In general, the fracture of the particles occurs during the plastic deformation of the local environment. Investigating the ductile fracture in aluminium alloys, Broek [69] has observed that only a small number of voids are formed at lower strains while most of the voids occur at relatively high stresses. The global fracture takes place by growth and coalescence of those voids [50]. To summarize, the fracture mechanism in Al-Si alloys consists of those three steps: void nucleation at Si particles, their growth and coalescence [39], whereby the fracture propagates primarily through the eutectic phase [74].

Each damage stage has been thoroughly discussed in the literature and appropriate models have been developed. The void nucleation has been shown to be a critical step in the damage development process [75]. Si particle cracking models can roughly be divided into two groups: models based on the theory of dispersion hardening combined with Weibull statistics [51] and models based on the dislocation pileup mechanism [71]. The former model implies that the probability of the particle cracking is expressed as a function of the stress in the particle computed using dispersion hardening models and depends on the particle aspect ratio and the equivalent circle diameter [51]. The latter mechanism allows to regard the particle cracking as a localized event occurred due to the stress concentrations induced by the

dislocation pileups, whereby the fraction of broken particles is related to metallurgical factors such as the particle size, pileup number and length, orientation factor etc.

Joseph and Kumar [72] have found that the modification of Al-Si alloys influences the fracture mechanism of Si particles. It has been shown that the particles fracture in modified and unmodified Al-Si-based alloys under compression loading occurs by two different mechanisms. In the unmodified alloy, fiber loading mechanism controls the particles fracture. It is revealed by the following fracture characteristics: the cracks in the unmodified Si particles have often been found in their middle part, parallel to each other and to the loading axis, and besides, the particles laying perpendicular to the loading axis and therefore dealing with maximum tensile stresses have been fractured more readily. The Si fiber in this case fractures when its fracture strength is reached, which can occur already upon the elastic deformation and therefore does not necessarily involve dislocations movement. On the contrary, Si particles in the modified alloy exhibit broader crack orientation distribution which argues for the cracks to be caused by the irregular dislocation pile-ups actively formed upon the plastic deformation. Such dislocation pile-ups induce large tensile stresses, whereby the cracks in Si particles occur along cleavage planes close to the directions of the maximum tensile stresses. The dislocation pile-up mechanism is also supported by the fact that the cracks in the modified Si particles have only been found after the onset of plastic deformation whereas elongated Si particles have still been subjected to the fiber loading. Therefore, the combined effect of the two mechanisms defines the fracturing of Si particles in the modified alloys.

Doglione et al. [76] have discussed the validity and limits of the Si particle cracking models by suggesting that none of them is able to account for interplay of Si particles size-shape characteristics and spatial arrangement of the eutectic phase. Indeed, 3D complexity and irregularities of Si particles may imply different stresses in the particles than the described models suggest. The particles containing irregularities like notches or neckings have shown to crack more readily. However, such shape configurations cannot be taken into account by simply regarding size and aspect ratio of the particles. Also, depending on the eutectic arrangement – interdendrite fine eutectic regions (channels) or large eutectic regions (clusters) – different damage behavior is observed. The fracture tends to propagate mostly through the interdendrite eutectic channels while in the large eutectic clusters the damage is widely spread.

Damage investigations are mostly realized after a specimen has already been fractured. Post-mortem study of damage, however, does not allow for the straightforward interpretation of results, since the metallographic preparation of samples often creates artifacts which make it difficult to evaluate the damaged components. In contrary, in-situ tensile tests provide direct information on the damage evolvement during the loading. For example, Doglione [58] has investigated the sequence of damage events and its effect on the ductility of a Na-modified Al-Si-Mg alloy A356-T6 with the help of in-situ tensile tests in SEM. It has been shown that the damage starts with the fracturing of Si particles or debonding of particles from the matrix due to the stresses created by the dislocation pile-ups at Si particles. With a further stress increment, adjacent microcracks merge together to form cavities along the boundaries between the eutectic and Al dendrites. These cavities continue to grow at the boundaries of Al dendrites creating macrocracks until the specimen's failure. Thus, the fracturing process occurs on different scales ranging from atoms and dislocations to microconstituents [44]. In this respect, different characteristic size features are important to characterize the damage at every length scale: the plastic collapse of a ligament between cracks in neighboring Si particles occurs on the length scale of the equivalent diameter of Si particles and inter-particle spacing (i.e. the spacing between Si particles along the interface with dendrites) whereas the collapse of dendrites boundaries takes place on the length scale of the size of dendrite arms. Global collapse of a specimen begins on the mesoscale with the collapse of several dendrites boundaries [58].

Lee et al. [77,78] have studied the role of shear bands and the interference of aluminium dendrite cells in the fracture propagation in different castings of the alloy A356 during in-situ SEM fracture tests. It has been shown that the cracks always initiate at Si particles whereas shear bands play an essential role in the crack propagation. The fractured particles falling along the shear bands direction pave a way to the crack propagation while the Al matrix, in contrary, hinders it. During the fracture toughness test, the crack propagation starts from the notch region and then pursues the repeated process of the crack propagation through the fractured particles along the shear bands, the crack propagation retardation upon the matrix interference, the crack blunting, the formation of new shear bands and so on (see Figure 2.5).

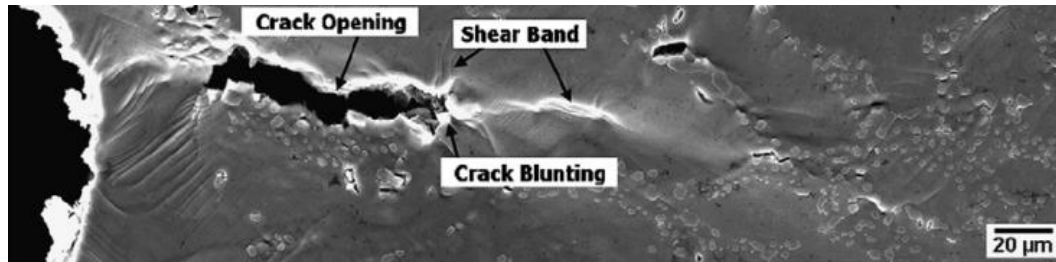


Figure 2.5: SEM micrograph (adapted from Lee et al. [78]) which illustrates the propagation of the crack along shear bands and interaction of the crack with aluminium matrix during the fracture toughness test on the compact tension (CT) specimens of Al-Si alloy A356.

As has been shown in [52–54], the final fracture mechanism is related to the degree of the interaction between slip bands and Si particles at the cell and grain boundaries. In particular, the cell boundaries in the alloys with large DAS have a higher density of Si particles and as a consequence, interact stronger with the plastic deformation than isolated Si particles at the cell boundaries in the alloys with small DAS which results in a higher probability of particle fracturing therein. Therefore, in the alloys with large DAS, the fracture evolves mostly along the boundaries of the dendrite cells and has a transgranular character, while in the alloys with smaller DAS, the fracture takes place preferentially along the eutectic grain boundaries and thus, has an intergranular type.

### 2.4.3 Impact of second phase particles

Damage characteristics in Al-Si alloys strongly depend on the morphology of second phase particles [57]. Hafiz and Kobayashi [39] suggest that the morphology of the eutectic Si exert an influence on the local stress state, crack initiation and fracture resistance as well as load-carrying capacity of the structure. High aspect ratio and irregular shape of unmodified Si particles results in high stress concentration regions in their vicinity. Therefore, the void nucleation at the particles with further coalescence of voids and collapse of the ligament between those particles takes place already at low strain levels. In contrary, more fine and regular modified particles have less stress concentration sites and can carry the load much better due to the more gradual damage evolution.

The influence of the connectivity of a rigid phase on the damage mechanism of Al-Si alloys has been studied in [79]. The Al-Si alloys containing Cu and Ni have been investigated in the as-cast and solution treated state after compression tests. In these alloys, Cu and Ni form different aluminides which together with the eutectic and primary Si build a network of strengthening phase in the Al matrix [80,81]. The damage induced by the compression of the

material involves the fracture of aluminides, the fracture of eutectic Si particles and the decohesion of Si particles from Al matrix, the decohesion of aluminides from the matrix and finally the cracking of primary Si particles. Most of voids caused by the compression loading are oriented in the loading direction that indicates a high load-carrying capacity of the rigid phase. During the solution treatment, the network of rigid phase undergoes partial disintegration and spheroidisation [81,82] which results in a decrease of the damage comparing to the as-cast alloys. However, the strengthening effect of the rigid phase is also reduced which is reflected by the decreased number of cracks aligned in the loading direction [79].

The aspect ratio of the particles influences their load-bearing capacity so that the elongated particles transfer the load more effectively than the spherical ones. Therefore, the stress within the high aspect ratio particles reaches the fracture stress level very quickly while spherical particles would exhibit only little damage under similar loading conditions. Besides, the probability of the elongated particles to fracture increases as their major axis approaches the direction of the tensile loading [83,84]. The fraction of fractured Si particles also increases with strain, particle size and decreasing the volume fraction of the particles [50]. Thus, the second phase particles exert a different influence on damage characteristics depending on their size, shape and spatial arrangement. The following summarizes the behavior of particles in terms of their fracture susceptibility:

- Large particles (1-10  $\mu\text{m}$ ) crack more readily during plastic deformation as compared to smaller particles [48,51,85]. However, regardless of the size of particles, their local environment also plays a significant role [86].
- Elongated particles are more susceptible to fracture than spherical particles [72,83,84].
- The particle cracking increases with stress and strain [48,51,71,72]. However, given the same strain level, the fraction of damaged particles under tension is higher than under compression [86].

Broek [69] has found that not all the particles in the plane generate voids. In other words, the voids nucleated at the particles which pave the fracture surface do not necessary lay in one plane. Therefore, the fracture surface is very rough and can significantly deviate from the flat section. Nevertheless, a good correspondence between the dimple spacing and inter-particle spacing in the alloy A356 has been observed by Lee et al. [77]. As has been stated above, the voids nucleate at Si particles and as a consequence, the size of dimples is limited by the voids

originated at surrounding inclusions and is roughly equal to the inter-particle spacing. Since the voids grow in the direction perpendicular to the tensile loading, they have a relatively shallow profile. So, for example, the depth-to-width ratio of 1/3 to 1/5 has been proposed by Broek [69], who investigated a ductile fracture in aluminum alloys. By approximating the voids with oblate ellipsoids, it has also been shown that the depth-to-width ratio of dimples has the same order as the size-to-distance ratio of Si particles. In general, the dimple depth-to-width ratio reported in earlier studies for different materials varies mostly between 0.4 and 1 [87,88].

#### **2.4.4 Damage modes of Si particles**

The principle damage modes of Si particles in Al-Si alloys are the particle cracking and the debonding of particles from the matrix. Dighe et al. [86] have investigated the damage behavior of the Sr-modified Al-Si-Mg alloy under different loading conditions such as the tension, compression, and torsion. It has been observed that Si particles exhibit both damage modes: the cracking of particles and the debonding from the matrix. However, the particle debonding has been found only in specimens under tensile loading while the cracking of particles has been observed in all specimens. Therefore, the debonding of Si particles from the matrix has been related to high local hydrostatic tensile stresses occurring around Si particles upon the tensile loading of the material. Lee et al. [40] have suggested that for the decohesion to occur it is necessary that the stress at the interface between Si particle and Al matrix exceeds the interfacial strength. Thus, different damage criteria have to be used for numerical simulations of the fracture and debonding of Si particles in Al-Si alloys: the maximum principle stress level in the particle can be applied as a fracture criterion while the maximum hydrostatic stress at the particle-matrix interface controls the debonding [10].

Horstemeyer and Gokhale [89] have also reported the occurrence of both the fracturing of Si particles and the interfacial debonding in the cast Al-Si-Mg alloy under the tension loading whereas under the compression and torsion only the Si particles fracturing has been observed. However, Joseph and Kumar [72] have observed the debonding of Si particles from the matrix also in compression specimens, but only at higher strain rates and only in the modified alloy. Still, the Si particle fracturing has been regarded as the dominant damage mechanism under the compression loading [57]. Furthermore, Caceres and Griffiths [51] and Wang [53] have not observed any cracks at the particle-matrix interface in tensile samples of Al-7%Si-0.4%Mg alloy. Also Broek [69] has reported a low occurrence of voids formed by the interface decohesion in investigated aluminium alloys. In particular, the voids have been

mostly found in second phase particles while barely observed at the particle-matrix interfaces which indicates an effective load transfer through the interfaces. This has been attributed to the high cohesive forces between the second phase particles and the Al matrix.

During the cyclic loading, the crack growth rate and the corresponding mechanism of the crack propagation affect the fatigue life of the structure. Gall et al. [90] have distinguished two mechanisms of the fatigue crack propagation in Al-Si alloys with respect to the crack growth rates: the debonding of particles occurs mostly at lower crack growth rates whereas the fracturing of particles takes place at higher rates. This study is interesting from the perspective of the transition between two damage mechanisms in accordance to the crack growth rate for the same microstructure. Thereby, the influence of microstructure is stated dominant, at least at smaller rates. At higher rates, particles situated ahead of the crack are already fractured due to the higher stress concentration at the crack tip and the crack propagates through the region weakened by the pre-cracked particles. It is important to note that the observations are made on the basis of 2D micrographs, where Si particles are assumed to be simply connected in a volume due to the modification and solutionizing treatment.

Lee et al. [40] have also found that the Si particle morphology plays a primary role in the fatigue crack propagation path. In particular, in modified Al-Si-Mg alloys the fatigue crack grows mostly by debonding Si particles whereas in unmodified alloys the crack grows primarily by fracturing Si particles. Thus, the probability of the particle cracking increases with the size of the particle. The coarse particles fracture more readily than the fine ones because the fracture strength strongly depends on the particle size so that it decreases as the particle size increases. When the stress level in a particle reaches its fracture strength, the particle will fracture (e.g. coarse unmodified particles); otherwise, when the fracture strength is still higher than the stress in the particle (e.g. fine modified Si particles), it will be debonded by the growing fatigue crack.

### **2.4.5 Orientation of cracks**

The orientation of cracks depends on the loading conditions: under the compression load, the cracks are mostly aligned in the loading direction whereas under the tension, the cracks are perpendicular to that one; under the torsion, the cracks do not exhibit any preferred orientation [86]. Similar observations on the crack orientation with respect to the loading axes have been reported in [44,57,69,75].

Yeh and Liu [71] have demonstrated that the crack in a particle can be located quite arbitrary: in the center or at the periphery, in the thin or in the thick part where multiple parallel or not parallel cracks can be observed (see Figure 2.6 (a)). It indicates that the crack location is mainly defined by the local environment like particle orientation, slip orientation and so on. Though most of the cracks are oriented perpendicular to the tension axis, as shown in Figure 2.6 (b), there is still a wide range of crack orientations that can be observed. However, the number of the cracks oriented close to 45 and 135 degrees is significantly smaller. The preferable orientation of the cracks perpendicular to the tension axis can be explained by the highest stresses carried by the structure in this plane during the uniaxial tensile loading. Dighe et al. [86] have found that in tension test specimens of Al-Si-Mg alloy, the cracks are mostly oriented in the range of  $80^\circ$  to  $100^\circ$  with respect to the loading axis, while in compression test specimens, the cracks are mostly oriented in the ranges of  $0^\circ$  to  $30^\circ$  and  $150^\circ$  to  $180^\circ$  to the compression axis. Similar observations have been reported in [72].

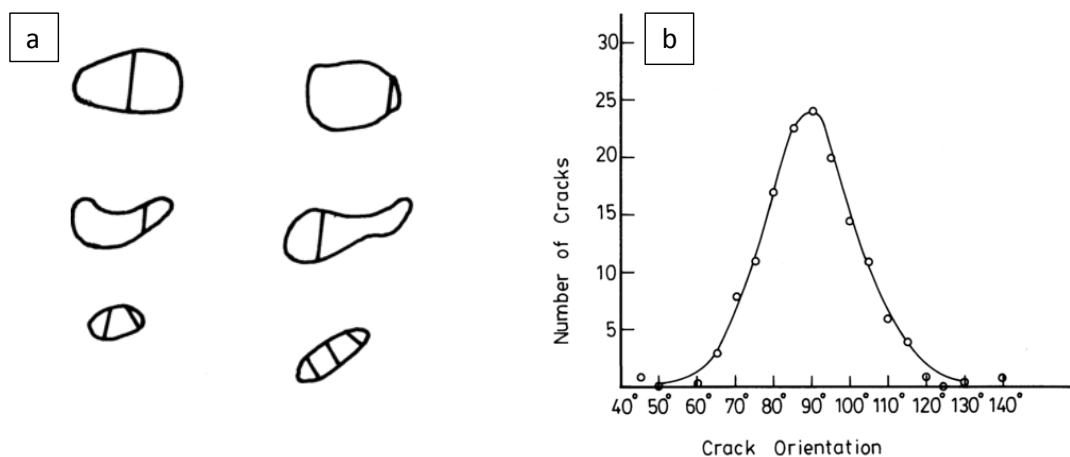


Figure 2.6: (a) Schematic illustration of possible localization of cracks in Si particles; (b) statistical distribution of crack orientations with respect to the tensile axis [71].

#### 2.4.6 3D damage characterization

Most of the time, the damage in Al-Si alloys is characterized by means of 2D techniques. 2D analysis requires the application of simplifying assumptions and stereological methods which are able to quantify only simple-shaped microconstituents. Therefore, the information derived from 2D investigations is likely to be incomplete or inaccurate, especially, for complex anisotropic structures [7]. Moreover, the amount of the damage in Al-Si alloys characterized by metallographic examination is often underestimated due to the aluminium matrix filling the voids during polishing [76,79,84]. Stereological methods of damage characterization have been applied to extruded Al-Mg-Si-based [91] and Al-Mg-based [92] alloys. It has been

shown that depending on the loading conditions, shape of particles and anisotropy of the microstructure, 3D number density of the cracked particles is either higher or lower than the number density computed using 2D metallographic images [91]. However, in general, 2D damage characterization leads to the underestimation of the real damage in the structure [92]. The limitations of 2D analysis can be overcome by 3D damage characterization techniques such as X-Ray tomography (XCT) and serial sectioning techniques like Light Optical Tomography (LOT) and Focused Ion Beam (FIB) tomography.

X-ray tomography is a non-destructive technique which is based on the X-ray absorption contrast between the analyzed microconstituents (e.g. phases, pores, cracks) which depends on the material density. Therefore, this technique does not allow to distinguish between materials with similar densities (e.g. Al and Si). Synchrotron tomography (sXCT) offers highly coherent beams with intensity up to  $10^6$  times higher than the intensity of the conventional XCT and enables a resolution in the submicrometer range. By varying the distance between the sample and detector, it is possible to record phase contrast images even for elements with similar attenuation coefficients like Al and Si [93]. Though the synchrotron computed tomography exhibits many advantages over the conventional XCT systems such as the lower amount of artifacts, improved contrast and higher resolution, it is still very expensive and has a limited availability. On the contrary, there are other very attractive modern systems like cone beam XCT with a  $\mu$ -focus ( $\mu$ XCT) and a sub- $\mu$ m (sub- $\mu$ XCT) source which also provide satisfactory results but at the same time they are user-friendly, easier to access and less costly than the synchrotron tomography [94].

X-ray microtomography is widely used to study the influence of the microstructure on the mechanical behavior of Al-Si alloys. In [95], in-situ X-ray tomography tensile tests have revealed large pores to cause the crack initiation in the material. However, the resolution used (voxel size of 1.7  $\mu$ m) has allowed to distinguish only intermetallics, pores and cracks, but has not been enough to resolve Si particle morphology. In [96], in-situ X-ray tomography tensile tests have been carried out to study the damage mechanism in a metal matrix composite reinforced by spherical ceramic particles as a function of the matrix hardness and the amount of the reinforcement. In [97], X-Ray tomography has enabled to estimate 3D porosity distributions in hypoeutectic alloy A356 and confirm the confidence of FEM simulations for studying the effect of different porosity levels and void distributions on the damage evolution. Normally, when the porosity level is small, the damage in Al-Si alloys is determined by the damage of second phase particles. When the initial porosity level is high, then the size and

distribution of pores can significantly affect the damage evolution and the fracture resistance. In particular, it has been shown that the randomly distributed porosity results in a lower elongation at fracture as compared to specimens with homogeneous porosity.

Light optical tomography has also proved to be useful for the 3D characterization of Si particles and eutectic grains in Al-Si alloys [35]. Asghar et al. [64] have compared the use of light optical and synchrotron tomography for the characterization of 3D network structures in AlSi12Ni alloy. The voxel size of 3D images acquired by means of LOT and sXCT has been  $0.1 \times 0.1 \times 0.5 \mu\text{m}^3$  and  $0.3 \times 0.3 \times 0.3 \mu\text{m}^3$ , respectively. It has been shown that, on one hand, LOT can provide a better resolution in imaging plan and can be carried out at a considerably lower cost than sXCT, but it has a destructive nature. On the other hand, non-destructive sXCT allows to analyze the same specimen in different conditions (e.g. as-cast and solution treated) and record larger volumes much faster than LOT, which is particularly important for the long-range and multiscale structures [98].

Much larger sample volumes can be reconstructed by using the montage serial sectioning technique [98,99] which is similar to the classical LOT, with the difference that in the montage technique every single metallographic image consists of several contiguous microstructural fields imaged at a high resolution. It has been successfully used for the reconstruction of 3D microstructure of metal matrix composites like for example the Al-alloy matrix composite reinforced with SiC particles [99] and the Al-Si-based alloy [98].

Since the light optical tomography relies on the recording of series of metallographic images, the damage characterization by this way is likely to be inaccurate due to the matrix filling the voids during the polishing. Therefore, damage investigations in Al-Si alloys with the light microscope solely can be misleading. In [79], Al-Si alloys containing Cu and Ni has been investigated after compression tests with the help of 2D Metallography and X-ray microtomography. X-ray microtomography has allowed to reveal the 3D arrangement of voids formed due to the debonding of aluminides and Si particles from the Al matrix and the fragmentation of aluminides. On the other hand, the light microscopy has complemented the tomographic data with information on fine cracks in particles which are not resolved by the sXCT. While the voids have been detected by the X-Ray microtomography, light microscope images have not shown any damage in the matrix and on its interface with Si and aluminides. X-ray microtomography has also provided information on the orientation and shape of the voids in 3D. According to the 3D data, the voids have either an elongated or platelet-like shape with a typical aspect ratio of 2-3.

In contrary to the LOT and X-ray tomography, focused ion beam/scanning electron microscopy (FIB/SEM) tomography can provide a spatial resolution high enough to enable the imaging of Si particles together with the cracks while avoiding the effect of the matrix filling the cracks induced by the metallographic preparation. In particular, FIB/SEM tomography has proved to be suitable to reveal the 3D architecture of the eutectic Si with a high resolution [82,100,101]. In [82], this technique has been used for the reconstruction of the Al-Si eutectic in the AlSi12(Sr) alloy with a spatial resolution of  $10^{-4}$  to  $10^{-3}$   $\mu\text{m}^3$ . Furthermore, the combination of FIB tomography with energy dispersive spectroscopy (EDS) and electron backscatter diffraction (EBSD) enables the 3D-mapping of chemical composition and crystallographic data of different phases, respectively [102]. The main drawbacks of the FIB/SEM tomography are that it is very costly and time-consuming and, besides, the morphology of a sampled structure is hardly predictable before analyzed in a destructive nature.

With regard to the damage investigations, the FIB/SEM tomography allows the investigation of fracture characteristics in materials at a small scale, whereby 3D morphological properties of the implicated microstructural constituents can also be revealed. For example, it has been used to reconstruct a fatigue microcrack in Ni-base alloy and examine its interaction with a grain boundary and precipitates at a high resolution in a submicrometer range ( $31 \times 39 \times 300$   $\text{nm}^3$ ), which is obviously beyond the synchrotron tomography resolution level [103]. Thus, the FIB/SEM tomography can also be used to investigate 3D damage characteristics in Al-Si alloys with respect to the local morphology of Si particles with improved resolution and contrast signals as compared to XCT while providing more accurate damage characterization than LOT. Therefore, it is considered to be an appropriate technique for the characterization of Si particle morphology and damage in Al-Si alloys in the present work.

### 2.4.7 Fracture toughness of Al-Si alloys

According to [104], Al-Si alloys have, in general, a high toughness that can range from around 20 to 40  $\text{MPa} \cdot \text{m}^{1/2}$ . The toughness variations between different alloys can be due to the chemical composition, casting procedure and thermal treatment which alter the microstructure of the material. In the following, the impact of every factor is elaborated in more detail.

One of the most important characteristics of a casting procedure is the cooling rate. Depending on the cooling rate provided by the casting, size of microstructural constituents

can vary significantly. Kumai et al. [105] have studied the influence of the cooling rate and the casting process on the microstructure and the fracture resistance of the alloys A356 which have a chemical composition of Al-7%Si-(0.3-0.4)%Mg. Here, permanent mold castings (PM) have been solidified at different mold temperatures (i.e. cooling rates) to vary the secondary dendrite arm spacing (DAS) in the structures: DAS has increased with the mold temperature due to the corresponding decrease in the cooling rate. Besides, a direct-chill casting (DC), which has the finest grain structure and the smallest DAS, has been compared with the permanent mold castings. The effect of Si refinement has been equalized in all alloys by the long homogenization treatment, so that the influence of DAS solely could be traced. The fracture toughness has been evaluated with the help of the tear test which enables an estimation of the energy needed for the crack initiation and crack propagation separately through the integration of different areas under the load-displacement curve, where the sum of both energies constitutes the total energy to fracture. The results of the investigations have shown that the smaller values of DAS are beneficial for the toughness of the permanent mold castings where the improvement of the resistance for fracturing is mostly determined by the increasing energy for the crack initiation. The direct-chill casting has also shown an increase of energy for the crack initiation as well as a considerable enlargement of the area associated with the energy needed for the crack propagation, as compared to the permanent mold castings. The difference between a balance of components of the energy to fracture in DC and PM castings is suggested to result from different fracture paths: in the permanent mold castings, the fracture surface is flat and quasi-perpendicular to the loading axis whereas in the direct-chill casting, it is mostly slanting which implies the higher tear toughness of the latter.

Lee et al. [77,78] have also studied the effect of different casting processes on the microstructure and the fracture toughness of the alloy A356. In contrary to the study of Kumai et al. [105], who have focused on the DAS effect, here the authors have mostly been focused on the impact of the distribution and the size of Si particles. The low-pressure casting (PC) has been characterized by the presence of casting defects, in particular, shrinkage pores which significantly decrease the ductility of the alloy but seem to be irrelevant for the fracture toughness in the present investigation. The casting-forging (CF) of the alloy has contributed to the more homogeneous distribution of Si particles while increasing at the same time the size and inter-particle spacing of Si due to the prior homogenization. The alloy has also showed the highest toughness along with other mechanical properties. The squeeze- (SC) and rheo-castings (RC) have exhibited a finer microstructure in terms of Si particles and inter-particle spacing facilitating by this way the crack propagation between Si particles. These

alloys have shown the lowest fracture toughness. Thus, it has been suggested that the more homogeneous distribution of Si and larger inter-particle spacing obtained by means of advanced casting processes contribute to the improvement of the toughness of Al-Si alloys.

The influence of the chemical composition on the fracture toughness in the eutectic Al-Si alloys has been studied by Hafiz and Kobayashi [55], who have investigated the effect of different levels of Sr-modification that produces structures with different degrees of the eutectic refinement. It has been shown that the morphology of the eutectic Si has a major impact on the fracture toughness of the material. In particular, the ratio  $(\lambda/DE)_{Si}$  of the inter-particle spacing,  $\lambda$ , to the equivalent particle diameter,  $DE$ , and the so-called void growth parameter,  $VGP$ , defined as  $\sigma_Y(\lambda/DE)_{Si}$  in [39], are strongly related to the fracture toughness. Increasing both the ratio  $(\lambda/DE)_{Si}$ , and  $VGP$  due to the eutectic refinement associated with decreasing the inter-particle spacing and the size of particles have been found to correlate with the improvement of the toughness. Dimple patterns of fracture surfaces in the modified structures have also indicated the higher plastic flows sustained by these structures before the rupturing. Hence, the finer the eutectic Si, the higher is the toughness of Al-Si alloys. This conclusion is however contradictory to the observations reported by Lee et al. [77,78].

Tohgo and Oka [106] have examined the impact of the thermal treatment of Al-7%Si-0.4%Mg on the fracture resistance of the alloy. The authors have compared the alloys in “as-received” state, i.e. after the solution treatment and aging, with the alloys pursued the additional coarsening treatment. The treatment has resulted in the growth and spheroidization of the Si particles as well as their more homogeneous distribution in the matrix which in turn has resulted in the improvement of the fracture toughness, whereby the fracture toughness has increased from 20.8 to 27.1 MPa · m<sup>1/2</sup>.

Alexopoulos and Tiryakioglu [107] have investigated the interplay of the strength, ductility and fracture toughness in the alloy A357 (Al-7%Si-0.6%Mg) for various aging conditions and chemical compositions. The fracture toughness of the alloy with different additions of chemical modifies has ranged from 24.7 to 28.9 MPa · m<sup>1/2</sup>. It has also been shown that increasing the strength leads to the reduction of the ductility and toughness while increasing the ductility is not necessary accompanied by the improvement of the toughness.

To summarize the effect of different factors on the toughness of Al-Si alloys, it is worth to highlight that the ability of the material to resist fracturing is mostly defined by the casting microstructure. The casting microstructure in turn depends on the chemical composition,

casting procedure and thermal treatment of the alloy. Thus, to increase the fracture toughness of the material, these factors have to be chosen in such a way as to obtain a necessary level of microstructure refinement and homogeneous distribution of microconstituents as well as to minimize the amount of casting defects. The main contradictory point here is the right balance between the increase of the yield strength and the fracture toughness: on the one hand, the microstructure refinement favors the increase of both the yield strength and the toughness whereas on the other hand, the increase in the yield strength leads to the reduction of the ductility and as a consequence, the fracture resistance [68].

#### **2.4.8 Fracture toughness estimation methods**

There have been several attempts to develop an empirical formula for the estimation of the plane strain fracture toughness of Al-7%Si-Mg alloys as a function of the yield strength, and in particular, a linear relationship has been proposed [108]. The potential value of the fracture toughness computed via this equation is always higher than the experimental one because of the presence of multiple defects in the cast structures. Though such equations could be very useful for the evaluation of the potential fracture toughness of different alloys for potential applications, these equations are limited to a very few specific alloys [108,109] and cannot be applied across the whole range of aluminium alloys.

Further attempts have been based on analytical formulae that relate the fracture toughness with tensile properties of a material and its fractographic characteristics such as the average distance between fractured particles [73] and the depth of dimples on the fracture surface [87,110]. The fracture toughness can also be computed as a function of the local fracture strain expressed through the relation to the depth-to-width ratio of dimples [88]. Similarly, a relation between the toughness and the energy needed to form a unit of fracture surface can be exploited where the latter is expressed as a function of the tensile strength and the depth of dimples. A good agreement between the values of stress intensity factor computed by this way and experimentally defined values makes evident the primary role of the plastic energy used to form a fracture surface in the capacity of material to resist the fracturing [87]. In [110], a further tailoring of this relation has been made in terms of the dimple depth: instead of using an average value of dimple depth for a structure, different size groups of dimples and their volume fractions have been considered to compute the weighted average of the fracture toughness.

For two-phase alloys like Al-Si alloys, the amount and morphology of both phases has to be taken into account to compute the fracture toughness of the material. In this relation, the linear rule of mixture or modified contiguity-based rule of mixture can be applied, where the latter has shown better correspondence with experimental measurements. It implies that the eutectic phase arranged in a network significantly lowers the fracture toughness of the alloy as compared to the same volume fraction of isolated eutectic islands, since the network morphology (a high contiguity) of the phase with lower fracture toughness facilitates the crack propagation through it [74].

Experimental techniques for measuring the toughness are well established and standardized [111–113]. However, the evaluation of the fracture toughness of Al-Si alloys by means of those methods is often problematic. Indeed, there are certain requirements related to the size of a specimen which have to be fulfilled in order to reach a plain-strain condition at the crack tip in the sample and define the plain-strain fracture toughness,  $K_{Ic}$ . However, to fulfill these conditions the size of a specimen made of a ductile Al-Si alloy has to be very large, sometimes up to a meter [105] that is hardly realizable in a laboratory environment. Otherwise, only the conditional fracture toughness,  $K_Q$ , that is specific for a given experimental setup, is determined. The fracture toughness can also be measured with the help of the so-called J-integral testing [113] and then can be converted into the  $K_{Ic}$  value given all conditions fulfilled. In general, smaller specimens can be used to obtain a valid value of the toughness by the J-integral testing method but the main drawback of this technique is that it requires much more experimental efforts as compared to the direct definition of the  $K_{Ic}$  value [68]. Therefore, instead of the plain-strain fracture toughness, the conditional fracture toughness of Al-Si alloys is often reported in literature [77,78]. It makes the evaluation and comparison of the experimental data complicated due to the lack of valid information.



## 3 Experimental methods

---

For the extensive characterization of the microstructure, mechanical behavior and damage characteristics of Al-Si alloys, a multidisciplinary approach including laboratory experiments and computer simulations has been applied. The following chapter will introduce methods used for investigations of 2D and 3D characteristics of microstructures and damage components in Al-Si alloys, such as the metallographic examination and FIB/SEM tomography, as well as techniques for the quantitative microstructure characterization. Further, techniques applied for the evaluation of the mechanical behavior of real and virtual specimens will be described. Afterwards, methods for the fracture toughness estimation and fracture surface characterization will be explained. And finally, stochastic models used to generate a large variety of virtual 3D structures of eutectic Si and to simulate a fracture surface appearance will be presented. Such a multidisciplinary approach to the investigation of the morphological genesis of the material properties has only been possible through the collaboration with other research groups. In particular, the expertise available at the Chair of Applied Mechanics in Saarland University has allowed to perform mechanical tests using laboratory equipment and FEM simulations. Fracture toughness measurements have been carried out at the Chair of Materials Science and Methods in Saarland University. The stochastic model of the eutectic Si has been developed at the Institute of Stochastics in Ulm University. The script for the fracture surface modeling has been elaborated at the German Research Center for Artificial Intelligence in Saarbrücken.

### 3.1 Elaboration of Al-Si castings

The investigated Al-Si alloys have been elaborated by Hydro Aluminium Rolled Products GmbH by means of the permanent mold casting [114] which implies the casting in a metal mold consisting of several removable parts. The process is also called a gravity die casting because the metal fills the die by gravity [19]. Although the alloys have the eutectic composition with Si content of 12 wt.%, the microstructure of the alloys exhibits the hypoeutectic phases, i.e. it consists of the primary Al dendrites and Al-Si eutectic. The shift of the eutectic point towards higher Si content is due to the non-equilibrium solidification. Three types of the alloy compositions corresponding to different eutectic structures have been casted into 75 ingots, 25 ingots of each type:

- 1) unmodified AlSi12;
- 2) AlSi12 modified with 212 ppm of Sr;
- 3) inhomogeneously modified AlSi12 with 208 ppm of Sr and 0.31 wt% of Mg.

Specifications of the alloys are given in Table 3.1. The geometry and dimensions of the ingots are shown in Figure 3.1.

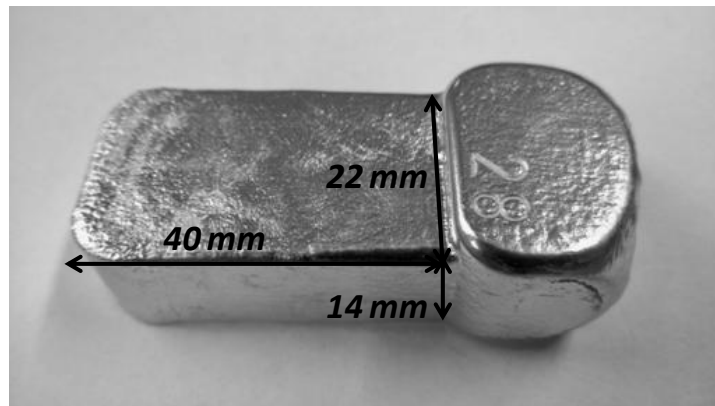


Figure 3.1: Ingot of a casted Al-Si alloy with dimensions of the investigation zone and the mold number.

Table 3.1: Specifications of the Al-Si alloys produced by the permanent mold casting. The content of Si is 12 wt%. The modified castings have been produced on the basis of the remelted unmodified alloy.

Reference in thesis	Mold No.	Mold T	Modification
2X	No. 1 – 25	250 °C	–
3X	No. 26 – 50	250 °C	212 ppm Sr
7X	No. 51 – 75	250 °C	208 ppm Sr + 0.31 wt% Mg

The alloys have been investigated in the as-cast (AC) and solution treated (ST) state. In particular, the T4 heat treatment cycle has been applied to the alloys. Specimens machined for the compression and tensile tests have been heated in a High Temperature Chamber Furnace type RHF 1600 of Carbolite Company. The standard solution treatment temperature used during the heat treatment of Al-Si alloys is 540 °C and the time varies between 20 min and several hours [19,22,82]. In this study, the T4 heat treatment cycle has been composed of the heating the samples up to 540 °C, solution treatment for 4 hours and then quenching in water near the boiling point to lower the level of induced residual stresses [19].

### **3.2 Metallographic examination**

The samples of Al-Si alloys have been prepared for the metallographic examination using standard preparation techniques for metallic materials [115]. The grinding of the samples has been carried out on silicon carbide papers up to 1200 grit size followed by the diamond polishing (6, 3, and 1  $\mu\text{m}$ ). The final polishing step has been performed with a colloidal Si-suspension (OP-S suspension by Struers).

Since the microconstituents in the investigated alloys can well be observed in the light optical and scanning electron microscopes without etching, no etching has been applied. Micrographs acquired by the light optical microscopy have been made in the bright field mode. Secondary electrons images have been taken in the scanning electron microscope (SEM) integrated in the dual-beam FIB system *FEI Helios NanoLab 600* using different detectors depending on the optimal image contrast in every investigated alloy (see Table 3.2). Besides, an energy dispersive X-ray analysis (EDX) has also been performed in SEM in order to identify a chemical composition of inclusions observed in the micrographs.

### **3.3 Focused Ion Beam/Scanning Electron Microscope (FIB/SEM) tomography**

The FIB/SEM tomography has been used to reveal a 3D morphology of the eutectic Si and damage in the eutectic phase induced by the tension/compression loading, which has enabled to investigate a spatial interaction of damage components with the internal architecture of the eutectic phase.

#### **3.3.1 Principles of FIB/SEM tomography**

The FIB/SEM tomographic reconstruction consists of an iterative milling of the sample with an ion beam and imaging of an exposed surface with an electron beam. Schematic illustration of the experimental setup during the FIB/SEM tomography is shown in Figure 3.2. The resolution in the milling direction,  $z$ , is defined by a thickness of the layer removed with the ion beam and depends on the milling precision. The resolution in the imaging plan,  $(x-y)$ , depends on the resolution of SEM images. The ion beam is parallel to the sample surface while the electron beam is located at the angle of  $52^\circ$  to the ion beam. Due to such an experimental setup the voxel size is anisotropic and is usually larger in the milling direction [116,117].

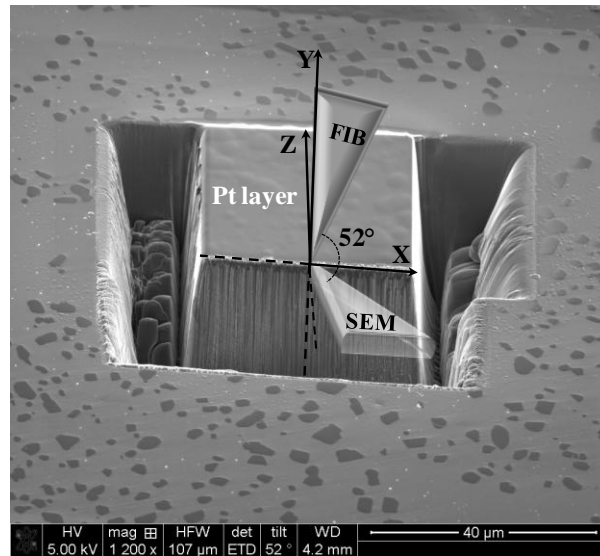


Figure 3.2: Schematic illustration of the experimental setup during the FIB/SEM tomography:  $(x-y)$  is the imaging plan,  $z$  is the milling direction.

In principle, the minimum required voxel size and sampling volume have to be balanced in order to enable a distinction of the smallest microstructure constituents, on the one hand, and a reconstruction of a volume relevant for the statistical interpretation, on the other hand. Indeed, while it is theoretically possible to reconstruct large samples reaching hundreds of micrometers in size, it is not practicable: large samples require much higher image acquisition and milling times. Moreover, sectioning of larger volumes often leads to surface undulations and misalignments increasing with the sectioning depth, like, for example, a deviation of a milling beam from a position parallel to the sectioned surface [116].

The FIB/SEM tomography proceeds as follows:

- Prior to the milling, the region of interest on a sample surface is covered by a Pt layer to protect the sample and reduce curtaining effects [116].
- A reference marker used for the slice alignment is placed above the upper left corner of the investigated area [100].
- A trench of ca.  $15\mu\text{m}$  width is milled at the front and the sides of the region to be reconstructed. This trench serves to minimize the re-deposition and shadowing effects [102].
- The parameters of the ion and electron beam are set with respect to the size of the microconstituents that have to be resolved. According to Holzer et al. [117], at least ten sections have to be made through a particle in order to enable a reliable reconstruction of microstructure features.

- The serial sectioning and imaging are processed in an automatic way. Depending on the process parameters and sampling volume, one image can be recorded approximately every 1 – 2 min [117–119].

#### 3.3.2 3D reconstruction

The 3D reconstruction has been carried out by means of the dual-beam FIB system *FEI Helios NanoLab 600*, which uses a Ga liquid metal ion source. The setup parameters such as the electron beam current and accelerating voltage, detector type, voxel size and number of slices used for the tomographic reconstruction of different Al-Si alloys are summarized in Table 3.2. The FIB has been operating at 30 kV accelerating voltage. Depending on the image contrast, two types of detectors have been used. In particular, Everhard Thornley Detector (ETD) has provided a better contrast in compression samples (7X\_ST and 2X\_AC) while Through Lens Detector (TLD) has shown better results in tension samples (3X\_AC and 3X\_ST).

Table 3.2: FIB/SEM setup parameters used for the tomographic reconstruction of different Al-Si alloys.

Sample	Current (nA)	Voltage (kV)	Detector	x (nm)	y (nm)	z (nm)	Number of slices
7X_ST	1.4	5	ETD	50	63.45	150	231
2X_AC	0.34	5	ETD	10.45	13.26	50	141
3X_AC	0.34	3	TLD	19.24	24.42	50	201
3X_ST	0.34	3	TLD	62.5	79.31	200	201

The voxel size  $x \times y \times z$  is computed taking into account the horizontal field width (HFW) and resolution of SEM images ( $1024 \times 884$ ) in  $x$ -direction ( $x = HFW/1024$ ), SEM imaging angle of  $52^\circ$  ( $y = x/\sin 52^\circ$ ) and distance between the FIB sections ( $z$ ). The recorded images are processed with the 3D visualization and analysis software Amira. First, a stack of 2D images is aligned and the region of interest is cropped out. Then, the labeling of different microconstituents (second phase particles, pores and cracks, see Figure 3.3) is carried out by manual segmentation due to the poor image contrast. The 3D reconstruction is processed by interpolation of the labeled features. Now the reconstructed 3D images and corresponding 2D images through the reconstructed volumes can be analyzed with respect to the morphological properties of damage and structure components by means of quantitative image analysis techniques.



Figure 3.3: A bunch of labeled SEM images. Each phase is given a different color: Si particles are in magenta, intermetallic phases are in cyan, cracks are in yellow and a large pore is in red, aluminium matrix is transparent. The 3D volume is reconstructed by interpolation of the labeled features given a voxel size.

The image contrast has been largely affected by the electron channeling. The strong electron channeling effect has been observed in the Al matrix in all investigated alloys. The channeling effect in the Al matrix can be recognized in Figure 3.4.

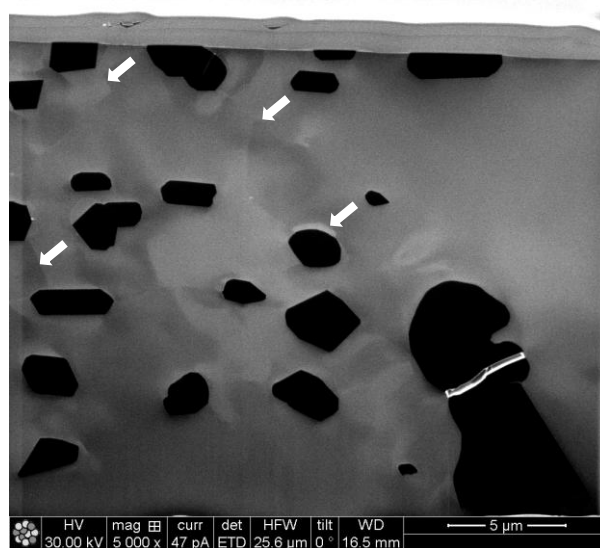


Figure 3.4: SEM image showing a channeling effect in the Al matrix. White arrows point on borders of individual Al grains in the matrix.

This effect occurs in polycrystalline materials and affects the contrast of secondary electron images. Depending on the crystallographic orientation, some grains are more preferable to the electron channeling than the others. In particular, at certain incidence angles, the electron may fall into the “channel” with the low packing density of atoms, and therefore, the probability of its interaction with the material’s atoms and returning as the backscattered electron or generating secondary electrons will be reduced [120,121]. In general, the grains aligned to a

low index direction exhibit a higher electron channeling, and as a consequence, will appear darker due to the reduced amount of the emitted secondary electrons than the grains aligned in other directions [116]. Of course, the sample deformation also exerts an influence on the electron channeling pattern of a material since the applied stress results in the accumulation of defects in the material's lattice and its local distortion [120]. Thus, the electron channeling contrast results in the grain contrast [121] as observed in the Al matrix in SEM micrographs of the investigated alloys after the compression/tension loading. Thereby, it hinders the microstructure segmentation.

### **3.4 Quantitative microstructure characterization**

The quantitative image analysis has been performed using different image analysis software. In particular, Archive4Images (a4i) software has been used for image processing and analysis of optical micrographs and scanning electron fractographs. Besides, an image processing software Fiji can be used for the same purpose. In this work, it has been used for generation of Voronoi tessellations. And finally, Modular Algorithms for Volume Images (MAVI) [67] has allowed to analyze quantitative characteristics of 3D microstructure images.

The estimation of statistical characteristics, such as the mean values of microstructural features, their standard deviations and frequency distributions has been performed using standard statistical methods [122]. Quantitative data has been represented in form of linear scale histogram plots. All distributions illustrate a relative frequency of features, i.e. the amount of the occurrence of a feature in a structure is normalized to the total amount of the analyzed structural elements. This way of the data representation allows the comparison of different sets of measurements.

#### **3.4.1 2D microstructure characterization**

2D morphological properties of microstructural constituents have been analyzed by means of image data as observed on metallographic sections as well as acquired by the FIB/SEM tomography. Aluminium dendrites have been characterized by the dendrite arm spacing (DAS) (see Figure 3.5 (a)). Microstructure constituents and fracture surface elements have been described by means of characteristics illustrated in Figure 3.5 (b) and listed in Table 3.3. Damage elements, such as cracks and voids, have also been described by their size-shape features as well as orientation distributions (see Section 3.4.4). Additionally, the dispersion of Si particles has been evaluated with the help of inter-particle spacing (see Section 3.4.5).

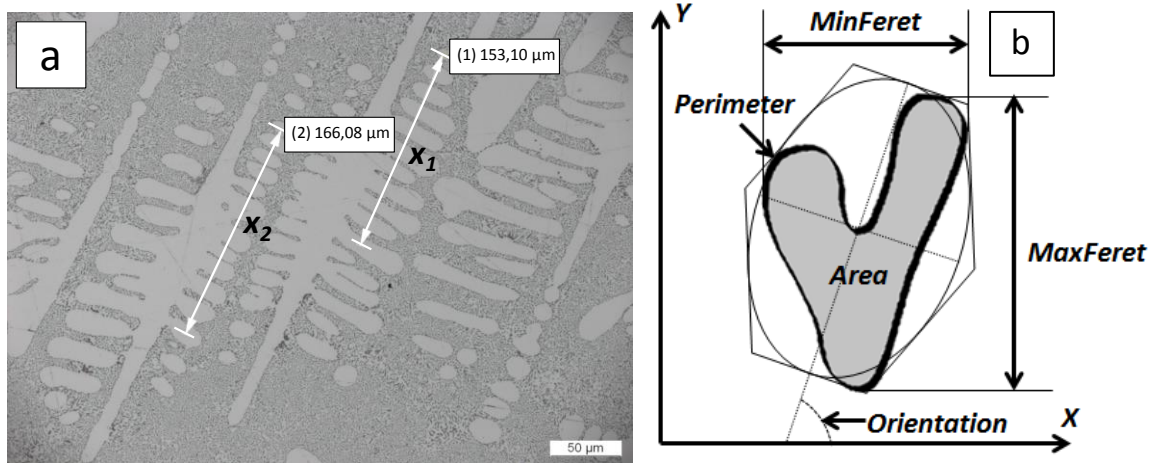


Figure 3.5: (a) Optical micrograph of the modified Al-Si alloy illustrating the DAS computation procedure. The first dendrite (1) has 11 arms (10 intervals) within the length  $x_1 = 153.10 \mu\text{m}$  and the second dendrite (2) has 12 arms (11 intervals) within the length  $x_2 = 166.08 \mu\text{m}$ , which result in  $DAS_{(1)} = 153.10/10 = 15.31 \mu\text{m}$  and  $DAS_{(2)} = 166.08/11 = 15.10 \mu\text{m}$ , respectively. At least 10 dendrites have to be analyzed by this way in order to compute a statistically representative mean value of DAS for the whole structure [123]. (b) Schematic illustration to the definition of an object's orientation in 2D images as well as size parameters of an object used by the a4i software to derive further size-shape characteristics, in particular, the aspect ratio, the shape factor and the equivalent circle diameter [122,124,125].

Table 3.3: 2D size-shape morphological descriptors derived from the parameters illustrated in Figure 3.5 [122–125].

Parameter	Formula	Definition
Aspect ratio	$\frac{MinFerret}{MaxFerret}$	defined as a ratio between the minimum ( <i>MinFerret</i> ) and maximum ( <i>MaxFerret</i> ) Feret diameter of an object
Shape factor	$\frac{4\pi * A}{P^2}$	defined as a ratio between the object's area ( <i>A</i> ) and the area of a circle which has the same perimeter ( <i>P</i> ) as the object
Equivalent circle diameter	$\sqrt{\frac{4 * A}{\pi}}$	defined as an object's equivalent area ( <i>A</i> ) circle diameter
Dendrite arm spacing	$\frac{x}{m - 1}$	defined as a ratio between the length of the analyzed dendrite stem ( <i>x</i> ) and the number of intervals between <i>m</i> dendrite arms within the length <i>x</i>

The aspect ratio and the shape factor characterize a shape of microconstituents from different perspectives: the aspect ratio provides information about the elongation of an object whereas the shape factor assesses an extent, in a range from 0 to 1, to which an object is similar to a circle with the same perimeter, where 1 stands for an ideal circle [125]. The equivalent circle

diameter is a derivative feature from the area; both parameters characterize the size of an object.

The dendrite arm spacing or DAS refers to the spacing between secondary dendrite arms. It depends on the solidification rate and to a certain extent exerts an influence on mechanical properties of Al-Si castings. To compute DAS, at least 10 dendrites have to be analyzed according to the procedure illustrated in Figure 3.5 (a). The final value is computed as the mean value of DAS measurements for every single dendrite [123].

#### 3.4.2 3D microstructure characterization

Size-shape features of objects in 3D have been described by means of the shape factor and the equivalent ball diameter as defined in Table 3.4. In 3D, the shape factor characterizes an object's shape as compared to an ideal sphere, similarly to its 2D counterpart, i.e. it assesses an extent, in a range from 0 to 1, to which an object is similar to a sphere with the same surface area, where 1 stands for an ideal sphere. The equivalent ball diameter is derived from an object's volume; both parameters characterize the size of an object [67].

Table 3.4: 3D size-shape morphological descriptors computed for every single object [67].

Parameter	Formula	Definition
Shape factor	$\frac{6\sqrt{\pi} * V}{\sqrt{S^3}}$	defined as a ratio between the object's volume ( $V$ ) and the volume of a sphere which has the same surface area ( $S$ ) as the object
Equivalent ball diameter	$\sqrt[3]{\frac{6 * V}{\pi}}$	defined as an object's equivalent volume ( $V$ ) ball (sphere) diameter

In general, there are four basic characteristics which can be defined in 3D for every object such that any further object's feature can be computed from the linear combination of the basic features with suitable constants according to the so-called Hadwiger's characterization theorem. These basic characteristics are the following [60]:

- the volume of an object ( $V$ );
- the surface of an object ( $S$ );
- the integral of mean curvature of an object ( $M$ );
- the integral of total curvature of an object ( $K$ ).

Since the mean and the total curvatures are less obvious characteristics than the volume and the surface, Figure 3.6 helps to explain the meaning of the former parameters. Consider a point  $P$  on the surface element  $dS$ , which has two principle normal curvatures  $k_1$  and  $k_2$  corresponding to reciprocals of radii  $r_1$  and  $r_2$  of the largest and smallest circles tangent to the surface element  $dS$  at the point  $P$ , respectively. Then, the mean curvature of the surface element  $dS$  is defined by  $\frac{1}{2}(k_1 + k_2)$  and the total curvature is  $(k_1 * k_2)$ . Finally, the integral of mean curvature,  $M$ , and the integral of total curvature,  $K$ , for an object are obtained by the integration of the corresponding local curvature values over the entire closed surface [65].

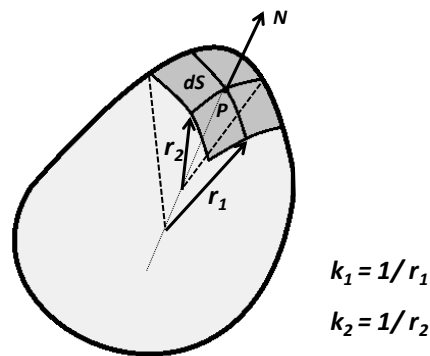


Figure 3.6: (a) Schematic illustration to the definition of principle normal curvatures  $k_1$  and  $k_2$  at the point  $P$  on the surface element  $dS$  (adapted from [65]).

The features described above are object-based since they can be computed for every individual object within an analyzed phase. However, for characterization of complex microstructures consisting of connected components, object-based features would not make so much sense. For example, a network of a microstructural component percolating an entire structure within an analyzed volume would be accounted for only one object. In this case, specific values of the basic characteristics computed for the analyzed structure as a whole are more useful in order to interpret its morphological features and compare them with other sets of measurements.

Obviously, specific features have to be determined in 3D. However, there are stereological methods which enable an estimation of the basic characteristics from 2D images, with the exception of the specific integral of total curvature:  $K_V$  can only be computed on the basis of 3D data [60,65]. The specific integral of total curvature,  $K_V$ , is related to the spatial arrangement of a phase which can vary from simply connected components to percolating network [60], i.e. it is related to the structure connectivity described in more detail in the next section.

### 3.4.3 Evaluation of connectivity

The connectivity of a component has been evaluated by means of the Euler number. The Euler number,  $\chi$ , represents the difference between the number of particles in a structure,  $N$ , and the connectivity,  $C$  [65]:

$$\chi = N - C \quad 3.1$$

Thus, the connectivity of Si particles,  $C$ , can be computed by simply subtracting the Euler number,  $\chi$ , from the number of Si clusters within an analyzed volume,  $N$ . For disconnected particles ( $C = 0$ ), the Euler number equals to the number of particles and for objects forming a strongly connected network ( $C$  is very high), the Euler number is negative [65].

The Euler number provides information on topological properties of a structure. In particular, the Euler number reflects the relation between different types of surface elements presented in the structure such as convex, concave, and saddle surfaces, which correspond to convex particles, holes, and tunnels, respectively [65]:

$$\chi = N - C = \frac{1}{2}(N_{convex} + N_{concave} - N_{saddle}) \quad 3.2$$

where  $N_{convex}$ ,  $N_{concave}$  and  $N_{saddle}$  are the number of convex, concave and saddle surface elements, respectively. Figure 3.7 shows an example of the estimation of the Euler number for two different particle sets with the help of an imaginary sweeping tangent plan. By sweeping down from the top, it forms tangent planes with different surface elements of the particles. Counting the amount of convex, concave and saddle surface elements and applying Equation 3.2 returns the Euler number [65].

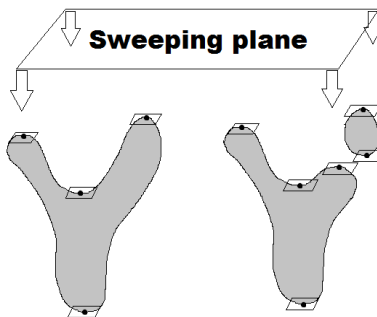


Figure 3.7: Schematic illustration to the estimation of the Euler number for two different particle sets with the help of an imaginary sweeping tangent plan (adapted from [65]). By moving the sweeping plan down from the top, tangent planes with different types of particle surface elements are formed. Then, according to Equation 3.2, the Euler number of the particle on the left is defined as  $(1/2)(3 + 0 - 1) = 1$  and for the particle set on the right, it is computed as  $(1/2)(5 + 0 - 1) = 2$ .

In practice, as in case of the basic characteristics, the Euler number is usually normalized to a sample volume. The specific Euler number,  $\chi_V$ , has a direct relation to the specific integral of total curvature by [60]:

$$K_V = 4\pi\chi_V \quad 3.3$$

#### 3.4.4 Orientation distribution of cracks

The orientation of cracks is analyzed in 2D and 3D images. The output information on the orientation distribution has, however, different forms. Orientation of objects in 2D is defined by a4i software [124] automatically. In principle, the program fits an ellipse in an octagon circumventing an object or inscribed in it. Then, the orientation is defined as an angle between the major semi-axis of the ellipse and the x-axis in the image in a range from 0 to 180° (see Figure 3.5 (b)).

MAVI software [67] provides a possibility to analyze 3D orientation distribution of fibers, where a relative frequency of voxels is computed with respect to 13 discrete directions on a unit sphere or, more precisely, on a semisphere. Since the directional analysis is performed on an entire structural component, i.e. the orientation distribution of fibers belongs to the field features, the output frequency does not provide information on the orientation of every single void, in contrary to the crack orientation distribution estimated on 2D images. Thereby, the output data is presented by a set of Cartesian coordinates with a relative frequency of voxels for every direction. The Cartesian coordinates are then transformed into a spherical coordinate system and mapped in MATLAB on a unit semisphere. In the spherical system of coordinates, the 3D orientation is described by vectors  $(r, \theta, \phi)$  where  $r$  is the radial distance ( $r = 1$ ),  $\theta$  and  $\phi$  are the azimuthal and polar angles, respectively. The amount of sampling directions plays an important role, so that the finer the sampling, the more accurate the measurements, on one hand, and the higher the computation time, on the other hand [126].

#### 3.4.5 Evaluation of inter-particle spacing

There are various methods of evaluation of the particle dispersion and the inter-particle spacing, in particular. Briefly, some techniques are appropriate to assess homogeneity of the particle dispersion without providing quantitative information about the spacing between the particles whereas other techniques regard only the nearest neighbor or particle centroids, the latter is useful to analyze structures with small particles and large inter-particle spacings [122].

When the particles are larger and the second phase occupies a considerable volume, the mean edge-to-edge distance or the mean free distance between particles,  $\lambda$ , can be used to assess the inter-particle spacing. The conventional method involves a counting of the phase interceptions with random straight lines per unit line length [115]. In the absence of this function in the image analysis software, the dilation and counting technique seems to be the most appropriate as it also provides the particle edge-to-edge spacing (in contrary to center-to-center spacing regarded in some other methods) and takes into account morphological features of the second phase [122].

The dilation and counting technique used in this study implies a successive dilation of the second phase particles with counting the particle number after each dilation step until all particles are merged together into a single particle [122]. The resulting data is transferred into the graph where the inter-particle spacing is plotted versus the cumulative percolation. Here, the inter-particle spacing is defined as two times the number of dilation steps,  $i$ , multiplied by the pixel size. The cumulative percolation is computed as  $1-(N_i/N_0)$ , where  $N_i$  is the number of  $S_i$  particles after the dilation step  $i$  and  $N_0$  is the original number of  $S_i$  particles. Then, the inter-particle spacing,  $\lambda$ , is defined as a value which corresponds to the median value of the cumulative percolation, i.e. to the percolation of 0.5 [127].

## 3.5 Characterization of mechanical behavior

### 3.5.1 FEM simulations

FEM simulations have been carried out on virtually designed and experimentally obtained samples of Al-Si eutectic phase. While virtually generated structures have been produced with an isotropic voxel size of  $46 \times 46 \times 46 \text{ nm}^3$ , 3D images obtained by the tomographic reconstruction have featured an anisotropic voxel size due to the experimental setup (see Section 3.3). Therefore, the experimental images have first been rescaled to the isotropic voxel size in accordance with the virtual samples.

The series of 2D binary images issued from the tomographic reconstruction have been merged into a 3D volume mesh and the material properties have been mapped on the barycenter of each voxel. The resulting amount of mesh cells have been very large requiring a high computational power. To speed up the computations and reduce memory requirements, the meshes have been coarsened with the help of an algorithm that combines several voxels into a larger voxel with respect to the volume fraction and properties of the materials therein. The influence of the coarsening level on the number of mesh cells and computational time has

been studied in [128,129]. Finally, the coarsening level 8 has been used for all the structures, which implies that every  $8 \times 8 \times 8$  voxels have been combined into 1 voxel.

The following properties have been assigned to the materials: A Young's modulus of  $E = 70$  GPa, a Poisson's ratio of  $\nu = 0.34$ , and a yield strength of  $\sigma_y = 40$  MPa have been applied to the aluminium, whereas a Young's modulus of  $E = 107$  GPa, a Poisson's ratio of  $\nu = 0.27$ , and a yield strength of  $\sigma_y = 7$  GPa have been assigned to the silicon.

The FEM simulations have been carried out with the help of the structural mechanics module of COMSOL Multiphysics, whereby an elasto-plastic material model with an isotropic hardening has been used. In particular, the aluminium has been modeled as an elasto-plastic material and the silicon has been modeled as a linear elastic material. The damage of the material and residual stresses have not been taken into account.

The following boundary conditions have been applied to the 3D samples for the FEM simulations of uniaxial compression: one side of the meshed volume has been fixed while the opposite side has been subjected to the compressive loading. Then, the stress-strain curves have been computed by using volume averages of stress,  $\overline{\sigma_{ij}}$ , and strain,  $\overline{\varepsilon_{ij}}$  [13]:

$$\overline{\varepsilon_{ij}} = \frac{1}{V} \sum_{m=1}^N \varepsilon_{ij}^{(m)} V^{(m)} \quad 3.4$$

$$\overline{\sigma_{ij}} = \frac{1}{V} \sum_{m=1}^N \sigma_{ij}^{(m)} V^{(m)} \quad 3.5$$

where  $V$  is the volume of the 3D sample,  $m$  is the cell number and  $N$  is the total number of mesh cells. Here, the von Mises stresses in the material have been calculated as they are usually applied to the mechanical characterization of ductile materials like Al-Si alloys [9]. More details on the FEM simulations procedure can be found in [129].

### 3.5.2 Compression tests

The compression tests have been carried out with the help of the E10000 Linear-Torsion Floor Instrument of Instron® Company which allows a maximum load capacity of 10 kN. All test specimens have been cut from similar parts of the castings into cubes with the side length of 5 mm. The tests have been performed at a constant cross-head speed of 0.001 mm/s. After the compression loading, the specimens have been sectioned in the center along the loading axis for further metallographic investigations.

#### 3.5.3 Tensile tests

The tensile tests have been carried out with the same machine as the compression tests. The specimens were machined according to the European Standard EN ISO 527-2 [130], where the gage has a square cross-section of  $2 \times 2 \text{ mm}^2$  and is 10 mm long. The specimen is fixed in the machine, so that the one end of the specimen remains static and the tensile load is applied to the other end of the specimen. The applied force and the corresponding elongation (amount of stretch) are recorded during the test. Then, the engineering stress-strain curve is computed by dividing the force by the initial cross-section area of the specimen and the amount of stretch of the gage by the initial gage length of the specimen, respectively. The results deduced from the stress-strain curve include the following mechanical characteristics: the Young's modulus, the yield strength, the ultimate tensile strength and the total elongation [131].

Since Al-Si alloys do not exhibit a pronounced yield point, an offset deformation of 0.2% has been used to define the yield strength. To do so, a line intersecting the strain axis at the pre-defined offset has been drawn parallel to the elastic part of the stress-strain curve. The stress corresponding to the intersection of this line with the stress-strain curve is the offset yield strength. The modulus of elasticity is equal to the slope of the elastic part of the stress-strain curve. The ultimate tensile strength has been defined as a maximum stress carried by the specimen. The elongation-at-fracture has been computed by dividing the amount of stretch to rupture by the initial gage length of the specimen. It can also be read from the stress-strain curve as a strain corresponding to the stress decreased by 10% from its maximum value [131,132].

In relation to the strain rate, the general rule is the following: the lower strain rate, the lower the strength and the larger the elongation obtained. For the aluminium, the maximal recommended strain rate is  $15 \times 10^{-5} \text{ s}^{-1}$  [131]; for the gage length of 10 mm it results in a cross-head speed of 0.09 mm/min. In [39], the tensile tests have been performed on cylindrical specimens of modified and unmodified AlSi8 alloys with a gage length of 30 mm and at the cross-head speed of 0.5 mm/min, i.e. the strain rate of  $2.8 \times 10^{-4} \text{ s}^{-1}$ . In [75,86], the tensile tests of Al-Si-Mg alloys have been carried out at the strain rate of  $1 \times 10^{-4} \text{ s}^{-1}$ . In [20,53], the strain rate of  $1 \times 10^{-3} \text{ s}^{-1}$  has been applied for the tensile testing of Al-Si-Mg alloys (gage length of 15 mm). Thus, to define an optimal strain rate for the measurements, a complementary set of experiments has been carried out at different strain rates. The stress-strain curves obtained during the tests are shown in Figure 3.8.

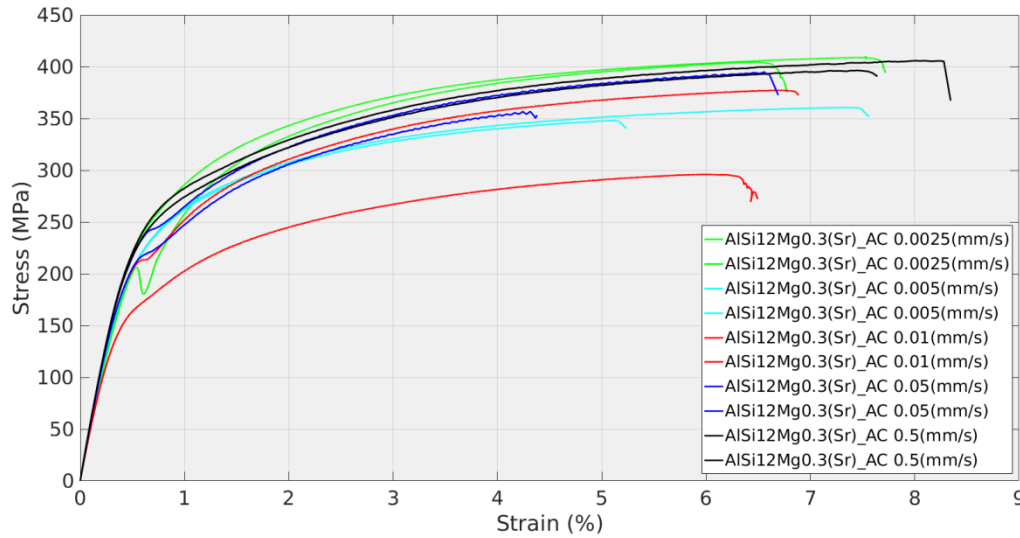


Figure 3.8: Influence of the strain rate (the cross-head speed) on the mechanical behavior of Al-Si specimens (alloy 7X\_AC).

As can be seen from Figure 3.8, no explicit influence of the strain rate on the mechanical behavior of the specimens can be observed. Therefore, the cross-head speed of 0.01 mm/s which corresponds to the strain rate of  $1 \times 10^{-3} \text{ s}^{-1}$  has been chosen for the tensile testing of Al-Si alloys. After the tension loading, the specimens have been sectioned in the center along the loading axis for further metallographic investigations.

### 3.6 Fracture surface characterization

The methods described in the following section have been used for the imaging and characterization of the fracture surface in the eutectic phase. The results have been summarized by Kruglova et al. in publication [133]. Sections 3.6.2 – 3.6.4 contain an excerpt from the section “*Materials and methods*” of the underlined publication.

#### 3.6.1 Fractography

Fracture surfaces of materials can be studied via different techniques, like Light Microscopy (LM), Scanning and Transmission Electron Microscopy (SEM and TEM). The former technique has however very limited depth of field and is often replaced by more powerful SEM and TEM fractography. The two latter techniques have a greater depth of field than LM, and therefore, they can provide the images with much more detail [47]. Electron fractography is a standard technique for studying the fracture surfaces in aluminium alloys [69], but it requires a preparation of thin foils and replicas of the surfaces which is, however, very elaborated procedure. Therefore, when possible, SEM fractography is preferred.

In this study, the conventional SEM technique has been chosen to study the fracture surfaces of Al-Si alloys. Also, SEM stereo imaging has been tested for the fracture surfaces under investigation. Thereby, SEM fractographs of the same sample area and at the same magnification are recorded with a certain tilt angle. The height difference  $\Delta z$  for any surface point is then computed as a function of the magnification, tilt angle and shift of the point coordinate along  $x$  or  $y$  directions between two images [47]. Though the resolution has been adequate to observe dimples on the fracture surface of a specimen, the information about their depth has not been accessible: the reference points at the bottom of the dimples required to compute the height difference could not be identified due to the lack of contrast, see Figure 3.9.

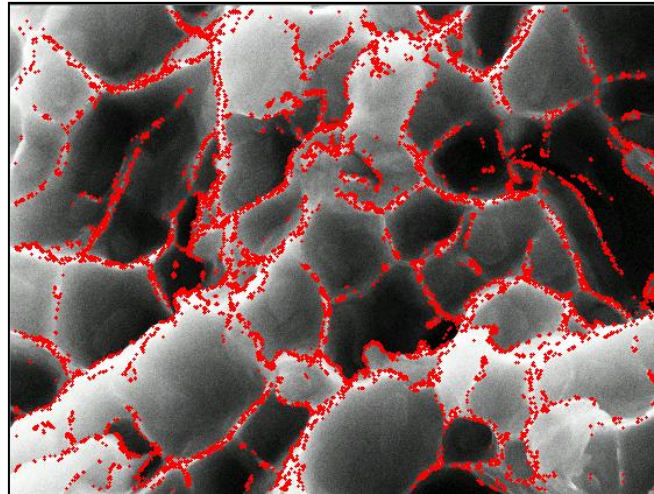


Figure 3.9: Stereo image obtained with SEM. Si particles at the bottom of the dimples cannot be distinguished by the software: red points proposed by the software for computing the height difference are located mostly at the borders of the dimples and do not represent any interest for the determination of the depth.

Thus, the quantitative fractography of the tensile test specimens has been based on SEM images of fracture surfaces and fracture surface profiles. Also, LM images of fracture surface profiles have been taken, but the resolution has been insufficient to resolve fine curvatures of dimple profiles and underlying Si particles.

#### 3.6.2 Image processing of fractographic images

At first, SEM images of fracture surfaces have been treated in such a way as to obtain the dimple borders only. To segment the borders of the dimples, a similar algorithm as for foam reconstruction [134] has been applied with the help of a4i Analysis software [124]: the binarization of images revealing the borders of the dimples has been followed by the dilation of the segmented phase to obtain a border network which divides an image plane into closed

cells. Then, the Euclidean distance transformation has been executed on the system of borders. The obtained distance map has been used as an input for the watershed transformation, which has enabled an extraction of a one-pixel-wide network of borders, bounding closed cells of dimples for further quantitative analysis. The image processing operations are summarized in Figure 3.10.

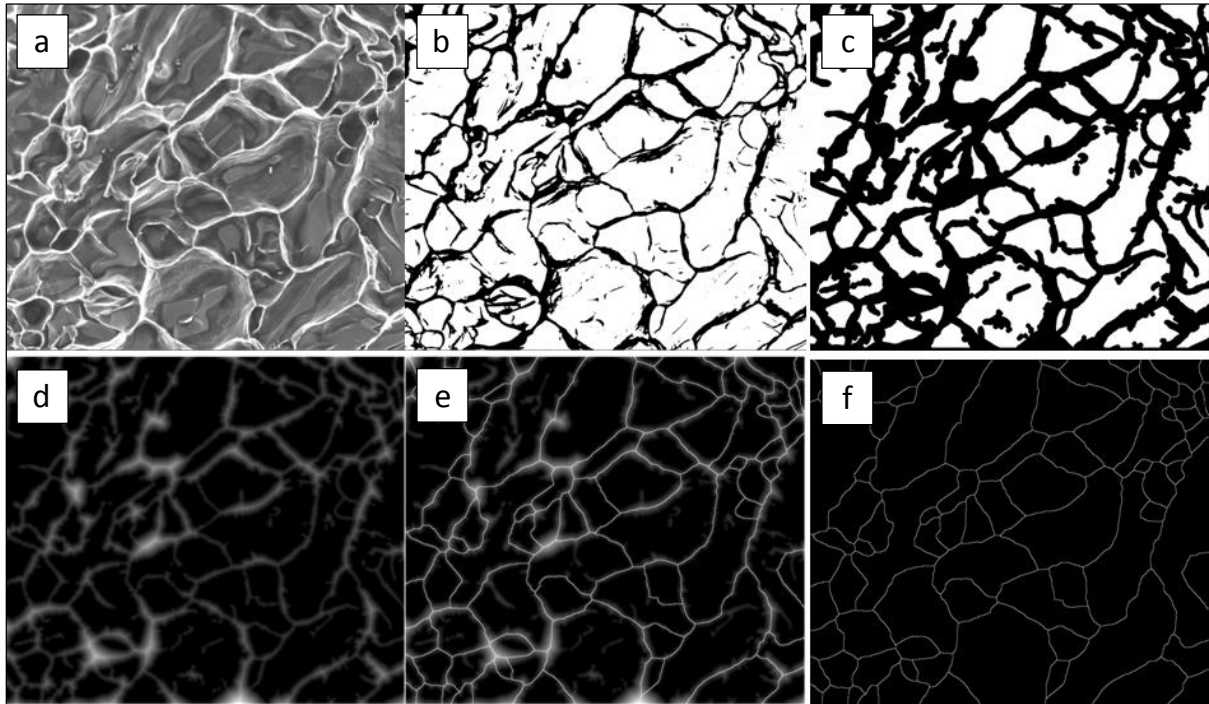


Figure 3.10: Image processing operations used to segment (a) dimples on the fracture surface include (b) image binarization; (c) dilation of the segmented dimple borders to obtain a border network and closed cells; (d) Euclidean distance transformation on the binary image; (e) watershed transformation on the Euclidean distance map; (f) segmentation of the watershed results [133].

Then, a4i Analysis software has been used to obtain quantitative characteristics of dimples from the segmented images. In particular, information on area, equivalent diameter, aspect ratio and shape factor has been obtained. In addition, distributions and areal densities of the computed characteristics have been determined. At least 5 fields have been analyzed for every alloy. As a next step, the dimple depth has been determined by using SEM images of fracture surface profiles.

### 3.6.3 Estimation of dimple depth-to-width ratio

Cross sections of fracture surfaces have been analyzed using SEM images that have been acquired during FIB tomography of the tensile test specimens. The FIB cuts do not necessarily pass through the middle part of the dimples, but the depth-to-width ratio of the

dimple remains almost the same for any random cut through it [69]. As soon as the ratio is computed in a statistically valid manner, the depth is defined as a product of the dimple's equivalent diameter and the ratio. Segmented fracture surface profiles have been analysed manually so that more than 200 measurements have been recorded. Actually, two types of ratios have been estimated, i.e. the average depth-to-width ratio and the ratio of the average depth to the average width. It has been shown on the example of the steel specimens mentioned in [47] that the ratios can differ significantly. Therefore, it has to be clearly stated which ratio will be used for further calculations.

#### 3.6.4 Estimation of fracture surface area

A fracture surface area can be estimated by applying different methods: from the approximation by triangular elements to the application of stereological equations [47]. In this work, an approximation of the fracture surface by oblate ellipsoids is proposed. The decision is motivated by the fact that the dimples on the fracture surface of Al-Si alloys are mostly shallow holes and that such an approximation has already been used by Broek [69] to show the relation between the depth-to-width ratio of the dimples and the size-to-distance ratio of the Si particles. Though the ellipses are not space-filling, the fracture surface is paved by the ellipses having the same area as the corresponding dimples (see Figure 3.11). In so doing, it can be assured that the area equal to the area of the analysed fractograph (i.e. the projection of the fracture surface) is taken into account.

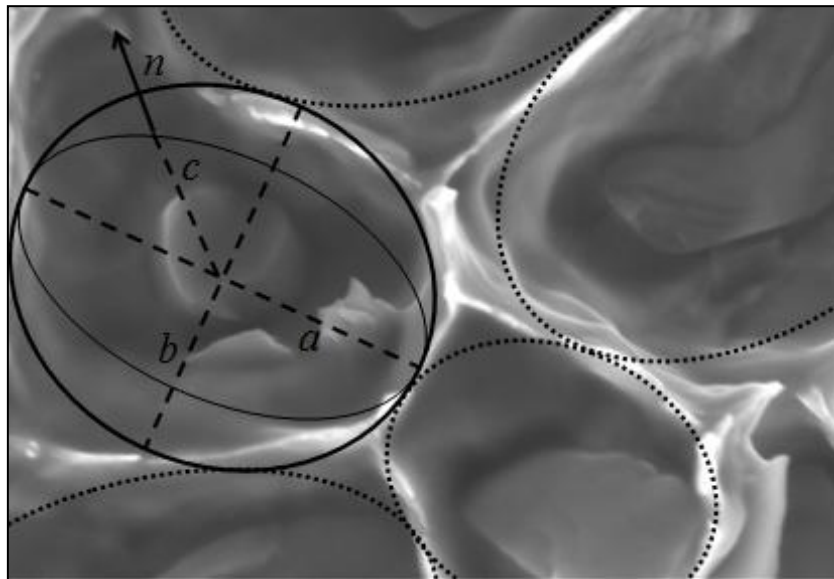


Figure 3.11 Schematic illustration of an ellipsoid fitting to the fracture surface of the Sr-modified Al-Si alloy, where  $a$ ,  $b$  and  $c$  are the principle semi-axes;  $n$  is the direction normal to the surface [133].

The oblate ellipsoid has two equal semi-axes  $a = b$  and a third semi-axis  $c$  that is smaller than the other two axes. Thus, the dimple itself can be described as a half of the oblate ellipsoid with the surface area of [60]:

$$S_i = \frac{1}{2} * 2\pi ac \left( \frac{a}{c} - \frac{c}{\sqrt{a^2 - c^2}} \ln \frac{a - \sqrt{a^2 - c^2}}{c} \right), c < a \quad 3.6$$

The fracture surface is then computed by summing up the surface area of every single dimple:

$$S_{total} = \sum_{i=1}^n S_i \quad 3.7$$

However, the dimples do not always exhibit a circular profile on SEM micrographs. As will be shown in Section 4.6.2, the apparent shape of dimples is determined by the shape of Si particles on which they have been nucleated. Thus, the approximation by oblate ellipsoids is physically motivated only for structures with circular profiles of Si particles. Equation 3.6 is therefore generalized by using an equivalent circle diameter instead of the principle semi-axes  $a$  ( $b$ ); the semi-axis  $c$  stands for the depth.

To check whether a chosen approximation is valid for a given structure, the surface roughness parameter,  $R_S$ , is computed as a ratio of the true surface area,  $S_t$ , to the projected area,  $A'$  (Equation 3.9 [47]) and is compared against the roughness parameter obtained via stereological equation [47]:

$$R_S = \left( \frac{4}{\pi} \right) R_L \quad 3.8$$

where  $R_L$  is the profile roughness parameter representing the ratio of the true profile length,  $L_t$ , to the projected length,  $L'$  (Equation 3.10 [47]). Here, the surface area,  $S_{total}$ , obtained via Equation 3.7 will be used instead of the true surface area,  $S_t$ . The projected surface area,  $A'$ , is equal to the area of the corresponding SEM image.  $R_L$  is experimentally accessible from the SEM images of the fracture surface profiles.

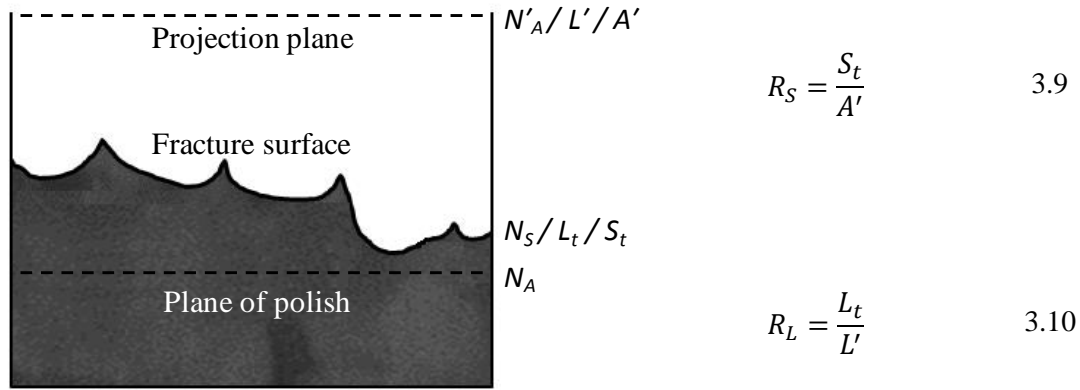


Figure 3.12: Schematic illustration to Equations 3.9 and 3.10.  $N'_A$ ,  $N_S$  and  $N_A$  are the particle densities on projection plane, fracture surface and plane of polish, respectively (modified after [47]).

And last but not least, it has to be verified whether the particle density on the polished plane,  $N_A$ , is similar to the particle density on the projected plane of the fracture surface,  $N'_A$  (see Figure 3.12). If this is the case, i.e.  $N_A = N'_A$ , then the quantities measured on the metallographic sections through the eutectic are also valid for the corresponding fractographs [47]. It enables the fracture surface modeling using 2D metallographic sections.

### 3.6.5 Fracture toughness measurements

Fracture toughness measurements have been performed with the help of Instron 8511.20 servohydraulic testing machine on a single edge bend specimen. A method applied for the toughness measurements is known as the three-point bending test. It consists of two stages: a first stage implies a fatigue loading of a single-notch specimen with a constant force amplitude until a crack is formed, and the second stage includes the crack growing until the unstable fracture propagation is recorded. The results are presented in form of the R-curve where the force is plotted versus the crack-extension (crack mouth displacement). The discontinuity in the curve indicates an onset of the unstable crack propagation. With the help of a secant line which is build from the origin of the curve with a 95% - slope with respect to the line tangent to the initial portion of the curve, the intersection point,  $F_5$ , of the secant line and the R-curve is determined. Depending on the location of a maximum force attained during the experiment,  $F_{max}$ , and the intersection point,  $F_5$ , relative to each other, the force  $F_Q$  is determined. The force  $F_Q$  is then used to compute a conditional fracture toughness,  $K_Q$ , according to Equations 3.11 and 3.12 [111,112]:

$$K_Q = F_Q \frac{S}{BW^{3/2}} f\left(\frac{a}{W}\right) \quad 3.11$$

$$f\left(\frac{a}{W}\right) = 3\left(\frac{a}{W}\right)^{1/2} * \frac{1.99 - \left(\frac{a}{W}\right)\left(1 - \frac{a}{W}\right)\left[2.15 - 3.93\left(\frac{a}{W}\right) + 2.7\left(\frac{a}{W}\right)^2\right]}{2\left(1 + \frac{2a}{W}\right)\left(1 - \frac{a}{W}\right)^{3/2}} \quad 3.12$$

where  $W$  is a width of a specimen,  $S$  is a support span ( $S = 4W$ ),  $B$  is a thickness of a specimen, and  $a$  is a crack length. The geometry of a specimen for the three-point bending test is shown in Figure 3.13. Taking into account the size of the available ingots, the specimens with the width,  $W$ , of 10 mm and the thickness,  $B$ , of 5 mm have been prepared. The crack length,  $a$ , has been around 5 mm.

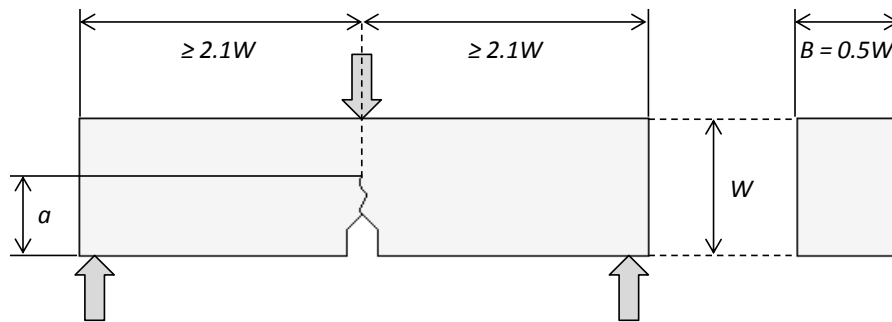


Figure 3.13: Schematic illustration of a specimen geometry for the three-point bending test (after [112]).

To determine whether the conditional fracture toughness,  $K_Q$ , computed via Equation 3.11 can be regarded as the plain-strain fracture toughness,  $K_{Ic}$ , two conditions have to be verified:

$$F_{max}/F_Q \leq 1.10 \quad 3.13$$

$$2.5(K_Q/\sigma_{YS})^2 < b_0 \quad 3.14$$

where  $\sigma_{YS}$  is a 0.2 % offset yield strength of the material, and  $b_0$  is a width of the uncracked ligament. If these requirements are not fulfilled,  $K_Q$  cannot be considered as  $K_{Ic}$  and larger specimens have to be tested in order to obtain a valid value of  $K_{Ic}$ . In other words, to be able to estimate a critical value of the fracture toughness, the plastic region around the crack-tip has to be much smaller than the ligament and the condition of plain-strain has to be attained [111].

### 3.6.6 Analytical estimation of fracture toughness

The fracture toughness has been computed via two different analytical formulae (Equations 3.15 – 3.16) and has been correlated with the values reported in the literature to demonstrate a practical use of the approach developed for the fracture surface modeling.

### 3.7 Stochastic modeling

---

A relation between the toughness on one side and the tensile strength and the depth of dimples on the other side has been proposed by Stüwe [87]:

$$K_C = (Eh_s\sigma_{UTS}/2)^{1/2} \quad 3.15$$

where  $E$  and  $\sigma_{UTS}$  are the Young's modulus and the tensile strength of the material;  $h_s$  is the dimple depth. Analytical values of  $K_C$  obtained via Equation 3.15 have shown a good agreement with experimental measurements for different materials. Further, Equation 3.15 has been modified by Qin et al. [110] to obtain a weighted average of the fracture toughness taking into account an inhomogeneous distribution of dimple sizes within a fracture surface:

$$\sum V_i K_{C_i} = K_{Ave} = \left(\frac{E\sigma_{UTS}}{2}\right)^{1/2} \sum_{i=1}^3 V_i h_{si}^{1/2} \quad 3.16$$

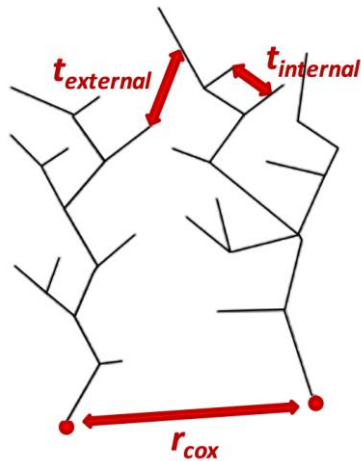
where  $V_i$  stands for the volume fraction of dimples having an average depth  $h_{si}$ . Here, only three groups of dimples have been considered, but Equation 3.16 can be equally applied to account for every dimple and its weight individually.

## 3.7 Stochastic modeling

### 3.7.1 Principles of competitive stochastic growth model

The virtual Al-Si eutectic structures have been generated by means of the Competitive Stochastic Growth Model (CSGM) introduced in [14]. The CSGM model has been developed to capture morphological features of coral-like Si particles in modified Al-Si alloys which are relevant for the mechanical performance of the structure. Furthermore, the modeling approach has proved to generate virtual structures that can reflect the mechanical behavior of the experimental data. Besides, the mechanical response of the virtual structures has shown to be sensitive to the variations of Si morphology controlled by model parameters [129]. Thus, by varying the model parameters, it has been possible to study the relations between the morphology of the eutectic Si and mechanical response of the structure [135].

A detailed description of the CSGM model is presented in [14]. In the following, a brief overview of the model is made to the extent necessary to understand the principles and parameters defining the stochastic model, and how these model parameters are used to vary the morphological features of virtual structures. The schematic representation of the competitive stochastic growth model and its parameters is provided in Figure 3.14.



- $t_{internal}$  determines the minimum distance between the branches belonging to the same particle and controls the degree of branching.
- $t_{external}$  determines the minimum distance between two disconnected particles.
- $r_{cox}$  determines the minimum distance between two starting points for two disjoint particles and influences the number of particles.

Figure 3.14: Schematic representation of the competitive stochastic growth model and parameters of the model, such as an external,  $t_{external}$ , and internal,  $t_{internal}$ , competition parameters and a hardcore radius,  $r_{cox}$  [135].

First, a single coral-like Si particle is modeled as a system of connected line segments defined by parameters of multivariate time series. Each single coral is composed of two elements: a stem and branches. The interaction between the branches within a single coral is controlled by a threshold value called the internal competition parameter,  $t_{internal}$ , which preserves the minimum distance between the branches [14].

In a second step, the aggregates of corals in the eutectic volume are modeled by a competitive growth model which controls the interaction between neighboring corals. The starting points for corals in the model are defined by a stationary and isotropic point process in a volume, where the minimum distance between two starting points has to be not smaller than the hardcore radius,  $r_{cox}$ . The distance between the neighboring corals is controlled by the external competition parameter,  $t_{external}$ , which prevents the corals from growing too close to each other [14].

And finally, the aggregation of corals presented so far by the line segments – a so-called “skeleton” of the eutectic Si or tree-like graph structure – is dilated to adapt the volume fraction of Si particles in the eutectic phase. In this step, two dilation variants have been applied [135]:

- (1) Each line segment is individually dilated by a spherical structuring element with a radius adapted so that the connectivity of particles is preserved, i.e. Si particles that have been disconnected in a “skeleton” structure remain disconnected after the dilation. This dilation variant has been used to study the influence of the number of Si particles on the mechanical behavior of the structure.

- (2) All line segments are dilated by a spherical structuring element with a constant radius, whereby neighboring particle can merge together upon the dilation. As it enables to vary the connectivity of Si particles, this dilation variant has been used to study the influence of the connectivity on the mechanical behavior of the structure.

Thus, the competitive stochastic growth model allows to generate random 3D morphologies of the eutectic Si with different structural properties by varying the model parameters within a certain range as to obtain realistic morphological scenarios.

#### **3.7.2 Parameters of competitive stochastic growth model**

The stochastic model CSGM has originally been developed to describe the morphology of the eutectic Si in the Sr-modified Al-Si alloy. Thus, the model has been fitted to the 3D image data obtained by means of the microstructure tomography in such a way as to minimize the discrepancy between the most relevant morphological features of the synthetic and experimental data. In particular, the conformity between the particle density and specific basic characteristics of Si particles (the volume density, the surface density, and the specific integral of mean and total curvature) in the experimental image data and stochastic model realizations has been verified. The parameters of the fitted stochastic model are defined by  $t_{internal} = 30$  voxels,  $t_{external} = 20$  voxels, and  $r_{cox} = 55$  voxels [14].

The 3D structure of the eutectic Si obtained by the tomographic reconstruction and its synthetic realization by means of the stochastic model are shown in Figure 3.15 (a) and (b), respectively. Similarly to the experimental prototype of the model, all synthetic structures generated by the model have the volume of  $35.0 \times 16.4 \times 25.2 \mu\text{m}^3$  and isotropic voxel size of  $46 \times 46 \times 46 \text{ nm}^3$ . The volume fraction of Si in the simulated structures is constant and corresponds to the eutectic content of Si (ca. 12%). However, the volume fraction of Si in the experimental samples is slightly overestimated due to the manual segmentation of FIB/SEM images, which is also warranted upon the interpretation of results [135].

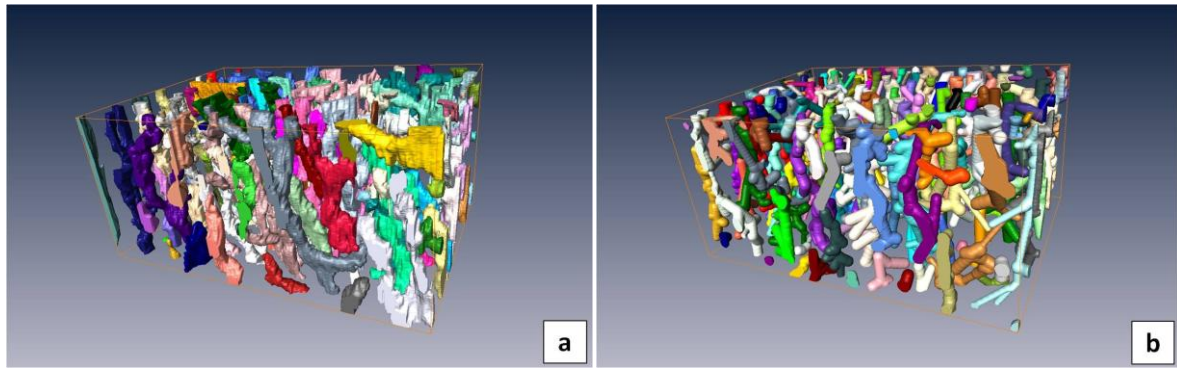


Figure 3.15: (a) Reconstruction of coral-like Si particles within Al-Si eutectic obtained by FIB/SEM tomography; (b) a realization derived from the competitive stochastic growth model that has been fitted to the experimental data (different colors represent disconnected particles) [135].

### 3.7.3 Experimental data for simulation study

Two types of experimental data previously studied in [128] have been considered together with synthetic data generated by means of the stochastic model to serve as a reference data for mechanical simulations. In particular, two Sr-modified Al-Si alloys produced by directional solidification and die casting have been investigated. The three-dimensional structure of the eutectic Si in the castings reconstructed by the FIB/SEM tomography is shown in Figure 3.16. The specifications of the experimental samples, including chemical composition, casting procedure, sample size, voxel size and Euler number density of Si in the analyzed samples are presented in Table 3.5.

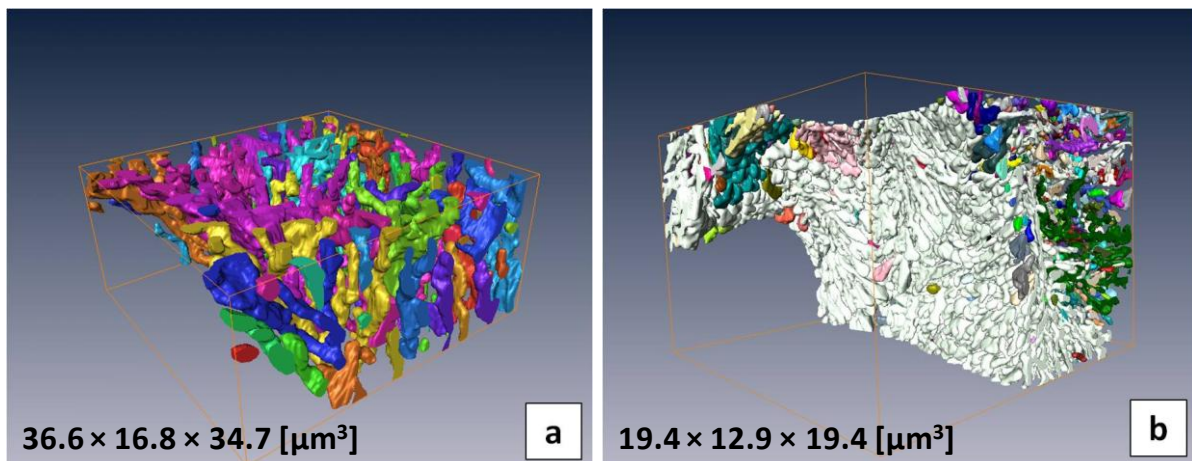


Figure 3.16: Reconstruction of Si particles in the Al-Si alloys obtained (a) by directional solidification (experimental sample no. 1) and (b) by die casting (experimental sample no. 2). Different colors represent disconnected Si particles; Al matrix is transparent. The sample in (a) consists of many disconnected Si particles. The sample in (b) comprises a large connected Si cluster in the middle of the reconstructed volume [128].

### 3.7 Stochastic modeling

Table 3.5: Chemical composition and casting procedure of the experimental samples of Al-Si alloys, as well as voxel size, sample size and Euler number density of Si in the analyzed 3D samples [135].

Experim. sample	Composition (wt. %)	Casting procedure	Voxel size (nm <sup>3</sup> )	Sample size (μm <sup>3</sup> )	Euler number density (m <sup>-3</sup> )
no. 1	7% Si, 0.015% Sr	directional solidification	46 × 59 × 180	35.0 × 16.4 × 25.2	4.80 × 10 <sup>14</sup>
no. 2	7% Si, 0.3% Mg, 0.02% Sr	die casting	25 × 32 × 80	9.7 × 8.3 × 8.5	-2.61 × 10 <sup>17</sup>

The directionally solidified casting shown in Figure 3.16 (a) contains coral-like Si particles arranged in disconnected Si clusters within the eutectic volume. It has served as a prototype structure for the stochastic model. The sample produced by the die casting comprises a highly connected Si particles building a network within the eutectic phase, which can be recognized by a large connected Si cluster in the middle of the reconstructed volume shown in Figure 3.16 (b). It illustrates the mechanical behavior of a structure with a high connectivity of Si particles.

It can be noticed, that the size of both samples reported in Table 3.5 is smaller than the reconstructed volumes shown in Figure 3.16. Indeed, Figure 3.16 has been included for illustration purpose solely: different Si particles are well observed within the bounding boxes. For FEM simulations and estimation of the Euler number density, the smaller samples comprising the eutectic phase have been cropped from the initially reconstructed volumes. In so doing, it has been ensured that the experimental samples are composed of the eutectic phase only, similarly to the virtual samples, and therefore, can be compared to each other.

Thus, two experimental samples provide 3D image data for FEM simulations representing a mechanical response of the real eutectic volume. Note that the mechanical behavior of the experimentally obtained and virtually generated eutectic samples can be compared at the microscale (in the frame of the mechanical simulations) allowing to assess solely the impact of Si morphology on the mechanical response of the eutectic structure without relation to any particular alloy composition. However, on the macroscale, the impact of Si morphology on the properties of the experimental alloys can be compared neither to the virtual samples nor to each other since the alloys have different chemical composition and phase constitution containing along with the eutectic phase primary aluminium dendrites.

### 3.7.4 Fundamentals of tessellation models

A microstructure modeling approach often represents a compromise between a simulation model complexity and an accuracy of a structure representation. Depending on the target structure morphology, different types of geometric stochastic models can be used [136]. Tessellation models are widely applied in materials science to model foams [134] and single-phase polyhedral structures [137]. Such models describe a microstructure morphology with a help of few parameters which leads to a significant data compression and generation of statistically equivalent structures free from noise and artifacts [138]. The models also help to reconstruct incomplete or inexact experimental data obtained for example from tomographic reconstructions [139]. Moreover, the stochastic models are more computationally efficient in terms of their use for mechanical simulations and studying structure-properties relationships [140].

The Voronoi tessellation is the most simple and well-known tessellation model parameterized by a set of generator points solely [138,140]. The principle of the Voronoi tessellation is a decomposition of the space/plane into nonoverlapping, convex and space-filling cells [60]. The Voronoi tessellation cell generated by a point  $x$  contains all points which have  $x$  as a nearest neighbor. Hereby, the Euclidean distance between the points is assessed. The tessellation cell is then defined as follows [136]:

$$C(x) = \{z \in \mathbb{R}^3 : \|z - x\| \leq \|z - y\| \text{ for all } y \neq x, y \in \varphi\}, \quad x \in \varphi \quad 3.17$$

where  $\varphi$  is a finite set of generator points  $\varphi = \{x_1, x_2, \dots, x_n\} \subseteq \mathbb{R}^n$ . The edges of the cells are located equidistant from the generator points. This tessellation property, however, limits its application in relation to patterns which can be generated [136]. Therefore, a weighted generalization of the Voronoi tessellation, such as the Laguerre tessellation, very often is more appropriate for a structure modeling [138]. The Laguerre tessellation is based on a power concept, i.e. to every generator point  $x$  a corresponding weight  $r$  is assigned, which can be represented in  $\mathbb{R}^2$  as a circle with the center  $x$  and radius  $r$ . Then, the power of point  $y$  in relation to the generator point  $x$  and the corresponding tessellation cell are defined as follows [134,136]:

$$pow(y, (x, r)) = \|y - x\|^2 - r^2, \quad r \geq 0 \text{ and } y, x \in \mathbb{R}^2 \quad 3.18$$

$$C((x, r), \varphi) = \{y \in \mathbb{R}^2 : pow(y, (x, r)) \leq pow(y, (x', r')), (x', r') \in \varphi\} \quad 3.19$$

Here, instead of the Euclidean distance between points, the power distance is assessed. Lautensack [141] provides a geometric interpretation of the power distance defined in Equation 3.18 as “the squared length of the tangent line from  $y$  to the sphere”. The tessellation cell is constituted from the points that have a smaller power distance with respect to the point  $x$  as compared to other neighboring generator points.

Still, the Laguerre tessellation is an isotropic growth model with a limited set of shape patterns that can be reproduced. The drawback of the classical Voronoi tessellation and its weighted generalization, the Laguerre tessellation, are that the convex cells only can be generated. The Laguerre tessellations show good results for simulations of convex structures, while leading to large deviations at the non-convex grain boundaries [139]. The Johnson-Mehl tessellation is another common isotropic growth model, where the generation of spherical germs proceeds in time, but the modeled cells can also have curved boundaries. However, these models also fail to reproduce anisotropic structures [142].

In contrast to the isotropic growth models, anisotropic growth models can provide more realistic reconstructions of microstructure features, since they can better capture irregularities and texture. It is particularly relevant for the simulation of complex non-convex structure elements [139,142]. The isotropic growth models such as the Laguerre and Johnson-Mehl tessellations are built on spherical germs while the anisotropic growth models rely on ellipsoidal germs. Thus, the anisotropic tessellation models are generalizations of the Laguerre and Johnson-Mehl tessellations, where the latter two are specific cases of the anisotropic tessellations built on spherical germs. The same principle is applied for the reconstruction of the anisotropic tessellation cells: a cell is constituted from the points which have the smallest distance to the corresponding germ. However, this distance can be computed according to different local metrics, which influence the position and curvature of cell boundaries [142]. The ellipsoidal growth tessellations are very promising stochastic models which have proved to be highly efficient for modeling of complex polycrystalline materials such as martensitic steel [142], rolled aluminium alloys [140] and extruded aluminium [139].

There are two approaches to microstructure simulation by means of the tessellation models: solving an inverse problem and optimization problem [138]. First of all, a realistic stochastic model for the representation of a structure has to be found [66]. Solving an inverse problem implies, first, to find a best-fit tessellation to a given structure and then, define a set of generating points that yield this tessellation [138]. Afterwards, the underlying model

parameters can be estimated. For example, for anisotropic tessellation models built on the ellipsoidal germs such parameters describe the germination process, size and orientation of the germs [66]. On the contrary, an optimization problem solving relies on the estimation of generating points that yield the tessellation best fitting the empirical data set. The performance of the model is usually assessed by a discrepancy measure. Obviously, the goal of the procedure is to minimize the discrepancy between the data set and the model realization [138].

### 3.7.5 Tessellation model of fracture surface

In the following section, a new approach will be proposed to model fracture surfaces by means of the weighted Voronoi tessellation. Hereby, a metallographic image is decomposed into several areas, each around a Si particle, so that each area is represented by a cell of the tessellation. The routine for generation of the weighted Voronoi diagram is implemented as a Java plugin for the Fiji environment. The results have been summarized by Kruglova et al. in publication [135]. This section contains an excerpt from the section “*Materials and methods*” of the underlined publication.

The motivation for using the random mosaic methods and their weighted version, in particular, will be thoroughly discussed in Section 4.7. For the moment, the approach is assumed to be appropriate for a given task, i.e. the modeling of a fracture surface (as projected on a fractograph) which consists of a set of space-filling dimples approached by the Voronoi cells. Here, the system of dimples consists obviously of both convex and concave types of cells. The deviation from convexity observed for certain system elements can be well captured by the cells of the weighted Voronoi tessellation.

As has been described in Section 3.7.4, the classical Voronoi tessellation is limited in terms of patterns that can be generated since the cell edges therein are built equidistant to the generator points [136]. Therefore, a weighted generalization of the Voronoi tessellation is sometimes more useful for structure modelling [138]. Hereby, the concept of the Euclidean distance to the generator point is replaced by a general norm that typically uses some weighting factor to express the idea that individual particles have different influence.

Thus, analogously to the Laguerre cell definition in [136] (see Equation 3.19), the weighted Voronoi tessellation cell of generator point  $x$  with weight  $w$  in the present model can be described as:

$$C((x, w), \varphi) = \{y \in \mathbb{R}^2 : wd(y, (x, w)) \leq wd(y, (x', w')), (x', w') \in \varphi\} \quad 3.20$$

where  $\varphi$  is a finite set of generator points  $\varphi = \{x_1, x_2, \dots, x_n\} \subseteq \mathbb{R}^2$  and  $wd$  is a weighted distance between the point  $y$  and generator points. Here, the generator points are the centroids of Si particles described by their coordinates in the image plane. A weight function equal to the square root of the particles' area is used for weighting the particles. The weighted distance,  $wd$ , is computed as a ratio of the Euclidean distance between a point and a particle centroid to the weight function of the corresponding particle. In so doing, the area of the particles is taken into account so that larger particles generate larger cells and vice versa, as observed in the experimental data. The principles of the model are shortly presented using an example in Figure 3.17.

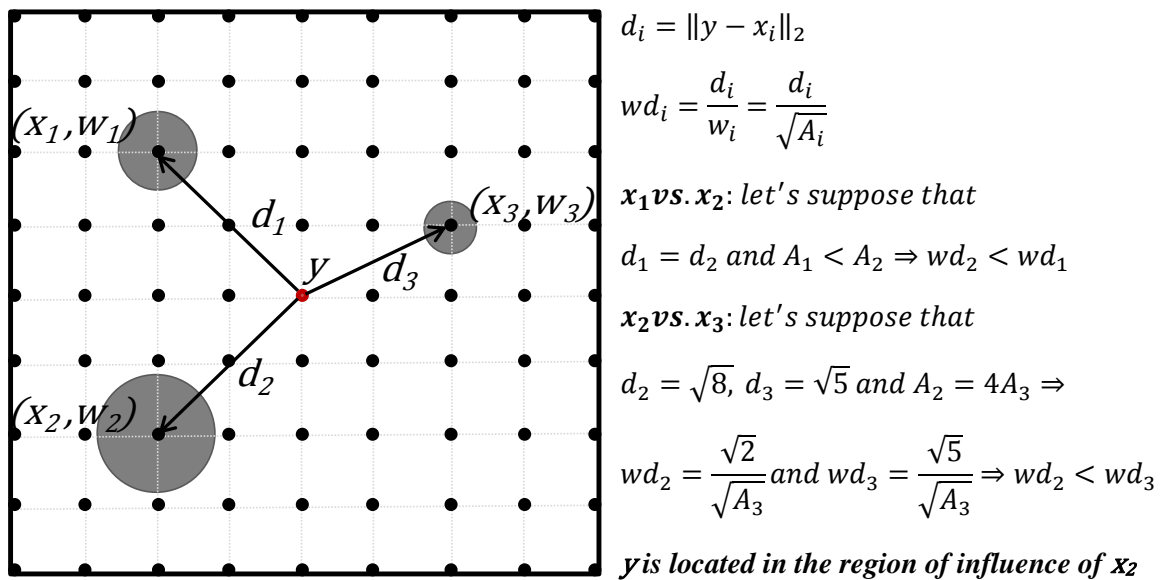


Figure 3.17: Illustration to the weighted Voronoi model with a simple computation example on the right side. Here, a generator point filed is constituted of three points  $x_1$ ,  $x_2$ , and  $x_3$  with weight functions  $w_1$ ,  $w_2$ , and  $w_3$ , respectively. The weight function  $w_i$  corresponds to the square root of the area  $A_i$  of a particle with centroid  $x_i$  and is depicted as a circle of the equivalent area with origin in  $x_i$ . The weighted distance  $wd_i$  is computed as a ratio of the Euclidean distance between the points  $y$  and  $x_i$  to the corresponding weight function. In the example illustrated above, the point  $y$  would belong to the cell generated by  $x_2$  since it has the smallest weighted distance to this point.

The weight function has been chosen based on the following reasoning: for every pair point – generator, an estimated distance is used to assign the point to the zone of influence of the nearest generator. Thus, the distance is a characteristic feature of the model. Since it is a 1-dimensional feature, the weight parameter has also to be reduced to the same dimension. Given the area of a particle as a weight, the desired weight function has been obtained by taking a square root of the weight.

Other weight functions have also been tested during the fitting procedure, but none of them has been able to capture the fracture surface features in an appropriate way. The fitting of the script parameters has been performed in a semi-automatic way. The borders of the dimples and Si particles lying at the core of every dimple have been traced with an electronic pencil in SEM fractographs. The parity between generated tessellations and segmented features has then been investigated by varying the weight function in the script. The highest parity, i.e. similar dimple density, mean values and distributions of principal size-shape characteristics, has been found by using a square root function.

## 4 Results and Discussion

---

The morphological impact of the eutectic Si on the mechanical performance of Al-Si alloys has been addressed from different perspectives, from virtual simulations to laboratory experiments. Thus, an extensive analysis of Si morphology, mechanical behavior and damage characteristics of the alloys under different loading conditions has been carried out. Besides, a model for the simulation of a system of dimples on the fracture surface of Al-Si alloys has been proposed. Furthermore, a methodology allowing for the effective study of the relation between the Si morphology and the eutectic fracture toughness based on simulated fracture surfaces has been described.

The following chapter can be divided into four major parts:

- The first part presents a simulation study that has been conducted by using the competitive stochastic growth model for the 3D morphology of the eutectic Si in Al-Si alloys in order to elucidate an influence of the Si connectivity on the mechanical behavior of the material. The results reported in Section 4.1 have also been summarized in publications [14,129,135].
- The second part comprises Sections 4.2 – 4.4. It is mostly concerned with the investigations of the mechanical behavior of Al-Si alloys under different loading conditions and its correlation with morphological properties of microconstituents such as Si particles and aluminium dendrites. The results have been partially published in [143].
- The third part is dedicated to the damage characterization in Al-Si alloys. In Section 4.5, the results of 2D and 3D damage characterization are presented. Thereafter, the limits and potentials of 2D damage investigations are discussed. Furthermore, fractographic observations on the specimens after the tensile loading are reported in Section 4.6.
- And finally, the model developed for the simulation of the system of dimples on the fracture surface of Al-Si alloys (as projected on a fractograph) is described in Section 4.7. The modeling approach enables an access to fractographic information in the eutectic region upon a potential fracture of a specimen without investigation of its actual fracture surface. Two examples of the application of the modelling results are

presented afterwards. The results reported in Section 4.7 have also been published in [133].

#### **4.1 Simulation study: Influence of Si morphology on compression strength**

The following section presents the results of the simulation study, where virtually generated structures of the eutectic Si enclosed in the Al matrix are first analyzed with respect to the morphological parameters of Si particles, and subsequently, the mechanical behavior of the eutectic phase is computed by FEM simulations.

It is well known that the mechanical behavior of Al-Si alloys has a morphological genesis, i.e. it is defined by the morphology and arrangement of the microconstituents [39], such as primary aluminium dendrites, silicon particles, intermetallic compounds and porosity. Since the major microconstituents of hypoeutectic Al-Si alloys are the primary  $\alpha$ -Al dendrites and the Al-Si eutectic, the properties of the material strongly depend on the morphology and the content of these two phases. By investigating the alloys via experimental methods (e.g. mechanical tests), it is difficult to assess the impact of every individual phase on the overall properties of the material. Therefore, the eutectic phase only has first been investigated by analyzing the mechanical behavior of 3D eutectic samples by means of FEM simulations.

The morphology of the eutectic Si exerts an influence on the load-carrying capacity, local stress state and fracture resistance of the structure [39]. In particular, the connectivity of Si particles has shown to strongly influence the mechanical behavior of Al-Si alloys [61,62]. The connectivity of microconstituents can only be determined in a volume [65], where it can be characterized either by the volume fraction of the largest single particle within the analyzed component [46] or by means of the Euler number [66]. The results of the connectivity estimation by the underlined methods are discussed later in this section.

In order to characterize the connectivity of the eutectic Si, 3D image data has to be analyzed. Therefore, two experimental samples with different connectivity of Si particles reconstructed by the FIB/SEM tomography have been used for the quantitative microstructure characterization and mechanical simulations. Besides, the virtual samples of the Al-Si eutectic phase with different Si morphologies have been generated by means of the Competitive Stochastic Growth Model (CSGM) introduced in [14]. Since the developed model is fitted to the experimental data, it allows to reduce drawbacks related to using idealized virtual models that usually miss microstructure irregularities and anisotropy. Moreover, the using of CSGM for studying the relations between the 3D morphology of the eutectic Si and the mechanical

response of the structure has the following advantages over 3D image data obtained via tomographic methods:

- The model allows to independently study the effect of particular features such as the connectivity of Si particles, branching degree and number of particles on mechanical response of the structure, which would not be possible in the context of casting material due to the difficulties in controlling every single feature during the casting process.
- The model enables a generation of a large amount of structures suitable for FEM simulations in a short time and cost-efficient way. Such synthetic data allows to avoid a time-consuming microstructure tomography procedure. Moreover, it does not require an image processing step which sometimes takes more time than the tomography itself.

Although the influence of the Si connectivity on the strength of different Al-Si alloys has been investigated over the past years, it has been limited to the comparison of the mechanical behavior of structures with interconnected Si particles versus structures with disconnected particles [61,62], where no quantitative evaluation of the connectivity has been made. Furthermore, Tolnai et al. [46] have used the volume fraction of the largest single particle within the analyzed component as a measure of the interconnectivity and have related it to the compression strength of macrosamples of AlMgSi alloys with a complex phase composition. Therefore, it can be suggested that the independent influence of the interconnectivity on the mechanical strength of the alloys has not been assessed.

In the present investigation, solely the impact of Si connectivity on the mechanical response of the eutectic structure will be evaluated without relation to any phase and/or chemical composition of the material. The advantages of the Euler number over the volume fraction of the largest single particle within the analyzed component for the characterization of the connectivity will be demonstrated.

The results of the simulation study have been summarized by Kruglova et al. in publication [135]. Sections 4.1.1 – 4.1.3 contain an excerpt from the section “*Results and Discussion*” of the underlined publication.

#### 4.1.1 Influence of connectivity and degree of branching of particles

The aim of this study is to describe and compare the influence of different Si morphologies on the mechanical behavior of the material in a qualitative way that gives important information on how a high-strength structure should look like. Therefore, to draw a conclusion on the morphological impact of Si on the material strength relying on results of FEM simulations, the following is assumed: By comparing mechanical performances of different morphologies, one structure is considered stronger than the other if its simulated stress-strain curve is located above the other.

The influence of the connectivity and the degree of branching of Si particles on the material strength is investigated by generating and analyzing nine virtual microstructures that have varying degrees of connectivity and branching. Note that branching and connectivity go hand in hand, wherefore the effect of branching and connectivity is analyzed simultaneously. The reason for this lies in the stochastic model. Decreasing a competition parameter ( $t_{external}$  or  $t_{internal}$ ) leads to higher branching and lower distances between branches. This increases the chance that they come very close to each other and merge together after the dilation (variant (2), see Section 3.7.1) of the simulated tree-like graph structure. Thus, a higher branching of Si particles results in increased connectivity.

The connectivity and the branching of particles are controlled via the external and internal competition parameters  $t_{external}$  and  $t_{internal}$ . Five virtual microstructures are generated by varying  $t_{external}$  and four by varying  $t_{internal}$ . Variations of the external and internal competition parameters are analyzed separately. The third important model parameter  $r_{cox}$  is fixed at  $r_{cox} = 55$  voxels (fitted value of this parameter, see Section 3.7.2) for all virtual microstructures. First, the parameter  $t_{external}$  is varied between 0.1 and 40 voxels while the parameter  $t_{internal}$  is set to 30 voxels (fitted value of this parameter, see Section 3.7.2). Figure 4.1 illustrates two extreme cases, one for  $t_{external}$  equal to 0.1 voxels and 40 voxels, respectively. Note that all remaining parameters (which are not listed here) are set equal to the model fitted to experimental sample no. 1. Morphological characteristics of the virtual microstructures are given in Table 4.1.

#### 4.1 Simulation study: Influence of Si morphology on compression strength

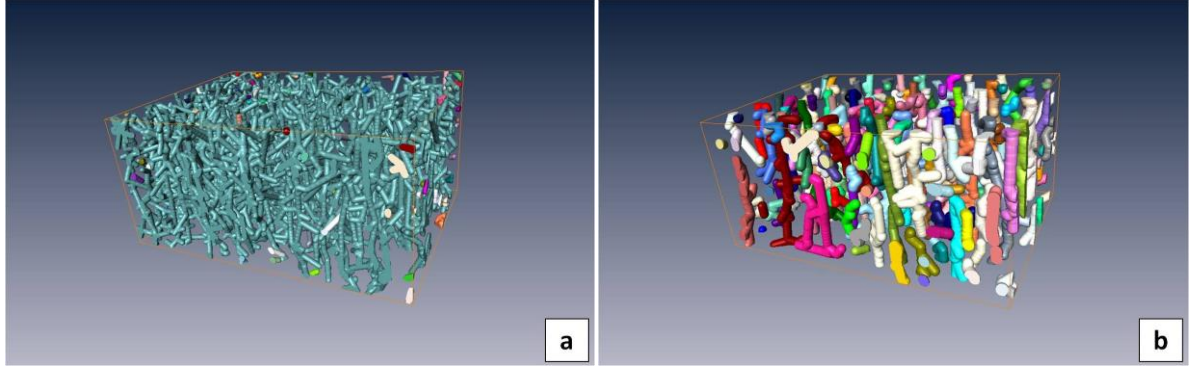


Figure 4.1: 3D images of simulation of eutectic Si with  $t_{external} = 0.1$  voxels (a) and  $t_{external} = 40$  voxels (b);  $t_{internal}$  is set to 30 voxels. When decreasing the external competition parameter  $t_{external}$ , a highly connected structure or network of the Si component is formed [135].

Table 4.1: Morphological properties of virtual microstructures generated by varying the external competition parameter  $t_{external}$ . With decreasing  $t_{external}$ , the volume fraction of the largest individual particle of Si ( $V_{MaxCluster}/V_{TotalSi}$ ) increases while the Euler number gets negative and decreases; both indicate an increase in the connectivity of Si [135].

Sample	$t_{external}$	Number of particles	$V_{MaxCluster}/V_{TotalSi}$	Euler number	Euler number density ( $m^{-3}$ )	Number of branches
sample no. 1	40	222	3	80	$5.55 \times 10^{15}$	1006
sample no. 2	20	178	7	-117	$-8.12 \times 10^{15}$	2064
sample no. 3	10	96	66	-425	$-2.95 \times 10^{16}$	3420
sample no. 4	5	79	90	-699	$-4.85 \times 10^{16}$	4650
sample no. 5	0.1	81	98	-1296	$-9.00 \times 10^{16}$	6725

As can be seen in Figure 4.1 and Table 4.1, decreasing  $t_{external}$  results in an increase in the volume fraction of the largest individual particle of Si and the number of branches and in a decrease in the number of particles and the Euler number. Due to the reduced external competition parameter, there is more space for branches to appear and to grow in-between neighboring particles: for instance, sample no. 5 has nearly 6 times more branches than sample no. 1. These complementary branches form new connections when filling the space and merging together after the dilation of the graph structure. As some particles merge together, the number of particles decreases and the volume of the largest particle increases: from 3% in sample no. 1 up to 98% in sample no. 5. Clusters in sample no. 1 (Figure 4.1 (b)) remain separated, whereas in sample no. 5 (Figure 4.1 (a)), there is only one large and highly connected Si particle in the center of the bounding box and several significantly smaller particles along the volume's edges, which are either cropped parts of the same particle or of

any other large particle. Furthermore, the Euler number gets negative indicating thereby an increase in connectivity and the presence of a network structure.

The influence of morphological changes on the mechanical behavior of the structures has been analyzed by comparing simulated stress-strain curves. Figure 4.2 shows stress-strain curves obtained by means of FEM simulations for the virtual microstructures and for the two experimental samples. Since all structures have shown nearly the same behavior in the elastic region, Figure 4.2 zooms in particularly on the plastic region, where the main difference in mechanical behavior appears. It can be easily seen that the strength of the virtual samples increases with a decreasing  $t_{external}$  and hence, with an increasing connectivity and branching of Si particles.

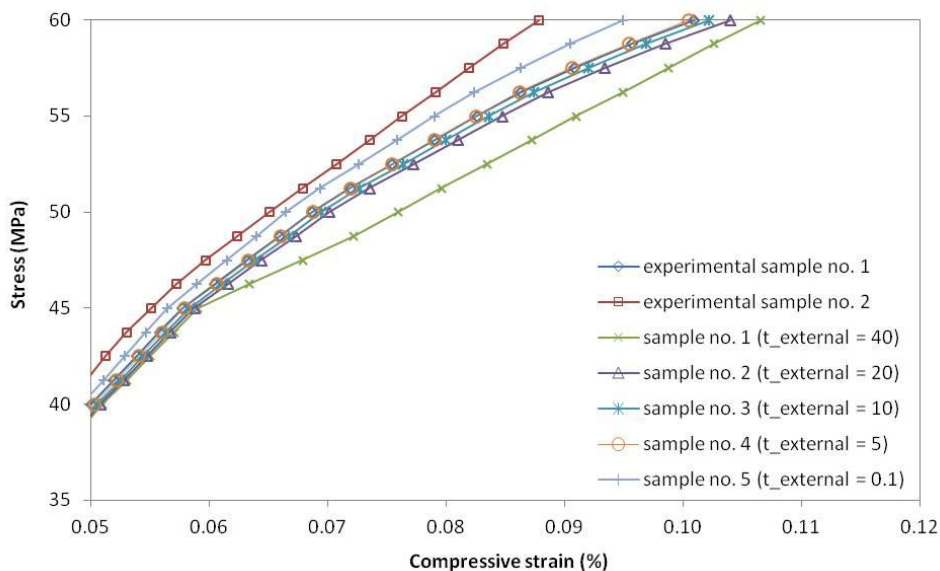


Figure 4.2: Finite element simulations on virtual structures with various external competition parameters and on two experimental samples: strength of the material increases with the connectivity of Si (i.e. with a decreasing  $t_{external}$  for virtual samples) [135].

Experimental sample no. 2 shows the highest strength as well as the most negative Euler number density:  $-2.61 \times 10^{17} \text{ m}^{-3}$  against  $-9.00 \times 10^{16} \text{ m}^{-3}$  for the most high-strength virtual sample no. 5. Experimental sample no. 1 has a positive value of the Euler number density equal to  $4.80 \times 10^{14} \text{ m}^{-3}$ . Therefore, a stress-strain curve of experimental sample no. 1 below the others would be expected. However, this is not the case. The behavior of experimental sample no. 1 is similar to samples no. 2, 3, and 4, but its strength is slightly overestimated due to the synthetically increased volume fraction of Si obtained as a result of a manual segmentation of the experimental images in contrast to the volume fraction of Si that is precisely matched in the virtual samples.

#### 4.1 Simulation study: Influence of Si morphology on compression strength

In the next part of the simulation study, the parameter  $t_{internal}$  is varied between 10 and 30 voxels (fitted value of this parameter, see Section 3.7.2). As shown in Figure 4.2, experimental sample no. 1 has exactly the same behavior as sample no. 4 with the parameters  $t_{internal}$  equal to 30 voxels and  $t_{external}$  equal to 5 voxels. Thus, we fix the parameter  $t_{external}$  to 5 voxels. In that case, the chosen value of the parameter  $t_{external}$  leads to the formation of network structures in all virtual microstructures since the dilation radius used for most of the simulations is slightly higher than the value of  $t_{external}$  used for a building the graph structure (prior to the dilation). Thus, after the dilation of the graph, many new connections are formed. In short, fixing  $t_{external}$  at 5 voxels yields highly connected microstructure which allows to analyze solely the effect of the degree of branching. Figure 4.3 shows two extreme cases, one for  $t_{internal}$  equal to 10 voxels and 30 voxels, respectively. Quantitative characteristics of the simulated structures are listed in Table 4.2.

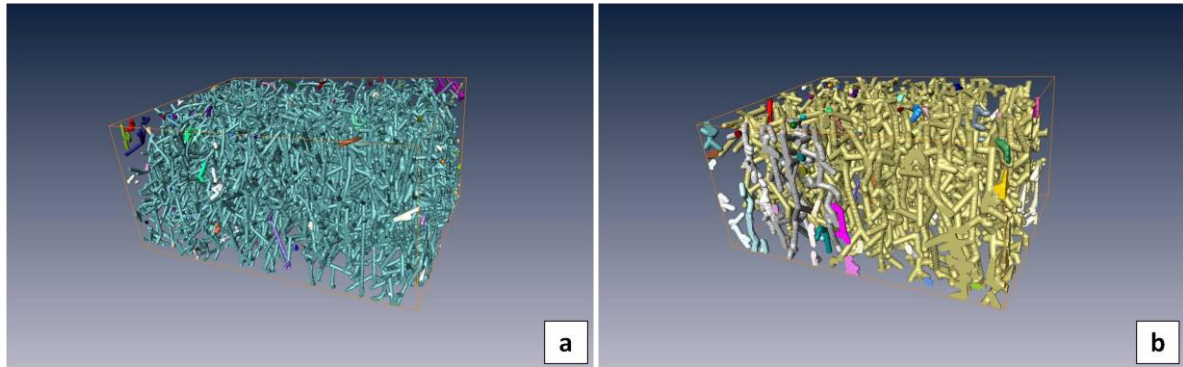


Figure 4.3: 3D images of virtual microstructures of eutectic Si with  $t_{internal} = 10$  voxels (a) and  $t_{internal} = 30$  voxels (b);  $t_{external}$  is 5 voxels. When decreasing the internal competition parameter  $t_{internal}$ , a highly connected and branched structure of the Si component is formed [135].

Table 4.2: Morphological properties of virtual microstructures generated by changing the internal competition parameter  $t_{internal}$ . With decreasing  $t_{internal}$ , the volume fraction of the largest individual particle of Si ( $V_{MaxCluster}/V_{TotalSi}$ ) slightly increases while the Euler number decreases; both indicate an increase in the connectivity of Si [135].

Sample	$t_{internal}$	Number of particles	$V_{MaxCluster}/V_{TotalSi}$	Euler number	Euler number density ( $m^{-3}$ )	Number of branches
sample no. 4	30	79	90	-699	$-4.85 \times 10^{16}$	4650
sample no. 6	25	77	94	-764	$-5.30 \times 10^{16}$	4925
sample no. 7	20	79	97	-981	$-6.81 \times 10^{16}$	5730
sample no. 8	15	93	96	-1965	$-1.36 \times 10^{17}$	9244
sample no. 9	10	131	98	-4151	$-2.88 \times 10^{17}$	14347

All structures are characterized by negative Euler numbers which indicates a network geometry. Analogous to the virtual microstructure in Figure 4.1 (a), they consist of a large particle in the center of the virtual microstructure, which comprises over 90% of the Si within the bounding box, and several particles along the sample's edges. The number of particles in Table 4.2 accounts mostly for those particles that are located along the edges of the bounding box; therefore, it is not relevant in this case. As for  $t_{external}$ , smaller values of  $t_{internal}$  lead to more space for new branches to be formed and to grow, building new connections: for example, sample no. 9 has nearly 3 times more branches and a 6 times higher Euler number density than sample no. 4.

By carrying out FEM simulations on the virtual structures with various internal competition parameters, a behavior similar to that of the structures with different external competition parameters can be observed (see Figure 4.4). This is, however, not surprising, since decreasing both parameters results in an increased connectivity. Similar to the previous case, a certain discrepancy appears during plastic deformation. Even if all structures show a high connectivity of the Si particles, which in itself implies a higher strength, the branching of the clusters does have an important influence. The connectivity and the branching of Si particles increase the strength of the material.

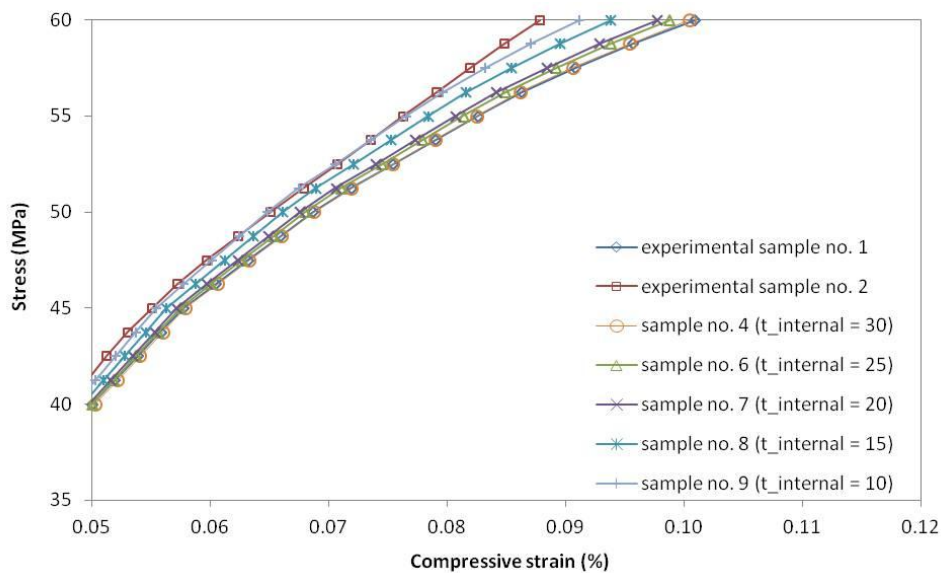


Figure 4.4: Finite element simulations on structures with various internal competition parameters and on two experimental samples: strength of the material increases with the connectivity and the branching of Si (i.e. with a decreasing  $t_{internal}$  for virtual microstructures) [135].

The stress-strain curve of experimental sample no. 2 partially overlaps with the curve of sample no. 9. Interestingly, both samples have a quite similar Euler number density:  $-2.61 \times 72$

#### 4.1 Simulation study: Influence of Si morphology on compression strength

---

$10^{17} \text{ m}^{-3}$  for experimental sample no. 2 against  $-2.88 \times 10^{17} \text{ m}^{-3}$  for sample no. 9, but correspond to different alloys. The stress-strain curve of experimental sample no. 1 with a positive Euler number density overlaps with the curve of sample no. 4; however, as has been mentioned before, the strength of experimental sample no. 1 has been slightly overestimated due to the increased volume fraction of Si.

In summary, it has been shown that the morphological variations generated by the stochastic model significantly influence the mechanical behavior at the microscale. A decrease of both external and internal competition parameters results in an increase in the material strength. On the morphological level, it implies that there is more space for new Si branches to appear and to grow. After the dilation step of the model, neighboring branches can merge together, forming thereby new connections. Thus, the strength of the material increases with the connectivity and the branching of Si particles.

The results of the present investigation fit the results obtained in [61] for an unmodified AlSi12 alloy; here, a strengthening effect of connected Si particles in an Al matrix has been presented. However, a higher connectivity of the strengthening phase reduces the ductility of the material [61]. For Al-Si alloys, there should be a balance between high strength and ductility. In [16], it has been shown that the modification of Al-Si alloys results in a moderated increase in strength while the increase in elongation is more significant. Thus, the ductility of the alloys is highly affected by the effect of modification and the morphology of microconstituents. In this respect, an optimal microstructure is rather characterized by the moderated strength and high ductility. Indeed, disconnected particles of Si can much better accommodate stress through the deformation of the eutectic Al and the movement of Si particles relative to each other, while in connected particles, the same stress is more probable to cause damage.

##### **4.1.2 Influence of number of particles in simply connected structures**

In this section, the influence of the number of Si particles on the material strength is analyzed. The external and internal competition parameters are chosen such that they preserve the connectivity of the particles, i.e. the neighboring particles separated in their graph structures also remain separated after the dilation. To vary the number of particles, the parameter  $r_{cox}$  varies between 55 (fitted value of this parameter, see Section 3.7.2) and 120 voxels, which results in 211 (see Figure 3.15 (b)) and 69 clusters (see Figure 4.5), respectively. Corresponding quantitative characteristics are given in Table 4.3.

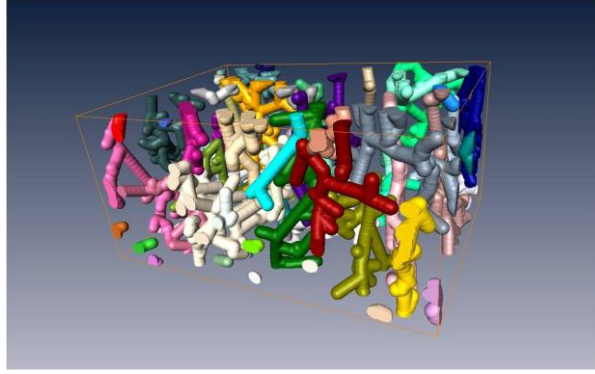


Figure 4.5: 3D image of simulation of eutectic Si with  $r_{cox} = 120$  voxels. When the parameter  $r_{cox}$  increases, the number of particles decreases while their branching increases [135].

Table 4.3: Morphological properties of virtual microstructures generated by varying values of  $r_{cox}$ . With increasing  $r_{cox}$ , the number of particles decreases while the number of branches per particle increases. The connectivity and the volume fraction of the largest individual particle of Si ( $V_{MaxCluster}/V_{TotalSi}$ ) undergo only minor changes. The connectivity is computed by subtracting the Euler number from the number of Si clusters [135].

Sample	$r_{cox}$	Number of particles	$V_{MaxCluster}/V_{TotalSi}$	Connectivity	Number of branches
sample no. 10	120	69	7	195	1411
sample no. 11	70	130	3	159	1158
sample no. 12	60	162	2	137	1200
sample no. 13	55	211	2	144	1683

Table 4.3 shows that an increase in the parameter  $r_{cox}$  corresponds to a decrease in the number of particles, since  $r_{cox}$  controls the density of particles in the stochastic model. At the same time, the number of branches per single particle increases. The volume fractions of the largest Si particle as well as the connectivity of particles remain (merely) constant for all samples. This means that the effect of the connectivity on the mechanical behavior can be neglected and the main difference in the behavior of the samples is mainly determined by the number of particles.

By applying FEM simulations to the virtual microstructures with various values of  $r_{cox}$ , as in the previous section, a similar behavior in the elastic region and a discrepancy in the course of plastic deformation can be observed (see Figure 4.6). The strength of the material increases with the number of particles. However, microstructures with  $r_{cox}$  of more than 70 voxels seem to be unrealistic, since their behavior significantly differs from the one of experimental

## 4.1 Simulation study: Influence of Si morphology on compression strength

sample no. 1 (analogue of virtual sample no. 13 in Table 4.3). It implies that isolated and highly branched Si clusters are hardly probable to occur in the material. Experimental sample no. 1 shows the highest strength.

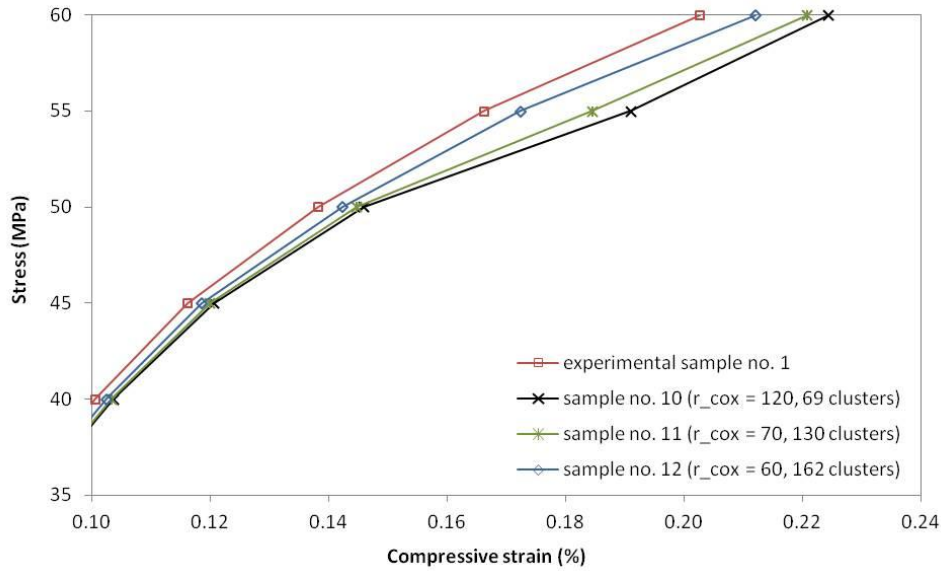


Figure 4.6: Finite element simulations on structures with various values of  $r_{cox}$  and on experimental sample no. 1: strength of the material increases with the number of particles (i.e. with a decreasing  $r_{cox}$  for virtual microstructures) [135].

Thus, in the case where the connectivity is not concerned, for example, in disjoint or simply connected structures which consist of disconnected Si particles, the number of particles plays a significant role in the material strength, i.e. the strength increases with the number of particles. However, it still remains below the strength of network structures.

### 4.1.3 Evaluation of Si connectivity in Al-Si alloys

In the simulation study, the connectivity of Si is evaluated by two parameters: The Euler number (Euler number density) and the volume fraction of the largest individual particle of Si relative to the total volume of Si within the bounding box, as in [46]. Figure 4.7 shows the evolution of both characteristics with the external competition parameter. When  $t_{external}$  is decreasing, on the one hand, the Euler number turns negative and increases in the absolute value which implies the presence of a network structure and, on the other hand, the volume fraction of the largest individual particle of Si approaches 100% which indicates that most of the Si component within the bounding box is comprised in only one connected particle. The mechanical strength increases with the connectivity of Si, i.e. with a decreasing Euler number and an increasing volume fraction of the largest individual particle of Si (see Figure 4.2 and Table 4.1).

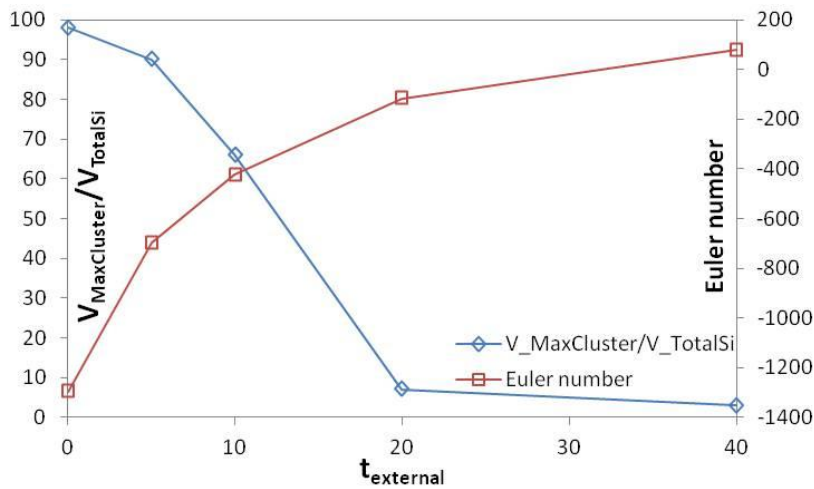


Figure 4.7: Evolution of the Euler number and the volume fraction of the largest individual particle of Si via the external competition parameter: both parameters reflect the connectivity changes [135].

However, Figure 4.8 illustrates that the volume fraction of the largest individual particle of Si ( $V_{\text{MaxCluster}}/V_{\text{TotalSi}}$ ) does not always reflect the connectivity changes. Here, when  $t_{\text{internal}}$  is decreasing, the volume fraction of the largest individual particle of Si does not change significantly which gives the illusion that the connectivity and strength remain constant, although the material strength increases (see Figure 4.4 and Table 4.2). At the same time, the Euler number increases by almost six times in absolute values and thus, indicates an increase in connectivity and material strength.

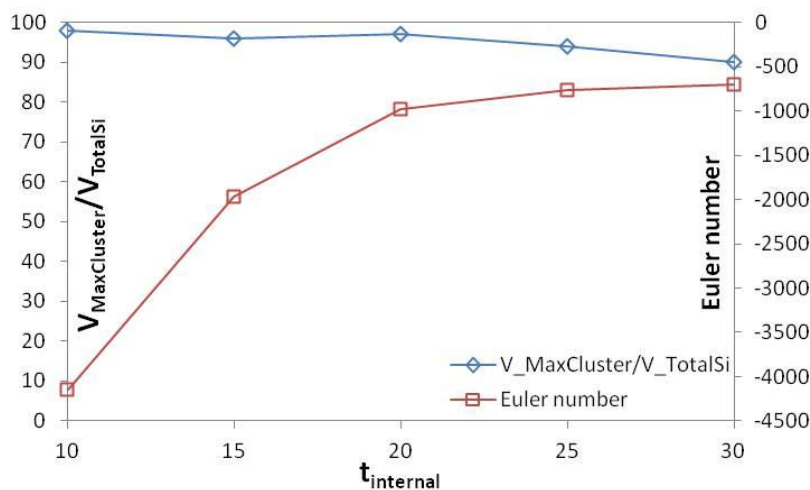


Figure 4.8: Evolution of the Euler number and the volume fraction of the largest individual particle of Si via the internal competition parameter: only the Euler number reflects the connectivity changes [135].

Thus, the Euler number is shown to be highly effective in characterizing the connectivity, as it provides additional information on topological properties of a structure which is not captured

when characterizing the connectivity by the volume fraction of the largest Si particle. Since the strength of the structure increases with decreasing the Euler number, it can be suggested that the Euler number is a relative, yet effective measure of the strength when it is necessary to compare the structures without mechanical tests.

### 4.1.4 Stress-strain state in simulation volume

As has been observed from the results of FEM simulations, an onset of the plastic deformation in the material occurs at much smaller strain levels than during the real mechanical tests. This is related to the inhomogeneous distribution of strain in the Al matrix within a simulation volume, where certain regions can pursue the plastic deformation while the overall material still remains elastic. A similar effect has been reported by Joseph et al. [12], who have found a localization of strain between Si particles or within Si clusters resulted from the onset of plastic flow at sharp corners of the particles. Although on the macro-scale only an averaged effect of the deformation in different phases is observed, on the micro-scale, an input of plastified regions in the Al matrix is much more pronounced. Thus, an onset of the plastic deformation on the stress-strain curves from FEM simulations is observed at very small strain levels already.

Evidently, the state of stress in Si particles and their fracture susceptibility in different morphological scenarios will vary due to the different load transfer from the matrix to Si particles, which depends on the particle size, shape, orientation and spatial arrangement (incl. the connectivity). FEM simulations have been shown to be highly effective in characterizing the mechanical behavior of the virtually designed and experimentally obtained samples of Al-Si eutectic in 3D, and thus complementing the results of FEM simulations performed using a 2D multi-particle model [9] and microstructure based model [12] of Al-Si eutectic phase. 3D FEM simulations have allowed to investigate the influence of the connectivity and branching of Si particles which is not accessible using 2D characterization techniques. Thus, 3D simulations deliver more accurate predictions of the stress state as compared to 2D simulations since they take into account 3D complexity of the structure. On the other hand, 2D FEM simulations have enabled to study the impact of morphological properties of Si particles (size, shape and orientation) on their stress state and as a consequence, fracture susceptibility in simply connected structures. In particular, the highest stress level has been detected in the particles oriented at  $0^\circ$  and  $90^\circ$  to the compression loading axis and exhibiting a higher aspect ratio [9], where the highest stress concentration within an individual Si particle has been found at sharp edges and bent regions [12]. However, one has to bear in

mind that although 2D FEM simulations are in general consistent with experimental observations, they have a limited predictive power in relation to complex irregular or network structures. Moreover, the discussed 2D and 3D simulations do not take into account the residual stresses in the particles and their failure criteria [12].

In order to deduce a morphological scenario of an optimal structure of Al-Si alloys for a certain application, further investigations are required: in particular, the investigations of the damage mechanism, consideration of residual stresses in the particles and their failure criteria during FEM simulations as well as analysis of properties and mechanical impact of the primary phase and its interplay with the eutectic phase morphology.

## **4.2 Micrographic analysis of eutectic phase in Al-Si alloys**

The following section is devoted to the micrographic analysis of the eutectic phase in Al-Si alloys. The results of the micrographic characterization of the alloys have been summarized by Kruglova et al. in publication [143]. The following section contains an excerpt from the section “*Results and discussion*” of the underlined publication.

Although the following section presents the micrographic analysis of the eutectic phase solely, it is important to note that the microstructure of the alloys consists of two major phases, primary Al dendrites and Al-Si eutectic. The alloys have de facto a slightly hypoeutectic microstructure with the amount of Al dendrites up to 30%. Therefore, one should bear in mind when interpreting the results of mechanical tests that the results issued from laboratory experiments and computer simulations cannot be compared directly: Compression and tension tests are performed on the two-phase specimens while FEM simulations are limited to the eutectic phase only.

### **4.2.1 As-cast Al-Si alloys**

The optical micrographs in Figure 4.9 show the (a) unmodified and (b) Sr-modified AlSi12 alloys. The modified structure is very fine and homogeneous: Si particles have mostly spherical cross sections that are simply the cuts through fibrous or coral-like particles in 3D [5]. The unmodified alloy exhibits less homogeneous Si profiles ranging from spherical to elongated ones as well as profiles of irregular shape. Such cross sections belong to the plate-like particles that are typical of unmodified Al-Si alloys [5]. Intermetallic phases are not observed. Although the unmodified Si particles are normally coarser than those of the

## 4.2 Micrographic analysis of eutectic phase in Al-Si alloys

modified alloy, both investigated structures are relatively fine because of the small dimensions of the ingots and high cooling rates during the casting in the permanent mold.

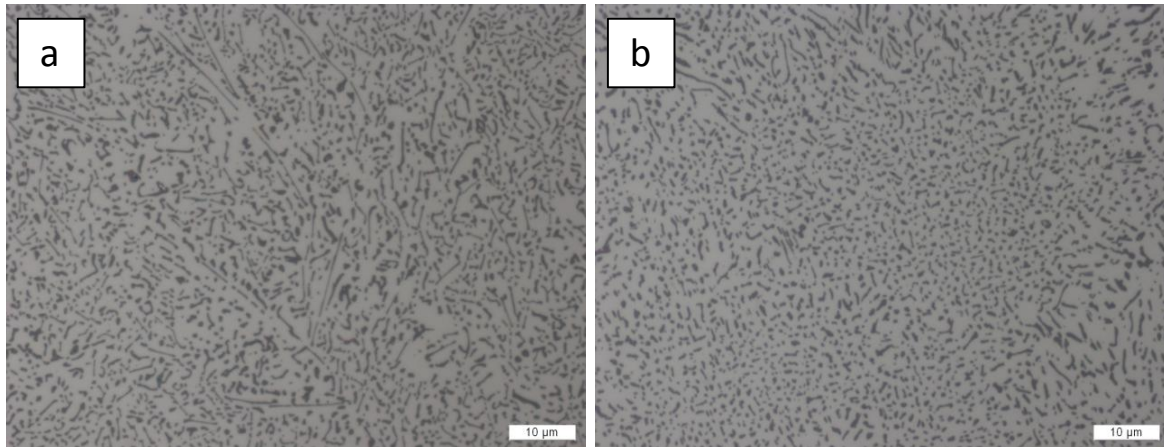


Figure 4.9: Optical micrographs of the (a) unmodified AlSi12 and (b) Sr-modified AlSi12, zoom in the eutectic region: The eutectic consists of dark-grey Si particles encompassed in the light Al matrix [143].

The optical micrograph of the Sr-modified AlSi12Mg0.3 alloy is shown in Figure 4.10 (a). The alloy is inhomogeneously modified, since the regions with the fine homogeneous eutectic alternate with the areas where Si has a coarse structure and irregular shape. Thus, two classes of Si particles can be distinguished in the alloy: fine modified particles and coarse particles with an irregular shape. The latter are mostly located at the eutectic grain boundaries. The grain boundaries can usually be identified by the coarse Si particles, inclusions of intermetallic phases and increased distance between the particles [119,144].

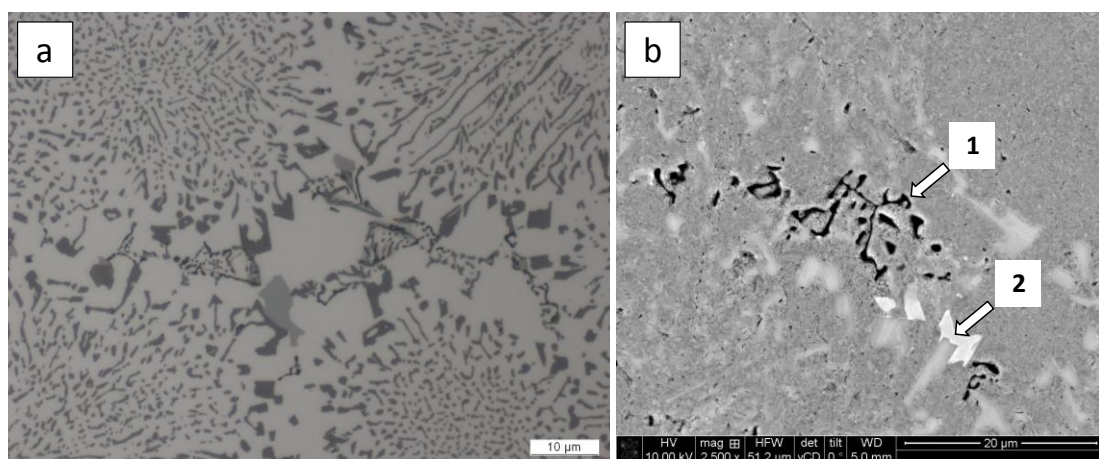


Figure 4.10: (a) Optical micrograph of the Sr-modified AlSi12 containing 0.31% of Mg, zoom in the eutectic region: the eutectic consists of Si particles (dark-grey), coarse inclusions (light-grey) and “Chinese-script” precipitates (black) encompassed in the light Al matrix. (b) SEM micrograph of the same alloy showing two types of inclusions used for the EDX analysis: black “Chinese-script” and light-gray coarse precipitates pointed by arrows (1) and (2), respectively.

Besides the eutectic Si particles, the eutectic phase contains two more types of inclusions: black “Chinese-script” and medium-gray coarse inclusions pointed by arrows (1) and (2) in Figure 4.10 (b), respectively. The EDX analysis conducted on the underlined inclusions have shown that the “Chinese-script” precipitates contain oxygen, Mg, Si and a large amount of Al that comes most probably from the background matrix signal. The atomic percents of Mg and Si are 3.95 at.% and 7.40 at.%, respectively, which differ from the atomic ratio of the  $Mg_2Si$  composition. It is known that  $Mg_2Si$  precipitates appear as a black “Chinese-script” in the optical micrographs of Al-Si-Mg alloys [25]. Therefore, it can be suggested that the observed inclusions are the precipitates of  $Mg_2Si$  phase since both elements, Mg and Si, have been identified within the particles exhibiting a typical  $Mg_2Si$  shape. The observed deviations in the chemical composition might result from the interference of the matrix signal since the inclusions have been very fine.

The light-gray coarse precipitates cannot be explicitly classified. According to the EDX analysis, these inclusions contain Fe, Mg, Al and Si (5.87 at.% of Fe, 18.06 at.% of Mg, 48.89 at.% of Al, and 27.18 at.% of Si). This composition can most closely be associated with  $FeMg_3Si_6Al_8$  precipitates observed in Al-7.0Si-0.3Mg alloy modified with Na [115]. According to [115], the second phase inclusions in this alloy are represented by dark grey Si particles, light-gray script of  $FeMg_3Si_6Al_8$  precipitates, medium-gray blades of  $Fe_2Si_2Al_9$  precipitates and black  $Mg_2Si$  particles as observed in the light optical micrographs [115].

Iron is the most frequent impurity in Al-Si alloys. It has a low solubility at room temperature and therefore, forms various intermetallic phases with the alloy elements [29,145]. Thus, possible intermetallic phases are not limited to only one chemical composition. So, for example, Fe-rich  $\alpha$ - and  $\delta$ -phases have been found in Sr-modified Al-Si alloys. The identified phases have shown various stoichiometry and morphology: Fe-rich  $\alpha$ -phases precipitate in form of blades whereas  $\delta$ -phases are rather platelet-like. In optical micrographs, clusters of  $\alpha$ - and  $\delta$ -phases are observed as “Chinese-script” and lamellae particles, respectively. Very often, the clusters constituted of individual particles in 2D appear to be interconnected in 3D. These phases precipitate mostly at the eutectic grain boundaries [119,144].

#### **4.2.2 Solution treated Al-Si alloys**

The optical micrographs in Figure 4.11 show the (a) unmodified and (b) Sr-modified AlSi12 alloys after the solution treatment at 540 °C for 4 hours and quench in boiling water. Both structures have undergone a considerable agglomeration and spheroidization of Si particles.

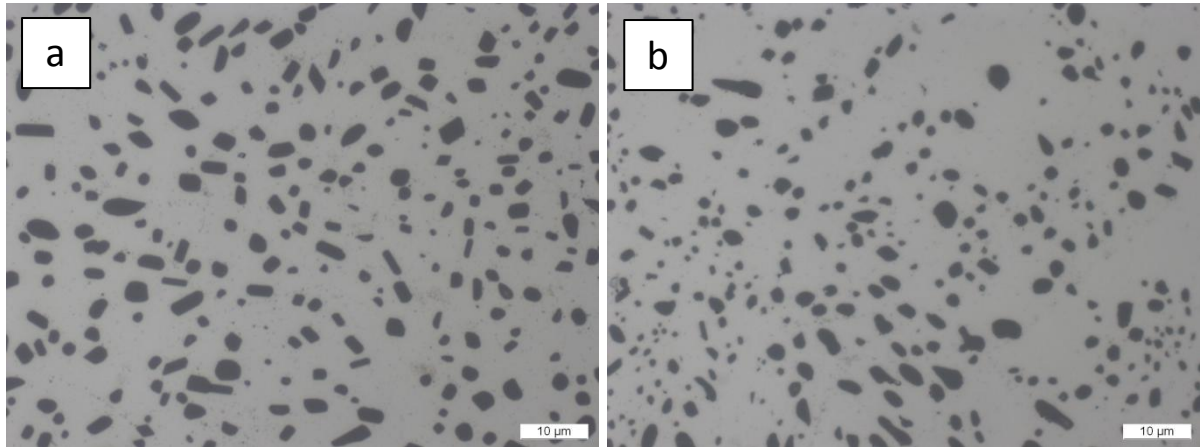


Figure 4.11: Optical micrographs of the (a) unmodified AlSi12 and (b) Sr-modified AlSi12, both are solution heat treated at 540 °C for 4 hours and quenched in boiling water. In both alloys Si particles have been agglomerated and spheroidized. The particles are much coarser in comparison to the corresponding structures of the as-cast alloys [143].

As reported in [22], Sr modification influences the kinetics of Si spheroidization and coarsening during the solution heat treatment in such a way that modified Si particles have more propensity for the spheroidization due to their initial smooth fibrous shape. On the contrary, unmodified Si plates are more resistant to shape changes and thus, rather undergo coarsening and, to a lesser extent, spheroidization. The authors also distinguish a shape-size diversity of Si particles in unmodified alloys to be an additional driving force for the coarsening. However, both structures in Figure 4.11 do not exhibit any pronounced difference in shape and/or size of the particles. Even if any difference did exist at a first stage of the temper, it should have been diminished after 4 hours since, on the one hand, both alloys have a priori shown a similarly fine eutectic structure, and on the other hand, the solution treatment time has been too extended for such small samples. Therefore, a similar mechanical behavior of the alloys after the solution treatment can be expected.

An optical micrograph of the Sr-modified AlSi12Mg0.3 alloy after the solution treatment is shown in Figure 4.12 (a). Similarly to the previous alloys, Si particles have been spheroidized and agglomerated. The effect of agglomeration of neighboring coarse particles and dissolution of smaller particles is well observed in the micrograph. Mg<sub>2</sub>Si particles have been dissolved and all the magnesium has moved to Al solid solution. Indeed, Mg content in the alloy is 0.3% that is lower than the amount of Mg which can be moved to solid solution at common solution treatment temperatures. In particular, during the solution treatment at 540 °C, up to 0.6% of Mg can be moved to Al solid solution [22].

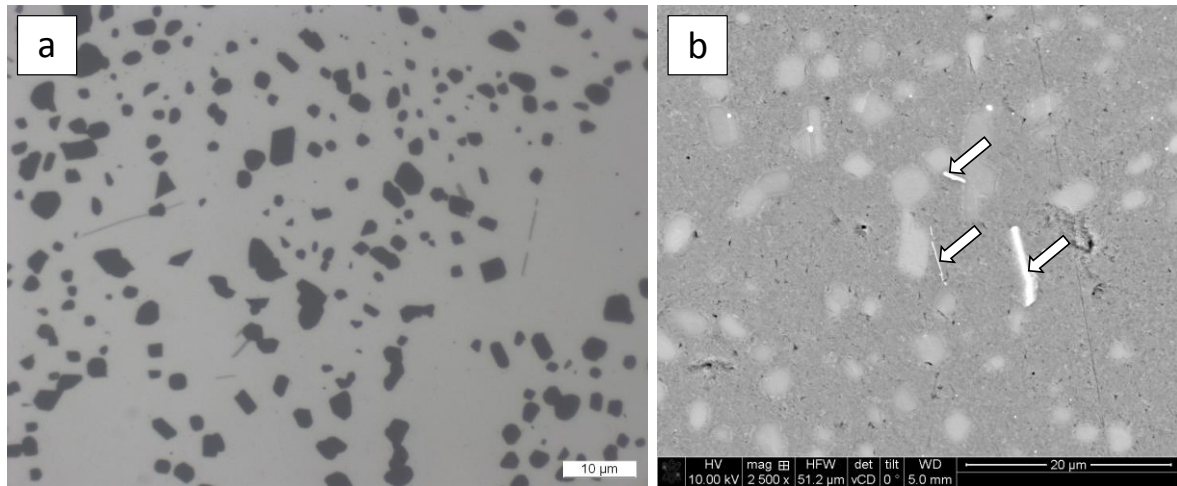


Figure 4.12: (a) Inhomogeneously modified AlSi12 containing 0.31% of Mg, solution heat treated at 540 °C for 4 hours, quenched in boiling water. The eutectic consists of Si particles (dark-grey) and needle-like inclusions (light-grey) in the light Al matrix. During the solution treatment, neighboring coarse particles have been agglomerating whereas smaller particles have been dissolving. (b) SEM micrograph of the same alloy showing the needle-like inclusions (pointed by arrows) used for the EDX analysis.

However, the intermetallic phases can still be found in the microstructure, but their morphology has eventually changed. In Figure 4.12 (a), fine needle-like precipitates are observed in light-grey. According to the EDX analysis, these precipitates (see Figure 4.12 (b)) contain Fe, Al and Si (17.30 at.% of Fe, 66.39 at.% of Al, and 16.31 at.% of Si). This composition can most closely be associated with  $\text{Fe}_2\text{Si}_2\text{Al}_9$  precipitates observed in the solution heat treated Al-7.0Si-0.3Mg alloy modified with Na [115]. According to [115], the second phase inclusions in this solution treated alloy are represented by Si particles and blades of  $\text{Fe}_2\text{Si}_2\text{Al}_9$  precipitates as observed in the light optical micrographs [115]. Guiglionda and Poole [84] have also found large thin plates of intermetallics appearing as fine lines of up to 25  $\mu\text{m}$  length and 0.5  $\mu\text{m}$  width in micrographs of Sr-modified eutectic Al-Si alloy after the heat treatment in similar conditions. However, these intermetallics have been attributed to  $\text{FeSiAl}_5$  ( $\beta$  phase). Closset and Gruzleski [29] have also identified needle-like  $\text{FeSiAl}_5$  in the heat treated Al-Si-Mg alloys modified with Sr.

### 4.2.3 Referencing of samples

In the following, to avoid long specifications of samples by their chemical composition and applied treatment, the following brief references are used: 2X, 3X and 7X represent the unmodified, the Sr-modified Al-Si alloys and the inhomogeneously modified Al-Si alloys with addition of 0.31% of Mg, respectively; AC and ST distinguish between the as-cast and the solution treated alloys, respectively.

### 4.3 Mechanical behavior of Al-Si alloys

The mechanical behavior of as-cast and solution treated Al-Si alloys has been investigated under compression and tension loading. The corresponding stress-strain curves are shown in Figure 4.13 and Figure 4.14, respectively. The results of the mechanical characterization have been summarized by Kruglova et al. in publication [143]. The following section contains an excerpt from the section “*Results and discussion*” of the underlined publication.

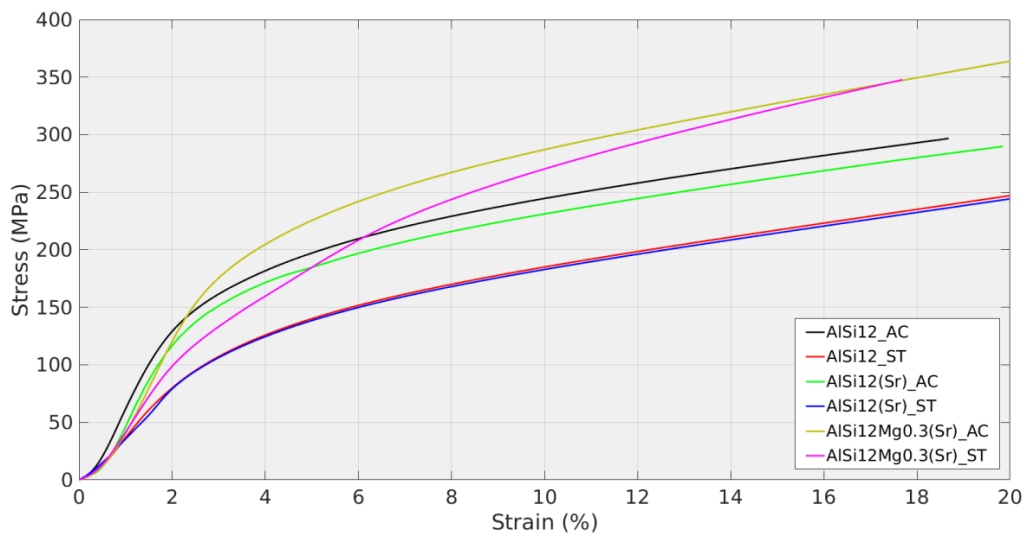


Figure 4.13: Averaged engineering stress-strain curves obtained from the compression testing of AlSi12 (2X), AlSi12(Sr) (3X) and AlSi12Mg0.3(Sr) (7X) alloys (extended from [143]).

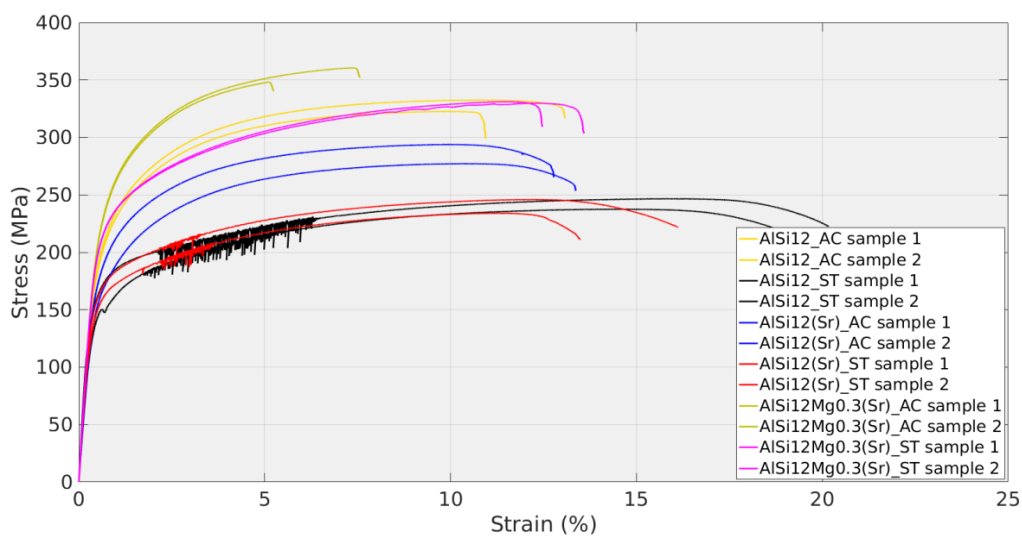


Figure 4.14: Engineering stress-strain curves obtained from the tensile testing of AlSi12 (2X), AlSi12(Sr) (3X) and AlSi12Mg0.3(Sr) (7X) alloys. The oscillations on the curves of the solution treated alloys, 2X and 3X, are due to the calibration of the testing machine to a softer material, and can therefore be neglected (extended from [143]).

As can be seen in Figure 4.13 and Figure 4.14, the as-cast samples exhibit a higher strength than the solution treated samples of the corresponding alloys. During the solution treatment, Si particles undergo disintegration and spheroidization, which lead to an unavoidable reduction of the load-carrying capacity of the structure [62]. According to Requena et al. [61], the stiff Si network in the ductile Al matrix increases the load transfer from the matrix to the reinforcement, which improves the strength. Therefore, the disintegration of the network of Si particles and as a consequence, the reduction of their connectivity induced by the heat treatment has an adverse effect on the strength of Al-Si alloys, although reducing the strength it improves their ductility.

The experimental results are also consistent with the observations on the influence of the Si connectivity on the compressive strength of Al-Si alloys reported in Section 4.1. In contrary to the partially interconnected Si particles in the as-cast alloys, Si particles in the solution treated alloys are simply connected (see section 4.5.2 for the 3D reconstruction of Si particles in the investigated alloys). Thus, the load transfer from the matrix to these particles is lower than the one to the Si particles with a higher connectivity. Hence, the strengthening effect of the spheroidized Si in comparison to the more complex-shaped particles is also reduced. The reduction of the load-bearing capacity of spherical particles in relation to the high aspect ratio particles (e.g. fibrous or plate-like particles) has also been discussed in [12,83,84].

At the same time, the ductility of the solution treated samples is higher than the ductility of the as-cast alloys. Similar observations have been reported by Guiglionda and Poole [84], who have examined an impact of the heat treatment on Si morphology and ductility of Al-Si eutectic alloys. In general terms, the fragmentation of Si particles with the subsequent spheroidization during the solution heat treatment is beneficial for the ductility of the material [22,53].

The Mg-containing samples, 7X, exhibit a higher tensile strength than Mg-free alloys, 2X and 3X, both in the as-cast condition and after the thermal treatment, respectively. In the as-cast state, the strengthening effect is due to the presence of  $Mg_2Si$  precipitates in the Al matrix which create barriers to dislocation movement. The strength of Al-Si-Mg alloys increases with Mg content, but at the same time their ductility decreases [20]. During the solution treatment, Mg moves to the solid solution [22] which leads to the solid solution strengthening: The presence of Mg atoms in the host Al matrix increases the local strains which also hinder the motion of dislocations. It is important to note that in a general industrial practice, after the solution treatment and quenching, the age hardening procedure is applied in order to obtain a

maximum strengthening effect [21]. During the aging, precipitate nuclei coherent with the matrix are formed at a first stage. Upon their growth, the coherence strain steadily increases and with it, the precipitate strengthening effect. As soon as the precipitate loses the coherence with the host matrix, no further strengthening occurs [19]. At the same time, the Mg-containing samples exhibit a lower ductility than the Mg-free samples. It is well known that Mg additions cause the reduction of the ductility due to the formation of intermetallic compounds exerting an adverse effect on the elongation to fracture [29,41].

There are two more observations that can be made in Figure 4.14. First, in contrary to the commonly accepted superiority of the strength characteristics and ductility of modified alloys as compared to unmodified ones, the unmodified alloy, 2X\_AC, exhibits a higher strength than its modified counterpart, 3X\_AC. The second observation is that in the ST condition, this difference disappears and the alloys show similar strength characteristics. Although it has been expected that the alloys with a similar microstructure (see Figure 4.11) have a similar mechanical behavior, the alloy 2X\_ST shows a higher elongation to fracture than the alloy 3X\_ST. Furthermore, the stress-strain curves of both alloys show strong oscillations that are most probably due to the calibration of the testing machine to a softer material and can therefore be neglected. To exclude the possibility that such a behavior is observed due to statistical issues, complementary tensile tests have been carried out. The results of the tensile tests performed on the modified and unmodified Al-Si alloys in the ST and AC conditions are shown in Figure 4.15 and Figure 4.16, respectively.

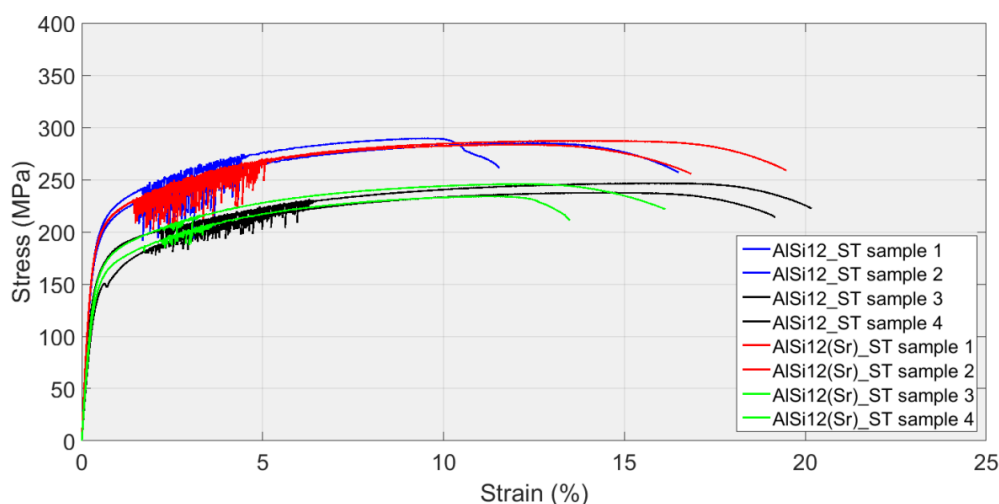


Figure 4.15: Engineering stress-strain curves obtained from the tensile testing of the unmodified (2X\_ST) and Sr-modified (3X\_ST) Al-Si alloys. The complementary tests have been carried out on samples 1 and 2 showing higher strength characteristics than the original samples 3 and 4 for both alloys. The oscillations are still present on the curves [143].

As can be seen in Figure 4.15, the complementary tests (samples 1 and 2) have yielded higher strength characteristics than the original tests (samples 3 and 4). However, the oscillations are still present on the curves but in contrary to the previous results, the stress-strain curves from the complementary tests show that the alloy 3X\_ST has a higher elongation to fracture than the alloy 2X\_ST. Yet, as expected, the alloys exhibit similar average strength characteristics and elongation to fracture. The quantitative data on the average mechanical properties of the investigated alloys derived from the stress-strain curved is shown in Table 4.4 and is discussed in Section 4.4.

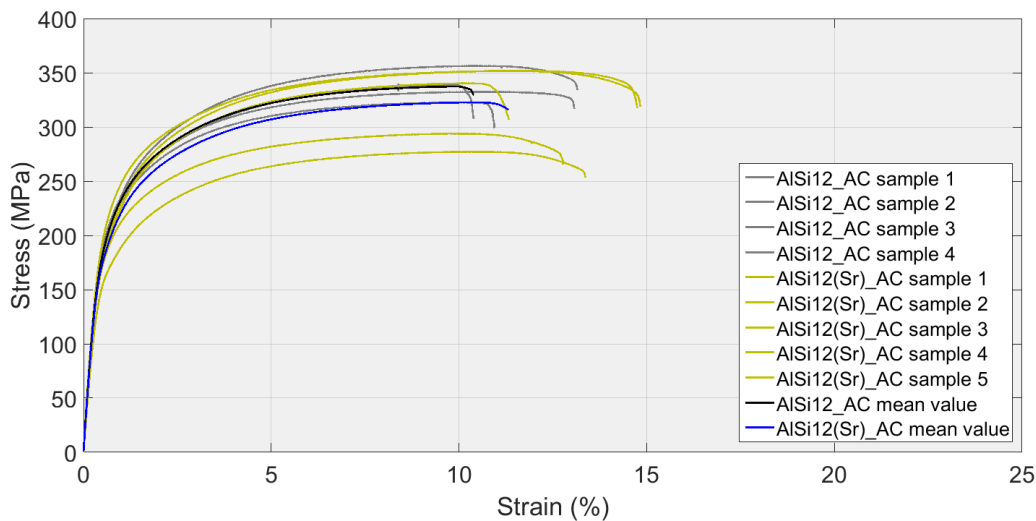


Figure 4.16: Engineering stress-strain curves obtained from the tensile testing of the unmodified (2X\_AC) and Sr-modified (3X\_AC) Al-Si alloys. Sample 5 of the unmodified AlSi12 alloy has been excluded on purpose due to its failure at the very beginning of the experiment and hence, unrepresentative behavior. On the average, the alloy 2X\_AC has a higher tensile strength than the alloy 3X\_AC. Note that the average stress-strain curves are computed for the stress values only [143].

Both the unmodified (2X\_AC) and modified (3X\_AC) Al-Si alloys have a similarly fine structure of the eutectic Si (see Figure 4.9). Therefore, as has been expected, both alloys also have a similar mechanical behavior under compression and tension loading, though with a slight strength superiority of the alloy 2X\_AC. As can be clearly seen in Figure 4.16, on the average, the strength of the unmodified alloy is higher than the strength of the modified alloy. The same observations have been made by analyzing the mechanical behavior of the alloys under compression loading (see Figure 4.13). However, metallographic observations of the eutectic Si morphology as well as the state-of-the-art in the field of Sr modification of Al-Si alloys [5,16,22,29,40,41] argue for the expectations of the opposite behavior. According to Hafiz and Kobayashi [39], more fine and regular modified particles have less stress concentration sites and can carry the load much better due to the more gradual damage

evolution. It can therefore be suggested that the clue to the understanding of the observed phenomena lies in the three-dimensional nature of the Si structure and/or properties of the primary aluminium phase.

Considering the influence of the primary aluminium phase, it has to be taken into account that the macro samples of Al-Si alloys used for the mechanical tests do not consist of the eutectic phase only but contain up to 30% of Al dendrites. The modification of hypoeutectic Al-Si alloys results in shifting the eutectic point toward a higher Si level and as a consequence, a higher amount of the primary phase in the solidified microstructure [16–18]. Liao et al. [45] have observed that the amount of the primary aluminium in the near-eutectic Al-Si alloys increases with increasing Sr content, in particular, when the amount of Sr is above 0.015%. However, this effect of the modification has not been observed in the investigated alloys. On the contrary, no significant difference in the primary phase content between the modified and unmodified alloys has been detected in the present investigation: The amount of Al dendrites in the modified alloy with 0.02% of Sr is even slightly lower than in the unmodified one (26% versus 28%, respectively), although they are both higher than the equilibrium level. Therefore, it can be concluded that a higher amount of the primary phase with respect to the equilibrium level is related to the high cooling rate during the solidification. This result is in accordance with the observations reported in [18]. Thus, it is likely that the effect of the high cooling rate dominates the effect of the modification, at least, in the present investigation.

Some researchers [43,51–54] suggest that both microconstituents, Al dendrites and Si particles, play an important role for the tensile properties and fracture behavior of the alloys. Therefore, the dendrite arm spacing (DAS) characterizing the size of the primary aluminium phase has been determined. It has turned out that DAS in the unmodified alloy (2X\_AC) is lower than the one in the modified alloy (3X\_AC) and is equal to  $14.08 \pm 2.01 \mu\text{m}$  and  $19.28 \pm 3.07 \mu\text{m}$ , respectively. In general, the refinement of the primary phase corresponds to the improvement of tensile properties [43], which agrees well with the experimental observations.

To analyze the impact of the three-dimensional structure of Si particles, the connectivity of the eutectic Si in both alloys has to be determined. The only available 3D data of the eutectic structure in the investigated alloys have been the samples reconstructed after the mechanical tests and used to characterize 3D damage within the eutectic phase under tension and compression loading (see Section 4.5.2). To measure the initial (prior to deformation) connectivity of Si in the investigated alloys, the cracks in Si particles induced by the mechanical loading have been filled using image editing methods. In so doing, the computed

connectivity could represent the connectivity of Si particles in the undamaged state [91]. Here, the connectivity of the eutectic Si is assessed with the help of the Euler number density [65,66]. The image analysis software MAVI [67] provides the values of the sample volume, the Euler number and the corresponding Euler number density of Si particles in the deformed samples. However, to compute the Euler number density of Si particles in the undeformed samples, the estimated Euler number has to be divided by the initial (undeformed) volume of the reconstructed samples. The detailed derivation of the relation between the initial volume,  $V_0$ , the deformed volume,  $V$ , where  $V = V_0 + \Delta V$ , and the strain level,  $\Delta L_l/L_0$ , of the samples given the Poisson ratio of Al-Si alloys,  $\nu$ , is presented in Appendix (see Section 6.1). Hereby, the initial volume of the reconstructed samples 2X\_AC and 3X\_AC has been estimated using Equation 4.1:

$$\frac{\Delta V}{V_0} \approx (1 - 2\nu) \frac{\Delta L_l}{L_0} \quad 4.1$$

After having computed the initial volume of the samples,  $V_0$ , using Equation 4.1, the Euler number density has been determined. According to the results of the simulation study in Section 4.1.2, a positive value of the Euler number density of  $4.41 \times 10^{17} \text{ m}^{-3}$  in the eutectic phase of the sample 2X\_AC against  $2.04 \times 10^{16} \text{ m}^{-3}$  in the eutectic phase of the sample 3X\_AC indicates a higher density of Si particle clusters in the unmodified alloy, and as a consequence, a higher strength of the material. This result also agrees well with the experimental observations.

Thus, it can be suggested that the strength characteristics observed in the modified and unmodified alloys have resulted from the combined effect of the eutectic Si morphology and the size of the primary aluminium dendrites. In general, the microstructure refinement, which implies the refinement of both phases, is beneficial for the strength [6,105] and ductility [53] of Al-Si alloys. In particular, the reduction of DAS results in the improvement of the tensile strength and ductility [40]. A higher number of particles in simply connected structures also improves the strength properties of the material [135]. These conclusions are supported by the experimental observations that the unmodified alloy with a lower DAS and a higher density of Si particles in the eutectic volume has a slightly higher strength than the modified alloy. At the same time, the alloys exhibit similar values of the average elongation to fracture (see Table 4.4). While the (slightly) finer and more homogeneous Si structure in the modified alloy should normally lead to a moderate increase of the strength in comparison to the unmodified alloy, the higher DAS values and lower particle density exert an opposite effect.

#### 4.4 Influence of Si morphology on mechanical properties

---

As a result, the density of the second phase particles and the size of the primary aluminium phase have proven to be more important for the strengthening of the alloy than the size-shape features of the eutectic Si induced by the modification. When the microstructure is fine, the advantages of the modified Si morphology for the ductility of the material might be overridden by the properties of the primary phase. The impact of the morphological characteristics of Si particles in the as-cast and solution treated alloys in relation to the mechanical properties of Al-Si alloys will be discussed in a separate section.

#### **4.4 Influence of Si morphology on mechanical properties**

Among all morphological properties of the eutectic Si, the spacing between Si particles is an important structural characteristic as it influences mechanical properties of the alloy and the fracture behavior [122]. Indeed, in Al-Si alloys the voids are initiated at Si particles [69], therefore the particle dispersion characterizes a relative resistance of a ligament between the particles to the void coalescence and the crack propagation. However, Hafiz and Kobayashi [39] show that it is not the inter-particle spacing but rather the ratio of the inter-particle spacing normalized to the particle equivalent diameter that better reflects the structural and functional property changes. In particular, upon the alloy modification, the coarse plates of Si are transformed into the fine Si fibers which results in decreasing the inter-particle spacing. At the same time, the structure obtained is much finer than the one in the unmodified alloy that results in a drastic increase of the ratio of the inter-particle spacing to the equivalent particle diameter. The authors have found that the increase of the ratio for modified alloys reflects the morphological transformations of the eutectic, on the one hand, and corresponds to the increase of the strength and toughness, on the other hand. Thus, the authors emphasize that the ratio of the inter-particle spacing normalized to the particle equivalent diameter is more informative characterization criteria than the inter-particle spacing alone. Therefore, the relation of this ratio to the tensile properties of the investigated alloys will be analyzed in detail. The corresponding structural and mechanical properties of the analyzed Al-Si alloys are summarized in Table 4.4.

To compute the inter-particle spacing, the dilation and counting technique described in Section 3.4.5 has been applied to binarized metallographic images of the eutectic phase in Al-Si alloys. The resulting cumulative percolation curves where the inter-particle spacing is plotted versus the cumulative percolation are shown in Figure 4.17. The inter-particle spacing,  $\lambda$ , is defined at the median value of the cumulative percolation which is equal to 0.5. It is important to note that such a method of the estimation of the inter-particle spacing may not be

precise in the case of noisy data [127]. The data set in Figure 4.17 is smooth and therefore, the value corresponding to the percolation of 0.5 can be defined by simple interpolation of the data points around it.

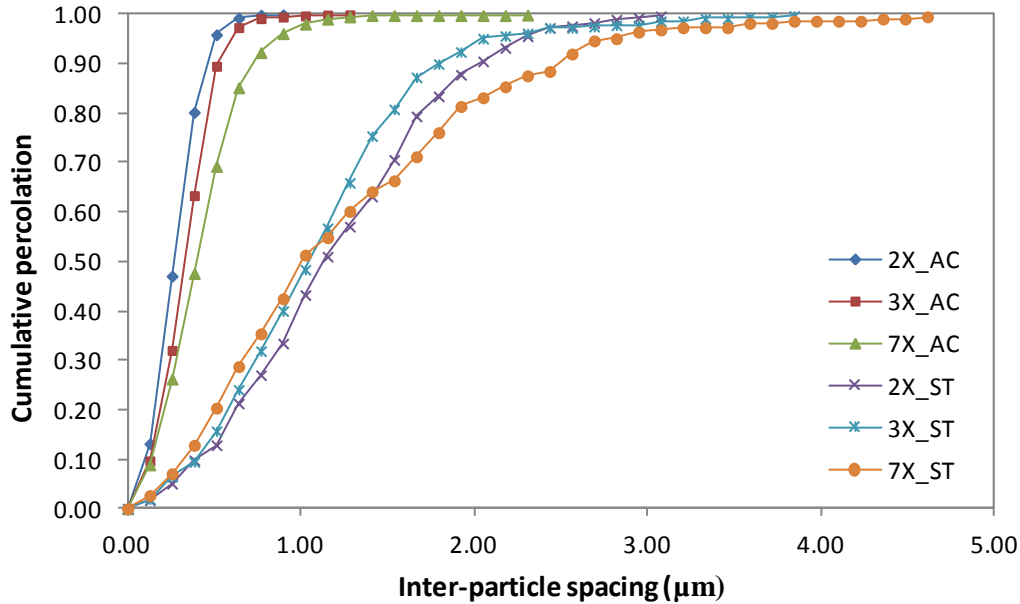


Figure 4.17: Cumulative percolation curves plotted by using the dilation and counting technique for binarized metallographic images of the eutectic phase in Al-Si alloys. The cumulative percolation is computed as  $(1 - (N_i/N_0))$ , where  $N_i$  is the number of Si particles after the dilation step  $i$  and  $N_0$  is the original number of Si particles [127].

Table 4.4: Mechanical properties of the analyzed Al-Si alloys represented by the yield strength,  $YS$ , the ultimate tensile strength,  $UTS$ , and the elongation,  $e$ , and corresponding morphological properties of the eutectic Si characterized by the inter-particle spacing,  $\lambda$ , the equivalent particle diameter,  $d$ , and their ratio  $\lambda/d$  (extended from [143]).

Alloy	$\lambda$ ( $\mu\text{m}$ )	$d$ ( $\mu\text{m}$ )	$\lambda/d$	YS (MPa)	UTS (MPa)	$e$ (%)
2X_AC	0.27	0.89	0.30	195	338	12
2X_ST	1.14	2.02	0.56	176	265	17
3X_AC	0.33	0.78	0.42	184	323	13
3X_ST	1.05	1.53	0.69	177	263	16
7X_AC	0.40	1.26	0.32	228	355	6
7X_ST	1.01	1.84	0.55	211	331	13

The first important remark is that the Young's modulus values derived from the stress-strain curves (in the range of 40 – 60 GPa) are not presented in Table 4.4 since they have all been largely underestimated for the investigated alloys. On the other hand, the Young's modulus of the alloys 3X\_AC and 7X\_AC defined by using another type of extensometer has shown

#### 4.4 Influence of Si morphology on mechanical properties

---

more precise values of 72 and 70 GPa, respectively. However, it has not been possible to perform these measurements for all the samples. The Young's modulus of the unmodified AlSi12 in the as-cast and solution treated state reported in the literature [146] is equal to 77 and 75 GPa, respectively. Normally, the solution treatment leads to a slight decrease in the Young's modulus due to the Si network disintegration [146].

The possible reason for the lower accuracy measurements in the present investigation is that the testing machine stiffness has not been taken into account when converting the load-displacement measurements into the stress-strain curves, although there are always elastic interactions between the machine and a specimen which contribute to the measured displacement values [147]. Also, the improper alignment of specimens with respect to the loading axis and slip of specimens between the wedge grips could induce bending stresses that are not taken into account in the computations as well [132]. Therefore, the values in Table 4.4 are used to assess the influence of the morphological parameters on the mechanical properties of the alloys on a comparative basis.

The ratio of the inter-particle spacing to the equivalent particle diameter,  $\lambda/d$ , in the modified alloy, 3X\_AC, is higher than in the unmodified alloy, 2X\_AC, and is equal to 0.42 and 0.30, respectively. According to Hafiz and Kobayashi [39], the increase in the ratio corresponds to the improvement of tensile properties. However, here it is not the case. As has already been discussed in Section 4.3, the unmodified alloy has higher strength characteristics. The modified alloy exhibits a slightly lower yield strength than the unmodified alloy which agrees well with the observations of Wang [53], who has investigated Al-Si-Mg alloys A356 (T6), but contradicts to the results of Hafiz and Kobayashi [39]. For the inhomogeneously modified alloys with Mg, 7X\_AC and 7X\_ST, the ratios are almost the same as for the unmodified alloys, 2X\_AC and 2X\_ST, in the corresponding conditions, but the tensile characteristics are very different.

The solution treatment leads to the fragmentation and spheroidization of Si particles which is expressed on the morphological level by reducing the aspect ratio of Si particles and increasing their size and inter-particle spacing [23,25]. Such a morphological change results in the improved ductility and fracture toughness of the heat treated alloys as compared to the as-cast alloys [23]. In the solution treated alloys, the ratio is in 1.6 – 1.9 times higher than in the corresponding as-cast alloys. However, only the ductility of the solution treated alloys has increased, the yield and tensile strength have in contrary decreased as compared to the as-cast alloys.

These results show the limits of the approach based on 2D characterization of Si morphology and considering features of only one phase while assessing the properties of a two-phase material. The results presented in Section 4.3 suggest the importance of the characterization of the primary aluminium phase and 3D structure of the eutectic Si for the understanding of the mechanical behavior of the material. Of course, the size and inter-particle spacing of Si particles in the eutectic phase do influence the mechanical properties of Al-Si alloys, but they are not the only and most important factors which have an impact on the properties. Actually, the morphology of both phases has to be considered simultaneously when analyzing the results of mechanical tests performed on the macro-specimens of the alloys. Even if the alloys have the eutectic chemical composition, they may still contain a considerable amount of the primary aluminium. Also, the chemical composition, presence of coarse intermetallics [57] and strengthening phases [19] as well as porosity level and distribution [49] strongly impact the tensile properties of Al-Si alloys. For example, the coarse intermetallic phases lower the ductility of the alloys [53] while  $Mg_2Si$  exert a strengthening effect [22,23] which can also be observed in the alloy 7X\_AC. Besides, as has been shown in the simulation study in Section 4.1 and by analyzing the three-dimensional Si structure in the deformed samples, the 3D particles density and complexity of the eutectic Si correlate better with the measured strength characteristics of the material than 2D size-shape features of Si particles. All this factors together are responsible for the mechanical properties of the material.

### **4.5 Damage behavior of Al-Si alloys**

The damage behavior and fracture resistance of Al-Si alloys along with their tensile properties are decisive for the structural applications of the alloys in the automotive and aircraft industries. Since damage characteristics in Al-Si alloys strongly depend on the morphology of the second phase particles [57], the next step will be the analysis of the damage behavior and fracture resistance of Al-Si alloys in relation to the morphology of the eutectic Si.

The damage behavior of Al-Si alloys has been studied by means of metallographic examination and tomographic reconstruction of samples after tension and compression loading. Morphological characteristics of cracks estimated on planar sections and in a volume have been compared in order to define the limits and explore the potentials of 2D damage characterization.

#### 4.5.1 Metallographic examination of damage

Figure 4.18 shows optical micrographs of different Al-Si alloys in the as-cast and solution treated conditions after applying a uniaxial tension or compression loading. In general, one can hardly recognize any damage in these micrographs. Therefore, some cracks in Si particles are pointed by white arrows. Obviously, the resolution of the optical light microscope is not enough to resolve fine cracks in Si particles, in particular, in the as-cast alloys with an extremely fine microstructure (see Figure 4.18 (a) and (b)). Since Si particles in the solution treated alloys are much coarser than the ones in the as-cast alloys, the cracks therein are easier to identify (see Figure 4.18 (c) and (d)).

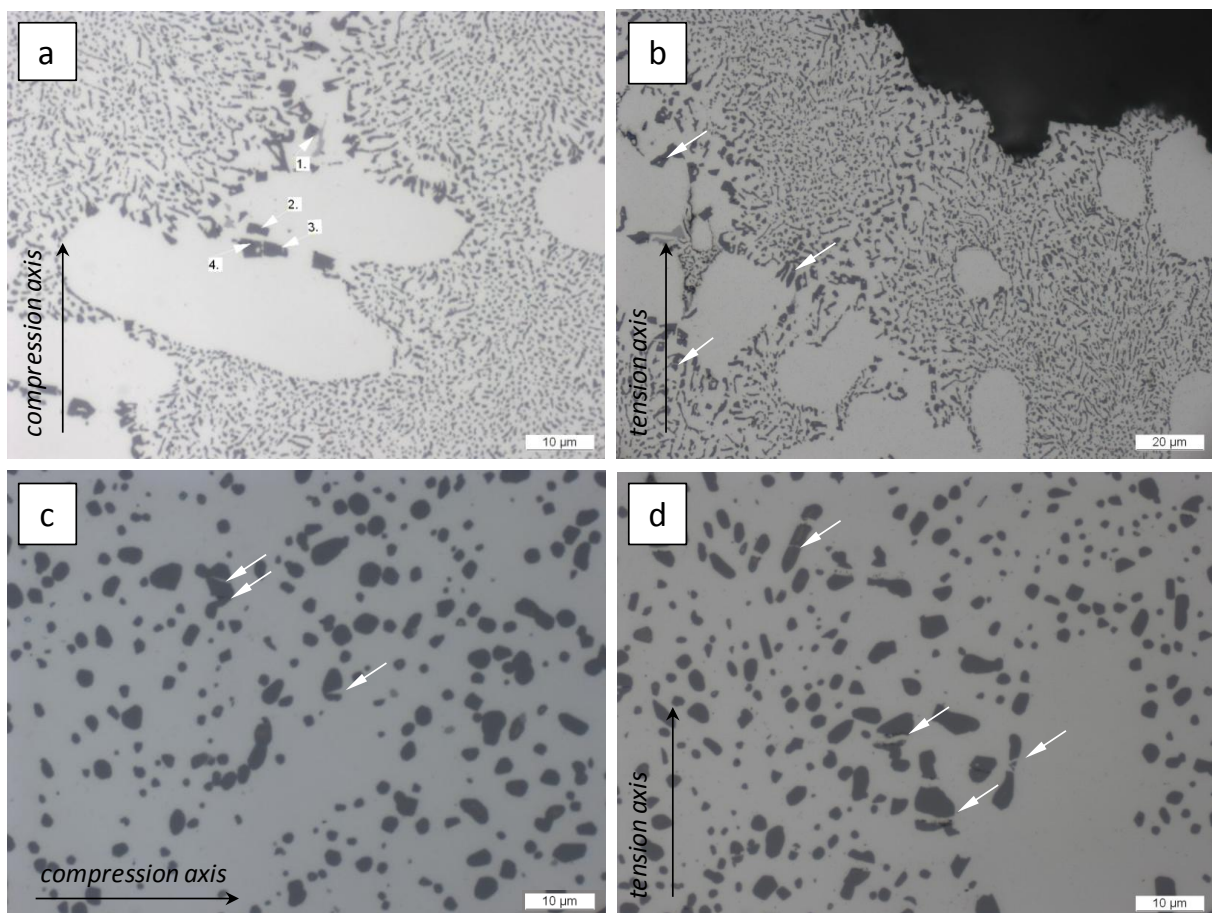


Figure 4.18: Optical micrographs of the as-cast inhomogeneously modified AlSi12 (7X\_AC) after (a) compression (20% deformation) and (b) tensile loading; (c) Sr-modified AlSi12 (3X\_ST) after compression loading (60% deformation) and (d) inhomogeneously modified AlSi12 (7X\_ST) after tensile loading, both are solution heat treated. White arrows point at fractured Si particles.

At the initial stage of damage, cracks in Si particles appear on metallographic images as very fine dark stripes which grow with a further loading until a full separation of broken parts of a particle. It is possible that during metallographic preparation soft aluminium fills in the

microcracks, and therefore, no matrix distortions and large cracks are observed. The effect of the aluminium matrix filling the voids during polishing has often been encountered in Al-Si alloys [76,79,84]. Most of the time, one can identify a broken Si particle due to the shape continuity of Si pieces located in direct vicinity (some examples are marked by white arrows in Figure 4.18).

In general, the cracks have been found in both Si particles and aluminides (if there are any). The observations on the crack orientation distribution are consistent with the observations reported in literature [44,57,69,75,86]: under compression loading, the cracks are mostly parallel to the loading axis whereas under tension loading, the cracks are perpendicular to the direction of the load applied. However, even when the compression deformation has increased up to 60%, the number of fractured Si particles detected in the micrographs has barely increased. The damaged particles have mostly been large Si particles whereas large aluminides have often (but not always) remained intact. Indeed, large particles crack more readily during the plastic deformation than smaller particles [48,51,85], because the critical stress necessary for a particle to crack is related to the particle morphology [12] so that it decreases as the particle size increases. However, there have also been large particles that have remained unbroken. Yeh and Liu [71] explain this phenomenon by regarding the particle cracking as a localized event which is related to the presence of dislocation pileups at the particles and thereby induced stresses.

Since during the metallographic preparation of samples for the damage investigation aluminium fills in the cracks within Si particles, it is sometimes difficult to unambiguously identify a damage event. One example is shown in Figure 4.19 (a) where it seems at first sight that the particle marked by the arrow has a large crack on its side. However, an image in Figure 4.19 (b) made at a higher magnification reveals two different Si pieces separated by the matrix. The question remains as to whether or not these parts have initially belonged to one Si particle. By making a FIB-cut through a broken Si particle that appears on a polished surface as two Si fragments separated by the aluminium matrix (see Figure 4.19 (c)), the filling of the crack in the particle with the aluminium can clearly be recognized (pointed by an arrow in Figure 4.19 (d)).

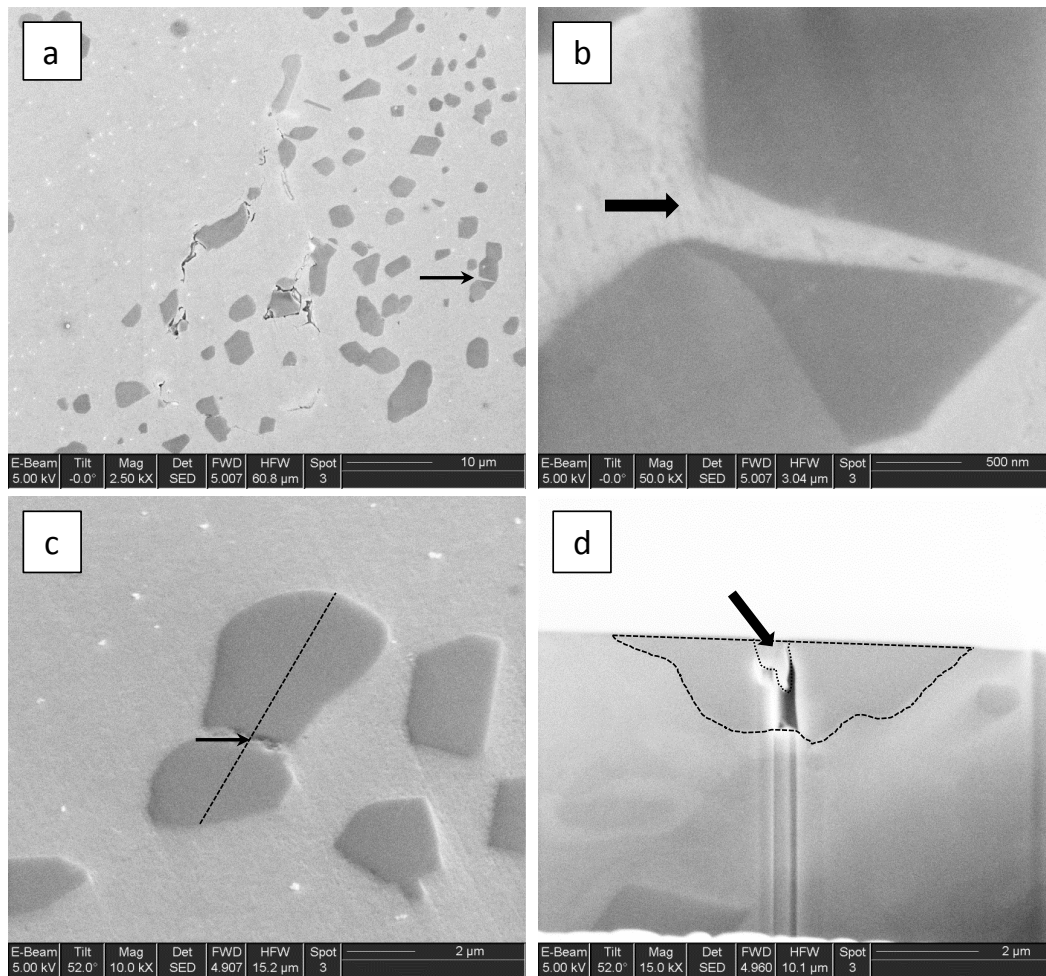


Figure 4.19: SEM micrographs of the inhomogeneously modified alloy 7X\_ST: (a) and (b) broken Si particle imaged at two magnifications that reveal different levels of detail; (c) location of the FIB-cut through a broken Si particle that is composed of two Si fragments separated by the aluminium matrix as observed on a polished surface; (d) cross-section through the particle shown in (c).

Thus, 2D damage characterization is very subjective in terms of the identification of damage events. Since it is not always possible to unambiguously distinguish between different fragments of a broken Si particle and several different particles with similar shape located in close vicinity to each other, the real amount of the microstructure damage is likely to be underestimated. Hence, 3D damage characterization shall help to evaluate reliability and limits of 2D analysis.

#### 4.5.2 3D damage investigation

3D damage in the eutectic phase of the as-cast and solution treated alloys after tension and compression loading has been investigated by means of the FIB/SEM tomography. Four samples of Al-Si alloys which present different combinations of the eutectic Si morphology

and loading conditions has been reconstructed to study their impact on the corresponding damage components such as cracks and voids.

The first two samples have been investigated after compression loading. Figure 4.20 (a) presents a reconstructed sample of the inhomogeneously modified Al-Si alloy after solution treatment (7X\_ST). A large phase displayed in red color in the middle of the reconstruction window is a pore which has most probably been formed during the casting process. Such casting defects are often encountered in the modified alloys and are detrimental for the ductility of Al-Si alloys [22,42].

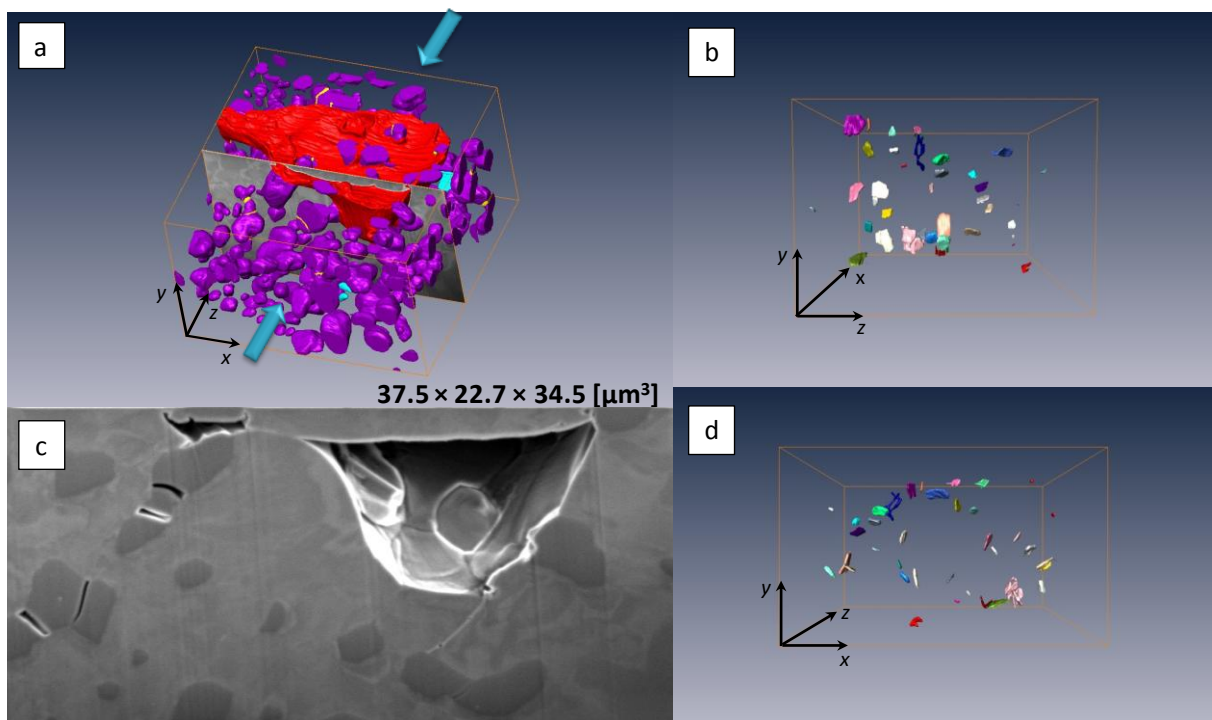


Figure 4.20: 3D reconstruction of the damage in the alloy 7X\_ST after compression loading (20% deformation, arrows indicate the direction of loading): (a) all reconstructed microconstituents including Si particles (in magenta), intermetallic phases (in cyan), cracks (in yellow) and a large pore in the middle of the reconstructed volume (in red) in aluminium matrix (transparent); (b) and (d) separate representation of the cracks within the reconstructed volume as viewed from different perspectives; (c) SEM image from the FIB/SEM image stack prior to segmentation.

The absolute majority of the cracks within the reconstructed volume have been found in Si particles. The debonding of Si particle from Al matrix has not been observed. Figure 4.20 (b) and (d) show separately cracks distributed in the volume from different perspectives. It can be recognized that the cracks are aligned in the direction of compression loading ( $z$ ) (see Figure 4.20 (d)) whereas the crack plains (flat surfaces in Figure 4.20 (b)) are nearly perpendicular to the directions of maximum tensile stresses.

## 4.5 Damage behavior of Al-Si alloys

As can be seen in Figure 4.20 (c), the contrast between Si and Al is very poor and is aggravated even more by the electron channeling effect resulting in the grain contrast [121] observed in the Al matrix (for more details, see Section 3.3.2). On the other hand, the cracks in Si particles can be well distinguished and the filling of cracks by the aluminium matrix is eliminated when eroding a surface with the ion beam. Thus, it can be argued that the FIB/SEM technique allows for an accurate damage characterization.

Figure 4.21 (a) shows a reconstructed sample of the as-cast unmodified Al-Si alloy (2X\_AC). The structure in the as-cast state is finer than in the solution treated alloy and Si particles are not completely independent, but connected into bigger clusters. However, the cracks within the particles remain simply connected.

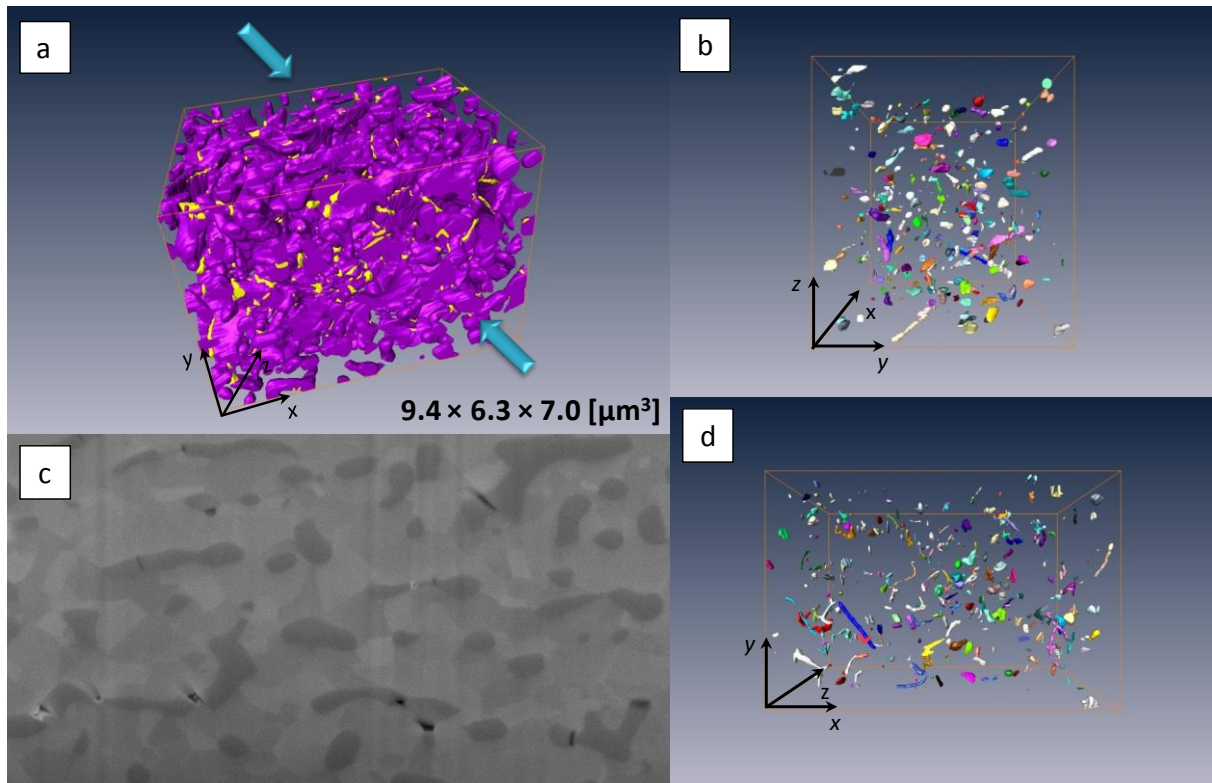


Figure 4.21: 3D reconstruction of the damage in the alloy 2X\_AC after compression loading (60% deformation, arrows indicate the direction of loading): (a) Si particles (in magenta) and cracks (in yellow) in aluminium matrix (transparent); (b) and (d) separate representation of cracks within the reconstructed volume as viewed from different perspectives; (c) SEM image from the FIB/SEM image stack prior to segmentation.

Similarly to the previous sample (7X\_ST), the damage is revealed by the cracking of Si particles. The arrangement of cracks relative to the loading axis is however difficult to observe because of the high density and small size of cracks in the reconstructed volume (see Figure 4.21 (b) and (d)). Here again, the contrast between Si and Al is extremely poor and the

channeling effect in the matrix is very pronounced (Figure 4.21 (c)). It makes the segmentation of images a challenging task.

The next two samples have been analyzed after tensile tests. A reconstructed sample of the as-cast modified Al-Si alloy (3X\_AC) with the delineated fracture surface is shown in Figure 4.22 (a). As can be seen, the fracture surface is composed of dimples formed around Si particles. One can also recognize large and partially branched Si particles (Figure 4.22 (b)) that are indeed connected into bigger clusters in a volume.

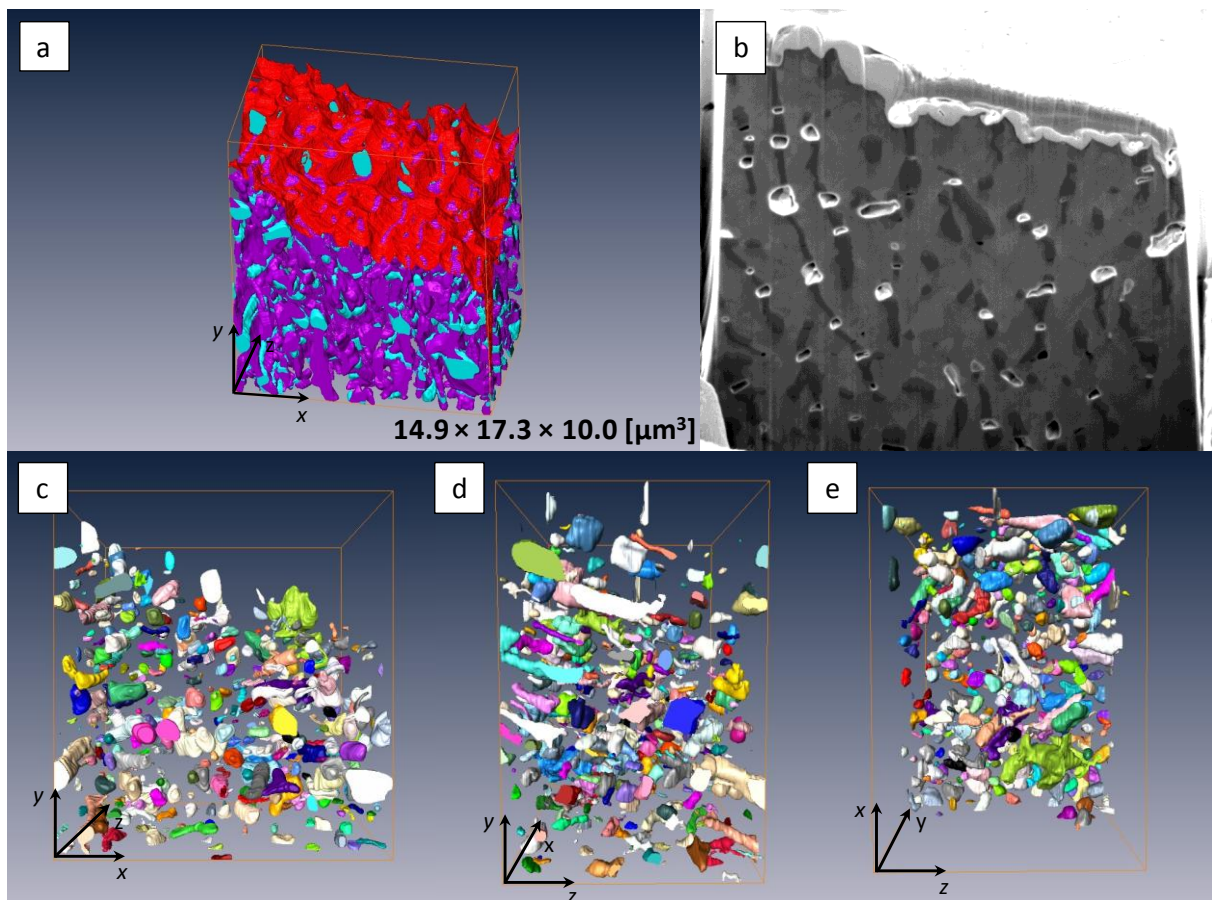


Figure 4.22: 3D reconstruction of the damage in the alloy 3X\_AC after tensile loading: (a) Si particles (in magenta) and cracks (in cyan) in aluminium matrix (transparent) and a fracture surface of the sample (in red); (b) SEM image from the FIB/SEM image stack prior to segmentation; (c) – (e) separate representation of cracks within the reconstructed volume as viewed from different perspectives.

The volume fraction and the size of cracks in the tensile test sample 3X\_AC are higher than in the compression specimen 2X\_AC (the quantitative data on the 3D damage is presented in Table 4.5 and Table 4.7). Therefore, it is even more difficult to describe an arrangement of the cracks on the basis of 3D images only. The quantitative analysis of the image data is required. However, by comparing the images (Figure 4.22 (c) – (e)) made in the planes parallel to the

tensile loading axis, ( $x$ - $y$ ) and ( $z$ - $y$ ), and in the plane normal to the loading axis, ( $z$ - $x$ ), it can be observed that the cracks have very often an elongated shape and tend to align perpendicular to the loading axis. The elongation of the cracks which can be clearly seen in Figure 4.22 (d) is related to their growth through preferential planes in branched Si particles. It seems that the morphology of Si particles does not make a direct influence on the morphology of cracks but indirectly it does: the branched and connected Si particles provide a longer way for the crack to grow through. Most of the cracks have been found in Si particles, no pure debonding of the particles from the matrix but only the debonding coupled with a crack growth through a particle has been observed.

Figure 4.23 (a) presents a reconstructed sample of the modified Al-Si alloy in the solution treated state (3X\_ST). The fracture surface has been displayed separately to better visualize the dimple pattern therein (Figure 4.23 (b)). The reconstructed volume does not consist of the eutectic phase only but also contains some primary aluminium cells. It is not desired but might happen because the volume for the reconstruction is usually chosen by observing the fracture surface or polished surface while the underneath structure is unknown before the sectioning of the material.

In contrast to the previous samples, it seems that the damage in the solution treated alloy with coarse, spherical and simply connected Si particles under tension proceeds by both cracking of Si particles and debonding of particles from the matrix. Figure 4.24 presents the sequence of images acquired by the FIB/SEM tomography where the origin of a large void observed in the last image (no. 12) can be traced. Hereby, it can be seen that the void has been formed by the growth of voids nucleated at the interfaces of two different Si particles and their coalescence in the loading direction. Thus, the size of this void is comparable with the inter-particle spacing.

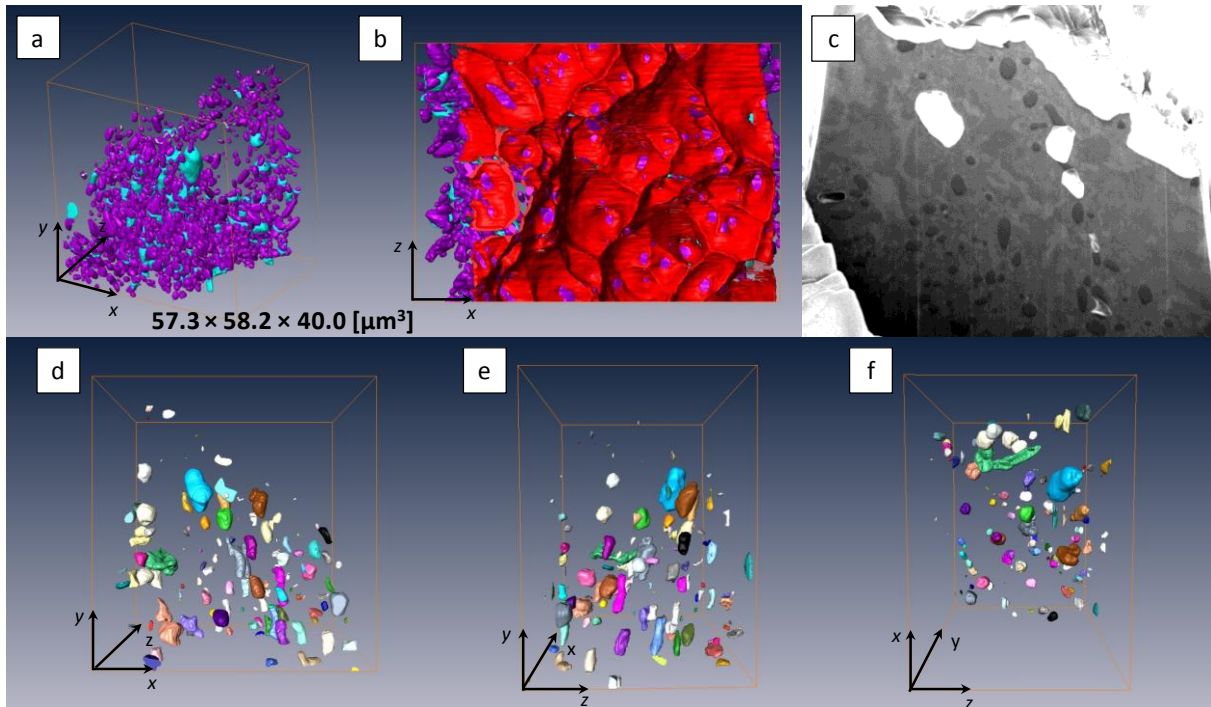


Figure 4.23: 3D reconstruction of the damage in the alloy 3X\_ST after tensile loading: (a) Si particles (in magenta) and cracks (in cyan) in aluminium matrix (transparent); (b) fracture surface of the sample (in red); (c) SEM image from the FIB/SEM image stack prior to segmentation; (d) – (f) separate representation of cracks within the reconstructed volume as viewed from different perspectives.

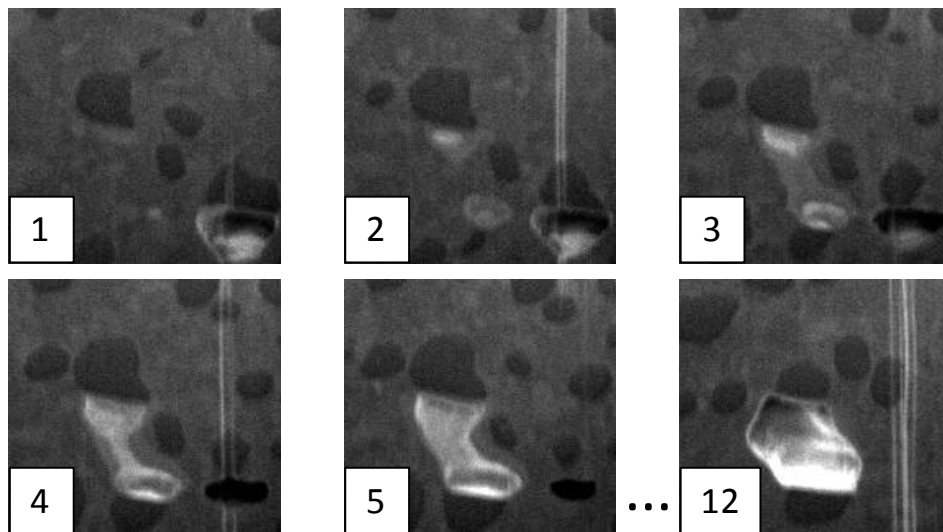


Figure 4.24: The local damage in the alloy 3X\_ST. The large void in the last image from the image series has been formed by coalescence of two neighboring voids that have resulted from debonding of Si particles from the matrix. Note that the figure presents a sequence of images as acquired by the FIB/SEM tomography, and not the images showing the damage development in time.

In contrary to the modified alloy in the as-cast state (3X\_AC), in the solution treated alloy (3X\_ST) there are many voids that are elongated in the direction of tensile loading which can

be observed in Figure 4.23 (d) – (f). These voids have most likely been formed by the coalescence of individual voids in the loading direction. This explanation conforms well to the suggestion that the damage in the solution treated alloy under tensile loading occurs by both cracking and debonding of Si particles, where the voids formed upon the debonding coalesce along the loading axis as illustrated in Figure 4.24. Therefore, it is expected that the crack orientation distribution in the alloy 3X\_ST will be different from the alloy 3X\_AC so that the former will contain a certain fraction of voids oriented close to the loading direction.

Thus, the debonding of Si particles from the matrix has only been observed in the modified Al-Si alloy in the solution treated state (3X\_ST). The different damage mechanism found in the alloy 3X\_ST influences the orientation distribution of voids. This observation does not contradict to the state-of-the-art observations on the crack orientation distribution in the alloys under tensile loading (see e.g. [71,86]) but complements it. Indeed, in the tensile test specimens most of the cracks are oriented nearly perpendicular to the tensile loading axis. The proposed explanation for the void orientation observed in the alloy 3X\_ST is the following: in the solution treated alloy, the voids originated at the particle/matrix interfaces grow also normal to the loading direction, but it is the “secondary” voids formed by the coalescence of the original voids along the loading axis which show a different orientation with respect to the loading axis.

The observations on the damage modes of Si particles agree well with the results reported by Dighe et al. [86] and Horstemeyer and Gokhale [89], who have found both damage modes, cracking and debonding of Si particles, in the cast Al-Si-Mg alloy under tension loading and the fracturing of Si particles solely under compression loading. According to Dighe et al. [86], the debonding of Si particles from the matrix is related to high local hydrostatic tensile stresses that occur around Si particles upon the tensile loading of the material. Besides, Lee et al. [40] have suggested that the decohesion occurs when the stress at the interface between Si particle and Al matrix exceeds the interfacial strength. On the other hand, a low occurrence of voids formed by the debonding of second phase particles in aluminium alloys has been attributed to high cohesive forces between the second phase particles and Al matrix [69].

The cracks have mostly an elongated or flat shape. Asghar and Reguena [79], who have investigated the 3D damage in compression test samples of Al-Si alloys containing a network of aluminides and Si particles, have also reported that the observed voids have either an elongated or platelet-like shape with an aspect ratio of 2-3. It can therefore be suggested that the elongation of cracks in Si particles is related to the Si morphology in 3D.

Last but not least, the damage characteristics in the investigated Al-Si alloys have been compared on a quantitative basis. The volume fraction,  $V_V$ , and the crack density,  $N_V$ , in the alloys have been computed using 3D image data and are presented in Table 4.5.

Table 4.5: The volume fraction of cracks,  $V_V$ , and the crack density,  $N_V$ , in the investigated Al-Si alloys estimated by analyzing 3D images.

	2X_AC	7X_ST	3X_AC	3X_ST
	compression	compression	tension	tension
$N_V$ ( $\mu\text{m}^{-3}$ )	0.845	0.002	0.281	0.002
$V_V$ (%)	0.507	0.228	5.565	2.077

In Table 4.5, it can be seen that the volume fraction of cracks in the samples under tension is much higher than in the compression samples, while the density of cracks in the as-cast samples is higher as compared to the solution treated samples regardless the loading. The density of cracks in the unmodified alloy 2X\_AC under compression is higher than the one in the modified alloy 3X\_AC under tension, while in the solution treated alloys 3X\_ST and 7X\_ST, the density of cracks is identical under both tension and compression loading. However, by comparing the alloys, one has to keep in mind that the alloys have been analyzed at different strain levels. According to Dighe et al. [86], given the same strain level, the fraction of damaged particles under tension loading is higher than under compression loading.

The lower volume fraction of voids in the solution treated samples with respect to the as-cast samples is related to the morphology of Si particles which influences the local stress state in the structure [39]. While the particles containing irregularities like notches or neckings crack more readily due to the high stress concentration sites therein [76], the spheroidization of Si particles during the heat treatment reduces the amount of stress concentration sites during the loading [79]. Besides, the load-bearing capacity of second phase particles depends on the shape of the particles where the elongated particles transfer the load more effectively than the spherical ones [83,84]. Guiglionda and Poole [84] have compared the load transfer to Si particles having spherical and fibrous or plate-like shape. Thereby, the stress in the spherical particles is approximately 1.5-2 times the tensile flow stress of the matrix. The stress in the fibrous particles ranges from approximately 10-20 times the matrix flow stress for the particles that are parallel to the loading direction to simply the tensile flow stress of the matrix for the particles that are perpendicular to the loading direction. The intrinsic fracture stress reported for Si particles is ca. 700 MPa. Close to the value proposed in [84], Joseph et al. [12]

have found the fracture stress of Si particles to be in the range 500 – 1000 MPa. Obviously, the stress level at which the fracturing of a particular Si particle might occur will depend on the particle's morphology. Due to the low load transfer efficiency to spherical particles, they are less likely to reach the fracture stress level than fibrous particles (for the same size category). Thus, the solution treated alloys having spheroidized Si particles exhibit a lower level of damage than the as-cast alloys [84].

The following bullet points summarize the results of the 3D damage investigation:

- The damage during uniaxial compression in the investigated Al-Si alloys occurs by the cracking of Si particles and aluminides (if there are any), where the cracks grow parallel to the loading direction. Under tension loading, the damage proceeds by the cracking of particles (AC alloy) or both cracking and debonding of particles from the matrix (ST alloy) depending on the morphology of Si particles. The crack orientation distribution under tensile loading is therefore expected to be wider in the solution treated alloy with coarse spheroidized Si particles as compared to the as-cast alloy with fine branched Si. It is important to emphasize, however, that the particle cracking still remains the principle damage mechanism in these alloys.
- The cracks have mostly an elongated or flat shape. It is suggested that the morphology of Si particles indirectly influences the morphology of cracks so that the branched and connected Si particles provide a longer way for the crack to grow through resulting in the elongated voids.
- The solution treated alloys exhibit a lower level of damage than the as-cast alloys due to the fragmentation and spheroidization of Si particles upon the heat treatment and as a consequence, the reduction of the load transfer from the matrix to the particles as well as the reduction of the high stress concentration sites within the spheroidized Si.

The knowledge on the damage characteristics and mechanism dominating for different combinations of microstructure and loading conditions is important for the right interpretation of results issued from 2D damage characterization.

### 4.5.3 Limits and potentials of 2D damage characterization

In the following section, the quantitative characterization of cracks on the basis of 2D and 3D image data is performed. The typical 2D images through 3D image data for every investigated alloy are shown in Figure 4.25. The size, shape and orientation distribution of cracks computed on the volume data and corresponding planar sections are compared and the revealed discrepancies are discussed. The shape of cracks is characterized by the shape factor and the size of cracks is described by the equivalent circle/ball diameter.

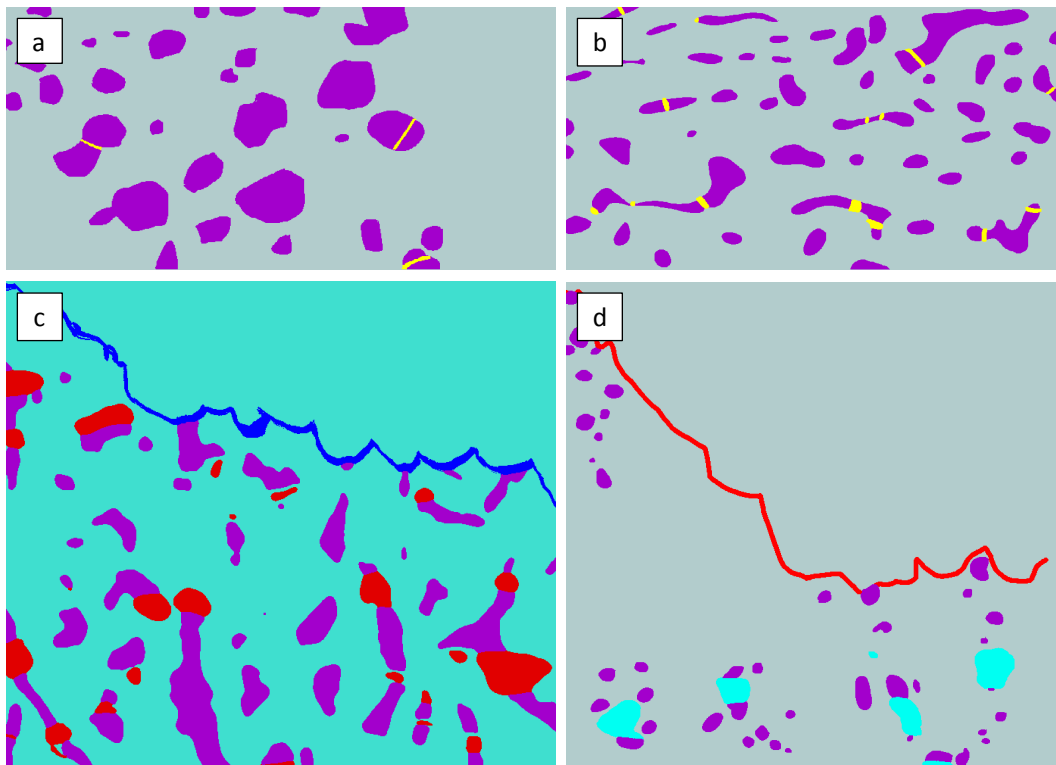


Figure 4.25: Typical 2D images through 3D image data: (a) the alloy 7X\_ST (cracks are in yellow); (b) the alloy 2X\_AC (cracks are in yellow); (c) the alloy 3X\_AC (cracks are in red); and (d) the alloy 3X\_ST (cracks are in cyan). Si particles are shown in magenta.

Figure 4.26 shows the frequency distributions of the shape factor of cracks in the as-cast modified (3X\_AC) and unmodified (2X\_AC) Al-Si alloys. As can be seen, the cracks exhibit different frequency distributions of the shape factor estimated on planar sections and in a volume in corresponding alloys. The average shape factors of cracks estimated on 2D and 3D image data of Al-Si alloys investigated in Section 4.5.2 are presented in Table 4.6.

## 4.5 Damage behavior of Al-Si alloys

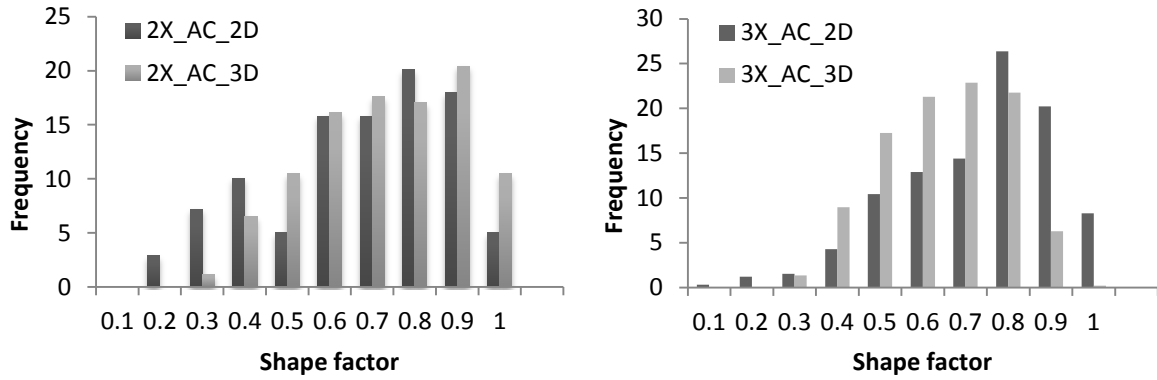


Figure 4.26: Frequency distributions of the shape factor of cracks estimated on 2D and 3D image data of the alloys 2X\_AC and 3X\_AC.

Table 4.6: Shape factors of cracks estimated on 2D and 3D image data of Al-Si alloys investigated in Section 4.5.2.

	2X_AC	3X_AC	3X_ST	7X_ST
	compression	tension	tension	compression
Shape factor_2D	$0.62 \pm 0.21$	$0.68 \pm 0.18$	$0.71 \pm 0.18$	$0.47 \pm 0.14$
Shape factor_3D	$0.68 \pm 0.18$	$0.60 \pm 0.14$	$0.68 \pm 0.14$	$0.48 \pm 0.15$

In general, the difference between 2D and 3D average shape factors is not significant and is much lower than the corresponding standard deviations. Keeping this in mind, it can however be noticed that the average shape factor of cracks derived from 2D images of samples under tension loading is slightly overestimated in comparison to the spatial values. As has been discussed in Section 4.5.2, the cracks are oriented nearly perpendicular to the tensile loading axis and the image plan is oriented along the loading axis. Therefore, the probability for the image plan to cross the elongated cracks along their major axes is very low, and thus, the cracks with an elongated shape appear to be more spherical in the planar sections (see Figure 4.25 (c) and (d)). This is reflected by the lower shape factor of cracks computed in 3D as compared to 2D values.

Similar results have been reported by Lasagni et al. [82], who have compared the 2D and 3D shape of Si particles in the modified AlSi12(Sr) alloys in the as-cast and solution treated state. The authors have found that the shape factor of Si particles computed on 2D images has largely been overestimated for the as-cast network structures and to a less extent in the solution treated alloys with simply connected Si particles. Here, the voids are also simply connected and their shape factor is overestimated as well. Thus, 3D analysis has proved to provide more realistic shape characteristics for both Si particles and damage components.

In the compression test sample 2X\_AC, the average shape factor derived from 2D images is, on the contrary, slightly underestimated in comparison to the spatial value. The cracks in the compression test samples exhibit very fine cross sections (see Figure 4.25 (a) and (b)) which argues for their flat platelet-like shape in 3D. A reason for the discrepancy between the 2D and 3D average shape factors could stem from the fact that the analyzed 2D images have been sectioned perpendicular to the compression loading axis while the cracks grow parallel to the loading direction (i.e. normal to the image plan). Thus, the width of cracks has been imaged while their length could not be assessed from the analyzed 2D images. Therefore, fine cross sections of cracks in 2D images have the shape factors that are either slightly lower (2X\_AC) or at least similar (7X\_ST) to the 3D shape factors of platelet-like cracks. However, in general, 2D planar sections reflect the shape features of cracks quite well; although the frequency distributions of the shape factor estimated on planar sections and in a volume are different (see Figure 4.26).

The frequency distributions of the equivalent diameter of cracks in the as-cast modified (3X\_AC) and unmodified (2X\_AC) Al-Si alloys are shown in Figure 4.27. The average equivalent diameters of cracks estimated on 2D and 3D image data of Al-Si alloys investigated in Section 4.5.2 are presented in Table 4.7.

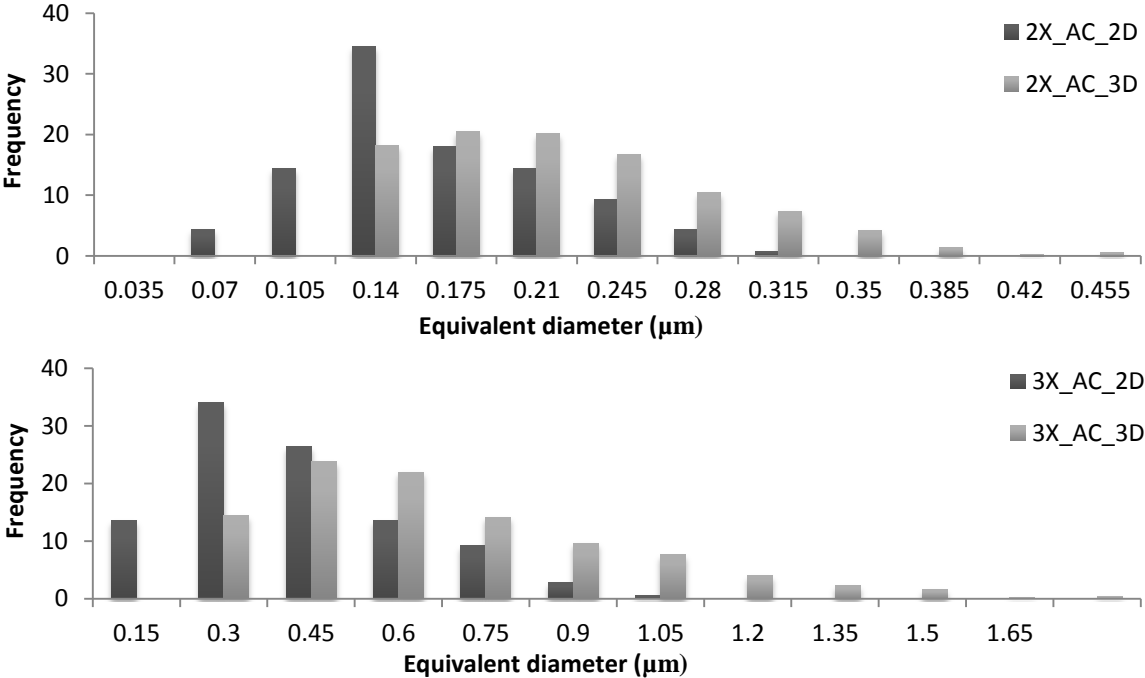


Figure 4.27: Frequency distributions of the equivalent diameter of cracks estimated on 2D and 3D image data of the alloys 2X\_AC and 3X\_AC.

## 4.5 Damage behavior of Al-Si alloys

Table 4.7: Equivalent diameters of cracks estimated on 2D and 3D image data of Al-Si alloys investigated in Section 4.5.2.

	2X_AC	3X_AC	3X_ST	7X_ST
	compression	tension	tension	compression
Equivalent diameter_2D ( $\mu\text{m}$ )	$0.15 \pm 0.05$	$0.35 \pm 0.20$	$1.66 \pm 0.91$	$0.75 \pm 0.22$
Equivalent diameter_3D ( $\mu\text{m}$ )	$0.21 \pm 0.07$	$0.59 \pm 0.30$	$2.11 \pm 1.28$	$1.19 \pm 0.43$

Obviously, the average equivalent diameter of cracks computed on 2D images is smaller than the average equivalent diameter of cracks computed in 3D and exhibits different frequency distributions on planar sections and in a volume. There are various stereological methods which allow a determination of 3D parameters of objects from their 2D features. The basic method is known as the Wicksell's corpuscle problem which enables a determination of the density of objects and their 3D size distribution function on the basis of the 2D density and size distribution function estimated on metallographic sections. However, the model is limited to spherical objects only [60]. There are also more sophisticated methods known as stereological unfolding problem which deals with the joint size-shape-orientation distribution of objects that can be approximated with prolate or oblate spheroids [148]. The cracks and voids in the investigated alloys though having a rather simple shape are not necessary spheroidal. It might be possible that for some alloys such an approximation could work more or less well. In any case, by analyzing the size characteristics of damage components in Al-Si alloys, the stereological relations between the 2D parameters defined on planar sections and corresponding 3D features have to be taken into account.

In general, the volume and the equivalent diameter of cracks in the compression specimens are lower than in the tension specimens in corresponding conditions. Obviously, the size of cracks in solution treated alloys is larger than in the as-cast alloys because of the coarser Si particles. These observations remain similar for 2D and 3D investigations.

Figure 4.28 shows the crack orientation frequency distribution in the tensile test specimens 3X\_AC and 3X\_ST. In general practice, to analyze the orientation distribution of cracks in 2D, the images have to be taken in the loading direction. While during the FIB/SEM tomography of the tension samples, the imaging has been carried out in the loading direction, for the compression samples, the imaging plan has been perpendicular to the compression axis. As a consequence, the acquired 2D images of the compression specimens 2X\_AC and 7X\_ST do not provide information on the orientation of cracks with respect to the loading

axis. Thus, the orientation distribution of cracks in the compression specimens is not presented since it cannot be interpreted directly.

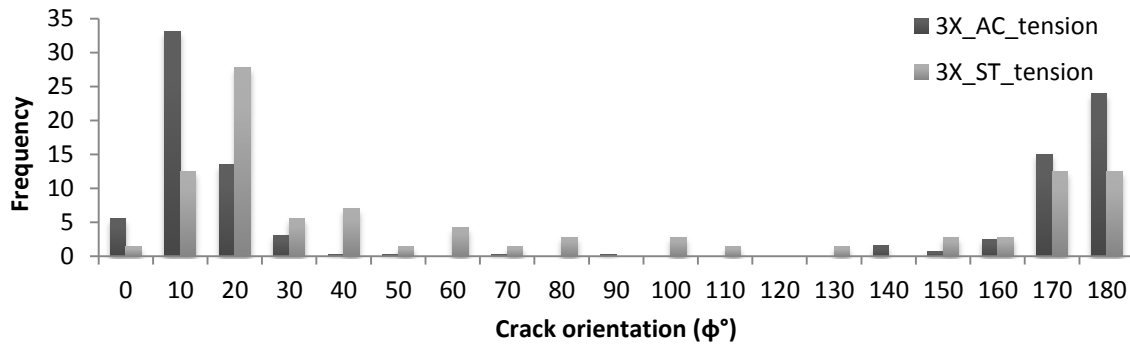


Figure 4.28: Crack orientation frequency distributions estimated on 2D image data of the tensile test specimens 3X\_AC and 3X\_ST.

In tension samples, the cracks are mostly oriented perpendicular to the loading axis. Remind that the orientation of cracks is defined with respect to the  $x$ -axis in the image while the tensile loading axis corresponds to the  $y$ -axis (i.e.  $90^\circ$  in Figure 4.28). For the majority of cracks, the orientation varies in very tiny ranges ( $(10\text{--}20^\circ)$  and  $(170\text{--}180^\circ)$ ). It is consistent with the observations on the orientation distribution of cracks with respect to the tensile loading axis made by Yeh and Liu [71] and Dighe et al. [86]. In particular, Dighe et al. [86] have observed the cracks oriented in the range of  $80^\circ$  to  $100^\circ$  with respect to the loading axis. Yeh and Liu [71] have reported the number of the cracks oriented close to  $45^\circ$  and  $135^\circ$  with respect to the loading axis to be significantly reduced.

Comparing the crack orientation frequency distributions in the alloys 3X\_AC and 3X\_ST, the impact of different damage mechanisms discussed in Section 4.5.2 can also be observed. In the as-cast alloy 3X\_AC, there are no cracks that are oriented in or close to the tension direction (i.e.  $90^\circ$  in Figure 4.28): in particular, there are no cracks oriented in the orientation range  $(40\text{--}130^\circ)$  at all. On the contrary, the solution treated alloy 3X\_ST exhibits a wider crack orientation distribution range, where 22% of cracks are oriented in the range of orientations  $(40\text{--}130^\circ)$  including the ones that are close to the loading direction. This difference between the alloys 3X\_AC and 3X\_ST can be explained by the occurrence of the debonding of Si particles from the matrix with subsequent coalescence of the voids in the loading direction taking place in the alloy 3X\_ST.

Although the 3D characterization of crack orientation distributions in the investigated samples has also been carried out, the results obtained do not allow for a quantitative interpretation

due to the limitations of the characterization method. In general, it has been found that most of the cracks tend to be oriented along the compression axis and perpendicular to the tension axis depending on the loading mode which supports the observations in 2D. Besides, the 3D analysis had allowed to identify several principle directions of the crack orientation which calls up to the fact that in 2D, the crack orientation distributions are also observed within certain orientation ranges. However, spatial deviations of the crack orientation from the directions of maximum stresses have also been detected. Such deviations may be partially due to the analysis method itself (see Section 3.4.4), which implies a division of a semisphere into 12 sectors, so that only one representative direction is given for every sector. The consideration of a larger amount of directions can provide more accurate measurements [126], but unfortunately, is not available in the analysis software used [67].

In summary, 2D analysis of FIB/SEM images can roughly reflect the size, shape and orientation characteristics of cracks in Al-Si alloys. A good correspondence between the average shape factors of cracks estimated on 2D and 3D images has been found. Also, the size distribution of cracks can potentially be estimated from 2D images when choosing an appropriate stereological method. However, 2D analysis alone underestimates the real size of cracks. In terms of the crack orientation distribution, it has been observed that most of the cracks are (nearly) perpendicular to the tension axis which conforms to the state-of-the-art observations [71,86] and observations made on 3D images. Besides, a wide crack orientation distribution range (incl. the cracks oriented close to the loading direction) exhibited by the solution treated alloy could be explained by the mixed damage mechanism (i.e. cracking and debonding of Si particles) proposed for the corresponding combination of Si morphology and loading condition.

Nevertheless, the information on the 3D shape and arrangement of cracks is not complete when analyzing the cracks in 2D. In particular, the advantage of 3D analysis is that it provides both polar and azimuthal angles for the crack orientation whereas 2D analysis enables to define the polar angle only (angle between a major semi-axis of an object and the x-axis in the image) as if the crack would lie perfectly parallel to the image plane. However, as has been observed in 3D images, there are always spatial deviations of the crack orientation from the directions of maximum stresses with respect to both angles. As a consequence, the information on the 3D arrangement of cracks is partially lost when analyzing the cracks in 2D. Thus, although 2D damage characterization is simple and can provide a rough estimation of object based parameters of cracks, it is still subjective and is not free of ambiguity. In

particular, when 2D analysis is performed on metallographic sections where the cracks are easily filled by the matrix, the unambiguous identification of damage events is complicated.

## 4.6 Fractography of Al-Si eutectic

Fractographic properties of a structure give an access to a lot of useful information such as the information on the type and mode of a fracture as well as the origin and evolution of the fracture in the particular material. Besides, topographic properties of the fracture surface can be related to the material's toughness. In Section 4.6.1, fractographic investigations performed on tensile test specimens of six different Al-Si alloys are presented. Section 4.6.2 elaborates on the correlation between the geometry of Si particles on metallographic sections and the geometry of dimples on fractographs of corresponding alloys. The results have been summarized by Kruglova et al. in publication [133]. Section 4.6.2 contains an excerpt from the section "*Results and discussion*" of the underlined publication.

### 4.6.1 SEM fractography

The investigated fracture surfaces correspond to the Mode I of the ductile fracture obtained under uniaxial tensile loading and exhibit characteristic dimple system with well-defined closed shapes. The damage mode of Si particles is evaluated by observing Si particles on the fracture surfaces of the samples: normally, the debonded particles have a smooth surface with rounded edges whereas the cleaved particles have planar surface with sharp edges [90].

Most of the investigated alloys have shown fracture surfaces passing preferentially through the eutectic phase. Thus, the fracture surfaces of the samples have mostly been composed of dimples with a typical for ductile fracture ripple pattern. The walls of dimples are covered by smooth ripples that have been originated from the slip-plane displacement at the inner surface of dimples during their growth [47]. The previous investigations on the fracture mechanism in Al-Si alloys [52–54] have also shown that in the alloys with smaller DAS (such as the alloys in the present investigation), the final fracture takes place preferentially along the eutectic grain boundaries, i.e. has an intergranular type. Also in [18], it has been shown that the fracture in the modified hypoeutectic Al-Si alloy propagates mostly through the eutectic phase circumventing the primary aluminum dendrites.

Typical fractographs of unmodified and Sr-modified Al-Si alloys are shown in Figure 4.29. It can be seen that the voids are nucleated at Si particles: a Si particle can easily be distinguished in the middle part of every dimple. The dimples follow roughly the shape of their nucleus

## 4.6 Fractography of Al-Si eutectic

particles, so that the equiaxed particles are found in the round dimples while the elongated or curved particles lodge in the prolonged or irregular dimples. The fracture surface patterns of both alloys have shown significant differences in their size-shape characteristics. The modified alloy exhibits regular and merely equiaxed dimples. The dimples on the fracture surface of the unmodified alloy are much larger and have irregular shape. The bedonded Si particles have not been observed. All Si particles observed in the dimples are broken and even splintered with typical for the brittle fracture multiple cleavage steps on the particle surfaces. Together with Si particles there are small inclusions observed on the walls of the dimples. The nature of these inclusions has not been identified.

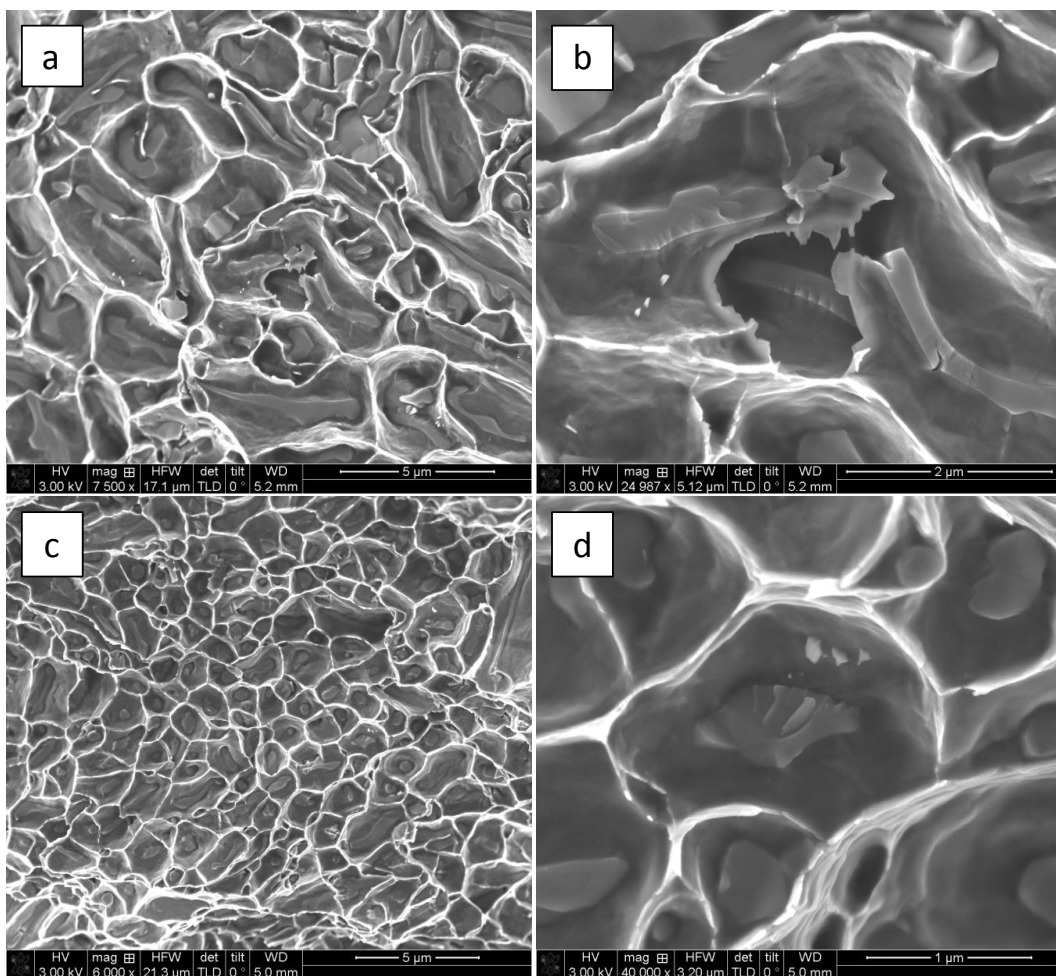


Figure 4.29: Fractographs of (a) unmodified AlSi12 [133], (b) Si particles in unmodified AlSi12 at higher magnification, (c) Sr-modified AlSi12 [133], (d) Si particles in modified AlSi12 at higher magnification. All alloys have typical ductile fracture surface consisting of dimples. The dimple system in the modified alloy is finer and more homogeneous than in the alloy without modification.

Fractographs of the unmodified and Sr-modified AlSi12 in the heat treated condition are shown in Figure 4.30. It is not surprising that the fracture surfaces of both alloys after solution

heat treatment look very similar as the analysis of their optical micrographs has also shown similar morphological characteristics of the eutectic Si. Thus, the dimples in both alloys have equivalent geometrical properties: the dimples are much larger than in the as-cast structures and have a regular shape. Though geometrical similarity, the fracture in the unmodified alloy has developed mostly through the Al phase (Figure 4.30 (c)) and not through the Al-Si eutectic as in the other investigated alloys. Since the absolute majority of the alloys have exhibited the large quota of the fracture surface passing through the eutectic phase, it can be assumed that the fracture behavior of the unmodified solution treated alloy has purely random occurrence which is likely to be due to the presence of microstructural defects. It is known that large microstructural defects like porosity [49] and microstructural extrema such as the largest Si particles [56] control the fracture properties of the material.

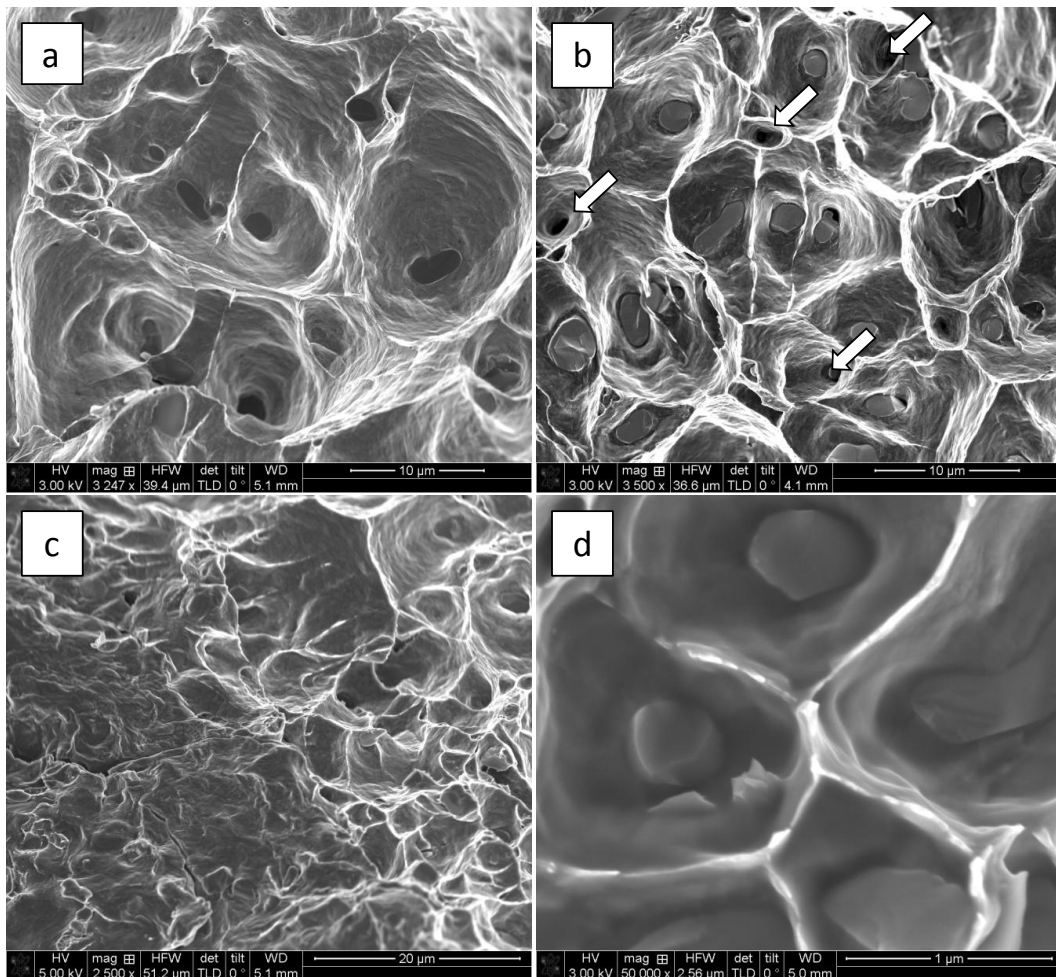


Figure 4.30: Fractographs of (a) unmodified AlSi12, solution heat treated, (b) Sr-modified AlSi12, solution heat treated [133], (c) fracture in primary Al in unmodified AlSi12, solution heat treated, (d) Si particles in the as-cast modified AlSi12 at high magnification.

Another observation made on the fractographs of the modified alloys (see Figure 4.30 (b) and (d)) concerns the damage mode of Si particles. Although all observed Si particles have been fractured, they often come partially up (“pulled out”) from the matrix as if two types of the damage, i.e. cracking of particles and debonding of particle from the matrix, have been proceeding at the same time. The observed phenomenon might be regarded from the perspective of fiber reinforced composite materials which exhibit a so-called “pull-out” effect upon the loading. Remind that the alloy 3X\_ST has shown a different damage mechanism as compared to other investigated alloys exhibiting both cracking and debonding of Si particles. Also, the alloy 3X\_AC has shown the debonding coupled with a crack growth through the particles, although no pure debonding of the particles from the matrix has been observed (see Section 4.5.2). Since the debonding of Si particles has occurred in one way or another in the modified alloys under tension loading, it can be suggested that either the stress at the interface between Si particles and Al matrix in these alloys exceeds the interfacial strength [40] or the interfacial strength in the alloys is low.

According to Bheemreddy et al. [149], the nature of the interfacial bonds in the fiber reinforced composites strongly influences their failure mechanism so that “... if the interfacial bond is weak, the oncoming crack can experience interface debonding, followed by crack deflection, crack bridging, fiber breakage, and finally fiber pull-out. All these failure mechanisms lead to enhanced fracture toughness of the composite and graceful failure.” Thus, considering the pull-out mechanism, the observed Si particles pulled out from the matrix might have resulted from the debonding of the particle/matrix interface followed by the crack bridging and particle breaking; this is, however, to a much lesser extent than observed in the fiber reinforced composites. An example of such phenomena is illustrated in Figure 4.30 (d). White arrows in Figure 4.30 (b) point at few holes which would, at first glance, appear as cavities left by the debonded particles. However, at higher magnification, the broken Si particles located very deep in the dimples can be observed. These cavities correspond to the counterparts to the pulled out Si particles located on the opposite half of the fracture surface. Such fracture patterns have been mostly observed in the modified alloys.

The size-shape dependency of the fracture surface geometry on the morphology of the eutectic Si is also observed in the fractographs of the inhomogeneously modified Al-Si alloy shown in Figure 4.31. Similarly to the metallographic sections of the as-cast alloy which have demonstrated two size classes of Si particles (see Figure 4.10), its fracture surface exhibits two size classes of dimples. On the one hand, small round dimples are associated with fine Si

particles that are so small that it is hard to distinguish them within the dimples in Figure 4.31 (a). On the other hand, large and less regular dimples contain Si particles of equivalent shape. At the same time, the solution treated alloy demonstrates more homogeneous particles/dimples size-shape distribution: dimples are coarser and have nearly equiaxed shape (Figure 4.31 (b)).

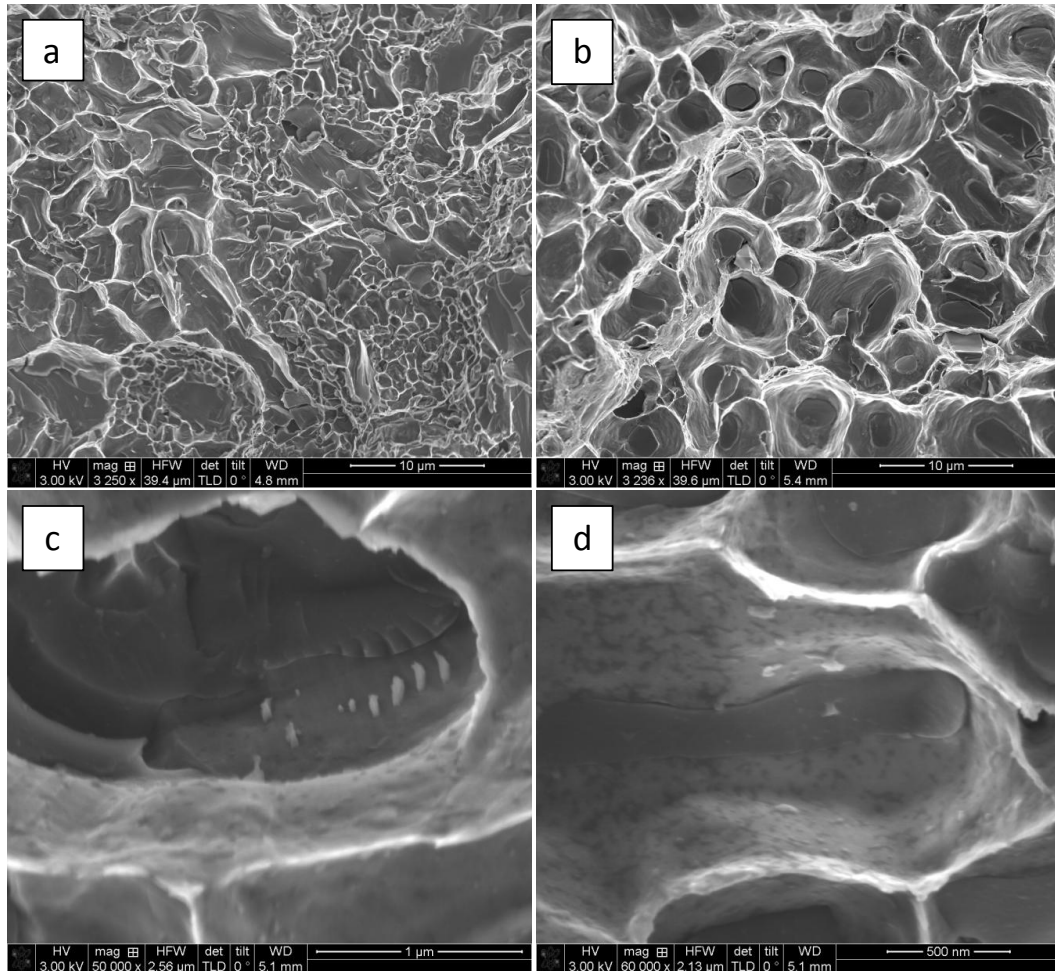


Figure 4.31: Fractographs of the inhomogeneously modified AlSi12 a), c), d) in the as-cast state at different magnifications, b) solution heat treated at 540 °C for 4 hours, quenched in boiling water. Two size classes of dimples can be distinguished in the as-cast alloy. The dimples in the heat treated condition are coarser and more homogeneous in size.

At higher magnification, one can distinguish different inclusions on the fracture surface of the as-cast alloy: light grey inclusions appear on the dimple interior walls and on the fracture surface of Si particles. The possible nature of these inclusions has been discussed in Section 0. However, it is worth to mention, that the inclusions in Figure 4.31 (c) are much smaller than those observed in the optical micrographs. Therefore, it cannot be excluded that these inclusions are indeed the fine particles of dust lying on the sample surface.

## 4.6 Fractography of Al-Si eutectic

Si particles exhibit a typical cleavage fracture pattern consisting of cleavage steps. The fracture surface of Si is not perfectly flat due to the different imperfections that deflect the fracture from its original direction. These imperfections can be, for example, grain boundaries or intermetallic inclusions [47]. As can be observed in Figure 4.31 (c), the fracture steps on the Si particle fracture surface are aligned relative to the inclusions which might indicate their local dominant influence on the fracture path.

Dark grey spots on the dimple walls in Figure 4.31 (d) have a convex topography and therefore, can be the impurity contamination coming from the environment. If this is the case, they have to be gone after cleaning the sample. Figure 4.32 shows a SEM micrograph of the fracture surface of the same sample after it has been cleaned in the ultrasonic bath with acetone and isopropanol. Now all impurities are removed, but instead, one can observe dark pits which are most probably due to the cavitation erosion appeared during the prolonged ultrasonic cleaning of the sample. In the ultrasonic bath, a liquid medium vibrating in the acoustic field generates the cavitation which amplifies the effect of the solvents to remove the dust from the surface. However, collapse of the oscillating cavities in the surface vicinity induces explosive shocks that cause the observed surface damage [150]. The fracture surface in Figure 4.32 is very rough, and therefore, it favors stable cavitation voids to be formed therein.

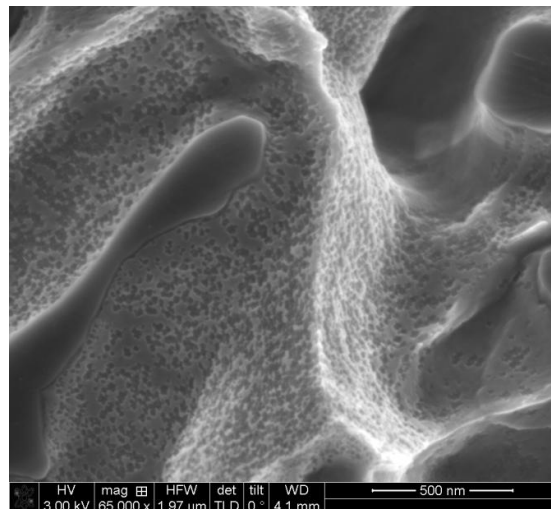


Figure 4.32: Fractograph of the as-cast Mg-containing AlSi12 alloy after the cleaning in the ultrasonic bath. The fracture surface exhibits a high density of cavitation pits.

And last but not least, it can be noticed that the dimple shown in Figure 4.31 (d) has a very regular polygonal shape that resembles a cell of a random mosaic. Interestingly, that the observed fracture patterns can be assimilated with tessellations, where the dimples would be

the cells with boundaries splitting the space into the so-called regions of influence of Si particles built around every Si particle on the fracture surface. These dimples cover completely the fracture surface observed on the fractographs. For the most part, they exhibit relatively simple, nearly convex shapes or shapes with curvilinear edges. It implies that the fracture surface can be simulated by using an appropriate tessellation model, whereby geometric properties of the simulated cells can be computed and correlated to material's properties.

#### **4.6.2 Correlation between dimples and Si particles geometry**

The microstructure of a material has a deterministic role for the fracture surface properties. In particular, the morphology of Si particles, which the fracture meets on its way, defines the dimple morphology, so that the dimple size increases with the particle size and inter-particle spacing, on one hand, while the number of dimples increases with the number of particles in a bulk microstructure, on the other hand [47]. A nearly one-to-one relation between the average dimple size and the average inter-particle spacing has been found for aluminium alloys [69]. However, there are no specific quantitative relations with respect to the influence of Si particles' size-shape distributions in a bulk structure on the fracture surface geometry. Therefore, the following section aims to determine which geometrical features of Si particles exert an influence on the dimple geometry and to what extent they do so. Thus, average properties and their distributions for both particles and dimples from corresponding alloys have been analysed. At the end, the number of investigated features has been limited to the area describing the size of objects, the aspect ratio and the shape factor describing their shape. Other size parameters, in particular the equivalent circle diameter and MaxFerret diameter, have shown equivalent distributions to the area distribution and will therefore not be presented here. The same holds for the shape parameters such as roundness and circularity, which describe different aspects of similarity between an object and a circle.

Figure 4.33 shows histograms of the area distribution of particles on metallographic sections that represent a bulk microstructure and the area distribution of dimples on the fracture surfaces of the corresponding alloys. Si particles and dimples exhibit very similar distributions with a low percentage of outliers consisting of particles/dimples with the area exceeding the average area by the factor of 3 or more. For the sake of comparison, the area and the frequency of particles/dimples have been normalised to the average value of objects area and the number of objects in every class, respectively. Matching distributions indicate a proportional relationship between the size features of particles and dimples. Thus, the area of

## 4.6 Fractography of Al-Si eutectic

the Si particles' cross sections is a characteristic feature that directly influences the fracture surface geometry.

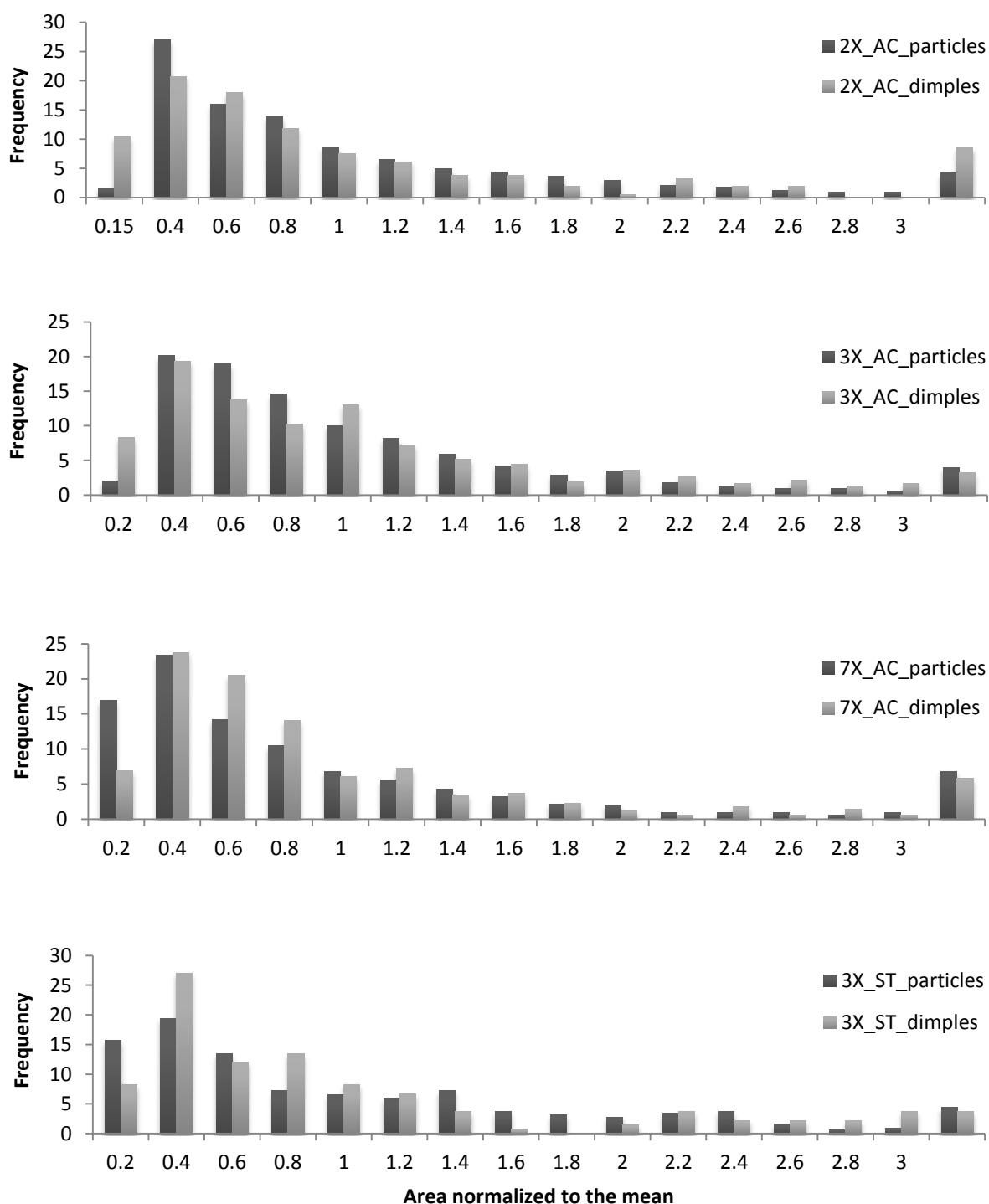


Figure 4.33: Distributions of particles' vs. dimples' area in the unmodified (2X\_AC), Sr-modified (3X\_AC and 7X\_AC) alloys in as-cast state and Sr-modified alloy after heat treatment (3X\_ST). Other ST alloys are not presented here because they have similar distributions to the one of the alloy 3X\_ST (extended from [133]).

Though the nature of the relationship between the size of particles and dimples can theoretically be determined, it is practically hardly possible. The difficulty to compute this relationship is due to the fact that analyzing the size of a Si particle and the size of a dimple corresponding to this particle is in principle not possible since:

- The size of particles is measured on the metallographic sections and the size of dimples is computed on the fractographs.
- Even if the Si particles and the corresponding dimples are both manually segmented on the fractographs, available image processing tools do not allow a tracking of their corresponding properties in the output data.

Attempts to filter particles and dimples by size, assuming that the smaller dimples correspond to the smaller particles, and fit an equation to the data scatter have provided different ratios for different samples. A comparison of the average size values for corresponding micrographs and fractographs has resulted in the ratio of the dimple equivalent area circle diameter to the particle equivalent area circle diameter, which varies between 1.3 and 3. Thus, there is no unique coefficient of proportionality that would fit all structures. The size of dimples depends not only on the size of nucleus-particles but also on the particles arrangement, i.e. the particles density and the inter-particle spacing [47]. Therefore, to predict dimple characteristics on the fracture surface, the geometry and arrangement of microstructural constituents have to be taken into account simultaneously.

Analogously to results reported by Broek [69], Figure 4.34 compares the average dimple equivalent diameter versus the average inter-particle spacing (more precisely, a sum of the average particle equivalent diameter and the interparticle spacing computed in Section 4.4). Few data points fall onto the one-to-one relationship, but in general, the dimple diameter is slightly below the one-to-one trendline which indicates a smaller particle density on the fracture surfaces as compared to the random sections through the material. Here, every particle on the fracture surface is assumed to cause a void initiation. Therefore, the particle density on the fracture surface is identical to the dimple density therein. On the other hand, the particle density on the metallographic sections has been compared with the dimple density on the fractographs and the corresponding data have been summarised in Table 4.8. A good correlation between the two densities can be found for most of the samples. The comparatively higher dimple density observed for the modified alloys 3X\_AC and 7X\_AC could be either due to the slight overestimation of the number of dimples that resulted from

#### 4.6 Fractography of Al-Si eutectic

the sophisticated dimple segmentation procedure or the low statistical representativeness of high resolution fractographs. In fact, the particle density and the average inter-particle spacing have been computed on the metallographic images with a high population of Si particles. The dimple density and the average dimple equivalent diameter have been determined for every alloy as the mean value of several fractographs showing different fields of the sample at high magnification (i.e. low statistics). Hence, a high standard deviation of the measurements can be seen in Table 4.8. Nevertheless, the values of both densities still have the same order of magnitude. Taking into account conclusions drawn from Figure 4.34 and Table 4.8, one can assume a certain degree of randomness of the fracture propagation path. This means that the distribution of Si particles in random metallographic sections through the structure can give a good approximation to the distribution of particles on the fracture surface.

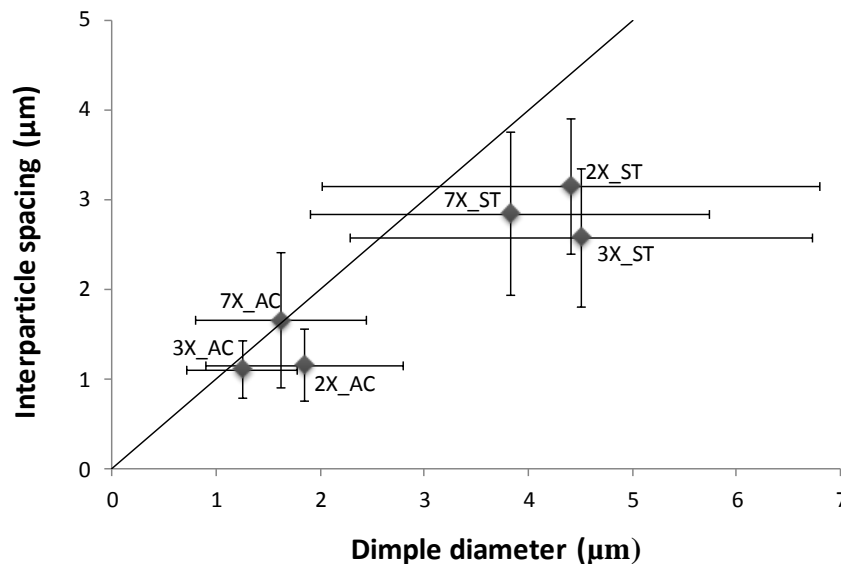


Figure 4.34: Dimple equivalent diameter vs. interparticle spacing in a bulk microstructure in the unmodified (2X), Sr-modified (3X) and inhomogeneously modified (7X) alloys in the as-cast (AC) and solution treated (ST) states. A straight line defines a one-to-one relationship between two data sets.

Table 4.8: Particle vs. dimple densities in different Al-Si alloys. The standard deviation of the dimple density is placed in parentheses. There is a good correlation between the two densities: corresponding densities for the samples have either similar values or at least, the values of the same order of magnitude (extended from [133]).

	2X_AC	3X_AC	7X_AC	2X_ST	3X_ST	7X_ST
Particle density ( $\mu\text{m}^{-2}$ )	0.31	0.37	0.16	0.04	0.05	0.05
Dimple density ( $\mu\text{m}^{-2}$ )	0.31	0.72	0.28	0.05	0.05	0.07
	(0.07)	(0.18)	(0.10)	(0.02)	(0.01)	(0.03)

A different situation is observed for the shape factor. As can be seen in Figure 4.35, the distributions of the shape factors of dimples and particles exhibit different shapes: particles show a higher standard deviation than the dimples for the shape factor, except from the solution treated alloy. Particles also have a higher fraction of objects with lower shape factors than dimples, whereas the dimple system is more homogeneous, i.e. it has a lower variability of the shape factor. According to the definition of the shape factor [124], which compares a particle area to the area of a circle with the same perimeter as the particle's perimeter, decreasing the shape irregularities is associated with a reduction of the object's perimeter, which, as a consequence, increases its shape factor. In this case it means that the shape irregularities present in cross sections of Si particles are transmitted to dimples in a reduced or smoothed manner. Thus, the complexity of the nucleus-particles' shape is not directly reflected by the shape of dimples.

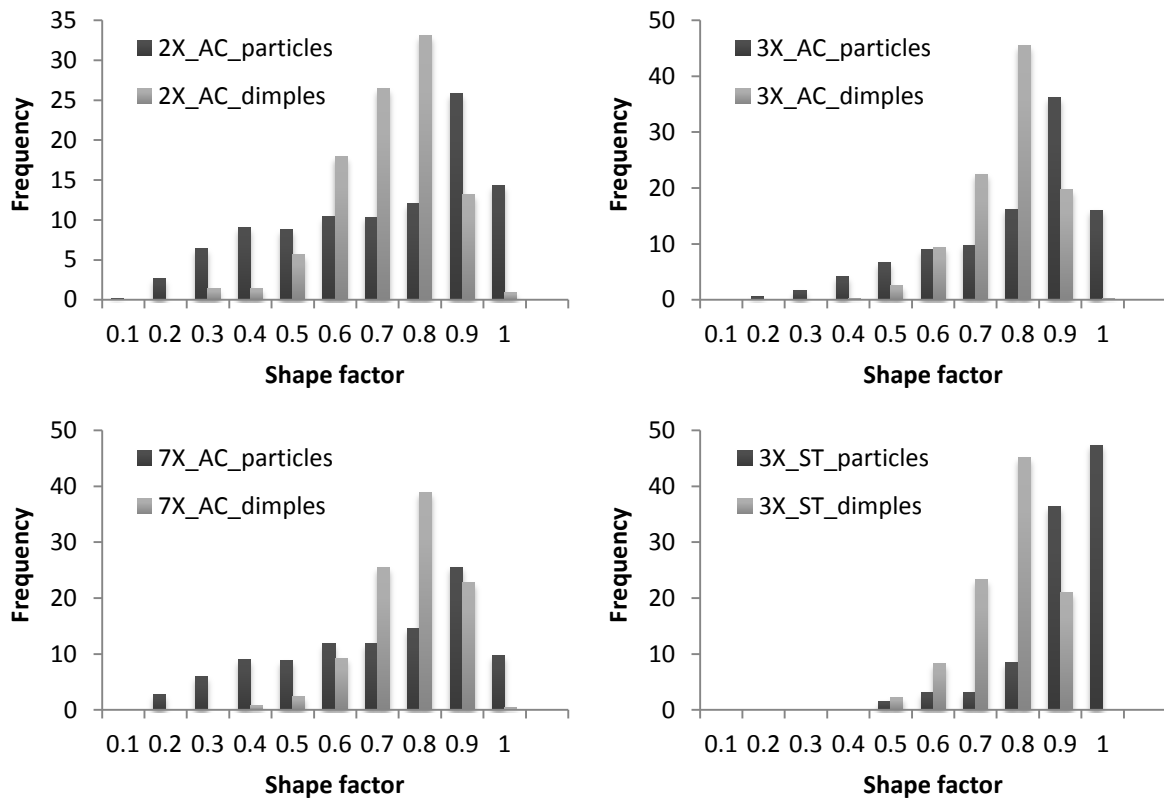


Figure 4.35: Distributions of particles' vs. dimples' shape factor in different Al-Si alloys. The shape factors of dimples and particles exhibit different frequency distribution shapes. No direct relation can be observed between the two data sets of the shape factors (extended from [133]).

The aspect ratio, however, shows better distribution correspondence between particles and dimples than the shape factor (see Figure 4.36). The relationship between the average aspect ratios of dimples and particles for corresponding samples is close to one-to-one (see Table 120

## 4.6 Fractography of Al-Si eutectic

4.9). Therefore, the elongation of particles is broadly transmitted to the dimples. Thus, the aspect ratio can be considered to be another characteristic feature of Si particles with a direct influence on the shape of dimples.

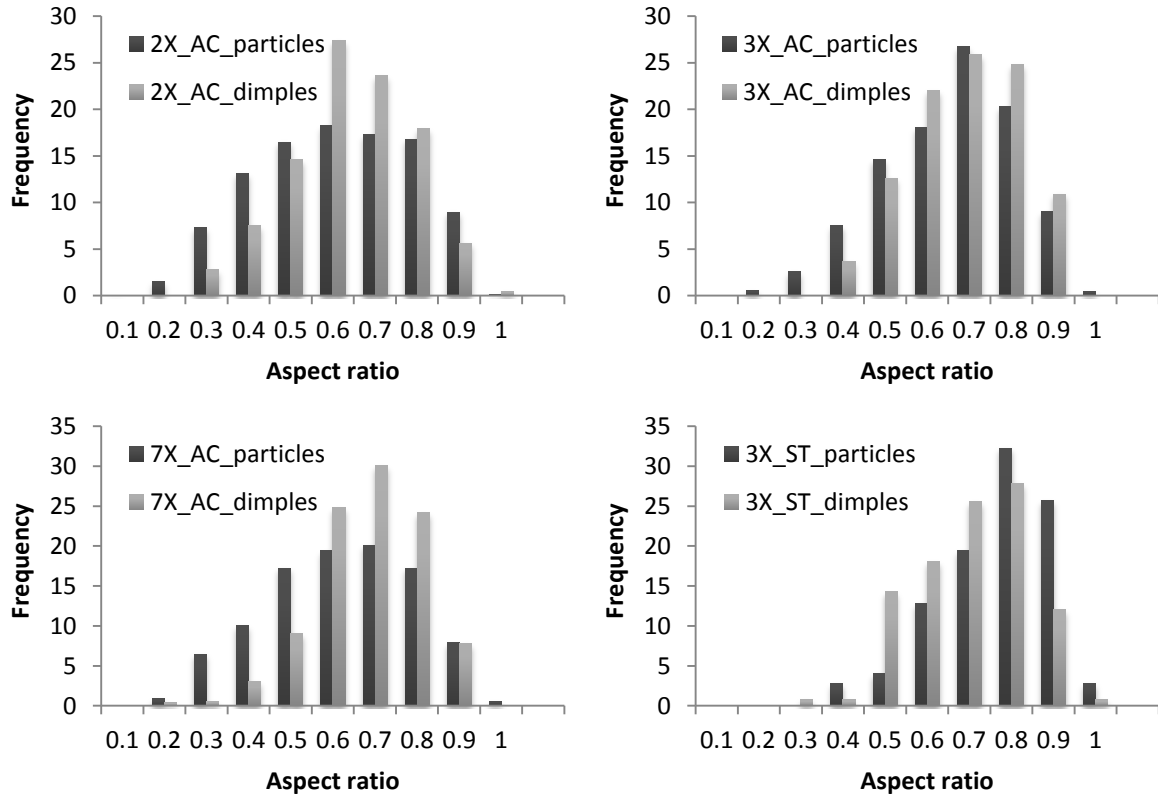


Figure 4.36: Distributions of particles' vs. dimples' aspect ratio in different Al-Si alloys. High conformity between the distributions can be observed (extended from [133]).

Table 4.9: Average particles' vs. dimples' aspect ratio for distributions presented in Figure 4.36. Particles and dimples from corresponding samples have similar average aspect ratios (extended from [133]).

	2X_AC	3X_AC	7X_AC	3X_ST
Particle aspect ratio	$0.56 \pm 0.18$	$0.61 \pm 0.15$	$0.57 \pm 0.17$	$0.71 \pm 0.13$
Dimple aspect ratio	$0.59 \pm 0.14$	$0.64 \pm 0.13$	$0.64 \pm 0.12$	$0.65 \pm 0.13$
Dimple/particle ratio	0.95	0.95	0.89	1.09

The conclusion that can be drawn from the investigation of empirical distributions of structural features on micrographs and fractographs is that there is a correlation between the geometry of dimples and Si particles. In particular, such features as the area, or more general, the size and the elongation of Si particles cross sections together with the arrangement of Si particles relative to each other define for the most part the fracture surface geometry.

## 4.7 Fracture surface modeling

The following section reports the results obtained by modeling the system of dimples on the fracture surface of Al-Si alloys using the weighted Voronoi tessellation. The tessellation model is applied to metallographic images of the eutectic phase to simulate a fracture surface appearance (as projected on a fractograph) which would potentially exhibit this structure if it had been fractured under uniaxial tensile loading. The simulation results are confirmed by experimental measurements indicating the credibility and usefulness of the model. Furthermore, two examples of the application of the modelling results for the determination of the surface roughness parameter and the fracture toughness of the eutectic phase are presented in Sections 4.7.4 and 4.7.5, respectively. However, before reporting the simulation results, a brief review of the previous observations is done to demonstrate the pre-conditions and motivation for using mosaic models and in particular, their weighted version for the fracture surface simulation. The results have been summarized by Kruglova et al. in publication [133]. Sections 4.7.1 – 4.7.4 contain an excerpt from the section “*Results and discussion*” of the underlined publication.

### 4.7.1 Pre-conditions and motivation

Considering that the classical Voronoi tessellation consists of non-overlapping, convex and space-filling polytopes [60], the structure to be modelled by means of a Voronoi mosaic has to comply with these requirements as well. As has been shown in Section 4.6.1, the dimples on the fracture surfaces most of the time cover a fracture surface plane completely and do not overlap. Some dimples have a more explicit polygonal shape while others are less regular, but on average, they can all be approached by cells with curvilinear edges. The deviations from convexity are not extreme and do not hinder simulations, because the weighted tessellation model allows for the generation of curvilinear cell edges.

Another important point to take into account when modelling the fracture surface on the basis of planar sections is that the fracture surface appearance is in most cases related to the microstructure underneath, so that the Si particles’ arrangement influences the fracture propagation path. Normally, the fracture propagates not on a single plane, but rather through preferential paths that are usually the planes with higher particle density. It means that the particle density on the polished plane,  $N_A$ , is not necessarily equal to the particle density on the projected plane of the fracture surface,  $N'_A$ . (see Figure 3.12). Here, both densities are identical (see Table 4.8) which is likely to be due to the very fine and homogeneously

distributed Si particles in the investigated alloys. This implies that the quantities measured on the micrographs of polished planes are also valid for the corresponding fractographs [47]. Moreover, geometric features of dimples strongly depend on those of Si particles, so that the shape and size of a nucleus Si particle will be reflected in proportional dimensions of a corresponding dimple. These are two important conclusions, which justify the modelling of fracture surface on the basis of 2D micrographs of planar sections.

The following bullet points summarise the essential preconditions for using the tessellation model to simulate fracture surfaces:

- Shape of the dimples can be approached by the Voronoi tessellation cells.
- Quantities measured on planar sections are valid for the corresponding fractographs.
- Geometrical features of Si particles on planar sections constitute sufficient input to model a dimple system on fracture surfaces.

### 4.7.2 Model fitting and verification

Basically, cells of the planar Voronoi tessellation divide a plane in such a way that their edges are located equidistant to generator points. This principle can be realised in many types of image processing software, simply by applying the Euclidean distance transformation on binary images followed by the watershed transformation. This basic idea has been applied to the binary images of the investigated alloys and the output tessellation has been compared to the system of dimples on the real fracture surface. The dimples and Si particles on a fractograph of the modified alloy (Figure 4.37 (a)) have been outlined manually to obtain the most accurate picture of the fracture surface for image analysis (Figure 4.37 (b)). The normal Voronoi tessellation has then been generated on the set of particles segmented from the same fractograph (Figure 4.37 (c)).

It is important to note, that the tessellation resulted from the described procedure, though called “normal Voronoi tessellation”, is not a Voronoi tessellation in its classical sense where it is built on the basis of generator points. Here, the borders of the tessellation are built with respect to the particle borders and not with respect to the particle centroids as the classical Voronoi mosaic would imply. However, since the principle remains the same – the borders between tessellation cells are located equidistant to generator points (here, particles) – and for the purpose of distinguishing from the developed weighted Voronoi tessellation, we call it the normal Voronoi tessellation. However, this tessellation exhibits slightly different geometric

properties as compared to the classical Voronoi mosaic: for example, the reconstructed cells are not necessary convex but contain also curved boundaries.

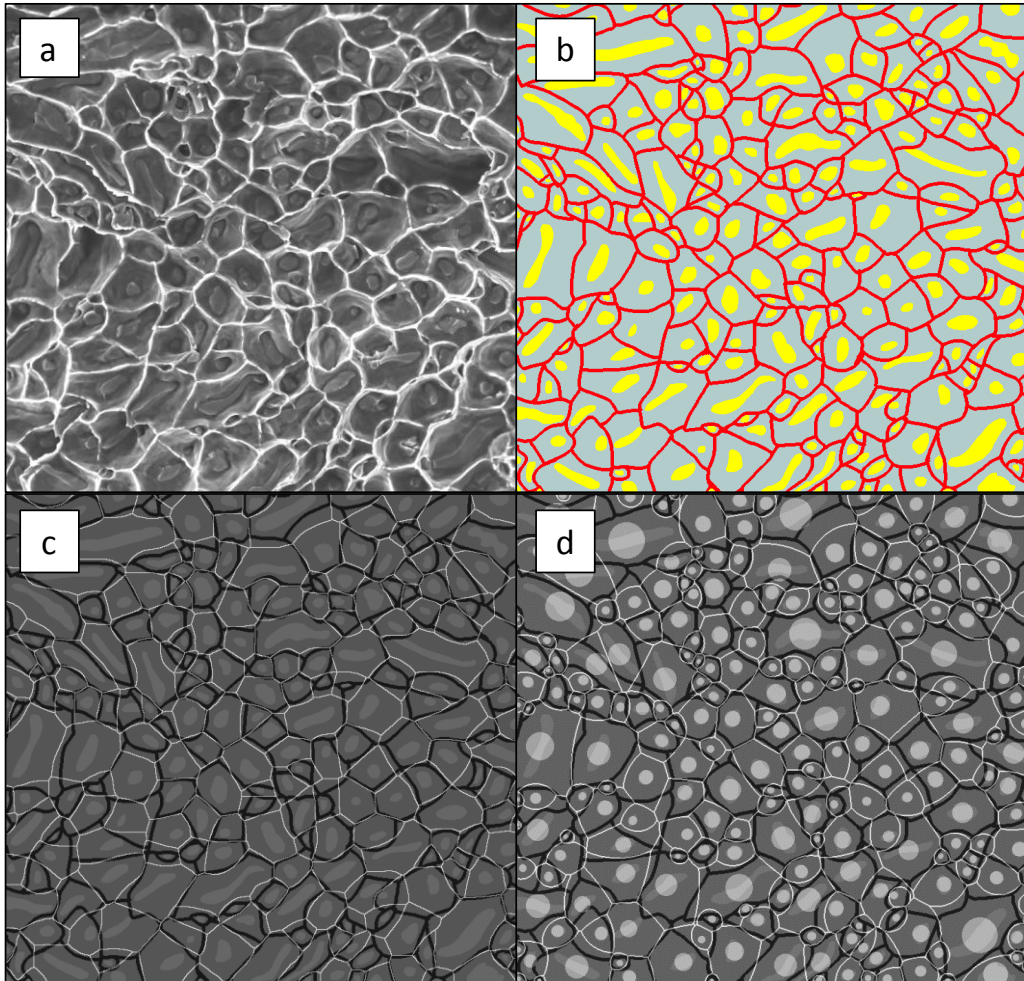


Figure 4.37: (a) Fractograph of the modified Al-Si alloy; (b) dimple system and Si particles segmented from the fracture surface; (c) realization of the normal Voronoi tessellation and (d) realization of the weighted Voronoi tessellation superimposed on the fracture pattern. Light gray lines correspond to the tessellations; black contours belong to the fracture surface. Light gray circles illustrate a weight given to every generator point by the weighted Voronoi model [133].

Though both the dimples in the real and the simulated fractographs have the same average dimple area of  $0.97 \mu\text{m}^2$ , the areal distributions in Figure 4.38 show that the normal Voronoi tessellation synthetically increases the area of dimples nucleated at small particles, so that the number of small dimples is underestimated. This discrepancy results from the principle of the Voronoi tessellation, where the border between neighbouring cells lies in the middle between their generators. In reality, the borders do not necessarily lie in the middle between the particles on the fracture surface but are rather shifted towards smaller particles, whereas larger particles have proportionally larger dimples, i.e. the particles' area proportionally amplifies the area of the corresponding dimple. This size effect cannot be captured by the normal

Voronoi tessellation. Therefore, the weighted mosaic model has been developed (Figure 4.37 (d)). As can also be observed in the experimental data, when two neighboring cells have different sizes, the smaller cell is usually convex while the larger one has concave boundaries. The similar effect has been observed in [142] by using Johnson-Mehl tessellation for the reconstruction of austenitic grain boundaries in steel. It seems that the weighted Voronoi tessellation can reproduce very well this geometrical feature of dimples on fracture surfaces whereas the classical Voronoi tessellation can generate the convex cells only.

The weighted Voronoi tessellation model uses the particles' area to weight every generator point, i.e. a particle centroid. Then, the weight function takes the square root of the particles' weight. The value thus obtained is used to compute a weighted distance between a generator and background points. According to the algorithm described in Section 3.7.5, every point is assigned to the zone of influence of the nearest generator. An important remark on the algorithm concerns the choice of the particle area as a weighting feature for the modelling. Geometrical properties of the dimples actually depend on those of the nucleus particles, as has been discussed in Section 4.7.1. The characteristic features for the modelling should therefore include both size and shape parameters. The size of dimples is sensitive to the area of nucleus-particles and thus is an appropriate characteristic feature for the modelling. Moreover, the dimple area and the equivalent diameter computed on the basis of the dimple area can be used to estimate further quantities such as fracture surface area, roughness and toughness. On the one hand, the primary goal has been to obtain a structure with similar distribution of the dimple area, rather than the perfect match between the edge system of tessellation and the fracture surface. On the other hand, the model should remain as simple as possible. As a result, only one size parameter has been used for weighting purposes. Of course, introducing a shape parameter could lead to a better fit and more variability of the model. At the same time, however, it would have a negative effect on the algorithm fitting procedure, i.e. it would make it more complex and time-consuming. In this respect, the weighted Voronoi tessellation developed for the simulation of fracture surfaces has the following advantages: low computation time and easy implementation, however, at the expense of the accuracy of the structure representation.

A graphical comparison of size and shape distributions of structural elements between the experimental data set and a model realization is often used to assess the quality of the model [140]. As can be seen in Figure 4.38, the dimple area distribution in the weighted Voronoi tessellation corresponds closely to the real fracture surface, although its average value of 0.88

$\mu\text{m}^2$  is slightly lower than the experimental value. However, the aspect ratio distribution of the normal Voronoi tessellation features better conformity to the real fracture surface than the weighted mosaic. But, as has been mentioned above, the model has not been aimed at providing perfect shape correlation, but primarily at size distribution matching. Since the areal distribution provided by the weighted tessellation corresponds well to the experimental distribution, the weighted Voronoi model has been shown to be effective in simulating the fracture surface geometry. Although some individual borders do not match perfectly, overall, the model developed captures quite well the size characteristics of dimple projections.

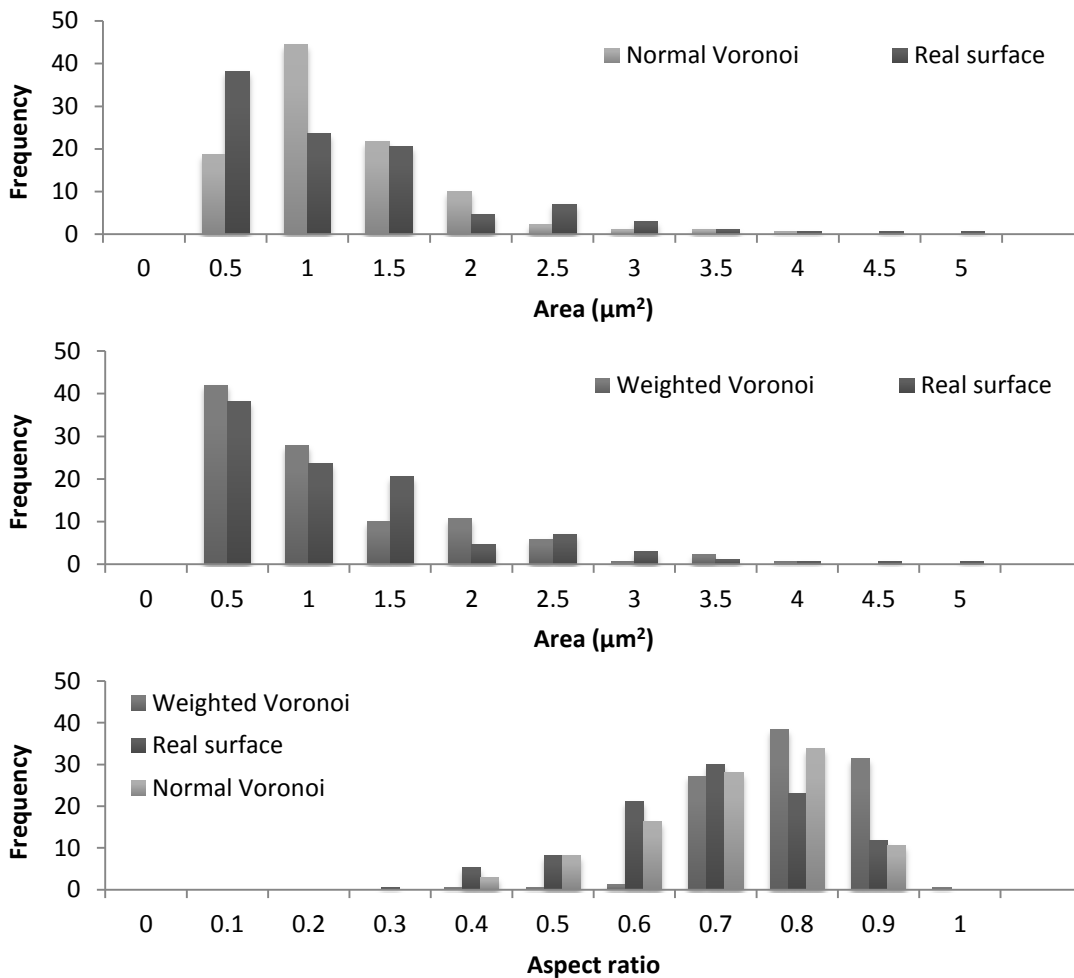


Figure 4.38: Distributions of dimple area and aspect ratio computed on the real fracture surface of the modified Al-Si alloy and its realizations via normal and weighted Voronoi tessellations. Areal distribution of the normal Voronoi tessellation overestimates the area of dimples nucleated at smaller particles, whereas the weighted Voronoi tessellation corresponds better to the real fracture surface. The aspect ratio distribution of the normal tessellation provides a better match of the real fracture surface than the one of the weighted tessellation [133].

Further improvements of a tessellation model performance can be made by using the anisotropic growth models (ellipsoidal growth models) described in Section 3.7.4 [139,142]

which allow to better capture irregularities and elongation of modeled elements. In the context of this study, however, it is not crucial since the modeled structures exhibit quite homogeneous shapes in both as-cast and solution treated states. Nevertheless, the anisotropic growth models would gain their relevance, for example, for the simulation of the fracture surface in the unmodified alloys containing coarse and irregular Si lamellae. The development of such models is however out of the scope of the present investigation that has a rather methodological character aiming at the demonstration of a new direction for potential use of tessellation models for the fracture surface modeling.

### 4.7.3 Simulation of fracture surfaces

The practical use of the weighted tessellation model has now been verified for the planar sections (in contrast to previous realizations for the set of particles located directly on the fracture surface). For six alloys under investigation, the weighted Voronoi tessellation is generated for the respective metallographic sections. Examples of simulated fracture surfaces are given in Figure 4.39.

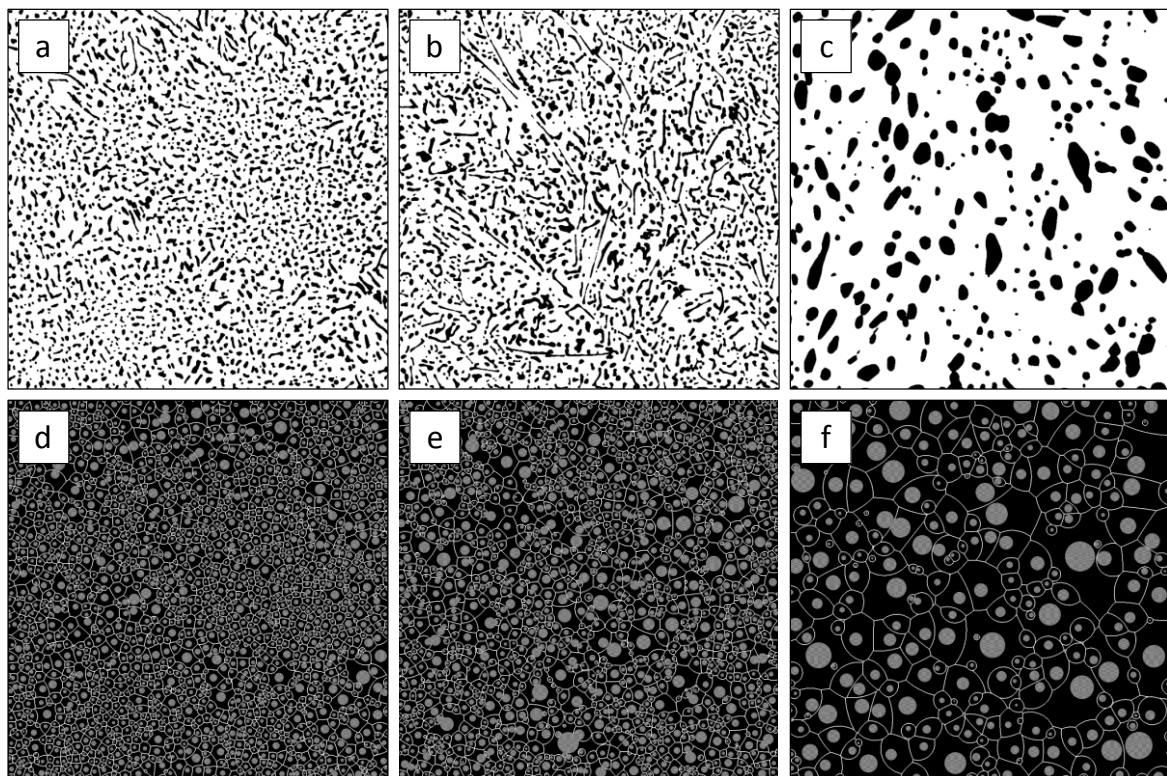


Figure 4.39: binary micrographs of (a) modified, (b) unmodified as-cast alloys and (c) modified alloy after solution treatment; (d) – (f) corresponding realizations of the weighted Voronoi tessellation [133].

The main requirement to the tessellation is its ability to reproduce characteristic features of fracture surfaces, so that a generated cell structure fits the corresponding fracture surface projection with respect to the principle size-shape parameters and in particular the areal distribution. Therefore, quantitative characteristics of the simulated fractographs have been compared to those of the dimple system on real fracture surfaces and are shown in Figure 4.40.

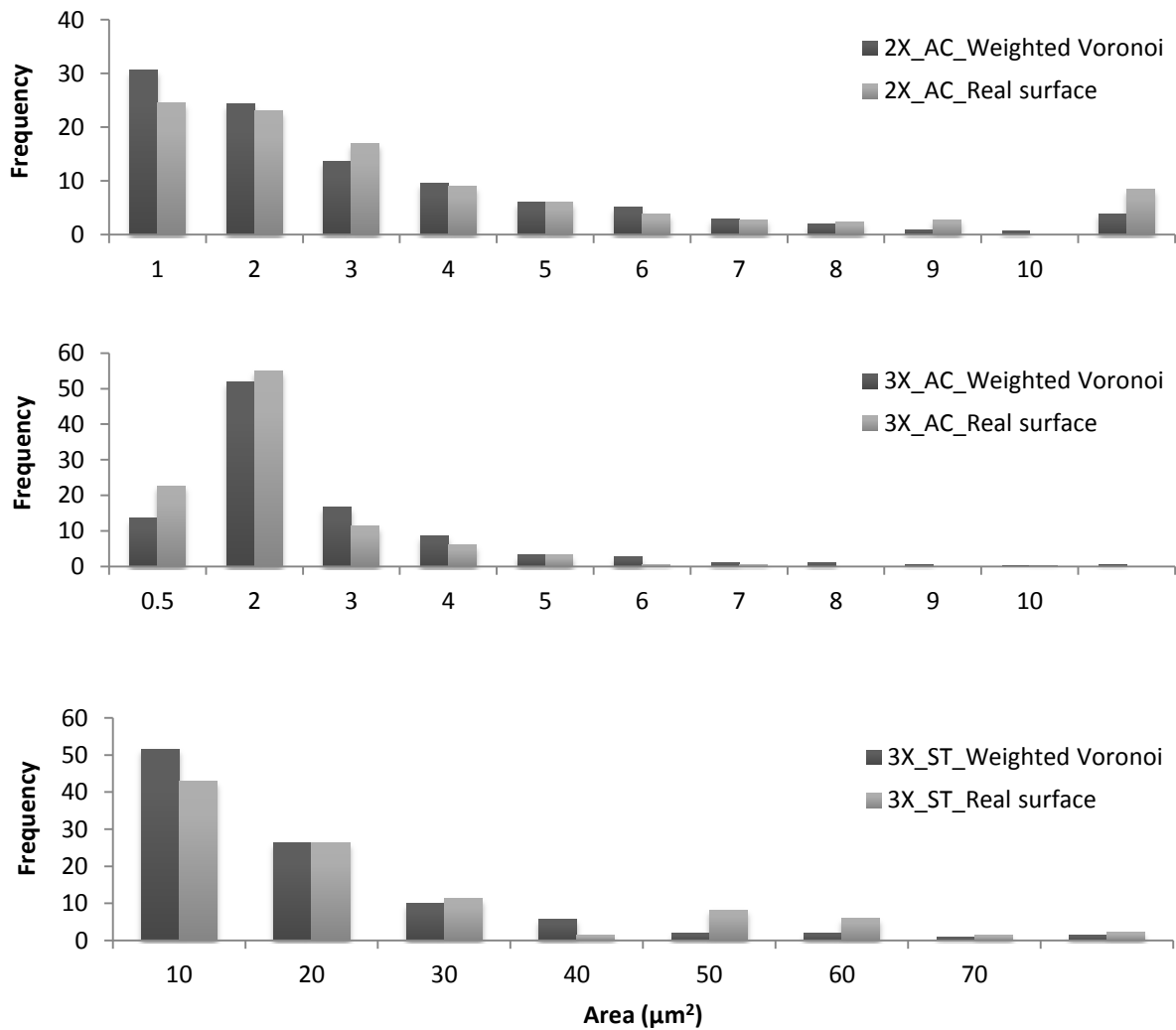


Figure 4.40: Distributions of dimple area on the fracture surfaces of the unmodified (2X\_AC) and modified (3X\_AC and 3X\_ST) Al-Si alloys and their realisations via weighted Voronoi tessellations on the metallographic images. The weighted Voronoi tessellation shows a good correlation to the real fracture surface with respect to the dimple size distribution [133].

As can be seen from the histograms, the model provides a realistic area distribution that can be used to estimate the topographic properties of fracture surfaces and a material's toughness. In principle, it does not matter on which dimple system the topographic quantities are

estimated because both virtual and real data show a high overlap. For demonstration purposes, computing of further quantities will be done on virtual fracture surfaces.

### 4.7.4 Estimation of topographic features

Once a virtual fracture surface has been generated, the fracture surface area,  $S_{total}$ , can be computed as a sum of the surface areas of every single dimple,  $S_i$ . In order to estimate the real surface area of a dimple, information available on 2D simulated fractographs has to be seen in relation to the topographic nature of the fracture surface. To do so, every dimple is approximated to a half of an oblate ellipsoid that has a diameter equal to the dimple equivalent area circle diameter and a third semi-axis equal to the dimple depth. The depth of dimples is computed from their width, given the depth-to-width ratio. The ratio values vary significantly depending on the material [87,88]. For aluminium alloys, it has the order of 1/3 to 1/5 [69]. Experimental measurements on FIB cross-sections of fracture surfaces in the modified Al-Si alloy 3X\_AC have yielded an average depth-to-width ratio of  $0.28 \pm 0.07$ . This value is consistent with the values reported in literature and will be used for further computations. Henceforward,  $S_i$  and  $S_{total}$  can be calculated according to Equations 3.6 and 3.7. The corresponding surface roughness parameter defined as a ratio of the true surface area,  $S_t$  (or  $S_{total}$ ), to the projected area,  $A'$ , is equal to 1.45 (Equation 3.9).

The accuracy of the approximation can now be verified by comparing the surface roughness parameter computed by using the ellipsoid-approximation versus stereological equations. A fracture surface profile analysis performed on FIB cross-sections of the modified Al-Si alloy returns the average true profile length,  $L_t$ , of  $17.26 \pm 0.98 \mu\text{m}$  and the projected length,  $L'$ , of  $13.97 \mu\text{m}$ , which results in the profile roughness parameter,  $R_L$ , of 1.24 (Equation 3.10). The corresponding surface roughness parameter,  $R_S$ , as computed via stereological Equation 3.8, is equal to 1.57.

As has been demonstrated by the calculations above, both surface roughness parameters show similar values, which points towards the accuracy of an approximation of a dimple with a half-ellipsoidal shape. A slightly higher roughness computed by stereological means could be due to the slight overestimation of the average true profile length,  $L_t$ , caused by the particular way it has been computed. Figure 4.41 illustrates an example of a fracture surface profile segmented from the FIB cross-section. Here, to compute the true profile length in a straightforward way, the profile perimeter has first been determined using image analysis software. It then has been divided by two, since the segmented surface is only a few pixels thick, i.e. the

profile thickness is negligible compared to the length. However, some profile areas have an increased thickness, as pointed out by the arrows in Figure 4.41. Hence, a slightly increased value of the true profile length and, as a consequence, an increased profile and surface roughness have been estimated.

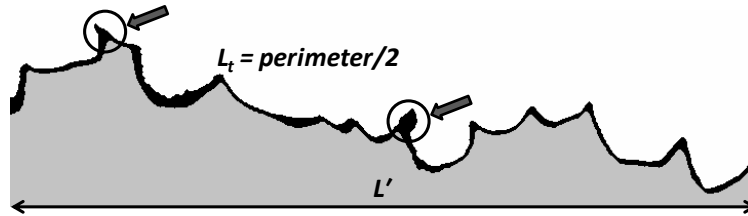


Figure 4.41: Fracture surface profile segmented from the FIB cross-section. The true profile length,  $L_t$ , is equal to the half of the perimeter.  $L'$  is the length of the profile projection. Arrows point at segmentation artifacts that lead to the profile perimeter increase [133].

Besides, the surface roughness parameter has been computed with the help of the tomographic data of the fracture surface in the modified alloy 3X\_AC (see Figure 4.42).

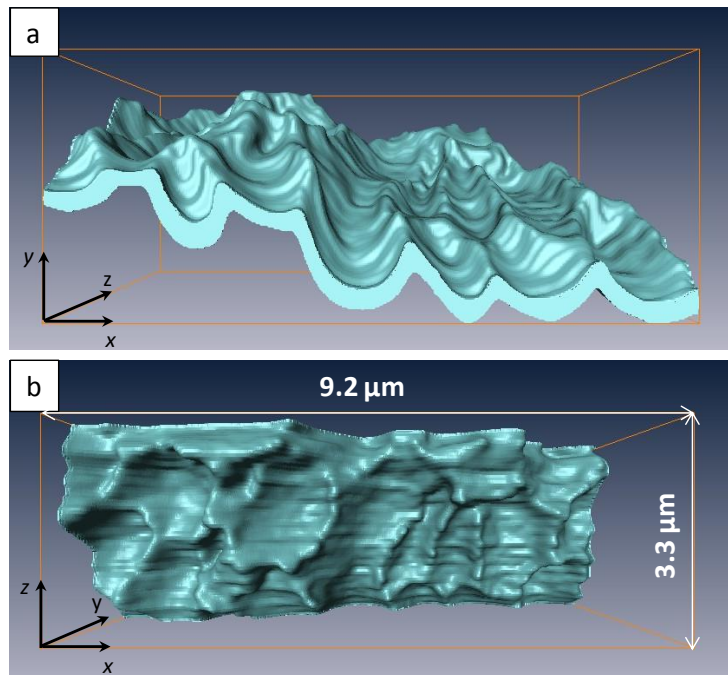


Figure 4.42: 3D reconstruction of the fracture surface in the alloy 3X\_AC after tensile loading as viewed from different perspectives ((a) and (b)).

Analogously to the true profile length estimation, the true surface area,  $S_t$ , has been computed by dividing the surface area of the fracture surface by two, since the thickness of the segmented surface is much smaller than the two other dimensions. Still, the surface thickness has been synthetically increased due to the challenging image processing procedure that has

## 4.7 Fracture surface modeling

been used to “close” multiple holes in the initially segmented fracture surface (artefacts of the interpolation of the labelled 2D images of the fracture surface in Amira) and obtain an integral surface for the analysis. As a consequence, the surface roughness parameter of 1.74 computed according to Equation 3.9 is also overestimated. Nevertheless, it is still close to the values defined using the ellipsoid-approximation and stereological equations thus confirming the validity of two latter methods.

The value of the surface roughness parameter is also very sensitive to the depth-to-width ratio. Figure 4.43 shows the surface roughness parameter of the considered structure as a function of the dimple depth-to-width ratio. A polynomial of a second order is fitted to the point scatter, so that by knowing the average depth-to-width ratio of dimples on a fracture surface or any particular region of the fracture surface, its roughness can easily be determined. Evidently, for the depth-to-width ratios larger than 0.5, the empirical function is no more applicable since an ellipsoid becomes prolate and the approximation is no more valid. Nevertheless, for the absolute majority of dimples observed experimentally, the depth-to-width ratio has been smaller than 0.5.

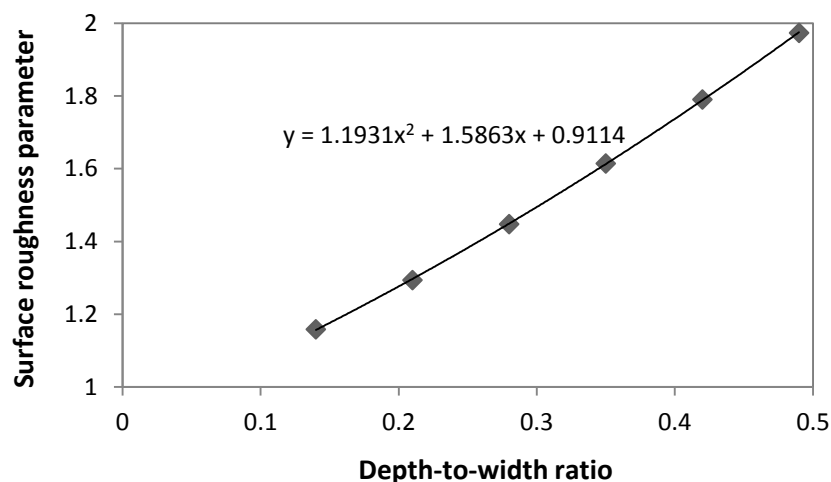


Figure 4.43: Surface roughness parameter plotted as a function of the depth-to-width ratio. Polynomial fitted to the point scatter expresses the roughness parameter by a second order function of the depth-to-width ratio [133].

These are very useful findings for practical applications considering that now both the fracture surface area and the roughness can be computed directly with the help of simulated Voronoi diagrams (given the depth-to-width ratio). In contrast to this, their stereological estimation requires an experimental input which can only be obtained by analyzing a statistically relevant number of fracture surface cross sections, for example, obtained from tomographic

reconstruction. Also, standard techniques such as SEM stereo measurements cannot always provide information on the topographic properties of a fracture surface. For example, SEM stereo imaging has not worked out for the investigated alloy due to the lack of contrast necessary to distinguish Si particles at the bottom of dimples (see Section 3.6.1). Topographic features estimated on the basis of simulated fracture surfaces given the depth-to-width ratio can further be used for computation of the fracture toughness via different analytical formulae.

#### **4.7.5 Example of fracture toughness estimation**

To illustrate a further potential use of the model, the fracture toughness represented by the stress intensity factor has been computed on the basis of the simulated fracture surfaces using analytical Equations 3.15 and 3.16 (see Section 3.6.6). The required values of the ultimate tensile strength of the alloys have been taken from Table 4.4 that summarizes morphological and mechanical characteristics of the alloys in Section 4.4. The dimple depth has been computed according to the procedure described in Section 3.6.3 with the average depth-to-width ratio of 0.28 as defined in the previous section. Furthermore, as has been discussed in Section 4.4, the experimentally defined values of the Young's modulus are largely underestimated. The more precise values of the Young's modulus have only been measured for two out of six alloys: in particular, the Young's modulus of 72 and 70 GPa has been estimated for the alloys 3X\_AC and 7X\_AC, respectively. Besides, the Young's modulus of 77 and 75 GPa has been found in the literature [146] for the unmodified AlSi12 in the as-cast and solution treated state, respectively. These values have been used to compute the fracture toughness of the unmodified alloys 2X\_AC and 2X\_ST. Thus, it has been decided to make computations only for the alloys with available data. The results obtained have been summarized in Table 4.10.

An important remark that has to be made before interpreting the results in Table 4.10 is that the fracture toughness determined via Equations 3.15 and 3.16 corresponds to the eutectic phase only and is not representative of the entire material. The eutectic phase has a lower toughness than the highly ductile aluminium cells. Thus, the major part of the toughness is conferred to the alloys by the primary aluminium phase. Though the eutectic input in the overall toughness of Al-Si alloys is reduced as compared to the primary phase, it cannot be neglected since the fracture propagates mainly through the eutectic phase [74]. Therefore, the influence of different morphological scenarios on the fracture toughness of the eutectic phase will now be analyzed.

### I. Fracture toughness of the eutectic phase

The fracture toughness of the eutectic phase in the investigated alloys computed via Equations 3.15 and 3.16 is presented in Table 4.10. Thereby, the fracture toughness is related to the energy required to form a unit of fracture surface and is adapted to fracture surfaces with a parabolic shape of the relief [87,110], hence, a factor  $\frac{1}{2}$  under the square root.

Table 4.10: The fracture toughness of the eutectic phase in different Al-Si alloys computed via analytical Equations 3.15 and 3.16. In Equation 3.15,  $E$  and  $\sigma_{UTS}$  are the Young's modulus and the ultimate tensile strength of the alloy;  $h_s$  is the average dimple depth. In Equation 3.16,  $V_i$  is the volume fraction of a dimple with the depth  $h_{si}$ .

$K_C$ (MPa · m <sup>1/2</sup> )	Analytical expression	2X_AC	3X_AC	7X_AC	2X_ST
$K_{C_{eutectic}(3.15)}$	$(Eh_s\sigma_{UTS}/2)^{1/2}$	2.5	2.2	2.8	3.6
$K_{C_{eutectic}(3.16)}$	$\left(\frac{E\sigma_{UTS}}{2}\right)^{1/2} \sum_{i=1}^n V_i h_{si}^{1/2}$	3.0	2.5	3.6	4.0

It is important to note that the computed  $K_C$  values serve to compare the fracture behavior of the eutectic phases with different Si morphology relative to each other and to determine which morphological scenario of the eutectic phase is more beneficial for the toughness. However, these values in no way should be interpreted quantitatively, since the stress intensity factor characterizes the fracture toughness in the linear elastic case and is usually used to assess the fracture resistance of brittle materials. It is therefore not valid for the materials exhibiting a substantial plastic deformation like the investigated Al-Si alloys. To evaluate the fracture toughness of the materials exhibiting the large plastic deformation, the J-integral is used instead. Yet, the model and the approach of computing the fracture toughness of materials on the basis of modeled fracture surfaces might deliver accurate results in the case of brittle materials.

Leaving aside for the moment the impact of the primary aluminium cells on the fracture toughness of the alloys, it is still possible to make important conclusions about the influence of different Si morphologies on the fracture toughness of the eutectic phase on a comparative basis. First of all, the fracture toughness computed via Equation 3.15 using the average dimple depth has shown lower values as compared to Equation 3.16 which takes into account the influence of every single dimple, and therefore, delivers more accurate values of the fracture toughness. Thus, only the results obtained via Equation 3.16 will be used for further discussions.

The following conclusions can be drawn from Table 4.10:

- The modified alloy 3X\_AC has the lowest toughness among the investigated alloys.
- The highest toughness among the as-cast alloys is obtained for the inhomogeneously modified alloy with Mg addition, 7X\_AC.
- The unmodified alloy 2X\_ST in the solution treated condition has a higher toughness than the as-cast alloy 2X\_AC.

In general, these comparative results are in good agreement with the state-of-the-art observations on Al-Si alloys. Keeping in mind the morphological and mechanical characteristics of the alloys reported in Table 4.4, the improved toughness of the solution treated alloy 2X\_ST can be explained by a larger size of Si particles and inter-particle spacing as well as their more homogeneous distribution in the matrix as compared to the as-cast alloy 2X\_AC [77,78,106]. The difference between the toughness of the modified and unmodified as-cast alloys, 3X\_AC and 2X\_AC, might be explained by a slightly larger size of Si particles and superior strength characteristics of the unmodified alloy. The former results in the higher fracture surface area while the latter leads to the increase of the fracture toughness according to Equation 3.16. The same holds true for the inhomogeneously modified alloy 7X\_AC. Nevertheless, it is interesting that the inhomogeneously modified alloy 7X\_AC has the highest toughness among the as-cast alloys. Normally, the increase in strength leads to the reduction of the ductility [68,107]. Here, however, the increase in strength is accompanied by the simultaneous increase of the average particle size and inter-particle spacing, which exert opposing effects on the fracture toughness. It seems that the given combination of structural properties has an overall positive effect on the toughness.

A good correspondence between the predictions of the impact of different Si morphologies on the toughness based on the simulated fractographs and the state-of-the-art observations of Al-Si alloys demonstrates the usefulness of the modeling approach. In particular, it allows to extract average values along with distributions of geometrical features of dimples for computing the stress intensity factor with a minimum of experimental effort. The model proves therefore to be efficient in generating virtual fractographs that can be used to assess the impact of Si morphology on the fracture toughness of different eutectic structures, at least on a comparative basis. Besides, the approach of computing the fracture toughness of materials on the basis of modeled fracture surfaces, though not perfect for Al-Si alloys, might still be accurate for brittle materials consisting of matrix with second phase particles.

## II. Fracture toughness of the alloy

A rough estimation of the fracture toughness of two-phase alloys can be made using a linear rule of mixture which sums up the toughness of each phase multiplied by the respective volume fraction. The fracture toughness computed by this way is however often overestimated since the fracture toughness of a bulk material and the toughness of the same material constituting a phase in a composite with a constraint deformation possibility are not the same [151]. Uggowitzner and Speidel [74] have compared the fracture toughness computed using the linear rule of mixture (Equation 4.2), the rule of mixture which takes into account the contiguity of phases (Equation 4.3) and the experimental measurements of the alloys with different volume fraction of the eutectic. Hereby, the fracture toughness of the composite has been defined by the J-integral,  $J_C^C$ :

$$J_C^C = J_C^\alpha V_V^\alpha + J_C^\beta V_V^\beta \quad 4.2$$

$$J_C^C = J_C^\alpha V_V^\alpha C^\alpha + J_C^\beta (1 - V_V^\alpha C^\alpha) \quad 4.3$$

where  $J_C^\alpha$ ,  $V_V^\alpha$  and  $J_C^\beta$ ,  $V_V^\beta$  are the fracture toughness and the volume fraction of the primary aluminium and the eutectic phase, respectively;  $C^\alpha$  is the contiguity of the primary aluminium which is defined by the authors as “the fraction of the total internal surface area of a phase that is shared by particles of the same phase” [74]. In [74], the contiguity-based rule of mixture has shown better correspondence to the experimental results whereas the fracture toughness defined by the linear rule of mixture has been significantly larger than the experimental one. However, as can be seen from Equations 4.2 and 4.3, for the alloy compositions with 0 and 100% of  $\alpha$ -aluminium (0 and 100% contiguity of  $\alpha$ -phase, respectively) both rules coincide. Therefore, the linear rule of mixture is considered to be applicable for computing the fracture toughness of the eutectic alloys and the alloys close to the eutectic composition.

Thus, to estimate the fracture toughness using Equation 4.2, it is necessary to define J-integral values of both phases and their respective volume fractions. The volume fraction of the phases can be defined by means of the image analysis of metallographic sections. The value of the fracture toughness of the primary aluminium can be found in the literature. According to results of Uggowitzner and Speidel [74], the J-integral fracture toughness of the primary aluminium equals 13.4 – 16.2 kJ/m<sup>2</sup>. Then, estimating the J-integral values of purely eutectic alloys with different Si morphologies would be of great importance in order to verify the analytically predicted impact of Si morphology on the fracture toughness of the material.

Although the J-integral fracture toughness can be computed using the stress intensity factor via Equation 4.4 [68,111]:

$$J_{IC} = \frac{(K_{IC})^2}{E}(1 - \nu^2) \quad 4.4$$

where  $E$  is the Young's modulus and  $\nu$  is the Poisson's ratio, this equation cannot be used to compute the J-integral fracture toughness of the eutectic phase in the present case. As has been discussed previously, the computed in Table 4.10 values of the stress intensity factor should not be interpreted quantitatively. Indeed, the investigated Al-Si alloys exhibit a ductile type of rupture. Therefore, the plastic component of the fracture toughness defined by the J-integral might be very high, which obviously cannot be taken into account by the stress intensity factor characterizing a linear elastic case. Thus, in the present case, two toughness measures are not equivalent.

Due to the size limitations of the ingots (see Figure 3.1), it has not been possible to prepare specimens for the J-integral testing method. On the contrary, small samples for the measurements of the stress intensity factor could still be machined. The fracture toughness measurements have been performed on two specimens of the as-cast alloys, 3X\_AC and 7X\_AC, by means of the three-point bending test [111,112]. However, only the conditional fracture toughness,  $K_Q$ , has been determined since the requirements of Equations 3.13 and 3.14 for the estimation of the critical value of the stress intensity factor,  $K_{Ic}$ , have not been met. Indeed, Al-Si alloys have a high toughness and normally exhibit a large plastic region near the crack-tip which, in this case, even exceeds the width of the ligament in the specimens. This contradicts, however, to the test requirement for the plastic zone around the crack-tip to be smaller than the thickness of a specimen [111]. Since the elaboration of larger specimens has also not been possible,  $K_{Ic}$  values could neither be determined.

In general, little data is currently available on the fracture toughness of the eutectic Al-Si alloys. Uggowitzer and Speidel [74] have reported the J-integral fracture toughness of the eutectic alloy of 3.2 – 4.6 kJ/m<sup>2</sup>. However, the morphological properties of Si particles, DAS and tensile properties of Al-Si alloys characterized in [74] have not been presented. Yet, the difference in these characteristics in the alloys with the same chemical composition might result in their different fracture resistance. Ranganatha and Srinivasan [152] have estimated the conditional stress intensity factor of 12.10 MPa · m<sup>1/2</sup> in AlSi12 alloy casted in a metal mould, but again, this value cannot be regarded as a valid plain-strain stress intensity factor.

## 4.7 Fracture surface modeling

---

Thus, due to the lack of valid experimental data for the eutectic Al-Si alloys, there is no solid basis for a comparison. The experimental estimation of the fracture toughness of the investigated alloys and optimization of the analytical estimation methods are still to be performed. To compute more accurate fracture toughness, further investigations can be made, such as:

- instead of using the average depth-to-width ratio, the dimple depth can be expressed as a function of its width;
- investigation of the interaction between the “plastic” primary aluminium phase and “elastic” eutectic phase; consideration of the effect of contiguity.

In summary, a methodology to make a rough estimation of the fracture toughness by means of the analytical methods applied to simulated fracture surfaces has been described, which demonstrates a potential use of the approach developed for the fracture surface modeling. However, to develop more accurate predictive schemas further investigations are required.



## 5 Conclusions and Outlook

---

### 5.1 Conclusions

This work has addressed the morphological impact of the eutectic Si on the mechanical performance of Al-Si alloys using a multidisciplinary approach including virtual simulations and laboratory experiments. Hereby, an extensive 2D and 3D analysis of Si morphology, mechanical behavior and damage characteristics of the alloys under different loading conditions has been carried out. It has enabled to define the limits of 2D characterization techniques and assess structural features that could only be determined in 3D allowing a more accurate interpretation of the material behavior. Furthermore, the model for the simulation of a system of dimples on the fracture surface of Al-Si alloys has been developed. Besides, the methodology allowing the application of simulation results for studying the relation between Si morphology and eutectic fracture toughness have been presented.

Regarding the influence of Si morphology on the mechanical properties of the material, the simulation study has first been conducted. This study has relied on numerical simulations of the mechanical behavior of the eutectic phase performed on virtual samples. The virtual samples of Al-Si eutectic have been generated by means of the Competitive Stochastic Growth Model introduced in [14] particularly for this type of material. By varying the model parameters, a large variety of synthetic Si structures with different connectivity, branching and number of particles have been produced. The mechanical strength of different morphological scenarios has then been evaluated in relation to the underlined structural features. In so doing, the influence of Si morphology on the mechanical behavior of the eutectic phase has been studied independently, i.e. without relation to any phase and/or chemical composition of the material. The following conclusions have been drawn from the simulation study:

- The strength of the material increases with the connectivity and the branching of Si particles as well as with the number of particles in disjoint or simply connected structures.
- The Euler number is highly effective in characterizing the connectivity, as it is able to capture topological properties of network structures in contrast to metric properties such as the volume (or the volume fraction) of the largest second phase particle.

- The strength of the structure increases with decreasing the Euler number. It has thus been shown that the Euler number is a relative, yet effective measure of the strength which can be used to compare the structures without mechanical tests.

By carrying out mechanical tests on the macro specimens of Al-Si alloys, it has been observed that the DAS values and Si particles density correlate better with the measured strength characteristics of the alloys than 2D size-shape features of Si particles. The results of the mechanical tests have made evident the limits of the approach based on 2D characterization of Si morphology and consideration of features of only one phase while assessing the properties of a two-phase material. The importance of the complex consideration of microstructural constituents by analyzing the results of mechanical tests has been illustrated. It has been suggested that the density of Si particles and the size of Al dendrites are more important for the strengthening of the alloys than the size-shape features of the eutectic Si induced by the modification. Besides, the advantages of the modified Si morphology for the ductility of the alloy might be overridden by the properties of the primary phase.

The knowledge on damage characteristics and mechanism dominating for different combinations of microstructure and loading conditions has been shown to be essential for the right interpretation of results issued from 2D damage characterization. In this respect, 3D damage investigations of the specimens after mechanical tests have yielded the following observations:

- Under uniaxial compression, the damage in the Al-Si alloys occurs by the cracking of Si particles and aluminides (if there are any), where the cracks grow parallel to the loading direction.
- Under uniaxial tension, the damage in the as-cast alloy proceeds by the cracking of particles while the solution treated alloy exhibits a mixed damage mechanism, i.e. cracking and debonding of Si particles from the matrix. Thus, a wider crack orientation distribution range observed in 2D images of the solution treated alloy as compared to the as-cast alloy has been interpreted relying on observations of damage characteristics made in 3D.
- It has been suggested that the damage mode of Si particles is defined by the combination of Si morphology and loading conditions. In particular, the mixed damage mechanism is likely to occur in structures with spheroidized Si under tension loading. It is important to mention, however, that the particle cracking still remains the

principle damage mechanism in Al-Si alloys under uniaxial loading. Besides, the morphology of Si particles indirectly influences the morphology of cracks so that the branched and connected Si particles provide a longer way for the crack to grow through, resulting in the elongated voids.

- The level of damage in a structure as analyzed on metallographic images of Al-Si alloys is largely underestimated due to the matrix filling the cracks during the metallographic preparation. Also, considering stereological principles and 3D image data, the real size of cracks is obviously underestimated by 2D analysis as well. Although the crack orientation distribution in 2D images conforms to the state-of-the-art observations implying that the cracks are (nearly) perpendicular to the direction of tensile stresses, according to 3D images, there are always spatial deviations of the crack orientation from the directions of maximum stresses. Acknowledging the limits of 2D characterization, yet it can be suggested that 2D analysis can roughly reflect the size, shape and orientation characteristics of cracks in the material.

And last but not least, a new model allowing to simulate the system of dimples on the fracture surface of the eutectic phase in Al-Si alloys by means of the weighted Voronoi tessellation has been proposed. It is implemented as a Java plugin for the Fiji interface and is easy to execute and modify. By applying the model to metallographic images of the eutectic phase, a fracture surface appearance (as projected on a fractograph) which would potentially exhibit this structure under uniaxial tensile loading can be simulated. Thus, the fractographic characteristics of the eutectic phase with different Si morphologies can be evaluated and compared to each other avoiding extensive mechanical tests and fracture surface imaging.

Two examples of the application of the modelling results have been presented. First, topographic features such as the fracture surface area and the roughness have been computed directly on the basis of simulated Voronoi diagrams (given the average depth-to-width ratio) by means of geometrical approximations, empirical and analytical relations. Furthermore, the methodology for the estimation of the fracture toughness of the eutectic phase and of the entire alloy using analytical formulae has been described. The predictions of the impact of different Si morphologies on the fracture toughness based on the simulated fractographs have shown to agree with the state-of-the-art observations. It demonstrates the usefulness of the modelling approach in studying the influence of Si morphology on the fracture toughness of different eutectic structures, at least on a comparative basis. More general, the method can be used for estimating the fracture toughness of materials consisting of matrix with second phase

particles with a minimum of experimental effort. It can thus contribute to understanding structure-property relationships. Besides, the fractographic statistics and structure optimisation with respect to the fracture resistance can benefit from the developed model. The proposed approach can thus be used to design new materials with tailored fracture toughness.

## 5.2 Outlook

The virtual tools used in the present work for studying structure-properties relationships, though proving to be efficient for the material characterization, can further be optimized. In particular, the integration of residual stresses in second phase particles and their failure criteria in FEM simulations will enable to study the impact of Si morphology on the ductility of virtual samples. It is also important to investigate the mechanical impact of the primary phase and its interplay with the eutectic phase in more detail. Although it has been suggested that both phases exert an influence on mechanical properties, the extent to which they do so is still not elaborated. It might be possible that one of the phases has a dominating mechanical impact under certain conditions or from a certain amount.

In regard to the developed tessellation model, it has been shown that the model reproduces the size features of fracture surface elements very well which provides a sufficient input to the estimation of topographic properties and fracture toughness. If necessary, the model can further be optimized with respect to the shape of fracture surface elements by using, for example, the anisotropic growth models. The weight function can also be adjusted with respect to different size classes and the number of particles. However, the intended balance between the model accuracy on one side and the model complexity and computational effort on the other side should to be respected.

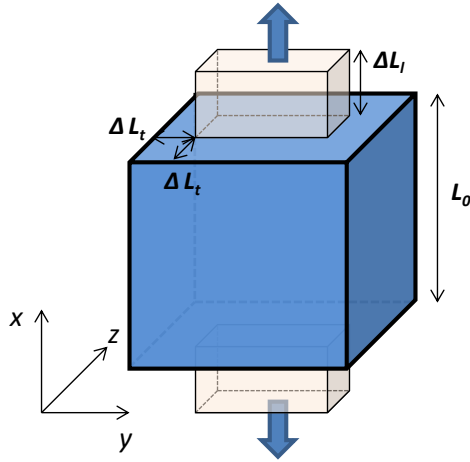
The methodology proposed for the analytical estimation of the fracture toughness of the material can also be refined by investigating the relation between the width and the depth of dimples and using this relation instead of the average depth-to-width ratio as well as considering the effect of the primary phase contiguity. Obviously, the experimental measurements of the fracture toughness of the investigated alloys would be of great importance in order to verify the analytically estimated values.

These investigations can contribute to further optimizing the available predictive schemas and defining the morphological scenario of a structure of Al-Si alloys tailored for a specific application with respect to the most relevant mechanical properties such as the strength, the ductility and the fracture resistance.

## 6 Appendix

### 6.1 Calculations of the volumetric change

Calculations of the volumetric change in a cube stretched/compressed in the  $x$ -direction.



Initial volume,  $V_0$ , of a cube with a side,  $L_0$ :

$$V_0 = L_0^3$$

Deformed volume,  $V$ :  $V = V_0 + \Delta V$

Poisson ratio,  $\nu$ :

$$\nu = -\frac{\varepsilon_t}{\varepsilon_l}$$

where  $\varepsilon_t$  and  $\varepsilon_l$  are the transverse and longitudinal elastic strain, respectively [131].

Figure 6.1: Schematic illustration of a volumetric change in a cube with a side,  $L_0$ , and initial volume,  $V_0$ , stretched in the  $x$ -direction, where  $\Delta L_t$  and  $\Delta L_l$  are the transverse contraction and longitudinal expansion, respectively. The basic relations used for the computation of the volumetric change are presented on the right side.

According to the definition of the Poisson ratio for the cube stretched in  $x$ -direction,

$$\nu = -\frac{d\varepsilon_t}{d\varepsilon_l} = -\frac{d\varepsilon_y}{d\varepsilon_x} = -\frac{d\varepsilon_z}{d\varepsilon_x}$$

$$-\nu \int_{L_0}^{L_0 + \Delta L_l} \frac{dx}{x} = \int_{L_0}^{L_0 - \Delta L_t} \frac{dy}{y} = \int_{L_0}^{L_0 - \Delta L_t} \frac{dz}{z}$$

$$-\nu \ln \left( \frac{L_0 + \Delta L_l}{L_0} \right) = \ln \left( \frac{L_0 - \Delta L_t}{L_0} \right)$$

$$\left( \frac{L_0 + \Delta L_l}{L_0} \right)^{-\nu} = \frac{L_0 - \Delta L_t}{L_0} \quad \text{or} \quad \left( 1 + \frac{\Delta L_l}{L_0} \right)^{-\nu} = 1 - \frac{\Delta L_t}{L_0}$$

The deformed volume,  $V$ , can be expressed as follows:

$$V_0 + \Delta V = (L_0 + \Delta L_l)(L_0 - \Delta L_t)^2$$

$$1 + \frac{\Delta V}{V_0} = \left( 1 + \frac{\Delta L_l}{L_0} \right) \left( 1 - \frac{\Delta L_t}{L_0} \right)^2$$

Taking into account the equation  $\left(1 - \frac{\Delta L_t}{L_0}\right) = \left(1 + \frac{\Delta L_l}{L_0}\right)^{-\nu}$ , the relative change of the volume,  $(\Delta V/V_0)$  can be expressed as:

$$\frac{\Delta V}{V_0} = \left(1 + \frac{\Delta L_l}{L_0}\right) \left(1 + \frac{\Delta L_l}{L_0}\right)^{-2\nu} - 1 = \left(1 + \frac{\Delta L_l}{L_0}\right)^{1-2\nu} - 1$$

Assuming that  $\Delta L_l$  and  $\Delta L_t$  are very small, the first-order approximation of the relative volume change using the Taylor series:

$$f(a) + \frac{f'(a)}{1!}(x-a) + \frac{f''(a)}{2!}(x-a)^2 + \frac{f'''(a)}{3!}(x-a)^3 + \dots$$

can be defined as follows:

$$\frac{\Delta V}{V_0} \approx f(0) + \frac{f'(0)}{1!}(x-0)$$

$$\begin{aligned} f(0) + \frac{f'(0)}{1!}(x-0) &= ((1+0)^{1-2\nu} - 1) + \left( (1-2\nu) \frac{1}{L_0} \left(1 + \frac{0}{L_0}\right)^{1-2\nu-1} - 0 \right) (\Delta L_l - 0) \\ &= (1-2\nu) \frac{\Delta L_l}{L_0} \end{aligned}$$

Thus, the relative change of the volume in the cube stretched in the  $x$ -direction can be defined as:

$$\frac{\Delta V}{V_0} \approx (1-2\nu) \frac{\Delta L_l}{L_0}$$

## 7 Bibliography

---

- [1] W.S. Miller, L. Zhuang, J. Bottema, A.J. Wittebrood, P. De Smet, A. Haszler, et al., Recent development in aluminium alloys for the automotive industry, *Mater. Sci. Eng. A*. 280 (2000) 37–49. doi:10.1016/S0921-5093(99)00653-X.
- [2] E. Ghassemieh, *Materials in Automotive Application, State of the Art and Prospects, New Trends Dev. Automot. Ind.* (2011) 365–394. doi:10.5772/1821.
- [3] S. Kores, H. Zak, B. Tonn, Aluminium alloys for cylinder heads, *RMZ – Mater. Geoenvironment*. 55 (2008) 307–317.
- [4] H. Ye, An Overview of the Development of Al-Si-Alloy Based Material for Engine Applications, *J. Mater. Eng. Perform.* 12 (2003) 288–297. doi:10.1361/105994903770343132.
- [5] J.E. Gruzleski, B.M. Closset, *The Treatment of Liquid Aluminum-Silicon Alloys*, American Foundrymen’s Society, Inc., Des Plaines, Illinois, 1990.
- [6] *ASM Handbook Volume 19: Fatigue and Fracture*, ASM International, 1996.
- [7] K. Thornton, H.F. Poulsen, Three-Dimensional Materials Science: An Intersection of Three-Dimensional Reconstructions and Simulations, *MRS Bull.* 33 (2008) 587–595. doi:10.1557/mrs2008.123.
- [8] A. Saigal, E.R. Fuller Jr., Analysis of stresses in aluminum-silicon alloys, *Comput. Mater. Sci.* 21 (2001) 149–158. doi:10.1016/S0927-0256(00)00224-X.
- [9] S. Joseph, S. Kumar, Finite Element Analysis of Stress Evolution in Al-Si Alloy, *J. Mater. Eng. Perform.* 24 (2015) 253–260. doi:10.1007/s11665-014-1288-x.
- [10] K. Gall, M. Horstemeyer, D.L. McDowell, J. Fan, Finite element analysis of the stress distributions near damaged Si particle clusters in cast Al-Si alloys, *Mech. Mater.* 32 (2000) 277–301. doi:10.1016/S0167-6636(00)00003-X.
- [11] N. Chawla, R.S. Sidhu, V.V. Ganesh, Three-dimensional visualization and microstructure-based modeling of deformation in particle-reinforced composites, *Acta Mater.* 54 (2006) 1541–1548. doi:10.1016/j.actamat.2005.11.027.
- [12] S. Joseph, S. Kumar, V.S. Bhadram, C. Narayana, Stress states in individual Si particles of a cast Al-Si alloy: Micro-Raman analysis and microstructure based modeling, *J. Alloys Compd.* 625 (2015) 296–308. doi:10.1016/j.jallcom.2014.10.207.
- [13] H. Shen, C.J. Lissenden, 3D finite element analysis of particle-reinforced aluminum, *Mater. Sci. Eng. A*. 338 (2002) 271–281. doi:10.1016/S0921-5093(02)00094-1.

- [14] G. Gaiselmann, O. Stenzel, A. Kruglova, F. Mücklich, V. Schmidt, Competitive stochastic growth model for the 3D morphology of eutectic Si in Al-Si alloys, *Comput. Mater. Sci.* 69 (2013) 289–298. doi:10.1016/j.commatsci.2012.11.051.
- [15] J.L. Murray, A.J. McAlister, The Al-Si (Aluminum-Silicon) System, *Bull. Alloy Phase Diagrams.* 5 (1984) 74–84. doi:10.1007/BF02868729.
- [16] N. Fat-Halla, Structural modification of Al-Si eutectic alloy by Sr and its effect on tensile and fracture characteristics, *J. Mater. Sci.* 24 (1989) 2488–2492. doi:10.1007/BF01174517.
- [17] G.F. Vander Voort, J. Asensio-Lozano, The Al-Si Phase Diagram, *Microsc. Microanal.* 15 (2009) 60. doi:10.1017/S1431927609092642.
- [18] N. Fatahalla, M. Hafiz, M. Abdulkhalek, Effect of microstructure on the mechanical properties and fracture of commercial hypoeutectic Al-Si alloy modified with Na, Sb and Sr, *J. Mater. Sci.* 34 (1999) 3555–3564. doi:10.1023/A:1004626425326.
- [19] ASM Handbook Volume 15: Casting, ASM International, 1988.
- [20] C.H. Cáceres, I.L. Svensson, J.A. Taylor, Strength-Ductility Behaviour of Al-Si-Cu-Mg Casting Alloys in T6 Temper, *Int. J. Cast Met. Res.* 15 (2003) 531–543.
- [21] E. Sjölander, S. Seifeddine, The heat treatment of Al-Si-Cu-Mg casting alloys, *J. Mater. Process. Technol.* 210 (2010) 1249–1259. doi:10.1016/j.jmatprotec.2010.03.020.
- [22] S. Shivkumar, S. Ricci, C. Keller, D. Apelian, Effect of solution treatment parameters on tensile properties of cast aluminum alloys, *J. Heat Treat.* 8 (1990) 63–70. doi:10.1007/BF02833067.
- [23] D.L. Zhang, L.H. Zheng, D.H. StJohn, Effect of a short solution treatment time on microstructure and mechanical properties of modified Al–7wt.%Si–0.3wt.%Mg alloy, *J. Light Met.* 2 (2002) 27–36. doi:10.1016/S1471-5317(02)00010-X.
- [24] S. Shivkumar, C. Keller, M. Trazzera, D. Apelian, Precipitation hardening in A356 alloys, in: *Proc. Int. Symp. Prod. Refining, Fabr. Recycl. Light Met.*, 1990: pp. 264–278.
- [25] A. Manente, G. Timelli, Optimizing the Heat Treatment Process of Cast Aluminium Alloys, *Recent Trends Process. Degrad. Alum. Alloy.* (2011) 197–220.
- [26] K. Matsuda, H. Gamada, K. Fujii, Y. Uetani, T. Sato, A. Kamio, et al., High-resolution electron microscopy on the structure of Guinier-Preston zones in an Al-1.6 mass Pct Mg<sub>2</sub>Si alloy, *Metall. Mater. Trans. A.* 29 (1998) 1161–1167. doi:10.1007/s11661-998-0242-7.

- [27] J.H. Li, M. Albu, T.H. Ludwig, Y. Matsubara, F. Hofer, L. Arnberg, et al., Modification of eutectic Si in Al-Si based alloys, *Mater. Sci. Forum.* 794-796 (2014) 130–136. doi:10.4028/www.scientific.net/MSF.794-796.130.
- [28] S. Hegde, K.N. Prabhu, Modification of eutectic silicon in Al-Si alloys, *J. Mater. Sci.* 43 (2008) 3009–3027. doi:10.1007/s10853-008-2505-5.
- [29] B. Closset, J.E. Gruzleski, Structure and properties of hypoeutectic Al-Si-Mg alloys modified with pure strontium, *Metall. Trans. A.* 13 (1982) 945–951. doi:10.1007/BF02643389.
- [30] S.-Z. Lu, A. Hellawell, The mechanism of silicon modification in aluminum-silicon alloys: Impurity induced twinning, *Metall. Trans. A.* 18 (1987) 1721–1733. doi:10.1007/BF02646204.
- [31] K.F. Kobayashi, L.M. Hogan, The crystal growth of silicon in Al-Si alloys, *J. Mater. Sci.* 20 (1985) 1961–1975. doi:10.1007/BF01112278.
- [32] M. Shamsuzzoha, L.M. Hogan, The crystal morphology of fibrous silicon in strontium-modified Al-Si eutectic, *Philos. Mag. A.* 54 (1986) 459–477.
- [33] M. Timpel, N. Wanderka, R. Schlesiger, T. Yamamoto, N. Lazarev, D. Isheim, et al., The role of strontium in modifying aluminium-silicon alloys, *Acta Mater.* 60 (2012) 3920–3928. doi:10.1016/j.actamat.2012.03.031.
- [34] J. Barrirero, M. Engstler, N. Ghafoor, N. De Jonge, M. Odén, F. Mücklich, Comparison of segregations formed in unmodified and Sr-modified Al-Si alloys studied by atom probe tomography and transmission electron microscopy, *J. Alloys Compd.* 611 (2014) 410–421. doi:10.1016/j.jallcom.2014.05.121.
- [35] C.M. Dinnis, A.K. Dahle, J.A. Taylor, Three-dimensional analysis of eutectic grains in hypoeutectic Al-Si alloys, *Mater. Sci. Eng. A.* 392 (2005) 440–448. doi:10.1016/j.msea.2004.10.037.
- [36] A.K. Dahle, K. Nogita, J.W. Zindel, S.D. McDonald, L.M. Hogan, Eutectic Nucleation and Growth in Hypoeutectic Al-Si Alloys at Different Strontium Levels, *Metall. Mater. Trans. A.* 32A (2001) 949–960. doi:10.1007/s11661-001-0352-y.
- [37] A.K. Dahle, K. Nogita, S.D. McDonald, C. Dinnis, L. Lu, Eutectic modification and microstructure development in Al-Si Alloys, *Mater. Sci. Eng. A.* 413-414 (2005) 243–248. doi:10.1016/j.msea.2005.09.055.
- [38] S. Shankar, Y.W. Riddle, M.M. Makhlof, Nucleation mechanism of the eutectic phases in aluminum-silicon hypoeutectic alloys, *Acta Mater.* 52 (2004) 4447–4460. doi:10.1016/j.actamat.2004.05.045.
- [39] M.F. Hafiz, T. Kobayashi, A study on the microstructure-fracture behavior relations in Al-Si casting alloys, *Scr. Metall. Mater.* 30 (1994) 475–480.

- [40] F.T. Lee, J.F. Major, F.H. Samuel, Effect of Silicon Particles on the Fatigue Crack Growth Characteristics of Al-12 Wt Pct Si-0.35 Wt Pct Mg-(0 to 0.02) Wt Pct Sr Casting Alloys, 26 (1995) 1553–1570.
- [41] M.M. Haque, Effects of strontium on the structure and properties of aluminium-silicon alloys, *J. Mater. Process. Tech.* 55 (1995) 193–198. doi:10.1016/0924-0136(95)01953-7.
- [42] J. Campbell, M. Tiryakioğlu, Review of effect of P and Sr on modification and porosity development in Al–Si alloys, *Mater. Sci. Technol.* 26 (2010) 262–268. doi:10.1179/174328409X425227.
- [43] Y. Bai, H. Zhao, Tensile properties and fracture behavior of partial squeeze added slow shot die-cast A356 aluminum alloy, *Mater. Des.* 31 (2010) 4237–4243. doi:10.1016/j.matdes.2010.04.005.
- [44] D. Broek, *Elementary engineering fracture mechanics*, Martinus Nijhoff Publishers, The Hague, 1982.
- [45] H. Liao, Y. Sun, G. Sun, Correlation between mechanical properties and amount of dendritic  $\alpha$ -Al phase in as-cast near-eutectic Al-11.6% Si alloys modified with strontium, *Mater. Sci. Eng. A.* 335 (2002) 62–66. doi:10.1016/S0921-5093(01)01949-9.
- [46] D. Tolnai, G. Requena, P. Cloetens, J. Lendvai, H.P. Degischer, Effect of solution heat treatment on the internal architecture and compressive strength of an AlMg4.7Si8 alloy, *Mater. Sci. Eng. A.* 585 (2013) 480–487. doi:10.1016/j.msea.2013.06.033.
- [47] *ASM Handbook Volume 12: Fractography*, ASM International, 1987.
- [48] G.T. Hahn, A.R. Rosenfield, Metallurgical factors affecting fracture toughness of aluminum alloys, *Metall. Trans. A.* 6 (1975) 653–668. doi:10.1007/BF02672285.
- [49] M. Kobayashi, Y. Dorce, H. Toda, H. Horikawa, Effect of local volume fraction of microporosity on tensile properties in Al-Si-Mg cast alloy, *Mater. Sci. Technol.* 26 (2010) 962–967. doi:10.1179/174328409X441283.
- [50] J. Gurland, N.M. Parikh, Microstructural aspects of the fracture of two-phase alloys, in: *Fract. Nonmetals Compos.*, Academic Press, Inc., New York, 1972: pp. 841–878.
- [51] C.H. Cáceres, J.R. Griffiths, Damage by the cracking of silicon particles in an Al-7Si-0.4Mg casting alloy, *Acta Mater.* 44 (1996) 25–33. doi:10.1016/1359-6454(95)00172-8.
- [52] Q.G. Wang, C.H. Cáceres, The fracture mode in Al–Si–Mg casting alloys, *Mater. Sci. Eng. A.* 241 (1998) 72–82. doi:10.1016/S0921-5093(97)00476-0.

- [53] Q.G. Wang, Microstructural Effects on the Tensile and Fracture Behavior of Aluminum Casting Alloys A356 / 357, *Metall. Mater. Trans. A.* 34 (2003) 2887–2899. doi:10.1007/s11661-003-0189-7.
- [54] C.H. Cáceres, C.J. Davidson, J.R. Griffiths, The deformation and fracture behaviour of an Al-Si-Mg casting alloy, *Mater. Sci. Eng. A.* 197 (1995) 171–179. doi:10.1016/0921-5093(94)09775-5.
- [55] M.F. Hafiz, T. Kobayashi, Fracture toughness of eutectic Al-Si casting alloy with different microstructural features, *J. Mater. Sci.* 31 (1996) 6195–6200. doi:10.1007/BF00354438.
- [56] M.D. Dighe, A.M. Gokhale, Relationship between microstructural extremum and fracture path in a cast Al-Si-Mg alloy, *Scr. Mater.* 37 (1997) 1435–1440. doi:10.1016/S1359-6462(97)00277-7.
- [57] S. Joseph, A. Tewari, S. Kumar, The fracture characteristics of a near eutectic Al-Si based alloy under compression, *Metall. Mater. Trans. A.* 44 (2013) 2358–2368. doi:10.1007/s11661-012-1580-z.
- [58] R. Doglione, In situ investigations on the ductility of an Al-Si-Mg casting alloy, *JOM.* 64 (2012) 51–57. doi:10.1007/s11837-011-0231-y.
- [59] N. Raghukiran, A.K. Mohamed, R. Kumar, Study of the Influence of Silicon Phase Morphology on the Microstructural Stress Distribution in Al-Si Alloys Using Object Oriented Finite Element Modeling, *Adv. Eng. Mater.* 15 (2013) 1–10. doi:10.1002/adem.201300096.
- [60] J. Ohser, F. Mücklich, *Statistical Analysis of Microstructures in Materials Science*, John Wiley & Sons, Chichester, 2000.
- [61] G. Requena, G. Garcés, Z. Asghar, E. Marks, P. Staron, P. Cloetens, The Effect of the Connectivity of Rigid Phases on Strength of Al-Si Alloys, *Adv. Eng. Mater.* 13 (2011) 674–684. doi:10.1002/adem.201000292.
- [62] G. Requena, G. Garcés, M. Rodríguez, T. Pirling, P. Cloetens, 3D architecture and load partition in eutectic Al-Si alloys, *Adv. Eng. Mater.* 11 (2009) 1007–1014. doi:10.1002/adem.200900218.
- [63] M. Sahoo, R.W. Smith, Mechanical Properties of Unidirectionally Solidified Al-Si Eutectic Alloys, *Met. Sci.* 9 (1975) 217–222.
- [64] Z. Asghar, G. Requena, H.P. Degischer, P. Cloetens, Three-dimensional study of Ni aluminides in an AlSi12 alloy by means of light optical and synchrotron microtomography, *Acta Mater.* 57 (2009) 4125–4132. doi:10.1016/j.actamat.2009.05.010.
- [65] J.C. Russ, R.T. Dehoff, *Practical Stereology*, Springer US, Boston, MA, 2000. doi:10.1007/978-1-4615-1233-2.

- [66] A. Odgaard, H.J.G. Gundersen, Quantification of connectivity in cancellous bone, with special emphasis on 3-D reconstructions, *Bone*. 14 (1993) 173–182.
- [67] Fraunhofer Institute for Industrial Mathematics ITWM, MAVI - Modular Algorithms for Volume Images. User manual, 2014.
- [68] M. Srinivasan, S. Seetharamu, Fracture Toughness of Metal Castings, in: *Sci. Technol. Cast. Process.*, 2012. doi:10.5772/50297.
- [69] D. Broek, Some Contributions of Electron Fractography to the Theory of Fracture, *Int. Metall. Rev.* 19 (1974) 135–182. doi:10.1179/095066074790137033.
- [70] D. Broek, *The practical use of fracture mechanics*, Kluwer Academic Publishers, Dordrecht, 1988.
- [71] J.-W. Yeh, W.-P. Liu, The cracking mechanism of silicon particles in an A357 aluminum alloy, *Metall. Mater. Trans. A*. 27 (1996) 3558–3568. doi:10.1007/BF02595447.
- [72] S. Joseph, S. Kumar, A systematic investigation of fracture mechanisms in Al-Si based eutectic alloy-Effect of Si modification, *Mater. Sci. Eng. A*. 588 (2013) 111–124. doi:10.1016/j.msea.2013.09.019.
- [73] M.A. Przystupa, T.H. Courtney, Fracture in Equiaxed Two Phase Alloys: Part I. Fracture in Alloys with Isolated Elastic Particles, *Metall. Trans. A*. 13 (1982) 873–879. doi:10.1007/BF02642402.
- [74] P. Uggowitzer, M.O. Speidel, Fracture Toughness of Cast Structures, in: *Proc. 4th Eur. Conf. Fract. – ECF4*, 1982: pp. 147–154.
- [75] M.F. Horstemeyer, J. Lathrop, A.M. Gokhale, M. Dighe, Modeling stress state dependent damage evolution in a cast Al–Si–Mg aluminum alloy, *Theor. Appl. Fract. Mech.* 33 (2000) 31–47. doi:10.1016/S0167-8442(99)00049-X.
- [76] R. Doglione, J.L. Douzich, C. Berdin, D. François, Tensile damage stages in cast A356-T6 aluminium alloy, *Mater. Sci. Technol.* 18 (2002) 554–562. doi:10.1179/026708302225001660.
- [77] K. Lee, Y.N. Kwon, S. Lee, Correlation of microstructure with mechanical properties and fracture toughness of A356 aluminum alloys fabricated by low-pressure-casting, rheo-casting, and casting-forging processes, *Eng. Fract. Mech.* 75 (2008) 4200–4216. doi:10.1016/j.engfracmech.2008.04.004.
- [78] K. Lee, Y.N. Kwon, S. Lee, Effects of eutectic silicon particles on tensile properties and fracture toughness of A356 aluminum alloys fabricated by low-pressure-casting, casting-forging, and squeeze-casting processes, *J. Alloys Compd.* 461 (2008) 532–541. doi:10.1016/j.jallcom.2007.07.038.

- [79] Z. Asghar, G. Requena, Three dimensional post-mortem study of damage after compression of cast Al-Si alloys, *Mater. Sci. Eng. A.* 591 (2014) 136–143. doi:10.1016/j.msea.2013.10.067.
- [80] Z. Asghar, G. Requena, E. Boller, 3D Interpenetrating Hybrid Network of Rigid Phases in an AlSi10Cu5NiFe Piston Alloy, *Pract. Metallogr.* 47 (2010) 471–486. doi:10.3139/147.110092.
- [81] Z. Asghar, G. Requena, E. Boller, Three-dimensional rigid multiphase networks providing high-temperature strength to cast AlSi10Cu5Ni1-2 piston alloys, *Acta Mater.* 59 (2011) 6420–6432. doi:10.1016/j.actamat.2011.07.006.
- [82] F. Lasagni, A. Lasagni, E. Marks, C. Holzapfel, F. Mücklich, H.P. Degischer, Three-dimensional characterization of “as-cast” and solution-treated AlSi12(Sr) alloys by high-resolution FIB tomography, *Acta Mater.* 55 (2007) 3875–3882. doi:10.1016/j.actamat.2007.03.004.
- [83] W.J. Poole, E.J. Dowdle, Experimental measurements of damage evolution in Al-Si eutectic alloys, *Scr. Mater.* 39 (1998) 1281–1287. doi:10.1016/S1359-6462(98)00326-1.
- [84] G. Guiglionda, W.J. Poole, The role of damage on the deformation and fracture of Al-Si eutectic alloys, *Mater. Sci. Eng. A.* 336 (2002) 159–169. doi:10.1016/S0921-5093(01)01971-2.
- [85] J. Gurland, J. Plateau, The mechanism of ductile rupture of metals containing inclusions, *Trans. ASM.* 56 (1963) 442–454.
- [86] M.D. Dighe, A.M. Gokhale, M.F. Horstemeyer, Effect of loading condition and stress state on damage evolution of silicon particles in an Al-Si-Mg-Base cast alloy, *Metall. Mater. Trans. A.* 33 (2002) 555–565. doi:10.1007/s11661-002-0117-2.
- [87] H.P. Stüwe, The work necessary to form a ductile fracture surface, *Eng. Fract. Mech.* 13 (1980) 231–236. doi:10.1016/0013-7944(80)90056-9.
- [88] A.W. Thompson, M.F. Ashby, Fracture surface micro-roughness, *Scr. Metall.* 18 (1984) 127–130. doi:10.1016/0036-9748(84)90489-7.
- [89] M.F. Horstemeyer, A.M. Gokhale, A Void-Crack Nucleation Model for Ductile Metals, *Int. J. Solids Struct.* 36 (1999) 5029–5055. doi:10.1016/S0020-7683(98)00239-X.
- [90] K. Gall, N. Yang, M. Horstemeyer, D.L. McDowell, J. Fan, The debonding and fracture of Si particles during the fatigue of a cast Al-Si alloy, *Metall. Mater. Trans. A.* 30 (1999) 3079–3088. doi:10.1007/s11661-999-0218-2.
- [91] H. Agarwal, A.M. Gokhale, S. Graham, M.F. Horstemeyer, Quantitative characterization of three-dimensional damage evolution in a wrought Al-alloy under tension and compression, *Metall. Mater. Trans. A.* 33 (2002) 2599–2606. doi:10.1007/s11661-002-0381-1.

- [92] A. Balasundaram, A.M. Gokhale, S. Graham, M.F. Horstemeyer, Three-dimensional particle cracking damage development in an Al-Mg-base wrought alloy, *Mater. Sci. Eng. A.* 355 (2003) 368–383. doi:10.1016/S0921-5093(03)00103-5.
- [93] J. Baruchel, J.Y. Buffiere, P. Cloetens, M. Di Michiel, E. Ferrie, W. Ludwig, et al., Advances in synchrotron radiation microtomography, *Scr. Mater.* 55 (2006) 41–46. doi:10.1016/j.scriptamat.2006.02.012.
- [94] J. Kastner, B. Harrer, G. Requena, O. Brunke, A comparative study of high resolution cone beam X-ray tomography and synchrotron tomography applied to Fe- and Al-alloys, *NDT&E Int.* 43 (2010) 599–605. doi:10.1016/j.ndteint.2010.06.004.
- [95] N. Limodin, A. El Bartali, L. Wang, J. Lachambre, J.Y. Buffiere, E. Charkaluk, Application of X-ray microtomography to study the influence of the casting microstructure upon the tensile behaviour of an Al-Si alloy, *Nucl. Instruments Methods Phys. Res. Sect. B Beam Interact. with Mater. Atoms.* 324 (2014) 57–62. doi:10.1016/j.nimb.2013.07.034.
- [96] L. Babout, E. Maire, R. Fougères, Damage initiation in model metallic materials: X-ray tomography and modelling, *Acta Mater.* 52 (2004) 2475–2487. doi:10.1016/j.actamat.2004.02.001.
- [97] M.F. Horstemeyer, K. Gall, K.W. Dolan, A. Waters, J.J. Haskins, D.E. Perkins, et al., Numerical, experimental, nondestructive, and image analyses of damage progression in cast A356 aluminum notch tensile bars, *Theor. Appl. Fract. Mech.* 39 (2003) 23–45. doi:10.1016/S0167-8442(02)00136-2.
- [98] H. Singh, A.M. Gokhale, Y. Mao, A. Tewari, A.K. Sachdev, Reconstruction and quantitative characterization of multiphase, multiscale three-dimensional microstructure of a cast Al-Si base alloy, *Metall. Mater. Trans. B.* 40 (2009) 859–870. doi:10.1007/s11663-009-9291-6.
- [99] H. Singh, A.M. Gokhale, Visualization of three-dimensional microstructures, *Mater. Charact.* 54 (2005) 21–29. doi:10.1016/j.matchar.2004.10.002.
- [100] F. Lasagni, A. Lasagni, C. Holzapfel, F. Mücklich, H.P. Degischer, Three dimensional characterization of unmodified and Sr-modified Al-Si eutectics by FIB and FIB EDX tomography, *Adv. Eng. Mater.* 8 (2006) 719–723. doi:10.1002/adem.200500276.
- [101] F. Lasagni, A. Lasagni, M. Engstler, H.P. Degischer, F. Mücklich, Nano-characterization of cast structures by FIB-tomography, *Adv. Eng. Mater.* 10 (2008) 62–66. doi:10.1002/adem.200700249.
- [102] G.D. West, R.C. Thomson, Combined EBSD/EDS tomography in a dual-beam FIB/FEG-SEM, *J. Microsc.* 233 (2009) 442–450. doi:10.1111/j.1365-2818.2009.03138.x.

- [103] C. Holzapfel, W. Schäf, M. Marx, H. Vehoff, F. Mücklich, Interaction of cracks with precipitates and grain boundaries: Understanding crack growth mechanisms through focused ion beam tomography, *Scr. Mater.* 56 (2007) 697–700. doi:10.1016/j.scriptamat.2006.12.025.
- [104] M.F. Ashby, H. Shercliff, D. Cebon, *Materials: engineering, science, processing and design*, Elsevier, Amsterdam, 2007.
- [105] S. Kumai, T. Tanaka, H. Zhu, A. Sato, Tear Toughness of Permanent Mold Cast and DC Cast A356 Aluminum Alloys, 45 (2004) 1706–1713.
- [106] K. Tohgo, M. Oka, Influence of Coarsening Treatment on Fatigue Strength and Fracture Toughness of Al-Si-Mg Alloy Casting, *Key Eng. Mater.* 261-263 (2004) 1263–1268. doi:10.4028/www.scientific.net/KEM.261-263.1263.
- [107] N.D. Alexopoulos, M. Tiryakioğlu, Relationship between fracture toughness and tensile properties of A357 cast aluminum alloy, *Metall. Mater. Trans. A Phys. Metall. Mater. Sci.* 40 (2009) 702–716. doi:10.1007/s11661-008-9742-8.
- [108] M. Tiryakioğlu, Fracture toughness potential of cast Al-7%Si-Mg alloys, *Mater. Sci. Eng. A.* 497 (2008) 512–514. doi:10.1016/j.msea.2008.06.037.
- [109] M. Tiryakioçlu, J. Campbell, Ductility, structural quality, and fracture toughness of Al–Cu–Mg–Ag (A201) alloy castings, *Mater. Sci. Technol.* 25 (2009) 784–789. doi:10.1179/174328408X378645.
- [110] E.W. Qin, L. Lu, N.R. Tao, J. Tan, K. Lu, Enhanced fracture toughness and strength in bulk nanocrystalline Cu with nanoscale twin bundles, *Acta Mater.* 57 (2009) 6215–6225. doi:10.1016/j.actamat.2009.08.048.
- [111] ASTM Standard E1820 - 11, Standard Test Method for Measurement of Fracture Toughness, ASTM International, West Conshohocken, PA, 2011. doi:10.1520/E1820-11E01.2.
- [112] DIN EN ISO 12737, *Metallische Werkstoffe - Bestimmung der Bruchzähigkeit (ebener Dehnungszustand) (ISO 12737:2010); Deutsche Fassung EN ISO 12737:2010*, Dtsch. Norm. (2011).
- [113] ASTM Standard B871-96, Standard Test Method for Tear Testing of Aluminum Alloy Products, ASTM International, West Conshohocken, PA, 1996. doi:10.1520/B0871-96.
- [114] Hydro, *Gießverfahren*, (2013). <http://www.hydro.com/de/Deutschland/Aluminium-Giessereiprodukte/Giessverfahren/> (accessed January 6, 2016).
- [115] *ASM Handbook Volume 9: Metallography and Microstructures*, ASM International, 1985.

- [116] L.A. Giannuzzi, F.A. Stevie, eds., Introduction to Focused Ion Beams, Springer US, 2005. doi:10.1007/b101190.
- [117] L. Holzer, F. Indutnyi, P.H. Gasser, B. Münch, M. Wegmann, Three-dimensional analysis of porous BaTiO<sub>3</sub> ceramics using FIB nanotomography, *J. Microsc.* 216 (2004) 84–95.
- [118] A. Velichko, C. Holzapfel, F. Mücklich, 3D characterization of graphite morphologies in cast iron, *Adv. Eng. Mater.* 9 (2007) 39–45. doi:10.1002/adem.200600175.
- [119] M. Timpel, Einfluss von Strontium auf die Mikrostruktur von Aluminium-Silizium Legierungen, Doctor thesis, Helmholtz-Zentrum Berlin für Materialien und Energie, 2012.
- [120] D.C. Joy, D.E. Newbury, D.L. Davidson, Electron channeling patterns in the scanning electron microscope, *J. Appl. Phys.* 53 (1982) 81–122. doi:10.1063/1.331668.
- [121] S. Canovic, T. Jonsson, M. Halvarsson, Grain contrast imaging in FIB and SEM, *J. Phys. Conf. Ser.* 126 (2008) 1–4. doi:10.1088/1742-6596/126/1/012054.
- [122] Practical Guide to Image Analysis, ASM International, 2000.
- [123] BDG Bundesverband der Deutschen Gießerei-Industrie, BDG-Richtlinie: Bestimmung des Dendritenarmabstandes für Gussstücke aus Aluminium-Gusslegierungen, 2011.
- [124] aquinto AG, a4i applications for imaging. Benutzerhandbuch: Erweiterte Bildanalyse, 2003.
- [125] A. Velichko, F. Mücklich, Bildanalytische Formanalyse und Klassifizierung der irregulären Graphitmorphologie in Gusseisen, *Prakt. Metallogr. Metallogr.* 43 (2006) 192–208.
- [126] O. Wirjadi, K. Schladitz, A. Rack, T. Breuel, Applications of Anisotropic Image Filters for Computing 2D and 3D-Fiber Orientations, *Proc. 10th Eur. Congr. ISS.* (2009).
- [127] L. Staniewicz, T. Vaudey, C. Degrandcourt, M. Couty, F. Gaboriaud, P. Midgley, Electron tomography provides a direct link between the Payne effect and the inter-particle spacing of rubber composites, *Sci. Rep.* 4 (2014) 7389. doi:10.1038/srep07389.
- [128] M. Roland, A. Kruglova, N. Harste, F. Mücklich, S. Diebels, Numerical Simulation of Al-Si Alloys With and Without a Directional Solidification, *Image Anal. Stereol.* 33 (2014) 29–37. doi:10.5566/ias.v33.p29-37.
- [129] M. Roland, A. Kruglova, G. Gaiselmann, T. Brereton, V. Schmidt, F. Mücklich, et al., Numerical simulation and comparison of a real Al-Si alloy with virtually generated alloys, *Arch. Appl. Mech.* 85 (2015) 1161–1171. doi:10.1007/s00419-014-0956-5.

- [130] CEN Europäisches Komitee für Normung, Kunststoffe - Bestimmung der Zugeigenschaften - Teil 2: Prüfbedingungen für Form- und Extrusionsmassen (EN ISO 527-2:1993 einschließlich Corr 1:1994), 1996.
- [131] ASM Handbook Volume 8: Mechanical Testing and Evaluation, ASM International, 2000.
- [132] ASTM Standard E8/E8M - 11, Standard Test Methods for Tension Testing of Metallic Materials, ASTM International, West Conshohocken, PA, 2012. doi:10.1520/E0008.
- [133] A. Kruglova, M. Roland, S. Diebels, T. Dahmen, P. Slusallek, F. Mücklich, Modelling and characterization of ductile fracture surface in Al-Si alloys by means of Voronoi tessellation, *Mater. Charact.* 131 (2017) 1–11. doi:10.1016/j.matchar.2017.06.013.
- [134] C. Redenbach, Modelling foam structures using random tessellations, in: *Stereol. Image Anal. Proc 10th Eur Congr. ISS*, 2009.
- [135] A. Kruglova, M. Engstler, G. Gaiselmann, O. Stenzel, V. Schmidt, M. Roland, et al., 3D connectivity of eutectic Si as a key property defining strength of Al-Si alloys, *Comput. Mater. Sci.* 120 (2016) 99–107. doi:10.1016/j.commatsci.2016.04.019.
- [136] J. Ohser, K. Schladitz, *3D Images of Materials Structures: Processing and Analysis*, Wiley-VCH Verlag GmbH & Co. KGaA, Weinheim, 2009. doi:10.1002/9783527628308.
- [137] F. Mücklich, J. Ohser, G. Schneider, Die Charakterisierung homogener polyedrischer Gefüge mit Hilfe des räumlichen Poisson-Voronoi-Mosaiks und der Vergleich zur DIN 50 601, *Zeitschrift Für Met.* 88 (1997) 27–32.
- [138] A. Spettl, T. Brereton, Q. Duan, T. Werz, C.E. Krill, D.P. Kroese, et al., Fitting Laguerre tessellation approximations to tomographic image data, *Philos. Mag.* 96 (2016) 166–189. doi:10.1080/14786435.2015.1125540.
- [139] A. Alpers, A. Brieden, P. Gritzmann, A. Lyckegaard, H.F. Poulsen, Generalized balanced power diagrams for 3D representations of polycrystals, *Philos. Mag.* 95 (2015) 1016–1028. doi:10.1080/14786435.2015.1015469.
- [140] K. Teferra, L. Graham-Brady, Tessellation growth models for polycrystalline microstructures, *Comput. Mater. Sci.* 102 (2015) 57–67. doi:10.1016/j.commatsci.2015.02.006.
- [141] C. Lautensack, *Random Laguerre tessellations*, Doctor thesis, Karlsruhe Institute of Technology, 2007.
- [142] H. Altendorf, F. Latourte, D. Jeulin, M. Faessel, L. Saintoyant, 3D reconstruction of a multiscale microstructure by anisotropic tessellation models, *Image Anal. Stereol.* 33 (2014) 121–130. doi:10.5566/ias.v33.p121-130.

- [143] A. Kruglova, M. Roland, S. Diebels, F. Mücklich, Combination of experimental and numerical methods for mechanical characterization of Al-Si alloys, *IOP Conf. Ser. Mater. Sci. Eng.* 258 (2017) 012004. doi:10.1088/1757-899X/258/1/012004.
- [144] M. Timpel, N. Wanderka, B.S. Murty, J. Banhart, Three-dimensional visualization of the microstructure development of Sr-modified Al–15Si casting alloy using FIB-EsB tomography, *Acta Mater.* 58 (2010) 6600–6608. doi:10.1016/j.actamat.2010.08.021.
- [145] ASM Handbook Volume 2: Properties and Selection: Nonferrous Alloys and Special-Purpose Materials, ASM International, 1990.
- [146] F. Lasagni, H.P. Degischer, Enhanced Young's Modulus of Al-Si Alloys and Reinforced Matrices by Co-continuous Structures, *J. Compos. Mater.* 44 (2010) 739–755. doi:10.1177/0021998309347649.
- [147] J.E. Hockett, P.P. Gillis, Mechanical testing machine stiffness: Part I - Theory and calculations, *Int. J. Mech. Sci.* 13 (1971) 251–264. doi:10.1016/0020-7403(71)90007-5.
- [148] V. Beneš, M. Jiruše, M. Slámová, Stereological unfolding of the trivariate size-shape-orientation distribution of spheroidal particles with application, *Acta Mater.* 45 (1997) 1105–1113.
- [149] V. Bheemreddy, K. Chandrashekhara, L.R. Dharani, G.E. Hilmas, Modeling of fiber pull-out in continuous fiber reinforced ceramic composites using finite element method and artificial neural networks, *Comput. Mater. Sci.* 79 (2013) 663–673. doi:10.1016/j.commatsci.2013.07.026.
- [150] J.R. Davis, ed., *Corrosion of Aluminum and Aluminum Alloys*, ASM International, 1999.
- [151] V.D. Krstic, On the fracture of brittle-matrix/ductile-particle composites, *Philos. Mag. A.* 48 (1983) 695–708. doi:10.1080/01418618308236538.
- [152] S. Ranganatha, M.N. Srinivasan, Fracture toughness of cast aluminium alloys, *Bull. Mater. Sci.* 4 (1982) 29–35.